ANNALS OF THE UNIVERSITY OF CRAIOVA
ANNALES DE L'UNIVERSITÉ DE CRAIOVA

ANALELE UNIVERSITĂȚII DIN CRAIOVA

SERIA: INGINERIE ELECTRICĂ
SERIE: ELECTRICAL ENGINEERING
SÉRIE: INGÉNIERIE ÉLECTRIQUE
Anul/Year/Année 48
No. 48, Vol. 48, Issue 1, 2024

December 2024

ISSN 1842-4805 (print)
ISSN 2971-9852 (online)
ISSN-L 1842-4805

EDITURA UNIVERSITARIA

ANNALS OF THE UNIVERSITY OF CRAIOVA

13, A.I. Cuza Str., CRAIOVA 200585
ROMANIA

We exchange publications
with similar institutions of country and from abroad

ANNALES DE L'UNIVERSITÉ DE CRAIOVA

Rue A.I. Cuza, No. 13, CRAIOVA 200585
ROUMANIE

On fait des échanges des publications
avec les institutions similaires du pays et de l'étranger

This journal is published by the Faculty of Electrical Engineering from the University of Craiova.
The authors are fully responsible for the originality of their papers and for accuracy of their notes.

REVIEWERS COMMITTEE

Lia-Elena ACIU – *Transilvania University of Braşov,* Romania
Maricel ADAM – *"Gh. Asachi" Technical University of Iaşi,* Romania
Mihaela ALBU – *University "Politehnica" of Bucharest,* Romania
Slavoljub ALEKSIC – *University of Niš,* Serbia
Horia BĂLAN – *Technical University of Cluj-Napoca,* Romania
Alexandru BITOLEANU – *University of Craiova, Romania*
Maria BROJBOIU – *University of Craiova,* Romania
Emil CAZACU – *University "Politehnica" of Bucharest,* Romania
Aurel CÂMPEANU – *University of Craiova,* Romania
Mihai CERNAT – *Transilvania University of Braşov,* Romania
Marian CIONTU – *University of Craiova,* Romania
Daniel Cristian CISMARU – *University of Craiova,* Romania
Grigore CIVIDJIAN – *University of Craiova,* Romania
Zlata CVETCOVIC – *University of Niš,* Serbia
Leszek CZARNECKI – *Louisiana State University*, USA
Daniela DANCIU – *University of Craiova,* Romania
Sonia DEGERATU – *University of Craiova,* Romania
Iuliu DELEŞEGA – *University "Politehnica" of Timişoara,* Romania
Silvia-Maria DIGĂ – *University of Craiova,* Romania
Peter DINEFF – *Technical University of Sofia,* Bulgaria
Radu DOBRESCU – *University "Politehnica" of Bucharest,* Romania
Mircea-Adrian DRIGHICIU – *University of Craiova,* Romania
Laurentiu Marius DUMITRAN – *University "Politehnica" of Bucharest,* Romania
Sorin ENACHE – *University of Craiova,* Romania
Virgiliu FIRETEANU – *University "Politehnica" of Bucharest,* Romania
Dan FLORICĂU – *University "Politehnica" of Bucharest,* Romania
Cristian FOŞALĂU – *"Gh. Asachi" Technical University of Iaşi*, Romania
Teodor Lucian GRIGORIE – *Military Technical Academy ''Ferdinand I'',* Romania
Stefan HĂRĂGUŞ – *University "Politehnica" of Timişoara,* Romania
Elena HELEREA – *Transilvania University of Braşov,* Romania
Eugen HNATIUC – *"Gh. Asachi" Technical University of Iaşi,* Romania
Kemal HOT – *Polytechnic of Zagreb,* Croatia
Eugen IANCU – *University of Craiova,* Romania
Nathan IDA – *University of Akron,* USA
Maria IOANNIDES – *National Technical University of Athens,* Greece
Valentin IONIŢĂ – *University "Politehnica" of Bucharest,* Romania
Mihai IORDACHE – *University "Politehnica" of Bucharest,* Romania
Marcel ISTRATE – *"Gh. Asachi" Technical University of Iaşi*, Romania
Wilhelm KAPPEL – *National Research and Development Institute for Electrical Engineering (ICPE – CA) Bucharest,* Romania
Liviu KREINDLER – *University "Politehnica" of Bucharest,* Romania
Gheorghe LIVINŢ – *"Gh. Asachi" Technical University of Iaşi*, Romania
Dumitru Dorin LUCACHE – *"Gh. Asachi" Technical University of Iaşi*, Romania
Lucian MANDACHE – *University of Craiova,* Romania
Gheorghe MANOLEA – *University of Craiova,* Romania
Andrei MARINESCU – *Romanian Academy of Technical Science, Craiova Branch,* Romania
Iliana MARINOVA – *Technical University of Sofia,* Bulgaria
Claudia MARTIŞ – *Technical University of Cluj-Napoca,* Romania
Ernest MATAGNE – *Université Catholique de Louvain,* Belgium

CONTENTS

DOI: 10.52846/AUCEE.2024.01

Performance Analysis of a Rotor Flux-Oriented Control in Induction Traction Motor

Tudor Mătușa*, Mihaela Popescu*, Alexandru Bitoleanu* and Constantin Vlad Suru*
* University of Craiova, Faculty of Electrical Engineering, Craiova, Romania, matusa.tudor.e8y@student.ucv.ro
mpopescu@em.ucv.ro, alex.bitoleanu@em.ucv.ro, vsuru@em.ucv.ro

***Abstract* - The superiority of using field-oriented control in electric drive systems based on induction motor has been proven over the years. To increase efficiency, maintainability, reliability and dynamic performance, modern electric traction systems use induction motors. In this context, this paper is focused on the performance determination and analyzing of the rotor flux-oriented control with voltage control, on an induction traction motor, in order to its implementation. First, the control scheme and calculation fundamentals are presented. Then, after the entire system modeling in Simulink environment, the performance of the system in dynamic and steady-state regimes is presented by simulating the operation of a real traction motor at three prescribed speeds. Also, a specific phenomenon of electric locomotives, respectively the passage of wheels over the rail joints is taking into account. To determine the performances, the results obtained from simulating the acceleration process by prescribing a speed ramp, operating in steady-state regime and then electric braking with energy recovery were analyzed. In the paper, three situations are presented: the prescription of a low speed, about 20 % of the nominal speed, of the highest speed, about 160 % of the nominal speed and of three speed steps up to the nominal speed. The analysis of the results leads to the conclusion that there is a very accurate tracking of the prescribed quantities by the actual quantities controlled in the system. It is also highlighted that the peak current through the motor does not exceed its limiting value and the switching frequency of the power electronic devices is lower than the imposed limit value. The analysis of steady-state performance shows that it is also very good.**

Cuvinte cheie: *control orientat după fluxul rotoric, motor cu inducție, sistem de tracțiune, control al vitezei..*

Keywords: *rotor flux-oriented control, induction motor, traction system, speed control.*

I. INTRODUCTION

It is well known that the principle of the field-oriented control proposed by Blaschke [1] starts from the goal of obtaining a behavior of the induction motor similar to that of the DC motor. Explicitly, this means that the torque and the magnetic flux are decoupled. In this way, the magnetic flux and the torque developed by the motor are controlled independently, and the synthesis of the regulators in the structure of the control scheme is more precise, because it operates with quantities whose steady-state values are constant. Most contributions in the literature over time are related to improving performance and also to the implementation of the controls strategies [2]–[20].

The main specific requirements for electric traction systems with induction motors refer to: high power, speed regulation in a wide range (from about 2% to (160-200)% of the nominal frequency), high starting torques, but with a sufficiently low increase in speed, to avoid the phenomenon of slipping, efficient braking with kinetic energy recovery and high reliability.

In order to respond to these requirements and to have a less complicated control, the rotor flux-oriented control is often adopted. It involves working in the (d, q) rotating reference frame, whose d-axis is aligned with the vector of rotor flux. In this way, the control of rotor flux is performed by means of the d-axis stator current of the motor, while the control of the torque is achieved through the q-axis stator current. Moreover, it is allowed to extend the speed variation range well above the nominal speed by weakening the field [4]–[7].

Regarding the type of adopted control (direct or indirect), it is specified that the most frequently used is indirect control [8]-[14]. Thus, the rotor flux and its position angle are calculated using some easily measurable quantities, using the induction motor model and it is not necessary to place sensors in the rotor circuit (as is specific to direct control).

The existence of four controllers (speed controller and active current controller in the first path and, respectively, rotor flux controller and reactive current controller in the second path) is specific to voltage control of the system. Among the modulation strategies adopted in the inverter control, sinusoidal modulation stands out [12], [15], [16].

Among the application areas of the field-oriented control, electric traction is also found [5], [12]–[18].

It should be noted that, in the case of railway traction, the control system must manage the behavior of the system when the wheels pass over the rail joints, so as to minimize the effects that occur. There are very few approaches in the literature on this topic. [19], [20].

This paper deals with the implementation of the rotor flux-oriented control with voltage control on a traction induction motor used in Romanian locomotives. Next, the structure of the paper is as follows. The adopted control scheme and the related calculation bases are the subject of Section II. The MATLAB SIMULINK implementation of the control algorithm is presented in the next section. Then, the performance of the traction system with rotor flux-oriented control is analyzed both in the dynamic regime and in the steady-state regime. Thus, the results obtained from simulating the acceleration process by prescribing a speed ramp, operation in steady-state regime and then electric braking with energy recovery, in three cases are presented, as follows: prescribing of a low speed

(about 20 % of the nominal speed); prescribing speed up to nominal value in three steps and braking in two steps; prescribing of the highest speed (about 160 % of the nominal speed). Finally, some conclusions are formulated.

II. The Control Scheme and Calculation Fundamentals

As illustrated in Fig. 1, there are two cascade control paths in the control system. Also, each o them contains two controllers, so that, there are four controllers.

In the first control path (of the speed and active current), the speed controller (R_ω) provides the prescribed active current (i^*_{sq}) and the active current controller (R_{iq}) provides the quantity u^*_{sq}, which is the prescribed voltage on the q axis of the system synchronous with the rotor flux vector.

In the second control path (of the rotor flux and reactive current), the flux controller (R_ψ) provides the prescribed reactive current (i^*_{sd}), and the reactive current controller (R_{id}) provides the quantity u^*_{sd}, which is the prescribed voltage on the d axis of the system synchronous with the rotor flux vector.

A two-step conversion of the prescribed quantities u^*_{sq} and u^*_{sd} follows. In the first stage (block B1), the conversion is from rotating coordinate system (d, q) to the fixed coordinate system (α, β).

In the second stage (block B2), the conversion is from fixed coordinate system (α, β) to the three-phase system (quantities u^*_a, u^*_b and u^*_c). Then, the sinusoidal modulator (PWM block) performs the synthesis of the control signals for the inverter transistors.

On the feedback path, the three stator currents $i_{sa,b,c}$ measured with current transducers T_i are transformed (in block B3), from the three-phase system (a, b, c) to the fixed coordinate system (α, β) characterised by the components $i_{s\alpha}$ and $i_{s\beta}$. Specific relationships are used for the transformation from one coordinate system to another [20].

As shown in Fig. 1, using the measured currents and the measured speed ω with the speed transducer T_ω, the rotor flux Ψ_r, and its position angle λ between the rotating coordinate system (d, q) and fixed coordinate system (α, β) are calculated in block B4.

The rotor flux components in the fixed coordinate system (α, β) are calculated as follows [20]:

$$\psi_{r\alpha} = \int \left(-p\omega\psi_{r\beta} - \frac{1}{T_r}\psi_{r\alpha} + \frac{L_m}{T_r} i_{s\alpha}\right) dt\,; \quad (1)$$

$$\psi_{r\beta} = \int \left(p\omega\psi_{r\alpha} - \frac{1}{T_r}\psi_{r\beta} + \frac{L_m}{T_r} i_{s\beta}\right) dt; \quad (2)$$

Thus, the calculated rotor flux is expressed as:

$$|\psi_r| = \sqrt{\psi^2_{r\alpha} + \psi^2_{r\beta}}\,; \quad (3)$$

In the above expressions, $T_r = L_r/R_r$, R_r and L_r are the resistance and inductance on a rotor phase referred to the stator, L_m is the magnetization inductance, p is the number of pole pairs, and the angle λ is determined by trigonometric functions [20]:

$$\cos(\lambda) = \frac{\psi_{r\alpha}}{|\psi_r|} = \frac{\psi_{r\alpha}}{\sqrt{\psi^2_{r\alpha}+\psi^2_{r\beta}}}\,; \quad (4)$$

$$\sin(\lambda) = \frac{\psi_{r\beta}}{|\psi_r|} = \frac{\psi_{r\beta}}{\sqrt{\psi^2_{r\alpha}+\psi^2_{r\beta}}}\,; \quad (5)$$

The transformation of the stator currents from the stationary reference frame (α, β) to the rotating reference frame (d, q) is achieved in block B5..

Finally, the sinusoidal modulation principle is implemented in the PWM modulator block, having as inputs the prescribed phase voltages.

III. Matlab-Simulink Implementation of the Control Algorithm

A specific Matlab-Simulink model has been created to determine the dynamic and steady-state performance of the system (Fig. 2). In addition to the main blocks, there are auxiliary blocks used to determine the quantities of interest.

The power part in Fig. 2 consists of the DC source equivalent to the intermediate circuit, the voltage inverter and the squirrel-cage induction motor.

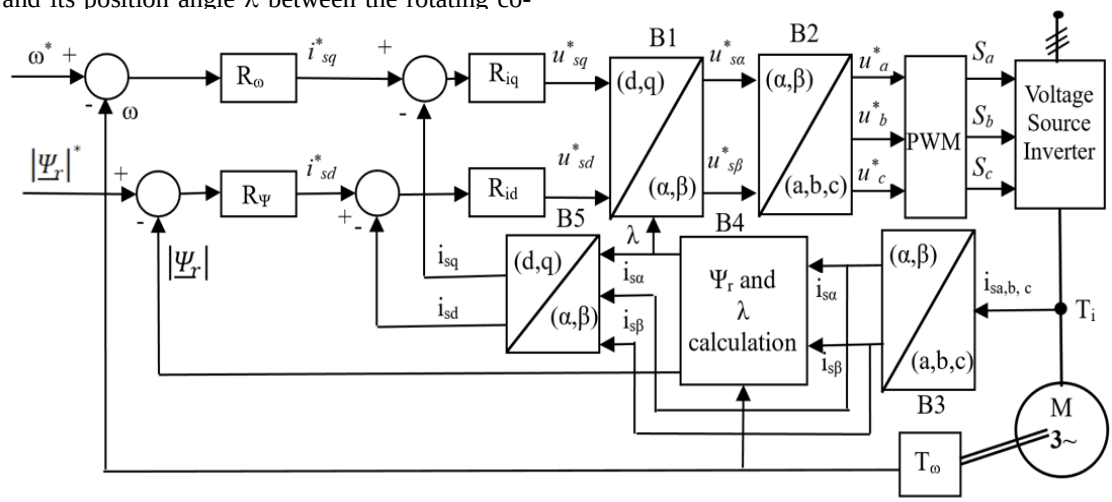

Fig. 1. Rotor flux and speed control scheme of a traction induction motor, based on rotor field-oriented control, with PWM modulator and voltage control.

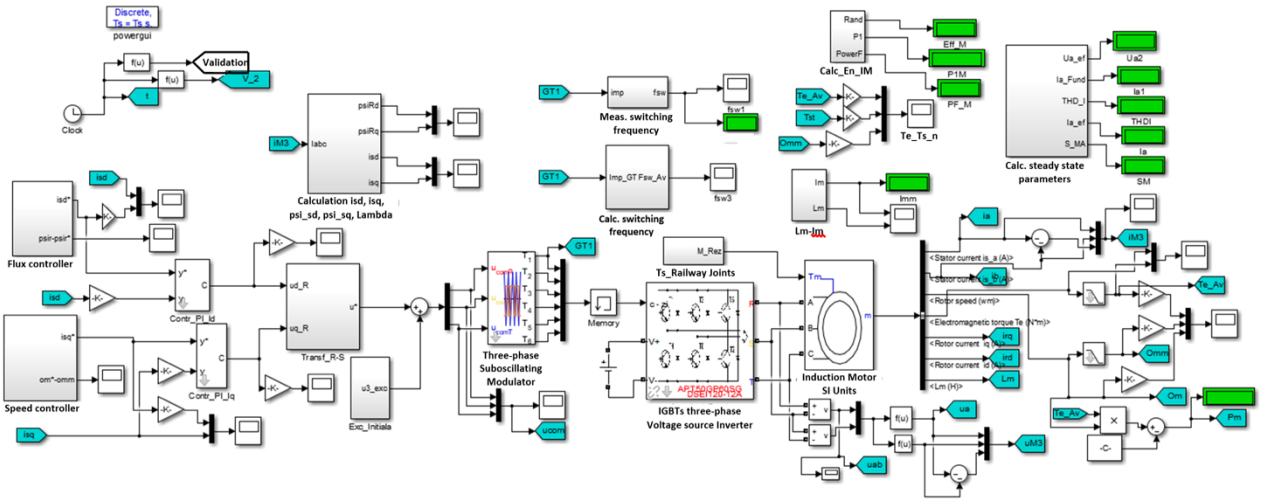

Fig. 2. Traction system Simulink model for testing the voltage control algorithm with sinusoidal PWM modulator and prescribing the rotor flux and speed.

In the control part, there are the rotor flux controller, the speed controller, the block for calculating the prescribed voltages on the motor phases from the stator current components in the rotor field oriented system "Transf_R-S", the three-phase sinusoidal modulator which also implements the voltage controllers for the three motor phases and the "Ts_Railway Joints" block which implements the resistant torque. There are also the current controllers and the three-phase sinusoidal modulator (block "Three-phase Suboscillating Modulator").

In the part of feedback control (block "Calculation isd, isq, psi_sd, psi_sq, Lambda), the main quantities are calculated by estimation. Also, the estimated magnetization inductance is used, which is obtained from the motor model based on the voltage – current dependence at idle conditions

There is a part for the calculation of steady-state energetic indicators (block "Calc. steady state parameters" which calculates and displays the phase voltage, the fundamental RMS current, total RMS current), harmonic distortion factor (*THD*) factor of the current through the motor and the apparent power).

Some quantities, such as the efficiency, power factor and active power related to the induction motor, are calculated and displayed in the block "Calc_En_IM". The three-axis oscilloscope "Te-Ts-n" displays the average torque, the resistant torque and the motor speed.

It should be noted that the speed controllers, as well as other calculation and display blocks, are validated by two signals obtained as functions of time, in the blocks at the top left of the figure. So, the speed and torque prescription takes place only after the motor is magnetized. Also, the rotor flux has the prescribed value.

A few more clarifications need to be made, as below.

The used controllers are of the proportional-integral (PI) type.

The rotor flux and the motor speed are prescribed as ramp signals.

For the limitation of the current, the outputs of the controllers are not limited to the input level (+10), but +5 V for the flux controller and +9.2 V for the speed controller.

In order to ensure the compatibility of the algorithm with the DSP system used on locomotives (Texas Instruments TMS320F28335), the Euler 1 integration method and the 40μs step (Ts) were used.

The sinusoidal PWM modulator operates with a switching frequency of 1 kHz.

In order to allow the overmodulation to achieve the nominal power at 100 Hz, the amplitude of the modulating (triangular) signal is 2.25 V, which also minimizes the current distortion and limits the noise.

IV. Performance of the Traction System

Table I and Table II illustrate the main parameters of the traction induction motor (a traction motor used in Romanian locomotives) and of the PI controllers. The value of the DC-voltage at the IGBT-based voltage source inverter input is 1800 V.

The motor start-up at constant resistant torque (T_s) and nominal rotor flux for speed below the rated value and diminished over the rated value, in case of three prescribed ramp speeds (248 rpm, three speed steps up to the nominal speed and maximal speed of 1983 rpm), are analyzed. Also, the periodic passage of wheels over rail joints was considered. For this, the load torque variation shown in Fig. 3 is considered, with the following parameters: $T_{sp} = 0.25 \cdot T_s$; $T_{sn} = -0.5 \cdot T_s$; $T_{mj} = 4$ s; $dt1 = 0.05 \cdot Tmj$; $dt0 = 0.1 \cdot dt1$; $dt2 = dt1$.

TABLE I.
Main Parameters of the Traction Induction Motor

V_N (V)	P_{2N} (kW)	f_{1N} (Hz)	I_N (A)	p	s_N	n_N (rpm)
1400	1150	62.5	576	3	0.0104	1237
T_N (N·m)	R_1 (Ω)	$L_{σ1}$ (mH)	R_2 (Ω)	$L_{σ2}$ (mH)	R_m (Ω)	L_{mN} (mH)
8877	0.021	0.288	0.012	0.275	89.38	9.46

TABLE II.
Parameters of the PI Controllers

$K_{pΩ}$	$T_{iΩ}$	$K_{pψ}$	$T_{iψ}$	K_{pid}	T_{iid}	K_{piq}	T_{iq}
100	0.004	10	0.04	0.3	0.1	0.15	0.6

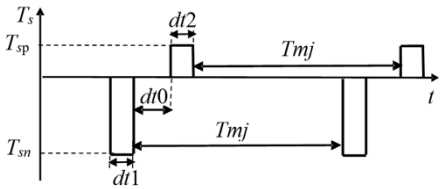

Fig. 3. Load torque during the passage of wheels over rail joints.

The evolution of several quantities (speed, rotor flux, electromagnetic torque, phase current, current and voltage components in the rotating reference frame, control and switching frequency) are analyzed. Also, different quantities specific to the steady-state operation and energetic indicators are given for each case study.

A. Case of Prescribed Speed of 248 rpm and T_s=T_N

When a low ramp speed of about 20% of the nominal speed (248 rpm) is prescribed at nominal resistant load, Fig. 4 – Fig. 14 illustrate the good response of the system.

It can be seen that the motor speed is very close to the prescribed value and, at the end of acceleration, the motor torque is very close to the load torque (Fig. 4). The speed is very little affected by the appearance of the rail joints, only ±2% (Fig. 4 and 5).

The rotor flux also faithfully follows the prescribed value (Fig. 6).

The i_{sd} current has a maximum for fast motor magnetization (Fig. 7), then become constant. The active current (i_{sq}) follows the evolution of the torque (Fig. 8). There are some current increases (about 1100 A, but maxim admissible value is 1200 A) related to the appearance of the rail joints (Fig. 9).

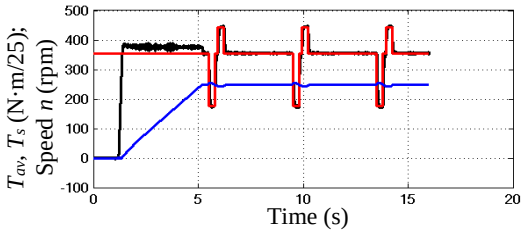

Fig. 4. Time evolution of the average torque (black), resistant torque (red) and speed (blue) at the prescribed speed of 248 rpm during the whole process.

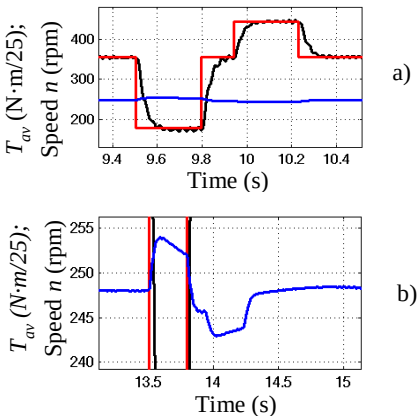

Fig. 5. Details in fig a) and b) regarding the evolution of the average torque (black), resistant torque (red) and speed (blue) during the passage of a wheel over a rail joint at the prescribed speed of 248 rpm.

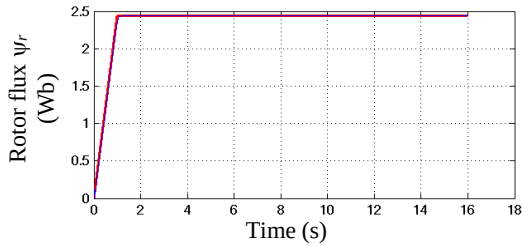

Fig. 6. Rotor flux (prescribed – in red and actual – in black) at the prescribed speed of 248 rpm.

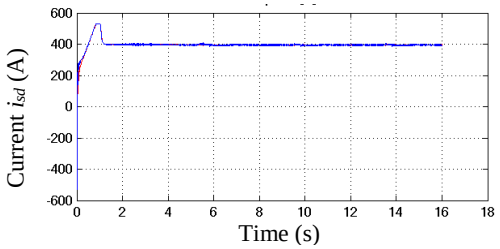

Fig. 7. d-axis stator current (prescribed – in red and actual – in black) at the prescribed speed of 248 rpm.

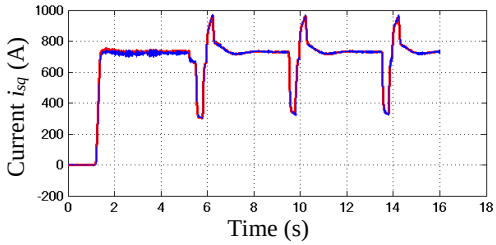

Fig. 8. q-axis stator current (prescribed – in red and actual – in black) at the prescribed speed of 248 rpm.

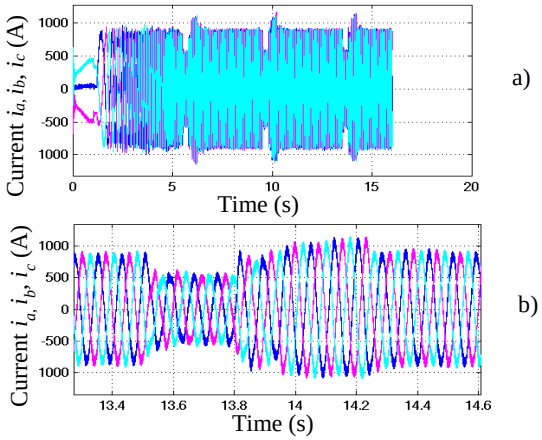

Fig. 9. Stator currents on the three phases at the prescribed speed of 248 rpm: a) during the whole process; b) detail on an interval of 1.2 s.

The resulted d and q components of the stator voltage are illustrated in Fig. 10 and Fig. 11, and show that there are low influences between them. As shown in Fig. 12 and Fig. 13, the switching frequency is variable, but it average value does not exceed 1 kHz. Fig. 13 shows the increase of the stator voltage frequency up to the value of about 13 Hz.

Table III synthesizes the dynamic performance of the system. δT and δn are the torque and speed variations. Table IV summarizes the steady-state performance. A low power factor (*PF*) of 37 % and a relatively low value of the current harmonic distortion (THD_I) of 7 % are highlighted.

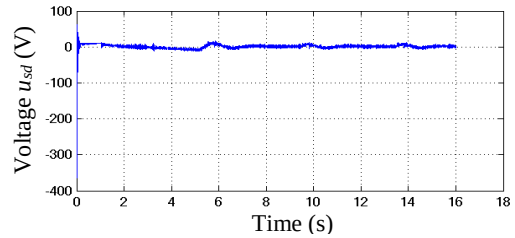

Fig. 10. d-axis component of the stator voltage at the prescribed speed of 248 rpm.

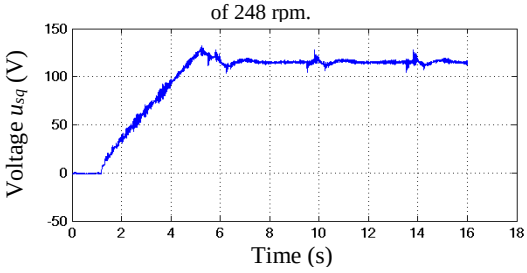

Fig. 11. q-axis component of the stator voltage at the prescribed speed of 248 rpm.

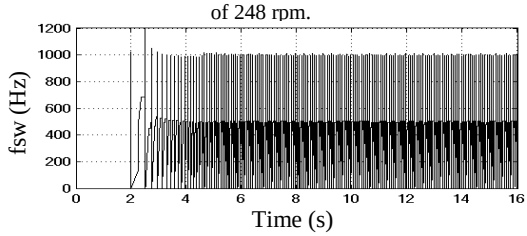

Fig. 12. Evolution over time of the average switching frequency at the prescribed speed of 248 rpm.

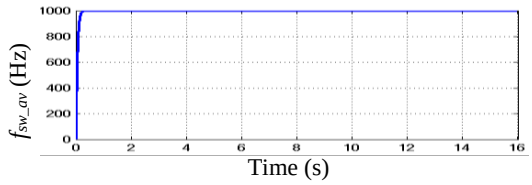

Fig. 13. The average switching frequency (averaged over 10 ms), at the prescribed speed of 248 rpm.

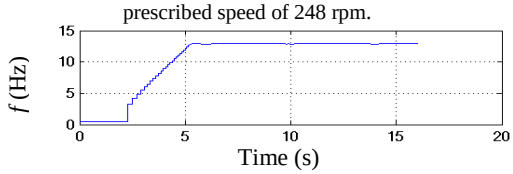

Fig. 14. The control frequency, at the prescribed speed of 248 rpm.

TABLE III.
DYNAMIC PERFORMANCE AT THE PRESCRIBED SPEED OF 248 RPM

T_{s-} (%)	T_{s+} (%)	δT (%)	δn_+ (%)	δn_- (%)	$I_{max.\_acc.}$ (A)	$I_{max.\_steady-st.}$ (A)	f_{sw_max} (kHz)
-50	25	100	2	2	1100	1160	1

TABLE IV.
STEADY-STATE PERFORMANCE AT THE PRESCRIBED SPEED OF 248 RPM

V (V)	I [A]	$I_{magn.}$ (A)	P_1 (kW)	P_m (kW)	S (kVA)	PF (%)	η (%)	THD_I (%)
398	596	209	260	225	701	37	86.73	7

B. Prescribing Speed up to Nominal Value in Three Steps and Braking in Two Steps

For prescribing speed step by step up to the nominal value, also with brake, the waveforms of the main quantities are illustrated in Fig. 15 - Fig. 24. (the passage of wheels over the rail joints is neglected).

First, new information is offered by d-axis stator current (Fig. 15) that, after 10 seconds decreases, although the rotor flux remains constant (Fig. 16). After the brake control is given, the current increases and reach the rated value. The speed follows the prescribed values both during the accelerating and braking regimes (Fig. 17). The q-axis stator current (Fig. 18) has the constant values in steady-state, increases in the time of acceleration and decreases in braking time. It is significant that, it does not have negative values, similar to the torque (Fig. 19). It means that the motor does not operate in braking regime and the decreasing of the speed is caused by the resistant torque only.

The phase currents of the motor are under 1000 A on the first two steps and exceed a little 1000 A at the nominal speed (Fig. 20). The average switching frequency is 1 kHz for speed under 1000 rpm, but decreases to 400 Hz when the speed is over 1000 rpm (Fig. 21).

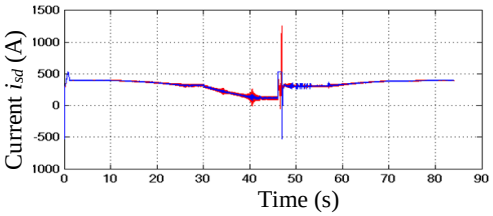

Fig. 15. Time evolution of stator current along the d-axis (prescribed in blue and actual in red) when speed is stepped up to nominal speed and braking.

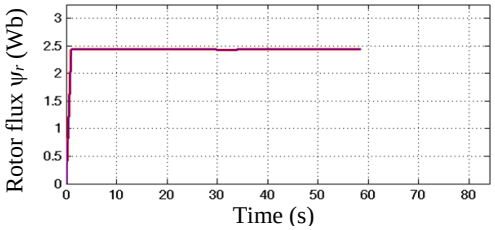

Fig. 16. The time evolution of the rotor flux (prescribed and actual in red) from speed prescription in steps up to nominal speed and braking.

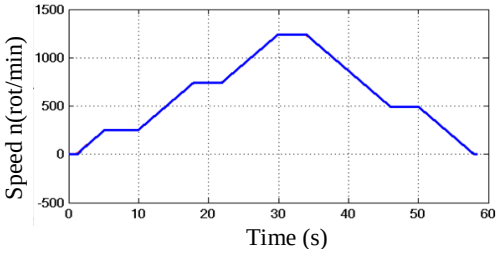

Fig. 17. Speed evolution over time (prescribed in blue and actual in red), in the case of speed prescription in gears up to nominal speed and braking.

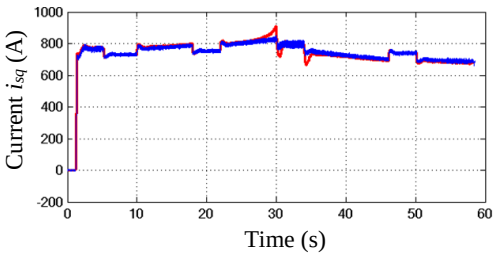

Fig. 18. The time evolution of the q-axis component of the stator current (prescribed in blue and actual in red), when prescribing the speed in steps up to rated speed and braking.

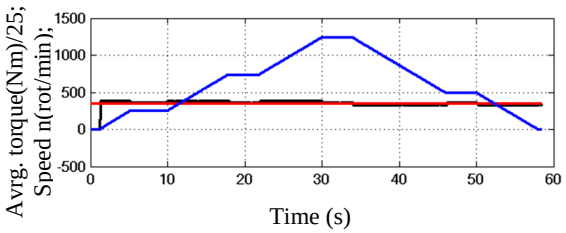

Fig. 19. Evolution over time of the average torque (black) and speed (blue), when prescribing the speed in gears up to nominal speed and braking.

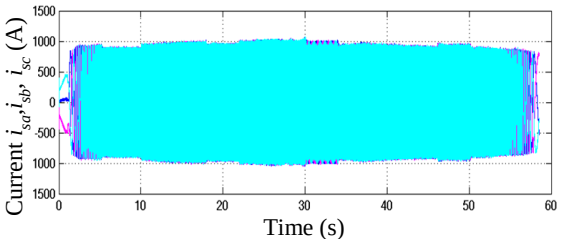

Fig. 20. Time evolution of the currents on the 3 phases, from speed prescription in steps up to nominal speed and braking.

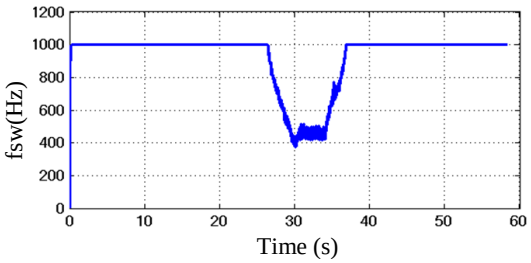

Fig. 21. The time evolution of the switching frequency averaged over 10 ms, when prescribing the speed in steps up to nominal speed and braking.

The time evolution of the stator voltage on the component along the d-axis is similar to that of the stator current of the same axis (Fig. 22), because the voltage determines the current.

Because the rotor flux is constant, the time evolution of the stator voltage component on the q-axis is similar to that of the torque (Fig. 23).

The form of the cosin of the rotor flux position angle (Fig. 24-a) proves a good orientation of the calculation system. The control frequency follows the speed as form (Fig. 24-b). It means that the slip is very low.

C. Case of Prescribed Speed of 1983 rpm and T_s=0.625·T_N

For the highest speed (1983 rpm), the waveforms of the main quantities are illustrated in Fig. 25 - Fig. 37 and the performance summary is presented in Table V and Table VI. The resistant torque is diminished so that, over the nominal speed, the power to be at nominal value.

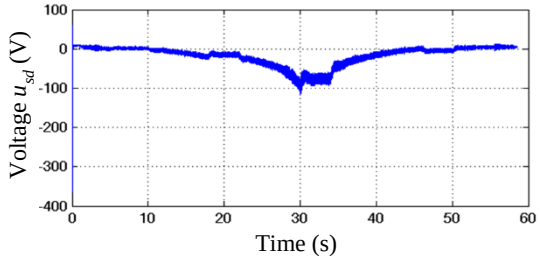

Fig. 22. The time evolution of the component along the d-axis of the stator voltage, in the case of stepped speed prescription up to rated speed and braking.

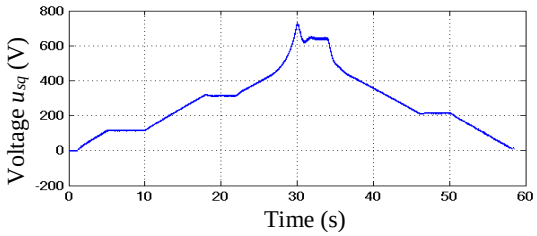

Fig. 23. The time evolution of the component along the q-axis of the stator voltage, in the case of stepped speed prescription up to rated speed and braking.

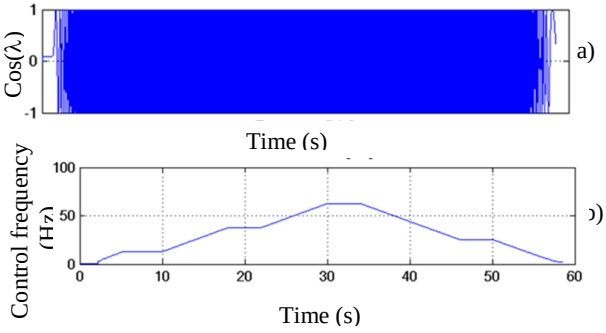

Fig. 24. The evolution over time of: a) the cosine of the angle of the rotating system; b) the control frequency, in the case of prescribing the speed in steps up to nominal speed and braking.

The prescribed speed is followed very well by the real speed and the effects of passing the joints are diminished (Fig. 25). The details from Fig. 26 and Fig. 27 underline some aspects. Thus, the motor torque does not follow the resistant torque, and its variation represents less than 50% of resistant torque variation. The total and the d-axis rotor flux are diminished over nominal speed and have a hyperbolic evolution (Fig. 28 and Fig. 29). Also, the q-axis rotor flux is null because the calculation system is well oriented (Fig. 29). The d-axis stator current decreases when the speed increases, especially over of the nominal speed (Fig. 30). At nominal speed, the d-axis stator current becomes near zero. The q-axis stator current increases when the speed exceeds the nominal value and magnetic flux decreases (Fig. 31). The real current does not have variations when the wheels passing over the joints.

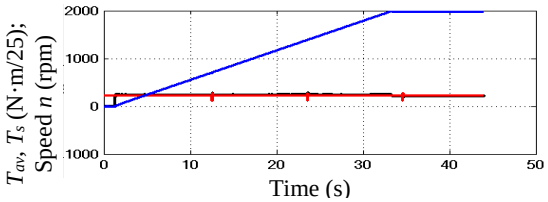

Fig. 25. Time evolution of the average torque (black), resistant torque (red) and speed (blue) at the prescribed speed of 1983 rpm.

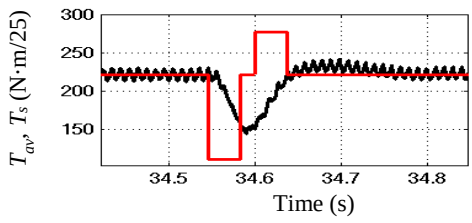

Fig. 26. Detail regarding the evolution of the average torque (black) and resistant torque (red) during the passage of a wheel over a rail joint at the prescribed speed of 1983 rpm.

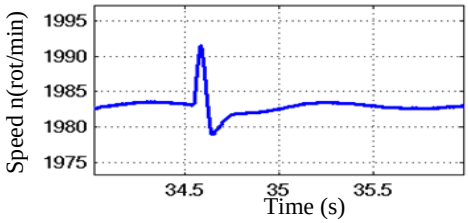

Fig. 27. Detail regarding the evolution of the speed during the passage of a wheel over a rail joint at the prescribed speed of 1983 rpm.

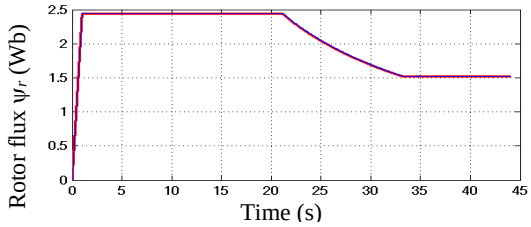

Fig. 28. Rotor flux (prescribed – in red and actual – in black) at the prescribed speed of 1983 rpm.

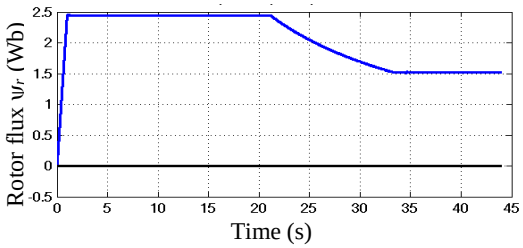

Fig. 29. Components of the rotor flux on the two axes (d-axis rotor flux – in blue and q-axis rotor flux – in black) at the prescribed speed of 1983 rpm.

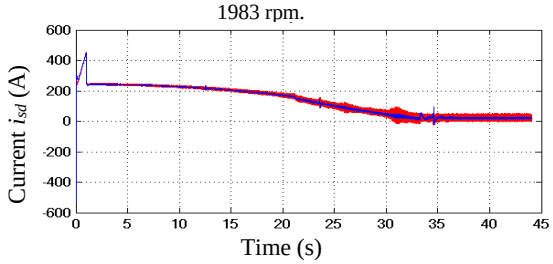

Fig. 30. d-axis stator current (prescribed – in red and actual – in black) at the prescribed speed of 1983 rpm.

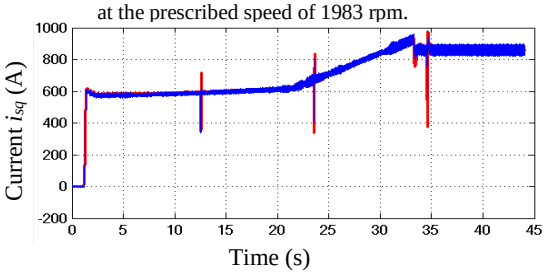

Fig. 31. q-axis stator current (prescribed – in red and actual – in blue) at the prescribed speed of 1983 rpm.

This aspect is showed better by phases current (Fig. 32). There is a little diminution of the current when the prescribed speed is obtained and the acceleration torque disappears. The d-axis component of the stator voltage evolves similarly to that of the corresponding current (Fig. 33). It should be noted that the final values are negative (about – 250 V).

Also, the q-axis component of the stator voltage evolves similarly to that of the active current (Fig. 34). After the nominal value of the supply voltage is obtained, the switching frequency decreases because the phase voltage is more little modulated (Fig. 35). The control frequency increases to 100 Hz, larger of 1.6 time from the nominal value (Fig. 36).

The magnetizing inductance and current (Fig. 37), shows that the inductance increases a little although the current decreases from 180 A to 100 A. This means that the motor is not saturated.

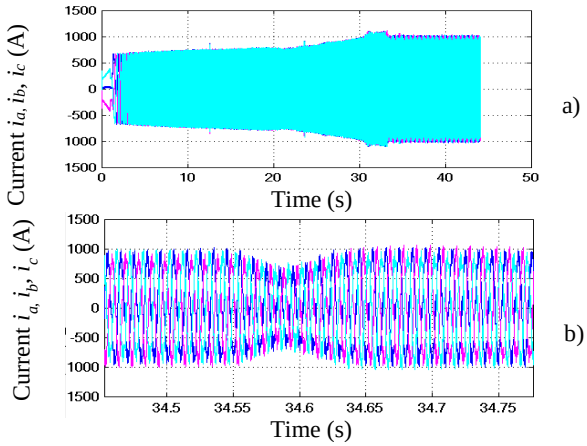

Fig. 32. Stator currents on the three phases at the prescribed speed of 1983 rpm: a) during the whole process; b) detail during the passage of a wheel over a rail joint.

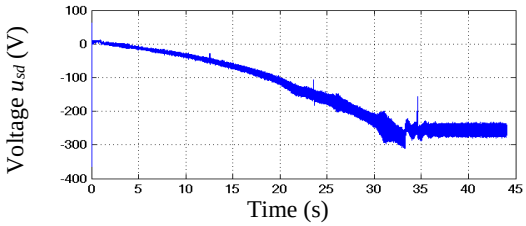

Fig. 33. d-axis component of the stator voltage at the prescribed speed of 1983 rpm.

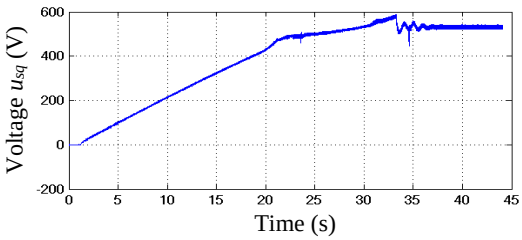

Fig. 34. q-axis component of the stator voltage at the prescribed speed of 1983 rpm.

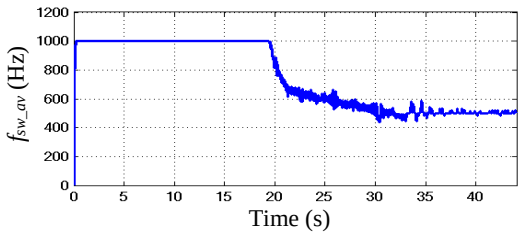

Fig. 35. The average switching frequency (averaged over 10 ms), at the prescribed speed of 1983 rpm.

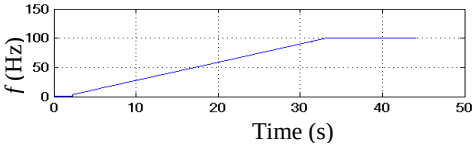

Fig. 36. The control frequency, at the prescribed speed of 1983 rpm.

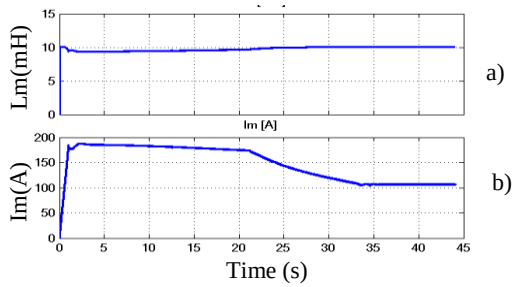

Fig. 37. Time evolution of: a) magnetizing inductance; b) magnetizing current, at the prescribed speed of 1983 rpm.

V. Possibility Of Implementation

The d-axis stator current decreases with increasing speed although the rotor flux is constant. This aspect does not respect the physical phenomenon and the operating equations of the induction motor in the rotor flux oriented system [12]:

$$0 = R_r i_{rd} + \frac{d}{dt}\Psi_{rd}; \tag{6}$$

$$\Psi_{rd} = L_r i_{rd} + L_m i_{sd}. \tag{7}$$

Equations (6) and (7) show that, if ψ_{rd}=constant, two very important aspects can highlight the correctness of the algorithm: $i_{rd} = 0$; $i_{sd} = \psi_{rd}/L_m$ = constant, because ψ_{rd} = constant also involves L_m = constant.

It is found that, even at very high speed, the performance is good (Tab. V and VI).

TABLE V.
Dynamic Performance at the Prescribed Speed of 1983 rpm

T_{s-} (%)	T_{s+} (%)	δT (%)	δn_+ (%)	δn_- (%)	$I_{max.\_acc.}$ (A)	$I_{max.\_steady-st.}$ (A)	f_{sw_max} (kHz)
-50	25	75	0.5	0.23	1100	1025	1

TABLE VI.
Steady-State Performance at the Prescribed Speed of 1983 rpm

V (V)	I [A]	$I_{magn.}$ (A)	P_1 (kW)	P_m (kW)	S (kVA)	PF (%)	η (%)	THD_I (%)
828	614	107	1184	1124	1526	77.6	94.95	17.23

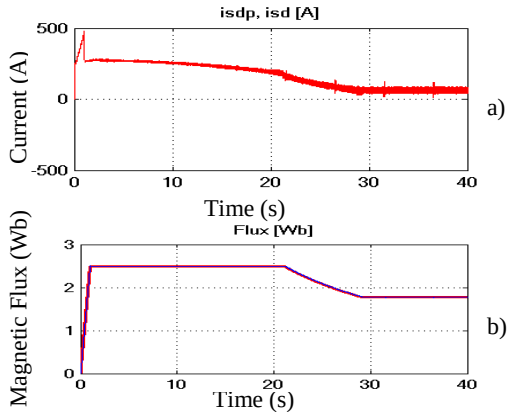

Fig. 38. Time evolution of: a) current; b) magnetic flux, at the prescribed speed of 1983 rpm.

It is appreciated that the appearance is determined by the calculation error, especially when calculating the position angle of the rotor flux. There are two ways to reduce calculation errors: using a smaller integration step and using an integration method of order 2 or higher. The first modality was verified for Ts=5μs (Fig. 38). But, this sampling period can't be used for real-time implementation, because it is too small.

In same time, the dSPACE 1103 prototyping board, used for the code generation operates by first order integration method, as the used processor too. Consequently, the research activity will continue with the development, implementation and testing of a calculation sequence that details the 2nd order integration. Only then, will tests be carried out on the physical model.

VI. Conclusions

Following the analysis of the energetic and dynamic performance of the traction system with rotor flux-oriented control in the acceleration, steady state and braking regimes, few aspects can be highlighted.

The evolution of all quantities, excepting d-axis stator current, respects the physical phenomenon and the operating equations of the motor.

The current absorbed by the motor is higher than the nominal value, by about 3% at the low prescribed speed and by about 10% at the highest prescribed speed.

The power factor is significantly lower than in sinusoidal supply conditions and increases with speed. The efficiency has very good values (86.73 % to 97.3 %). *THDI* has a low value (7%) at low speed and increases at high speed (17.23%).

The maximum average switching frequency is below the maximum allowed value of 1100 Hz.

When passing over the rail joints, the torque accurately follows the variations of the resistant torque, so the speed variations are very small. In conclusion, the rotor flux-oriented control leads to good performance when applied to the traction induction motor.

Acknowledgment

Source of research funding in this article: Research program financed by the University of Craiova.

Contribution of authors:

First author – 50%

First coauthor – 30%

Second coauthor – 10%

Third coauthor – 10%

Received on September 7, 2024

Editorial Approval on December 2, 2024

References

[1] F. Blaschke, "The principle of field orientation as applied to the new transvector closed loop control system for rotating field machines," *Siemens Rev*, vol. 39, no. 5, pp. 217–220, May 1972.

[2] B. Robyns, B. François, P. Degobert, and J.P. Hautier, *Vector Control of Induction Machines*, Springer, 2012.

[3] N.P. Quang and J.-A. Dittrich, *Vector Control of Three-Phase AC Machines*, Springer, 2015.

[4] S. Peresada, Y. Nikonenko and S. Kovbasa, "Field-weakening methods for torque-flux direct field-oriented control of induction motors," *2022 IEEE 8th International Conference on Energy Smart Systems (ESS)*, Kyiv, Ukraine, 2022, pp. 292-296.

[5] M. Popescu, A. Bitoleanu and C. V. Suru, "Influence of locomotive wheels slipping on a traction system with rotor flux-oriented

control and hysteresis current controllers," *2023 13th International Symposium on Advanced Topics in Electrical Engineering (ATEE)*, Bucharest, Romania, 2023, pp. 1-6.

[6] P. Xie, G. Li, F. Xie, C. Hu and X. Qi, "Research on field-weakening control of induction motor based on torque current component of the voltage closed-loop," *2015 IEEE 10th Conference on Industrial Electronics and Applications (ICIEA)*, Auckland, New Zealand, 2015, pp. 1618-1621.

[7] F. Briz, A. Diez, M. Degner, and R. Lorenz, "Current and flux regulation in field-weakening operation [of induction motors]," *IEEE Trans. On Industry Applications*, vol. 37, no. 1, pp. 42-50, 2001.

[8] S. K. Kakodia and G. Dynamina, "A Comparative study of DFOC and IFOC for IM drive, " *2020 First IEEE International Conference on Measurement, Instrumentation, Control and Automation (ICMICA)*, Kurukshetra, India, 2020, pp. 1-5.

[9] I. Ferdiansyah, S. D. Nugraha, O. A. Qudsi, L. P. S. Raharja, D. S. Yanaratri and R. P. Eviningsih, "Implementation of FPGP-PID for dynamic speed control of three phase induction motor based on IFOC," *2019 6th International Conference on Instrumentation, Control, and Automation (ICA)*, Bandung, Indonesia, 2019, pp. 24-29.

[10] H. Kim, Y. Han and K. Lee, "Improved Q-MRAS based online rotor time constant compensation for IFOC induction motor drives," *2023 IEEE Applied Power Electronics Conference and Exposition (APEC)*, Orlando, FL, USA, 2023, pp. 1-6.

[11] S. Yadav and A. K. Mishra, "Performance evaluation in IFOC induction motor drive with various PWM techniques," *2020 International Conference on Electrical and Electronics Engineering (ICE3)*, Gorakhpur, India, 2020, pp. 65-70.

[12] M. Popescu, A. Bitoleanu and C. V. Suru, "Performance of traction system with induction motor and rotor field orientation by voltage control", *2022 22nd International Symposium on Electrical Apparatus and Technologies (SIELA)*, Bourgas, Bulgaria, 2022, pp. 1-4.

[13] M. Popescu, A. Bitoleanu and C. V. Suru, "Estimation of the rotor flux in the traction systems with induction motors and field-oriented control," *2023 International Conference on Electromechanical and Energy Systems (SIELMEN)*, Craiova, Romania, 2023, pp. 1-6.

[14] A. Bitoleanu, M. Popescu and V. Suru, "Experimental evaluation of rotor field orientation control and hysteresis controller for induction traction motor," *2021 12th International Symposium on Advanced Topics in Electrical Engineering*, Bucharest, Romania, 2021, pp. 1-6.

[15] C. V. Suru, M. Popescu and M. Linca, "Implementation of rotor field orientation by voltage control on dSPACE system," *2022 22nd International Symposium on Electrical Apparatus and Technologies (SIELA)*, Bourgas, Bulgaria, 2022, pp. 1-4.

[16] M. Popescu and A. Bitoleanu, "New achievements in the rotor field -oriented control for autonomous locomotives. Part 1: System synthesis and theoretical investigations," *The 7th International Symposium on Electrical and Electronics Engineering (ISEEE 2021)*, October 28-30, 2021 Galați, Romania, pp. 1–6.

[17] R. Garg, P. Mahajan, N. Gupta and H. Saroa, "A comparative study between field oriented control and direct torque control of AC traction motor," *International Conference on Recent Advances and Innovations in Engineering (ICRAIE-2014)*, Jaipur, India, 2014, pp. 1-6.

[18] V. Burenin, J. Zarembo, G. Kobenkins and O. Krievs, "Implementation of hybrid PWM with smooth transitions between modulation modes for railway traction field-oriented control system," *2023 IEEE 64th International Scientific Conference on Power and Electrical Engineering of Riga Technical University (RTUCON)*, Riga, Latvia, 2023, pp. 1-7.

[19] M. Popescu and A. Bitoleanu, "Diagnosis of passing over railway joints and reducing the effects in modern traction systems," *2023 IEEE 14th International Symposium on Diagnostics for Electrical Machines, Power Electronics and Drives*, Chania, Greece, 2023, pp. 436-442.

[20] T. Mătușa, M. Popescu, A. Bitoleanu and C. V. Suru, "Behavior of a Traction Induction Motor with Rotor Flux-Oriented Control," *2024 International Conference on Applied and Theoretical Electricity (ICATE)*, Craiova, Romania, 2024, pp. 1-6.

DOI: 10.52846/AUCEE.2024.02

The Implementation of Quasi-Oriented Rotor Field Control Algorithm for Induction Motor Traction Systems

Mihăiță Lincă*, Constantin Vlad Suru*, Mihaela Popescu*, Alexandru Bitoleanu* and Cristian Bratu*

* University of Craiova, Faculty of Electrical Engineering, Craiova, Romania, mlinca@em.ucv.ro, vsuru@em.ucv.ro, mpopescu@em.ucv.ro, a_bitoleanu@yahoo.com, cbratu@elth.ucv.ro

***Abstract* - A rotor field quasi-oriented control algorithm for drive systems equipped with a low cost DSP system has been implemented and experimentally validated in this paper. The system is designed for induction motor traction systems. The control algorithm implementation was done for a dSPACE DS1103 prototyping board in the Matlab Simulink environment. The control algorithm principle is based on the assumption that the current system is oriented by the rotor flux and the real flux follows the imposed value. Therefore, the rotor flux estimation is no longer necessary as well as the flux control loop. This makes the control algorithm suitable for low cost industrial DSP applications. The drawback is given by the fact that the current projections on the dq axes cannot be regulated, the current control being done by means of the current phasor magnitude. The control system implementation was validated with good results, in terms of current and speed regulation especially at variable mechanical load (such as track joints or switches), making this method suitable not only for low cost traction systems, but especially for railway vehicles.**

Cuvinte cheie: *control cu orientare după câmp, motor de inducție, sistem de tracțiune.*

Keywords: *field oriented control, induction motor, traction system.*

I. INTRODUCTION

The induction motor is the standard motor used in general modern electric drive systems [1]. The same is valid for electric traction systems used in modern electric vehicles and especially in high power railway systems [2]. As catenary fed vehicles are not power limited by the battery, the traction system power can be very large. For these traction systems the field oriented control is an advantageous choice as it offers high torque at low speed and high dynamic performance [3]. A particularity of traction systems is the use of the traction motor above the rated speed. In this regime, the field oriented control gives good performance, given the fact that it implies higher frequency of the motor currents [1]. This is important because high power drive systems imply relatively low switching frequency (which affects the performance of the control system). At the same time, the motor current relatively high frequency needs a fast and high computing power DSP to execute the control algorithm in real time. Because the rotor field oriented control requires high computation power, unavailable for standard industrial DSPs, the aim of this paper is the implementation of a simplified, quasi-oriented rotor field control algorithm on a dSPACE DS1103 prototyping board. The experimental validation of the implemented control algorithm was done on an experimental railway traction stand.

II. ROTOR FIELD QUASI-ORIENTED CONTROL ALGORITHM

For the rotor field oriented control the motor currents are expressed in the dq referential which rotates with the rotor flux [1-8]. To avoid the estimation of the flux, assuming that the current phasor is oriented and the real rotor flux correctly follows the imposed flux, the real time determination of the flux phasor can be avoided. Therefore, the flux control loop, which gives the magnetizing current on the d axis of the referential, can be also avoided. This can lead to an important simplification of the control algorithm, effective for drive systems that use less powerful DSPs [9].

The control algorithm for traction systems with simplified rotor field orientation (quasi-orientation) is synthetized in [9], where [8]:

- $R\omega$ - speed controller;
- $|I_m|$ - current magnitude computation block;
- R_i - current controller;
- VSI - voltage source inverter;
- ≋ - three phase sinusoidal control signal generator;
- f_2^* - slip frequency computation block.

The algorithm inputs are the imposed rotor flux and the imposed speed. For the given flux value, assuming as stated that the system is oriented, the value of the imposed magnetizing current is obtained [8][9]:

$$i_{sd} = \frac{1}{L_m} \cdot \left(\Psi_{rd} + T_r \cdot \frac{d\Psi_{rd}}{dt} \right), \tag{1}$$

where [8]:

- T_r - rotor circuit time constant:

$$T_r = \frac{L_r}{R_r} = \frac{L_m + L_{\sigma r}}{R_r}, \tag{2}$$

- L_m - magnetizing inductance;
- $L_{\sigma r}$ - rotor leakage inductance;
- R_r - rotor resistance.

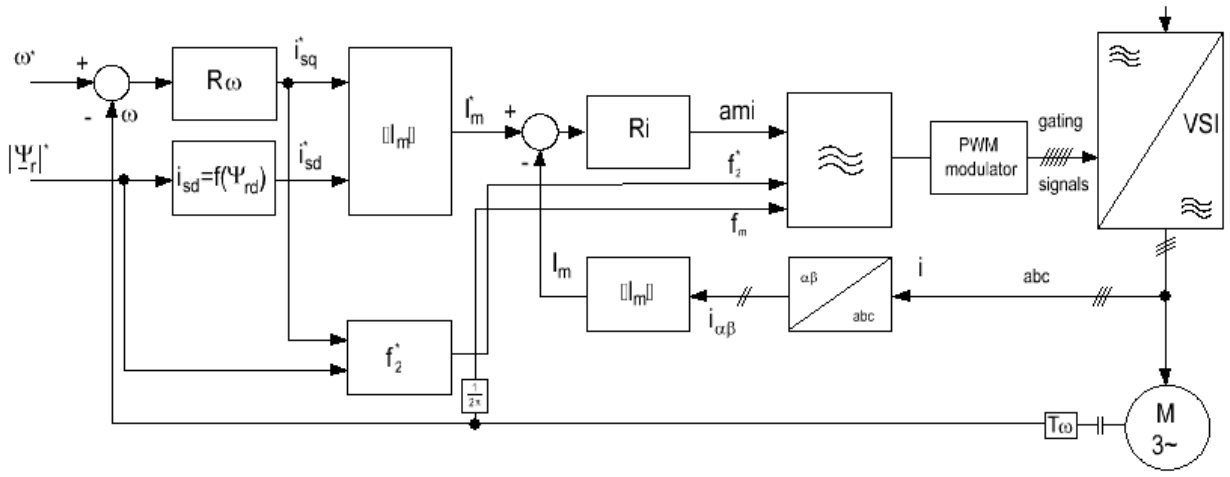

Fig. 1. Rotor field quasi-oriented control algorithm.

The imposed active current is obtained at the output of a proportional integrative speed controller [9].

The two currents are further used to compute the imposed motor current phasor magnitude (Fig. 1) used for the current control loop (which also uses a proportional integrative controller) [9]:

$$I_m^* = \sqrt{i_{sd}^2 + i_{sq}^2} \tag{3}$$

The feedback information is the real motor current phasor magnitude, computed from the measured three-phase currents [9]:

$$I_m = \sqrt{i_{s\alpha}^2 + i_{s\beta}^2} \tag{4}$$

where, i_α and $i_{s\beta}$, are the stator current phasor projections on the stationary reference frame [1], [6].

The output of the current magnitude controller is the amplitude modulation index ("ami" in Fig. 1) of the three phase sinusoidal control signals generated and applied to the PWM modulator. The frequency of these signals is obtained by summing to the motor shaft frequency, the imposed slip frequency [8]:

$$f_2^* = i_{sq} \cdot \frac{L_m}{2 \cdot \pi \cdot \Psi_{rd} \cdot T_r} \tag{5}$$

III. DS1103 Implementation of Rotor Field Quasi-Oriented Control Algorithm

The rotor field quasi oriented control algorithm was implemented for the experimental traction system in the Matlab Simulink environment. This was possible because the control subsystem of the traction system is made entirely by the dSpace DS1103 prototyping board, which can be programmed using this graphical programming environment. Of course, the experimental stand includes additional electronic circuits, but used only for auxiliary purposes (such as initialization, overcurrent/overvoltage protection, gate drivers, etc.), the control algorithm being completely implemented by the prototyping board.

Because the experimental stand is used to test a complete traction system it also includes the single phase rectified which feeds the traction inverter. It must be mentioned that the rectifier (which is a PWM boost rectifier) is not controlled by the prototyping board, but by a dedicated DSP (as it does not make the object of this study).

As illustrated in the prototyping board control model (Fig. 2), the control algorithm (Fig. 3) is grouped into a subsystem, for better clarity.

The link between the power system and the control algorithm (model) is done by the power section transducers (voltage, current and speed) and the DS1103 acquisition system. Each analog to digital converter (connected to a transducer) have a corresponding Simulink block (from the Real Time Interface library) which outputs a Simulink signal, further de-normalized (with the appropriate Gain blocks). Some of the converted signals are not needed for the control algorithm, but only for system monitoring purposes.

The speed transducer which was used is an incremental encoder therefore it was connected to the DS1103 incremental encoder specialized input. This gives at the output port of DS1103ENC_POS_C1 the number of increments further used to obtain the speed. Because of the relatively low number of pulses, the sliding window averaging technique was used to smooth the speed.

The output of the control algorithm (the IGBT gating signals) are obtained by applying the three phase generated control signals to the DS1103 hardware PWM modulator (by means of the DS1103SL_DSP_PWM3 block).

The actual control algorithm is illustrated in Fig. 3. It is also grouped in several subsystems for better understanding of the model, given the algorithm typical sections:

- The motor current magnitude – computed from the acquired three phase motor currents (in the αβ referential);
- The d axis (magnetizing) current obtained as a function of the imposed motor flux (for the assumption that the system is oriented);

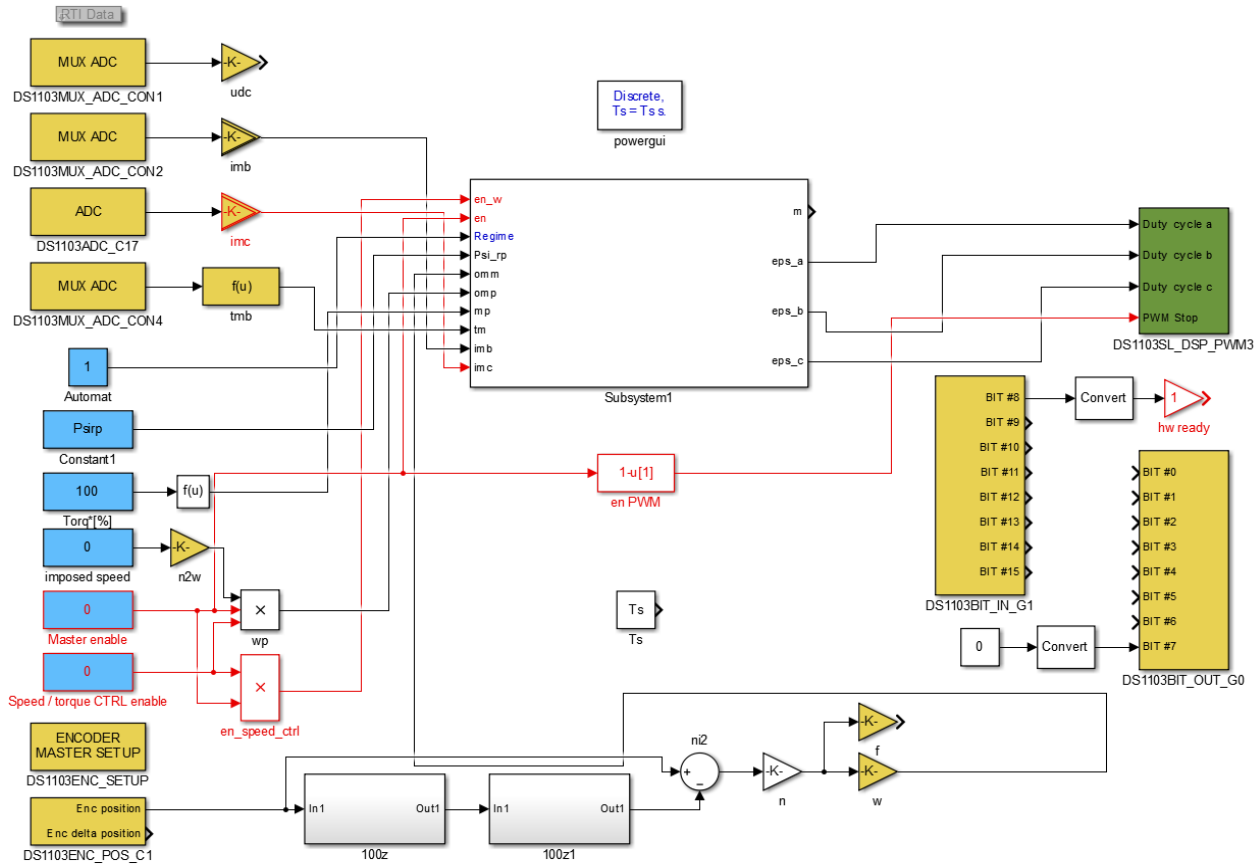

Fig. 2. The DS1103 Simulink control model.

- the slipping frequency, from the motor speed and motor equations;
- The imposed active stator current in the dq referential (i_{sq}).

The active current, i_{sq}, is imposed in two manners:

- Manual mode - the motor torque is directly imposed, from which the active current is computed.
- Automated mode – the active current is imposed at the output of the speed controller.

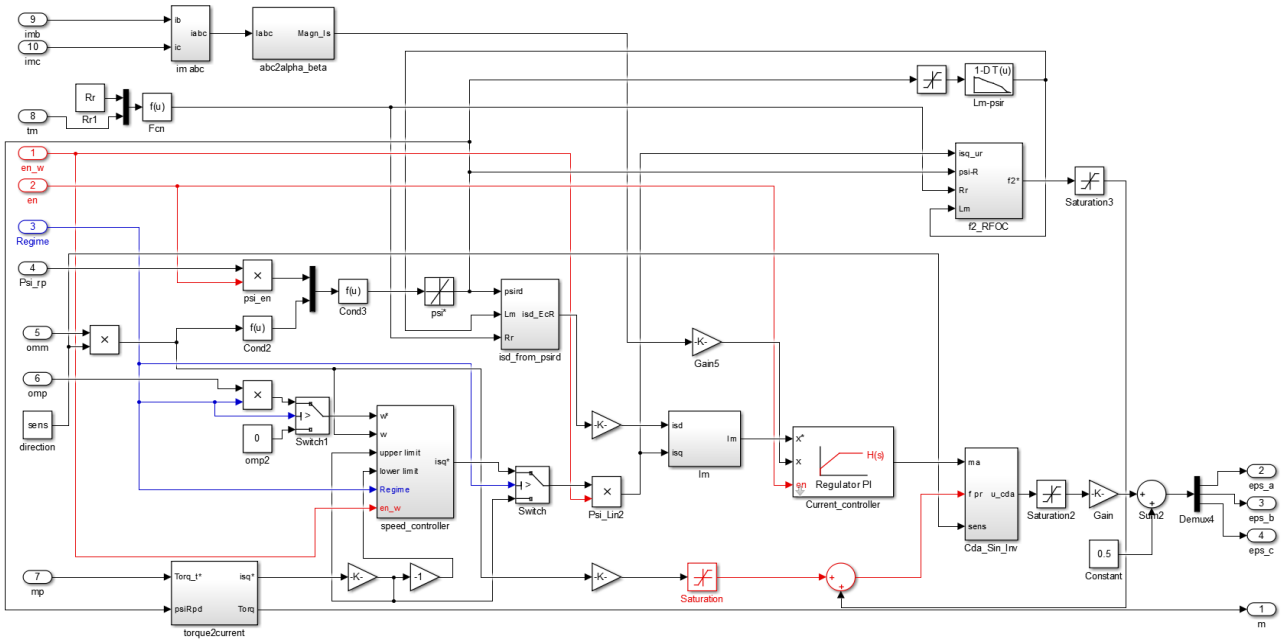

Fig. 3. The rotor field quasi-oriented control algorithm.

The q axis (active) current is obtained as a function of the imposed torque in the manual operating mode, and as the output of the speed controller, in the automated mode. For the latter, we still have the imposed torque, which in this case gives a corresponding current value which is further used to limit the speed controller output.

The two imposed currents are used to obtain the imposed current magnitude applied to the motor current magnitude controller. Its output is further applied as an amplitude modulation factor to the block which generates the three phase control signals. The frequency of the generated signals is obtained from the motor measured frequency by adding the slipping frequency.

Because the DS1103SL_DSP_PWM3 block (PWM modulator) accepts the duty factors for each inverter column, the three phase sinusoidal control signals are previously transformed to duty factors.

The real time control of the experimental traction system is done by means of a virtual control panel built in ControlDesk NG (which is the dSPACE specific control software) - Fig. 4 [11][12][13]**Error! Reference source not found.**. The control model blocks are linked to the virtual instruments of the control panel by means of block parameters or output signals [16][17]. The real time control is obtained by modifying block parameters (by the virtual instrument) and the output signals are used to monitor the system status and qualitative analysis of the system performance (by means of the virtual oscilloscopes). An important fact related to the virtual oscilloscopes (time plotters) for the analyzed case (Fig. 4) is that because of the extensive acquisition time length (25 s) the acquisition samples had to be decimated, therefore only part of the samples had been recorded (for the 100 μs sample time). This can lead to aliasing, for the periodic signals which is the case of the three phase control signals which seems to have low frequency at very high speed - Fig. 4. The same data illustrated on the time plotters of the control panel was also recorded, for offline analysis in Matlab [15][16][17].

IV. Experimental Setup

The DS1103 control system was embedded in a scale experimental traction system for railway vehicles composed of:

- Single phase PWM boost rectifier (controlled by local DSP);
- Three-phase inverter (controlled by DS1103);
- Three phase induction motor.

The rated parameters of the traction motor are:

- U_N = 380 V, I_N = 88 A, P_N = 50 kW;
- f_N = 65 Hz; n_N = 1917 rpm.

The mechanical load of the traction motor is a DC machine used as generator feeding a passive constant resistive load. Consequently, the traction motor mechanical load was controlled by means of the DC machine field current.

V. Experimental Results

The traction system performance was analyzed by accelerating the motor to twice the rated speed, simulating the railway joints.

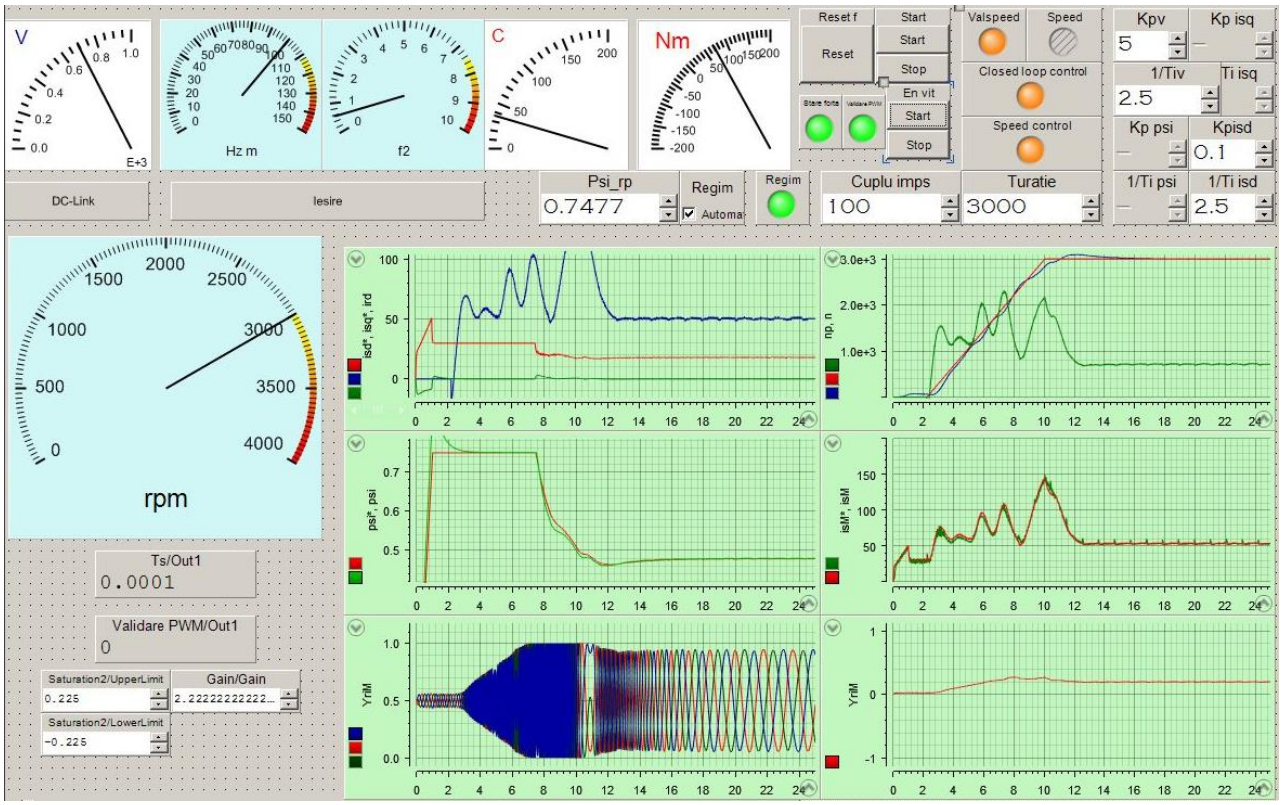

Fig. 4. The experimental system ControlDesk real time control panel.

The railway joints are the devices that connect two adjacent rails of the railway track. The passing of the wheel over the joint lead to high current transients due to the fact that the adjacent rails are not continuous but have an interstice necessary to allow their expansion. This means that the next rail the wheel is passing to can be slightly above or below the previous rail (with or without a gap). Depending on the position of the next rail (compared to the previous one) the torque at the traction motor shaft could have a steep increase or decrease leading to steep increase of the motor current or motor speed.

Not to exceed the DC machine rated power, the field current was set at 2 A (bellow the rated speed the field current can be increased up to 5A), but in order to simulate the railway joints, sudden, significant, positive or negative variations were imposed on it.

The evolution of the motor speed during the experiment is illustrated in Fig. 5. The traction motor was accelerated after the motor was magnetized. For this, the q axis component of the imposed motor phasor current magnitude was applied after the motor flux reached steady state operation (Fig. 6).

It can be seen that the speed is well regulated, with an overshoot of about 99 rpm (3.3% of the imposed speed). It must be taken into consideration that the motor accelerates under significantly variable load. Moreover, during the acceleration, a variation of the speed around the prescribed value can be observed, according to whether the static torque was positive or negative

Also, during magnetization, although the imposed speed is null (as well as the q axis imposed current) the real motor speed is not null (but about 68 rpm). This is because, in order to have sinusoidal magnetizing current at motor standstill, a minimum frequency of about 1.6 Hz was used. This gives a slow rotation of the motor shaft if the motor is idle. It must also be mentioned that during the magnetization the speed controller is inhibited, therefore the active current is null. Also, because the mechanical load is a DC generator, the motor is idle at standstill and no mechanical brake was applied.

The motor imposed flux is illustrated in Fig. 6. It can be seen that during magnetization, the flux increases linearly to its rated value and remains constant until the motor rated speed is reached. Above the rated speed the motor flux is weakened to avoid magnetic saturation. Because the flux weakening is done as a function of the real speed, the speed overshoot is "visible" on the imposed flux. This flux gives the imposed d axis current in Fig. 7.

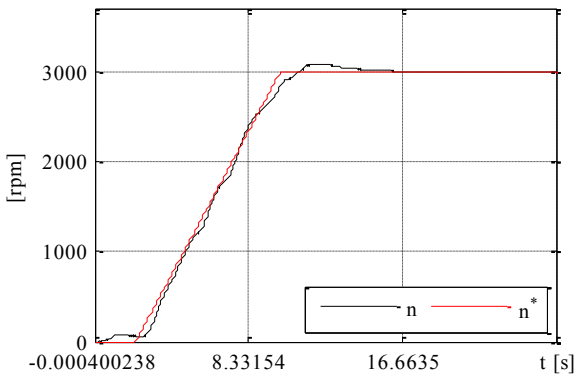

Fig. 5. The traction motor speed.

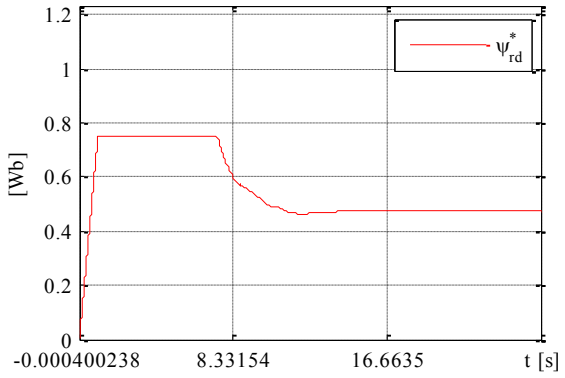

Fig. 6. The motor imposed flux.

Given the flux derivative in the magnetizing current expression, and as the flux depends on the actual speed (when weaken, above the motor rated speed), the speed variations are transmitted to the magnetizing current as seen in Fig. 7.

The active current is illustrated in Fig. 8. It can be seen that when the speed controller is activated, about 2.2 s after the motor magnetization had begun; the active current is initially negative, because of the motor slow rotation when magnetized. Subsequently it becomes positive as the imposed speed exceeds the real speed and the motor accelerates.

The imposed and real current are illustrated in Fig. 9. The torque variation (created by varying the DC machine field current) can be seen in the q axis imposed current shape, as the speed controller reacts to the steep variations of the mechanical load.

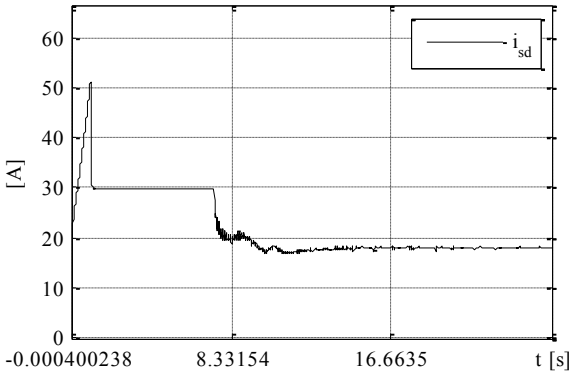

Fig. 7. The d axis imposed current.

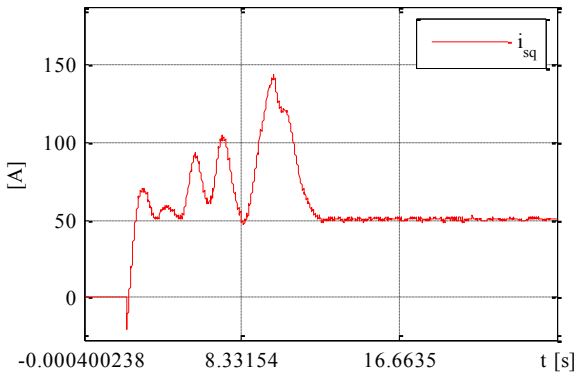

Fig. 8. The imposed q axis current.

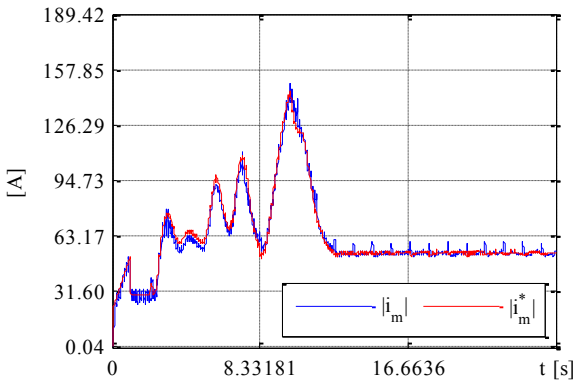

Fig. 9. The imposed and obtained motor current magnitude.

A small ripple can also be observed on the active current, but unlike the magnetizing current whose ripple appears only above the rated speed, the active current have ripple all the time (the speed controller is active). This is because the speed measured by the incremental encoder is not smooth (as the speed measured by a tachometer), but it has significant ripple, given by the limited number of pulses per revolution. Although it was greatly reduced by the two sliding window filters, the remaining ripple (amplified by the speed controller amplification (given by the proportionality constant) appears in the controller output, and consequently in the active current.

CONCLUSIONS

The rotor field quasi-oriented control algorithm for traction induction motors was experimentally implemented and validated in this paper. The obtained results proved the correct implementation of the control algorithm as well as the validity of the proposed system. Although the orientation of the system is only assumed and not really controlled, it gave good results both in static and dynamic regimes (in terms of current and speed regulation especially at variable mechanical load typical for railway vehicles such as track joints or switches). Driving the motor above the rated speed at weaken flux is also obtained with good results. The advantage of this control algorithm is given by the low computing resources required making it feasible for implementation on low cost control systems - the described experiments had been conducted with a time sample of 100 μs. The disadvantages of the proposed algorithm are given by the motor being unable to standstill when only magnetized (even with the speed controller inhibited, therefore, null active current). The motor speed is obtained by the slip frequency, but is null for null q axis current. In this situation it tends to rotate at low speed (if idle). This is because the motor magnetization is done with sinusoidal current, with a minimum frequency of 1.6 Hz, and the d axis current and q axis current cannot be controlled separately, but by means of the current magnitude. Although, this inconvenience appears only when the motor is idle, which is rarely met in practice as the railway vehicle is a considerable load itself. Moreover, it can be simply overcome by mechanically breaking the vehicle.

ACKNOWLEDGMENT

This work was supported by European Regional Development Fund, Competitiveness Operational Program, project PACETSINEFEN, ID: P_40_196/105687, (2016–2021).

Contribution of authors:

First author – 20%

First coauthor – 20%

Second coauthor – 20%

Fourth coauthor – 20%

Fifth coauthor – 20%

Received on September 9, 2024

Editorial Approval on November 29, 2024

REFERENCES

[1] A. M. Bazzi, A. P. Friedl, S. Choi and P. T. Krein, "Comparison of induction motor drives for electric vehicle applications: Dynamic performance and parameter sensitivity analyses," *2009 IEEE International Electric Machines and Drives Conference*, Miami, FL, USA, 2009, pp. 639-646, doi: 10.1109/IEMDC.2009.5075273.

[2] L. K. Jisha and A. A. Powly Thomas, "A comparative study on scalar and vector control of Induction motor drives," *International Conference on Circuits, Controls and Communications*, Bengaluru, India, 2013, pp. 1-5.

[3] T.C. Pană, O.C. Stoicuța, *Stability of Vector Drive Systems with Induction Motors* (*Stabilitatea sistemelor de acționare vectoriala cu motoare de inducție*), Cluj-Napoca: Mediamira, 2016.

[4] *Field Orientated Control of 3-Phase AC-Motors*, Literature Number: BPRA073, Texas Instruments Europe, February 1998.

[5] T. A. Wolbank, A. Moucka and J. L. Machl, "A comparative study of field-oriented and direct-torque control of induction motors reference to shaft-sensorless control at low and zero-speed," *Proceedings of the IEEE Internatinal Symposium on Intelligent Control*, Vancouver, BC, Canada, 2002, pp. 391-396, doi: 10.1109/ISIC.2002.1157795

[6] M. Popescu and A. Bitoleanu, "New achievements in the rotor field-oriented control for autonomous locomotives : Part 1: system synthesis and theoretical investigations," *2021 7th International Symposium on Electrical and Electronics Engineering (ISEEE)*, Galati, Romania, 2021, pp. 1-6.

[7] A. Bitoleanu, M. Popescu and V. Suru, "Experimental evaluation of rotor field orientation control and hysteresis controller for induction traction motor," *2021 12th International Symposium on Advanced Topics in Electrical Engineering (ATEE)*, Bucharest, Romania, 2021, pp. 1-6, doi: 10.1109/ATEE52255.2021.9425040.

[8] A Kelemen, M Imecs, *Sisteme de reglare cu orientare după cîmp ale mașinilor de curent alternativ*, Bucharest: Academiei, 1989.

[9] M. Linca, C. V. Suru, M. Popescu and A. Bitoleanu, "Rotor field quasi-oriented control algorithm implementation for railway traction systems on dSPACE DS1103," *2024 International Conference on Applied and Theoretical Electricity (ICATE)*, Craiova, Romania, 2024, pp. 1-6, doi: 10.1109/ICATE62934.2024.10748608.

[10] Real-Time Interface (RTI and RTI-MP) Implementation Guide for release 5.2, dSpace Gmbh, 2006.

[11] Simulink Coder – Target Language Compiler, © COPYRIGHT 2002–2017 by The MathWorks, Inc., www.mathworks.com

[12] Simulink Coder – User's Guide, © COPYRIGHT 2002–2017 by The MathWorks, Inc., www.mathworks.com

[13] Simulink Coder Reference, © COPYRIGHT 2002–2017 by The MathWorks, Inc., www.mathworks.com

[14] ControlDesk Next Generation Reference For ControlDesk 5.3, Release 2014‑B – November 2014.

[15] ControlDesk Next Generation Measurement and Recording Tutorial, For ControlDesk 5.3, Release 2014-B – November 2014.

[16] ControlDesk Next Generation Experiment Guide, For ControlDesk 5.3, Release 2014-B – November 2014.

[17] ControlDesk Experiment Guide, Release 2014-B – November 2014.

DOI: 10.52846/AUCEE.2024.03

Equipment for Energizing and Controlling the Operation of Synchronous Power Motors

Gheorghe-Eugen Subțirelu[*], Petre Pistol[†], Adrian Vintilă[†] and Cosmin Ionuț Toma[*]

[*] Faculty of Electrical Engineering, University of Craiova, Craiova, Romania, esubtirelu@em.ucv.ro, ctoma@em.ucv.ro

[†] National Institute for Research, Development and Testing in Electrical Engineering (ICMET) Craiova, Romania petrepistol@icmet.ro, adrian_vintila@icmet.ro

Abstract **- It is known that the use of synchronous motors in variable speed drives to simultaneously generate mechanical power and reactive power is among the most effective methods of improving the power factor in electrical distribution networks. Also, the adoption of automatic excitation control has expanded the application field of synchronous motors to handle high-load shock drives. Modern digital control systems designed for controlling the excitation of synchronous motors have revitalized the significance of these machines. This paper presents a synchronous motor excitation control system that provides a fully digital solution for the design of equipment to supply excitation and control the operation of high power synchronous motors. This system can be easily parameterized for low and medium voltage synchronous motor drives of various rated powers, with asynchronous starting capability. An application of the system to the realization of an equipment for excitation power supply and operation control of high power synchronous motors is also presented. The equipment was realized in prototype version and after successful laboratory tests it was successfully produced in series and used to build electric drives for ore mills using asynchronous motors of 2.93 MVA.**

Cuvinte cheie: *excitație motoare sincrone, sisteme digitale de control și reglare, rețele electrice de distribuție.*

Keywords: *synchronous motor excitation, digital control and regulation systems, electric distribution networks.*

I. INTRODUCTION

This paper describes an excitation and control equipment for the operation of synchronous motors. It represents a continuation and extension of the work originally presented at International Conference on Applied and Theoretical Electricity (ICATE) 2024 [1].

The automatic control and regulation system presented in the paper is intended for the design and practical implementation of an equipment for supplying the excitation winding and controlling the operation of high-power synchronous motors.

In the past, the synchronous machine was mainly used as a generator, and its use as a motor was mainly hindered by the starting process. Today, advances in power and control electronics have eliminated the difficulties associated with the starting process. This has made the use of synchronous machines increasingly attractive up to the highest power ratings [2], [3]. Despite the starting difficulties, the synchronous motor is used in these cases instead of the cage-rotor induction motor because it has a number of advantages. It therefore helps to improve the power factor when operating in overexcited mode and has a higher operating reliability than asynchronous motors, especially at high power and low speed, due to the larger air gap. Compared to the asynchronous motor, the torque of the synchronous motor is more stable to variations in the supply voltage and the efficiency is better due to the higher power factor [4].

In order to optimize the performance of high power synchronous motor electric drives during start/stop and constant speed operation, it is necessary to efficiently control the machine through its excitation current.

Classical synchronous motor excitation systems are designed with DC generators controlled by regulators included in the excitation circuit of the exciter machine. For this purpose, the excitation circuit includes a variable resistor controlled by an electromechanical regulator. Disadvantages of this solution are:

- High response time;
- Low energy efficiency;
- Relatively high cost of implementation.

Another solution for the excitation supply is the use of rectifiers with controlled semiconductor devices, supplied by a transformer equipped with taps in the secondary winding, where the excitation current is controlled by switching them.

The disadvantages of this solution are:

- Coarse tuning of the excitation current;
- Relatively high implementation cost.

It is also worth mentioning the solution of using compound excitation systems with semiconductor devices. Disadvantages of these systems are:

- High cost due to use of special current transformers;
- Composite systems are difficult to size;
- Analog control scheme is relatively complicated;
- Relatively low efficiency.

In modern drives with high power synchronous motors, the excitation circuit is powered by controlled rectifiers fed by fixed ratio transformers.

This solution allows optimal control of the operating modes by efficiently controlling the excitation current. The control schemes of the machine operation, as well as the implementation of the excitation current control algorithm, can be done with analog technology or with digital electronic solutions.

This paper presents an advanced solution for a fully digital excitation command, control and regulation system for use in high power, constant speed, asynchronous squirrel cage synchronous motor drives.

The advantages of this solution are:

- The control system is fully automatic and digital, using a state-of-the-art DSP processor;
- The control software application is developed using a programming platform specifically designed for electric actuators, allowing easy parameterization for a wide range of actuator motor powers and speeds.
- Low cost;
- Safety in operation.

II. Theoretical Aspects

Below are briefly presented some theoretical aspects that describe the main operating modes of the synchronous motor. These will constitute the main requirements for the design of the automatic control and regulation equipment presented further in the paper [4]…[10].

The mains synchronous motor normally operates at a constant (synchronous) speed given by the frequency of the supply voltages and has a rigid characteristic.

The synchronism velocity is given by the relationship:

$$n_s = 60\,\frac{f}{p} \tag{1}$$

where f is the mains frequency and p is the number of pole pairs.

The power absorbed by the motor from the mains is converted into torque at the shaft according to the equation:

$$M = m\frac{UE_0}{X_d\,\omega_1}\sin\theta = M_{\max}\sin\theta \tag{2}$$

where:

m – number of motor phases

U – voltage applied to the terminals [V]

E_0 – electromotive force (EMF) [V]

X_d – motor longitudinal reactance [Ω]

ω_1 – rotor angular speed [rad/sec]

θ – internal angle of the motor [rad]

The problems that require particular attention in high power synchronous motor drives relate to the process of starting, stopping and maintaining synchronism under variations in torque and supply voltage (the stability problem).

For drives with high shock loads, it is necessary to over-excite the motor to prevent it from entering the unstable operating range with the risk of out-of-sync.

The V curves of the synchronous motor [3] show (Fig 1):

- To the left of the cosφ=1 curve, the synchronous motor is operating in INDUCTIVE MODE, absorbing reactive energy from the mains (under-excited synchronous motor).
- To the right of the cosφ=1 curve, the synchronous motor is operating in CAPACITIVE MODE, generating reactive energy in the mains (overexcited synchronous motor).
- If the field current falls below the *Iexmin*. curve, the motor will enter the unstable range and may go out of synchronisation.

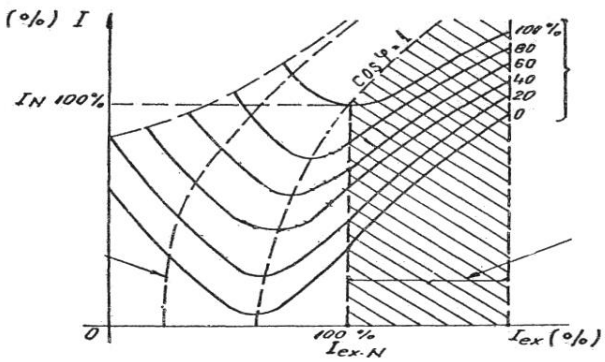

Fig. 1. V-curves of the synchronous machine [5]

- If the field current is increased above the value Iex_N in order to absorb some load shocks on the shaft, there is a risk of exceeding the heating limit of the field winding.

The conclusions are as follows:

- The upper part of the CAPACITIVE operating range is the heating limit of the field winding and therefore of the "Iex_{max}" protection characteristic;
- The lower part of the INDUCTIVE operating range is the stability limit of synchronous motor operation, i.e. the "Iex_{min}" protection characteristic.

The minimum supply voltage at which the synchronous motor can be maintained in operation at rated load (Mn) and rated field current [9]:

$$U_{min} = \frac{X_d\,\omega_1 M_n}{mE_n} \tag{3}$$

where: *En* is rated EMF value

Forced excitation results in increased EMF (E) and therefore increased torque. This keeps the motor synchronised when the mains voltage drops below *Umin.*

For fast excitation, the excitation supply must provide three times the rated excitation voltage.

The main operating modes of the synchronous motor are briefly described below.

A. Starting the Synchronous Motor

The synchronous motor can be started [3] in several ways: by an auxiliary drive motor, by a variable frequency supply and by asynchronous starting. Asynchronous start is the most commonly used start method. During the first part of the starting process, the motor operates as an induction motor with a winding in the pole shoes, usually a squirrel cage, but sometimes a winding with coils and slip rings.

The size of this winding, called the starting winding, depends on the motor power and the parameters required for the starting process.

The asynchronous starting process is as follows: the field winding is disconnected from the excitation source terminals and connected to a resistor called the discharge resistor, which has a resistance 9-10 times higher than that of the field winding.

In this situation the synchronous motor is connected to the mains, either directly or via a 2 to 4 stage voltage transformer (or via a starting autotransformer).

The machine operates as an induction machine. When the slip is at a steady state value of 2-3%, the field winding is disconnected from the resistor and connected to the DC source, generating the field current flowing through it.

From this moment on, the mains synchronisation process begins, which is the result of a damped transient process. If a starting transformer is used, the voltage steps must be switched to increase the voltage to the rated value before the field current is set. This is also the case when using the autotransformer starter.

The lower the value of the slip Si at the time of setting the DC field current, called the input slip, the easier it is to achieve synchronism.

The best conditions for synchronisation are at idle. When starting on load, synchronisation is more difficult and is facilitated by proper control of the field current through a forced excitation process.

B. Stopping the Synchronous Motor

The synchronous motor is switched off [3] by disconnecting it from the mains after adjusting the field current so that the stator current is at a minimum. Reconnection of the field winding to the discharge resistor is mandatory for protection reasons and to prepare the synchronous motor drive for possible restart.

C. Synchronous Motor Operation in Synchronous Compensator Mode

Compensator mode [4] is a special synchronous motor operating mode. In this mode the machine exchanges reactive power with the grid according to the set field current. With respect to the mains, the synchronous machine, in this case the synchronous motor is equivalent to a capacitor bank when over excited (field current set higher than rated field current) and to a coil when under excited (field current lower than rated field current).

The maximum range of reactive power exchanged with the mains, obtained by correct control of the field current, is obtained when the motor is running at no load, in which case it draws from the mains only the active power necessary to cover the specific losses.

The synchronous compensator mode may also be available in on-load operation, especially when the load is variable and predominantly lower than the rated value.

Adequate control of the excitation current, obtained by using controlled rectifiers controlled by electronic regulators as a DC power source, allows excellent performance criteria to be obtained in the control of the reactive power flow exchanged with the power supply network, while maintaining stable operation of the actuators.

III. Equipment for Energizing and Controlling the Operation of Synchronous Power Motors

Below is presented the equipment for energizing and controlling the operation of synchronous power motors, built at ICMET Craiova, Microproduction Division, under the commercial name EEx-MS-500A-01 (Fig. 2).

The EEx-MS-500A-01 provides power supply and protection of the excitation winding of the synchronous motor, control of the synchronous motor operation (starting, load operation, intentional and fault shutdown) and implementation of criteria for optimizing the operation with respect to the synchronous motor power supply network.

The system was tested in all modes of operation on a dedicated prototype bench and then produced in small batches for delivery to beneficiaries throughout the country.

In the commercial version produced at ICMET Craiova, the device, coded Eex-MS 500V/500A-01, has been parameterized for synchronous motor drives with the following technical specifications:

- Motor Type: СДС 19-56-40Y4;
- Rated power: 2500 KW;
- Apparent rated power: 2930 kVA;
- Rated power factor: $\cos\varphi=0,9$;
- Nominal speed 150 rot/min.
- Stator:
  - -connection: Y;
  - -rated voltage 6 KV;
  - -rated frequency: 50 Hz;
  - -rated current 282 A.
- Rotor:
  - -rated excitation voltage: 145 Vcc;
  - -rated magnetizing current: 278 A;
  - -rotor inertial mass: 13.540 Kg.

The stator supply voltage of synchronous motor is measured using a voltage transformer (TMT) and the stator current is measured with a current transformer (TMC) (Fig. 2).

The excitation winding of the synchronous motor is supplied with a direct voltage obtained from a power transformer (TA) and a controlled rectifier (RC).

The motor excitation current is connected as follows, using the voltage of static contactor (realised with thiristors T7, T8) applied on discharge resistor (RD). At the same time, the rectifier pulses are blocked and the opening command of the I1 switch is activated.

As can be seen from (Fig. 2), the entire equipment is designed and built around the SRAEx system as the main automatic control and regulation system.

All control, protection and automation functions of the equipment and the motor are performed by the SRAEx-MCSK-2.0 - 01 synchronous motor automatic excitation control system.

The control of the static contactors is done from the SRAEx via the BCST block, using the control devices on the gate (BCT).

The cabinet in which the equipment is mounted is shown in (Fig. 3) (front view, with operator panel and inside view).

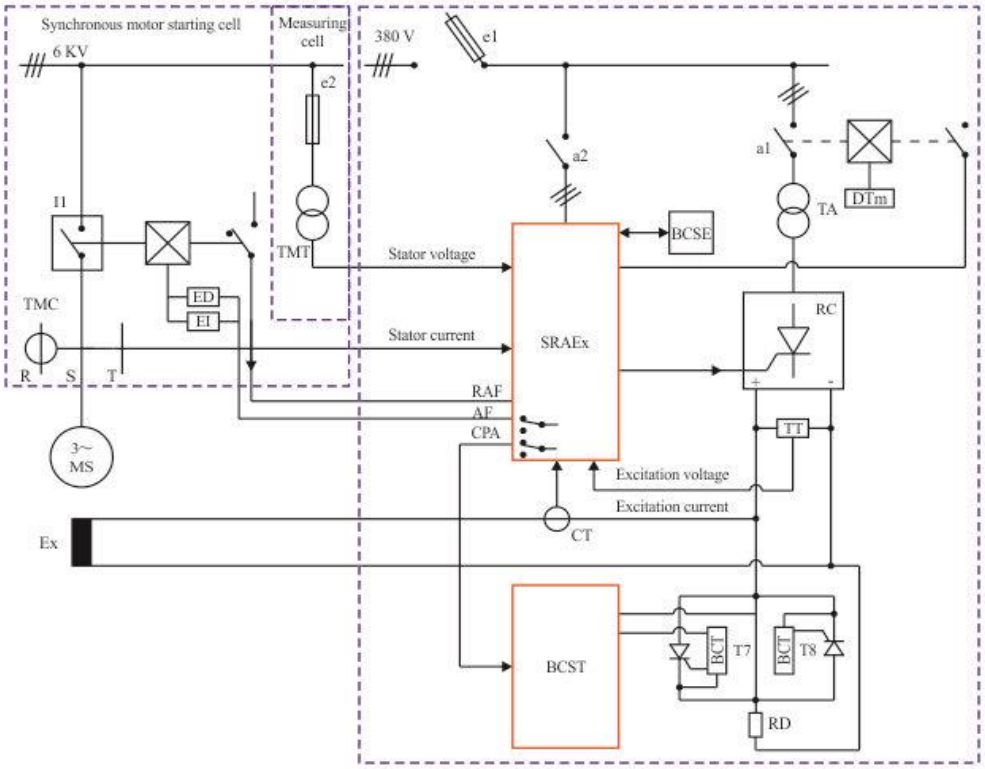

Fig. 2. Diagram of the Eex-MS 500V/ 500A-01 unit BCSE - External control and signalling unit; SRAEx - Automatic excitation control system; RC – Controlled rectifier; TC – Current transformer; TT – Voltage transformers; BCST - Thyristor control and monitoring unit; RD - Discharge resistor; TMT - Voltage transformer; TMC - Current transformer; TA - Mains transformer [1]

Fig. 3. The equipment cabinet Eex-MS 500V/500A-01

The central part of the presented equipment is constituted by the automatic control and regulation system.

It was designed and produced in the digital version at ICMET Craiova under the code SRAEx - MS - MCSK 2.0 - 01 (Fig. 4).

The automatic excitation control system (SRAEx) has the following operating modes:

A. Asynchronous Start

Asynchronous start is automatic according to the protocol described in section II.A and is controlled by the **SRAEx - MS - MCSK 2.0 - 01** control system**.**

B. Load Operation in:

*1) **MANUAL** mode with field voltage regulator*

In MANUAL mode, the output voltage of the rectifier (RC) supplying the synchronous motor excitation can be adjusted between zero and the maximum value set.

The minimum value of the bridge's control angle must correspond to the maximum voltage at its output. The minimum imposed value of the control angle should be considered as a parameter so that the same maximum excitation voltage can be obtained using transformers to supply the excitation bridge with different secondary voltages.

In MANUAL mode, the TEST option can be used to check the operating status of the excitation supply equipment, tune the control loops and troubleshoot. MANUAL mode can also be selected in FAULT mode as an operating option in the event of faults in the automatic control part of the system.

The rectifier voltage in MANUAL mode is set by a potentiometer/encoder and the mode is selected by a five-position switch (CRF) set to MANUAL together with a two-position switch: TEST or FAULT.

*2) **AUTOMATIC** mode*

*a) **CONSTANT CURRENT** with field current regulator*

In this mode, the excitation current is maintained at a prescribed value between the minimum field current and the maximum permissible field current, regardless of variations in the excitation rectifier (RC) supply voltage or variations in the field winding resistance.

The automatic control system uses a current regulator with a field current response provided by a Hall probe current sensor.

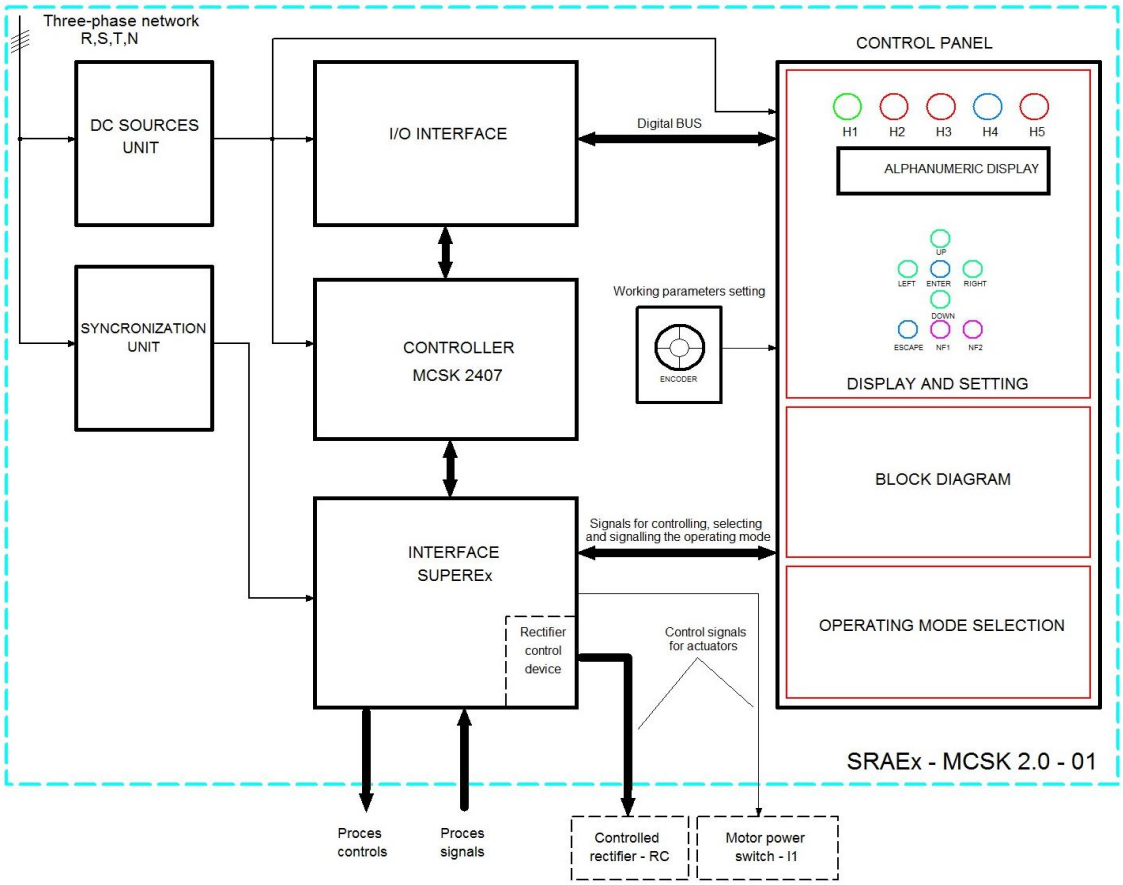

Fig. 4. Block diagram of the automatic control system SRAEx-MS-MCSK 2.0-01 [1]

*b) **CONSTANT STATOR VOLTAGE** with stator voltage regulator*

In this mode, the voltage at the motor terminals is maintained at a prescribed value between 0.9 and 1.1 of the rated stator voltage, with reactive power offset, regardless of the variation of the motor supply voltage (mains voltage).

In CONSTANT VOLTAGE mode, the terminal voltage is in the range 0.9÷1.1 UN and the setting refers strictly to this range (limitation of the prescribed values).

The CONSTANT VOLTAGE mode is selected with the CRF switch and the voltage is set with a potentiometer/ encoder.

The automatic control system operates as a stator voltage regulator with field current monitoring.

Response information is obtained using voltage transformers with the appropriate transformer ratio.

*c) **CONSTANT POWER FACTOR** with power factor regulator*

In this mode, the power factor at which the motor operates is maintained at a prescribed value between 0.5IND-1-0.5CAP, regardless of the active power corresponding to the motor load and the motor supply voltage.

The voltage and current reaction signals for calculating the current power factor are obtained from voltage or current measuring transformers with appropriate transformer ratios.

Important: The voltage and current reaction signals from the three-phase motor supply system required for the calculation of the power factor cosα and the reactive power are two current signals and two voltage signals on the same phases.

The control system acts as a power factor controller by limiting the stator voltage and field current (keeping them within the permissible range).

The CONSTANT POWER FACTOR mode is selected with the CRF switch and adjusted with a potentiometer/ encoder.

The control system acts as a reactive power controller by limiting the stator voltage and field current.

NOTE: The power factor, i.e. the reactive power, must be maintained at the prescribed value for a stator voltage range limited below 0.9 (0.7÷0.95) and above 1.1 (1.05÷1.3) of the rated voltage. If these limits are exceeded, operation at constant voltage without offset is required within the limits imposed by the field current.

Parallel, not cascade, limiting control is used.

The CONSTANT REACTIVE POWER mode is selected with the CRF switch and adjusted with a potentiometer/ encoder.

*C. Deliberate or Fault **STOP***

The controlled (intended) stop of the synchronous motor is selected by activating an appropriate command from the front panel of the excitation equipment (two-position

ON-OFF switch) and/or from the control panel of the SRAEx.

The fault stop occurs when the out-of-sync protection is activated, only during synchronous operation of the motor, if the motor goes out of synchronism due to an overload. This protection is not active during start-up.

It is based on monitoring the frequency of the AC component of the current induced in the field winding and controlling the motor to stop if the frequency rises above a certain value. If the frequency of the detected alternating component is lower than the threshold (2.5 Hz), the SRAEx controls the forced excitation to resynchronise the machine.

If the frequency of the AC component of the field current rises above the threshold during the operation of the forced excitation, the SRAEx controls the lowering of the ignition threshold of the thyristors T7, T8 in the static excitation discharge contactor (Fig. 2).

The SRAEx MS- MCSK 2.0 system allows the drive-specific protection to be parameterised using the technical data of the synchronous motor entered via the control panel, and provides the following protection functions [3], [6]:

- Minimum field current protection
- Maximum field current protection
- Out-of-sync protection
- Stator winding overheating protection
- Protection against two-phase rectifier operation
- Field winding short-circuit protection

The automatic control and regulation system SRAEx-MS-MCSK 2.0-01 consists of the following function blocks (Fig. 4):

- MCSK 2407-V02 digital control module (supplied by Technosoft Romania) with functionality adapted for synchronous motor control, based on the TMS 320 LF 2407 Digital Signal Processor (DSP) controller from Texas Instruments, designed for Digital Motion Control (DMC) applications;
- Dedicated interface module SUPEREx (manufactured at ICMET Craiova), which performs signal acquisition from the transducer/sensor system and transmission of commands to the actuators (mainly to the three-phase controlled rectifier bridge and to the synchronous motor power supply switch in the synchronous motor excitation supply equipment circuit);
- Figure 5 shows the SUPEREx interface together with the MCSK 2407 2407-V02 modules and the I/O interface.
- I/O interface between the control module and the control panel;
- The control panel is equipped with an alphanumeric display for setting parameters, programming operating modes and displaying signals and status (Fig. 6);

The synchronisation and power supply module contains the synchronisation transformers and the AC/DC converters that provide the supply voltages for the system.

Fig. 5. SUPEREx interface with MCSK 2407 development system and I/O interface [1]

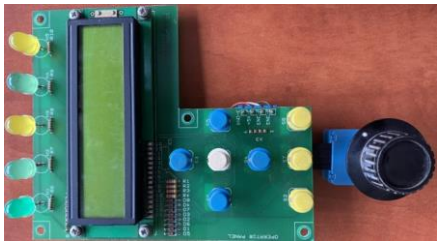

Fig. 6. Control panel [1]

IV. CONCLUSIONS

The equipment presented in the paper is produced by the National Institute for Research - Development and Testing in Electrical Engineering - ICMET Craiova and represents the final result of the collaboration with the University of Craiova.

The collaboration began with the design and development of an automated digital system to control and regulation the excitation of synchronous motors [1]. The SRAEx -MS-MCSK 2.0-01 is a fully digital solution for the design of equipment to supply excitation and control the operation of high power synchronous motors, and can be easily parameterised for low and medium voltage synchronous motor drives of various rated powers, with asynchronous starting capability.

ACKNOWLEDGMENT

Source of research funding in this article: Research program financed by the University of Craiova.

Contribution of authors:

First author – 35%

First coauthor – 35%

Second coauthor – 20%

Third coauthor – 10%

Received on September 12, 2024

Editorial Approval on November 26, 2024

REFERENCES

[1] Gh. E. Subțirelu, P. Pistol, A. Vintilă, and C. I. Toma, "Digital system for high power synchronous motor excitation control", *2024 International Conference on Applied and Theoretical Electricity (ICATE)*, October 2024, pp.1-6, DOI: 10.1109/ICATE 62934.2024.10748893.

[2] I. Săvulescu, P. Junie, O. Dinu, G. Condur, C. Eremia, "Automatic system with microprocessor and synchronous motor for user reactive power control" (in Romanian), *Revista Română de Informatică şi Automatică*, vol. 22, nr. 1, 2012.

[3] T. Dordea, *Electrical Machines* (in Romanian), Bucharest: Editura didactică şi pedagogică, 1977.

[4] Al. Fransua, A. Nicolaide, and Gh. Trifu, *Common Electrical Machines* (in Romanian) - *Exploatare şi regimuri de funcționare*, Bucharest 1973.

[5] Electric Motor Catalogue Electroputere (in Romanian), 1987.

[6] D. K.Shah and S. N.Jani, "Simulation and development of automatic excitation control for synchronous motor", *International Journal of Emerging Technology and Advanced Engineering*, Volume 2, Issue 3, March 2012, pp. 49-53.

[7] B. Marinka and U. Azatuhi, "Investigating the regulation system of the synchronous motor excitation mode serving as a reactive power source", *World Academy of Science, Engineering and Technology International Journal of Electrical and Information Engineering* Vol:13, No:6, 2019, pp. 427 - 431.

[8] A. Dulevic, "Automatic control system of speed of synchronous motor", *International Journal of Modern Engineering Research (IJMER)*, Vol. 7, 12 December 2017, pp. 37-41.

[9] V. R. Gasiyarov, A. S. Maklakov, S. S. Voronin, and E. A. Maklakova., "Automatic control system of speed of synchronous motor", *International Conference on Industrial Engineering*, ScienceDirect, Procedia Engineering 129, 2015, pp. 57 – 62.

[10] V. Manoliu, "Functional characteristics of a synchronous motor supplied by a static frequency converter from diagrams" (in Romanian), *Simpozionul de maşini electrice SME'15*, 23 October, 2015.

DOI: 10.52846/AUCEE.2024.04

Performance Comparison of Ensemble Classifiers Algorithms Used in Transformer Fault Detection

Maria-Cristina Nițu [*], Ancuța-Mihaela Aciu [*], Marcel Nicola [*,†] and Claudiu-Ionel Nicola [*,†]

[*] National Institute for Research, Development and Testing in Electrical Engineering – ICMET Craiova/Research and Development Department, Craiova, Romania, cristinamarianitu@yahoo.com, ancutu13@yahoo.com

[†] University of Craiova/Department of Automatic Control and Electronics, Craiova, Romania, marcel.nicola@edu.ucv.ro, claudiu.nicola@edu.ucv.ro

***Abstract* - Power transformers are essential elements in the production and distribution of electricity, and keeping them in optimum operating condition is a constant concern for specialists in the field. The condition of power transformers is mainly determined by the condition of the mixed insulation system, i.e. solid cellulose paper insulation and liquid insulating oil insulation. The identification method, described in this paper in order to determine the fault condition for power transformers is based on the fact that the assessment of their condition is mainly determined by the condition of the mixed insulation system, namely the solid insulation made of cellulose paper and the liquid insulation made of insulating oil. This is why the Three Ratio Technique (TRT) is used with good results for the early detection of power transformer faults. This method is considered as simple, but at the same time efficient in interpreting the results of dissolved gas analysis. It uses three new gas ratios to differentiate between thermal and electrical faults. In this paper, the ratios defined by the TRT method are used to train a machine learning classifier based on Ensemble Classifiers using Bagged Trees (random forest), Boosted Trees, and RUSBoosted Trees algorithms. The validation of the power transformer fault identification software application for the proposed method is carried out in the experimental section.**

Cuvinte cheie: *transformator de putere, analiza gazelor dizolvate, tehnica cu trei rapoarte, pădure aleatoare.*

Keywords: *power transformer, dissolved gas analysis, three ratio technique, random forest.*

I. INTRODUCTION

High-power transformers have proven to be elementary equipment of the power system. The importance of their functioning in optimal parameters makes it mandatory to ensure an active maintenance program. It is known that the state of degradation of the mixed insulation system (paper-oil) is a decisive indicator in keeping/taking the transformer out of service [1, 2].

The methods for diagnosing the fault condition of power transformers have been the subject of many studies in the specialized literature. The most common methods are based on Dissolved Gas Analysis (DGA), this method has proven to be highly effective and at the same time economically convenient [3].

A multitude of DGA techniques have been developed to interpret incipient transformer faults, such as Doernenburg ratio [4], Rogers ratio [5], IEC ratio [6], Duval triangle/pentagon Duval/pentagon triangle [7], Gouda triangle [8] and three ratio technique (TRT) [9].

Fault states or anomalies occurring in the mixed insulation system is signaled by the formation of gases dissolved in oil. Depending on the gas concentrations (hydrogen H2, methane CH4, ethane C2H6, ethylene C2H4, acetylene C2H2, carbon monoxide CO, carbon dioxide CO2, nitrogen N2 and oxygen O2), with the help of DGA, the faults can be identified and localized at their early stages [10].

The methods listed above have advantages as well as weaknesses. To increase diagnostic accuracy it is recommended to use complementary methods or to improve them by developing an analysis program based on one or more methods.

The prediction and monitoring of the condition of electrical equipment has evolved in the sense that a complete characterization of the paper-oil insulation condition can be done by DGA tests, tests that give much information about the phenomena occurring in this equipment. Monitoring key parameters for detecting the transformer condition can be done online or off-line by realizing DGA from oil. It is unanimously accepted that both electrical and thermal faults can be determined from this analysis [11-13].

Regarding the development of transformer fault analysis/detection software, we mention the use of fuzzy logic based systems [14], neural networks [15] and classifiers based on machine learning algorithms [16].

In the case of the application in this paper, the aim is to use a machine learning type classifier which, after appropriate training, is able to estimate with an accuracy of more than 95% the type of fault of a transformer for which the dissolved gas concentrations are known. Based on their values, using the TRT type method with the ratios defined in it, are used as attributes of each training sequence of the classifier that will provide as output the type of defect. Based on the TRT method for DGA analysis, this paper presents a transformer fault condition classifier based on random forest algorithms [17-19].

The paper is structured as follows: Section II presents the TRT-type method and Section III presents the implementation of a random forest classifier. Test results for identifying power transformer faults using the TRT-type method and random forest classification algorithms are presented in Section IV, while the final section presents some conclusions and proposals for future work.

II. THREE RATIO TECHNIQUE

Osama E. Gouda, developed the TRT (DGA technique used in transformer oil) in order to increase the precision/accuracy of transformer fault diagnosis compared to classical methods such as Duval triangle 1, Doernenburg ratio, IEC ratio and Rogers ratio.

In accordance with the theory of thermodynamics, which is based on the equilibrium pressures of hydrocarbon gas formations at different temperatures, in oil-immersed transformers, each hydrocarbon gas varies with respect to the others in relation to the decomposition temperature. So we can conclude that there is an increasing proportion of hydrocarbon gases with respect to temperature fluctuation.

The maximum rate of formation of a gas is reached at a certain temperature, and each individual gas can reach its maximum rate at a different temperature.

Fig. 1 shows the formation of fault gas as a function of temperature and type of fault [13]. These are the same in all mineral oil electro-technical equipment (e.g. current or voltage transformers, free-breathing or sealed power transformers, bushings, etc.).

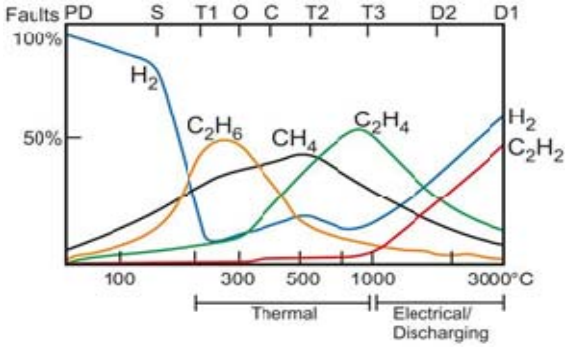

Fig. 1. Defect gas formation as a function of temperature.

The TRT is a simple and effective method of interpreting dissolved gas analysis results. It uses three new gas ratios to differentiate between thermal and electrical faults. The three new ratios are the result of reorganizing the five key gas concentrations into gas pairs that can clearly classify faults for each ratio. These ratios are [9]:

$$R1 = \frac{C_2H_6 + C_2H_4}{H_2 + C_2H_2} \quad (1)$$

$$R2 = \frac{C_2H_2 + CH_4}{C_2H_4} \quad (2)$$

$$R3 = \frac{C_2H_2}{C_2H_4} \quad (3)$$

The faults identified with the three ratios can be exemplified as follows:

- R1 distinguishes between thermal, DP and arcing faults;

- R2 distinguishes between D1 and D2 faults, between thermal faults from very low to high levels of thermal energy. This ratio can also assess the severity of thermal, electrical and partial discharge faults.

- R3 distinguishes between thermal and electrical faults, but cannot differentiate between DP, D1 and D2 faults. This ratio is also used in the Rogers, Doernenburg and IEC methods and it only confirms the fault condition identified with R1.

As with the other gas ratio methods, this technique is used when the concentration of at least one gaseous hydrocarbon exceeds the normal limits given in Table I.

TABLE I.
REFERENCE VALUES FOR KEY GAS CONCENTRATIONS

Dissolved gases	H_2	CH_4	C_2H_2	C_2H_4	C_2H_6	CO	CO_2
Reference concentrations [ppm]	100	120	1	50	65	350	2500

The TRT method is a simple and effective method of interpreting dissolved gas analysis results. By analysing these ratios, the method can effectively classify the type and severity of faults such as thermal, partial discharge and arc faults.

The evaluation of the ratios between the concentrations of three main gases: H_2, CH_4 and C_2H_4, and the comparison of these ratios with reference values lead to the identification of the different types of faults that can occur inside the transformer. For example, H_2 indicates the presence of partial electrical discharges or arcing, CH_4 results from overheating of oil or insulating materials, and C_2H_4 is associated with high energy partial electrical discharges.

By using the three combinations of gas ratios, a clearer classification of fault types and severity is achieved (Table II) [9].

TABLE II.
DIAGNOSTIC CODING OF TRT INTERPRETATION

The range of reports			Code
R1	*R2*	*R3*	
R1 < 0.05	R2 <1	R3 < 0.05	0
0.05 ≤ R1 ≤ 0.9	1 ≤ R2 ≤ 3.5	0.05 ≤ R3 ≤ 0.5	1
R1 > 0.9	R1 > 3.5	R3 > 0.5	2

TABLE III.
FAULT DIAGNOSIS WITH TRT METHOD

R1	R2	R3	Fault type	Fault code
1or 2	0	0 or 1	High temperature thermal fault T > 700°C	T3
1or 2	1	0 or 1	Medium temperature thermal fault 300°C < T < 700°C	T2
1or 2	2	0 or 1	Low temperature thermal fault 150°C < T < 300°C	T1
1	—	0	Low temperature thermal fault T < 150°C	T0
0	1 or 2	0 or 1	Low partial discharge	PD1
0	1 or 2	2	High partial discharge	PD2
0 or 1	0 or 1	2	High energy discharge	D2
1 or 2	2	2	Low energy discharge	D1
2	0 or 1	2	Combination of electrical and thermal faults	DT

The advantages of the TRT method include:

- has a high accuracy compared to other methods that use ratios and also to the Duval Triangle1;
- has the ability to distinguish more reliably the faults according to their severity;
- leads to a significant reduction in cases (without decision) specific to methods that use ratios due to obtaining values of ratios outside the specified range and thus the inability to identify the fault.

Limitations of the technique:

- in some situations, the interpretation of the results can be difficult, especially in the case of old transformers or transformers with a complex fault history;
- the technique cannot detect all types of faults, such as natural ageing of oil or insulating materials;
- gas concentrations may be influenced by other factors such as temperature, pressure or humidity.

While the TRT method is a valuable tool, it is important to consider the following:

- The age of the transformer oil can affect the gas composition and therefore the accuracy of the results.
- Factors such as load cycling, temperature variations and moisture content can also affect gas content and diagnostic conclusions.
- Complementary analysis - the TRT method should be used in conjunction with other diagnostic tools and expert judgement for a complete assessment.

DGA using the TRT is a valuable method of monitoring the condition of power transformers However, for correct interpretation of the results, a complex analysis is recommended, taking into account both the absolute values of the gas concentrations and their evolution over time. In addition, the interpretation of results should be confirmed by other diagnostic techniques.

III. Implementation of Random Forest Algorithms in Matlab for Transformer Fault Detection

A classifier, after appropriate training, estimates the relationship between the class attribute and the other feature attributes. It extracts the model from the training data and tries to minimise the mean squared error.

The limitations of the model (consideration of the linear model versus a highly non-linear real model) result in a relatively large bias. Due to the limited amount of training data, we obtain a variance above the practically acceptable limits. In this sense, Random Forest uses multiple decision trees and performs a combination of their predictions to improve accuracy and avoid over-fitting. In the case of the application in this paper, the aim is to use a machine learning type classifier which, after appropriate training, is able to estimate with an accuracy of more than 95% the type of fault of a transformer for which the dissolved gas concentrations are known.

Based on their values, using the TRT type method described in the previous section, the ratios R1, R2 and R3 are obtained, which are the inputs of each training sequence of the classifier that will give as output the type of defect. Fig. 2 shows the block diagram of the software application for power transformer fault identification using the TRT method and the ensemble Bagged Trees classifier.

For this application, we used ensemble classifiers via the Classification Learner application from Matlab Statistics and Machine Learning toolbox. After training on a set of 200 samples, Table IV shows the training performance for the following categories of ensemble classifiers: Boosted Trees, Bagged Trees, Subspace Discriminant, Subspace KNN, and RUSBoost Trees.

It can be observed that the best performance is obtained using the Bagged Trees classifier, which is based on the Random Forest algorithm. It should be noted that this type of algorithm generally gives the best results for the range of classifiers presented [17-19].

Fig. 3 shows the confusion matrix resulting from ensemble bagged tree classifier training for the corresponding dataset. It can be seen that there is a relatively high percentage of confusion between D2 and PD2 faults. This is explained by the way they are defined, so that a large percentage of the membership intervals of the three dissolved gas ratios overlap. Confusion matrix is a visual representation of a classification model's performance and compares predicted class labels to the actual true labels.

This is also reflected in Figs 4 and 5, as the receiver operating characteristic (ROC) value for the PD2 error is less than 1, whereas the ROC value for the D2 error is less than 1. ROC curves are primarily used for evaluating the performance of binary classifiers. These classifiers predict one of two possible outcomes (positive/negative).

Another common performance ranking parameter of the algorithms used is the Area Under Curve (AUC) number. Also, AUC is a performance metric that quantifies the overall ability of a binary classifier. It represents the probability that a randomly chosen positive instance will be ranked higher than a randomly chosen negative instance by the classifier. This parameter is an overall qualitative measure of the classifiers.

TABLE IV.
Ensemble Classifier Performance For Power Transformer Fault Identification

Ensemble classifier type	Accuracy [%]
Bagged Trees	95.7
Boosted Trees	95.4
RUSBoosted Trees	95.1
Subspace KNN	73.5
Subspace Discriminant	72.7

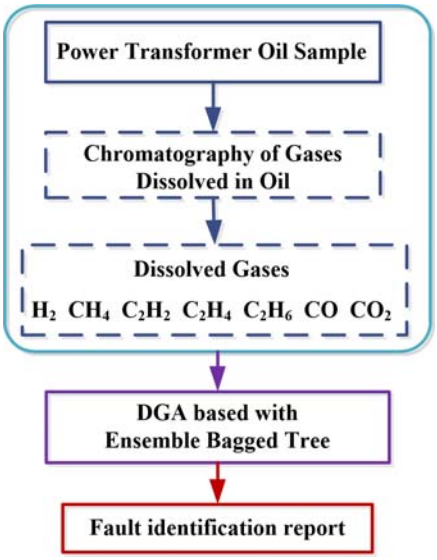

Fig. 2. Block diagram of the software application for power transformer fault identification using the TRT method and the Ensemble Bagged Trees classifier.

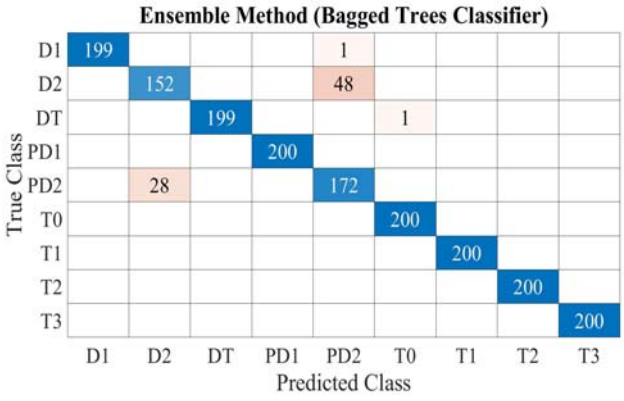

Fig. 3. Confusion matrix used to train the Bagged Trees ensemble classifier for transformer fault detection.

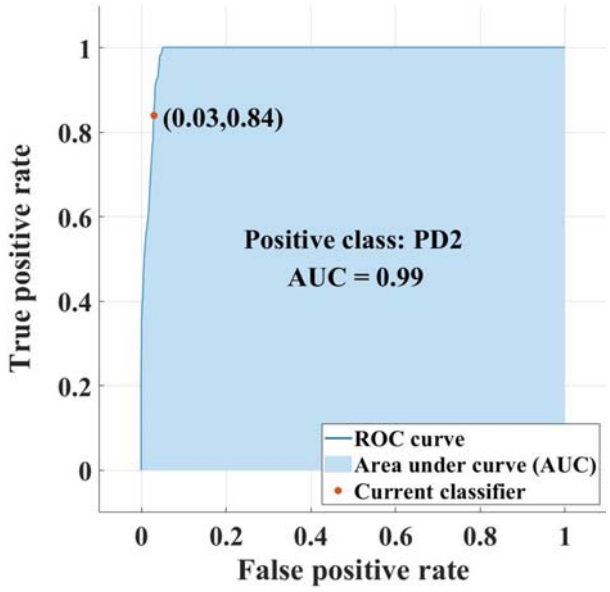

Fig. 4. ROC curve corresponding to the Bagged Trees ensemble classifier training for the PD2 error.

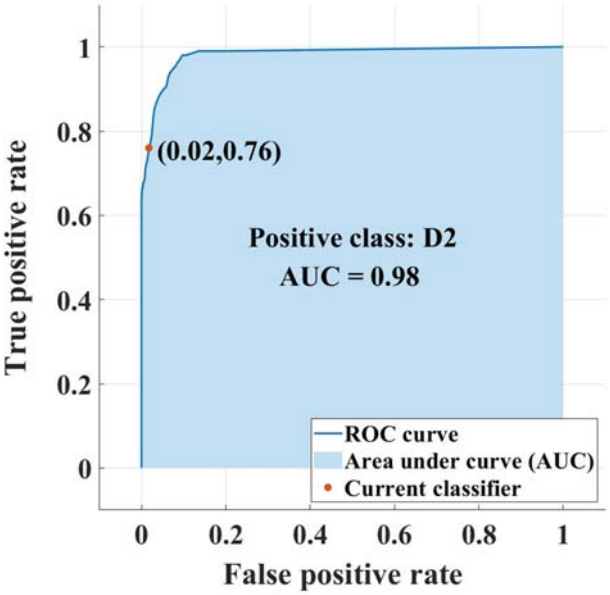

Fig. 5. ROC curve corresponding to the Bagged Trees ensemble classifier training for error D2.

Fig. 6 shows a prediction of the separation of the 9 defect classes corresponding to attributes R2 and R3, resulting from training the Bagged Trees ensemble classifier.

The study of the predictions in terms of defect class separation using the Bagged Trees ensemble classifier is shown in Fig. 7. Thus, depending on the values of the 3 ratios (R1, R2 and R3) corresponding to the training samples, a graphical image of the predicted position of the 9 defect types is obtained. In the following, in order to highlight the ranking accomplished in Table IV from the point of view of the accuracy of the classification algorithms used, we present the results obtained after training for the Boosted Trees and RUSBoosted Trees algorithms.

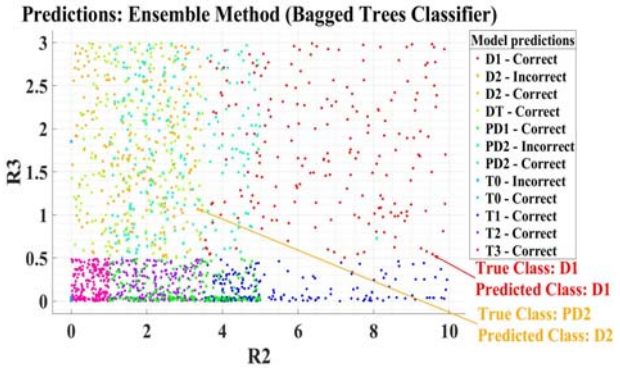

Fig. 6. Separation of defect classes using the Bagged Trees ensemble classifier and attributes R2 and R3.

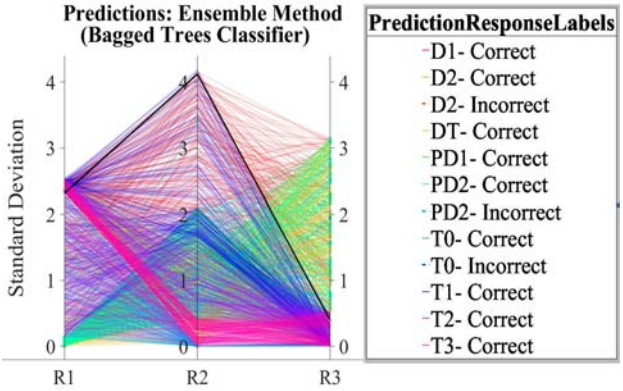

Fig. 7. Study of predictions by separation into 9 defect classes using the Bagged Trees ensemble classifier.

Thus, the resulting training confusion matrix for the Boosted Trees algorithm is presented in Fig. 8. ROC curves corresponding to this algorithm in terms of classification errors for defect classes PD2 and D2 are presented in Fig. 9 and Fig. 10. Fig. 11 shows a prediction of the separation of the 9 defect classes corresponding to attributes R2 and R3, resulting from training the Boosted Trees ensemble classifier. The resulting training confusion matrix for the RUSBoosted Trees algorithm is presented in Fig. 12. The ROC curves corresponding to this algorithm with respect to the classification errors for the PD2 and D2 defect classes are presented in Fig. 13 and Fig. 14.

Fig. 15 shows a prediction of the separation of the 9 defect classes corresponding to attributes R2 and R3, resulting from training the RUSBoosted Trees ensemble classifier. For the PD2 and D2 defect classes, it can be observed that the AUC decreases by 0.1 for the Boosted Trees algorithm and 0.2 for the RUSBoosted Trees algorithm compared to the Bagged Trees algorithm.

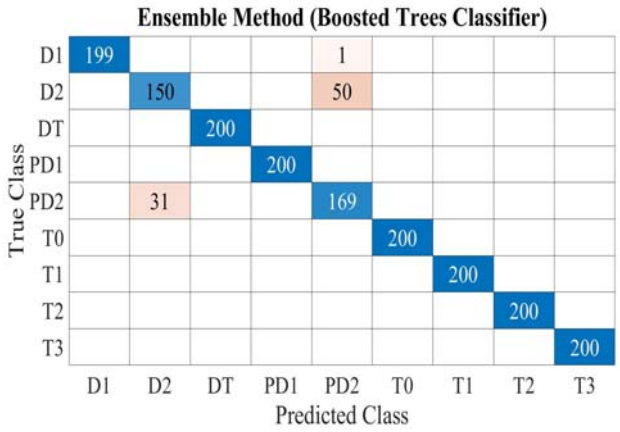

Fig. 8. Confusion matrix used to train the Boosted Trees ensemble classifier for transformer fault detection.

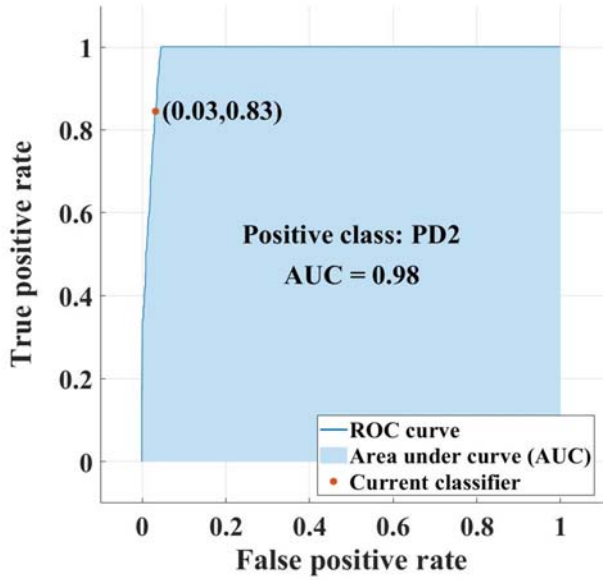

Fig. 9. ROC curve corresponding to the Boosted Trees ensemble classifier training for the PD2 error.

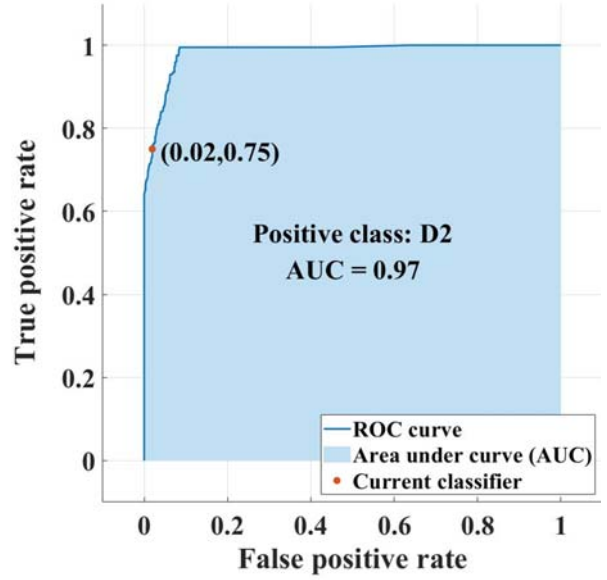

Fig. 10. ROC curve corresponding to the Boosted Trees ensemble classifier training for the D2 error.

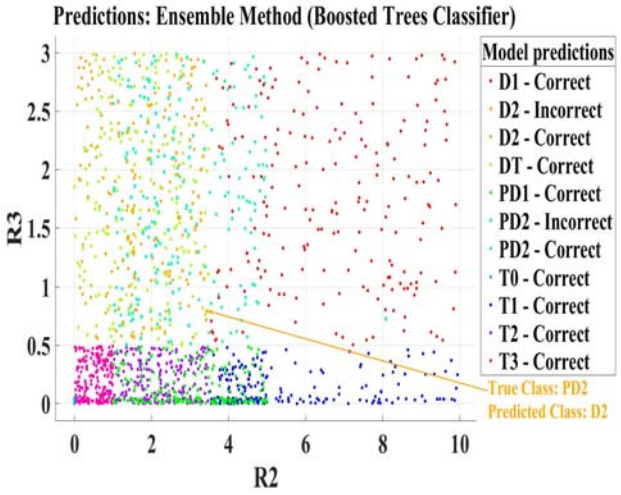

Fig. 11. Separation of defect classes using the Boosted Trees ensemble classifier and attributes R2 and R3.

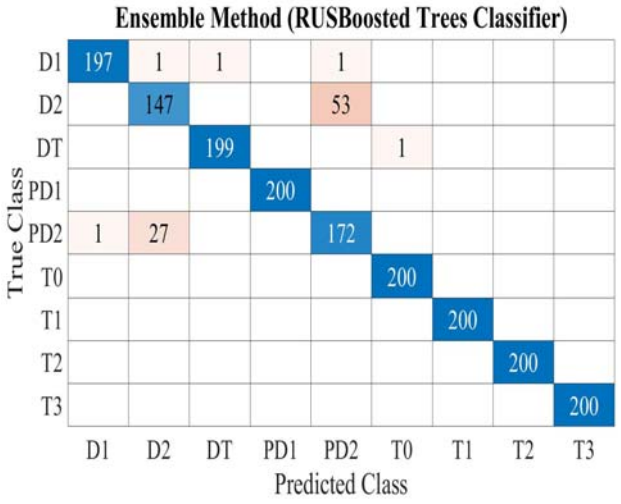

Fig. 12. Confusion matrix used to train the RUSBoosted Trees ensemble classifier for transformer fault detection.

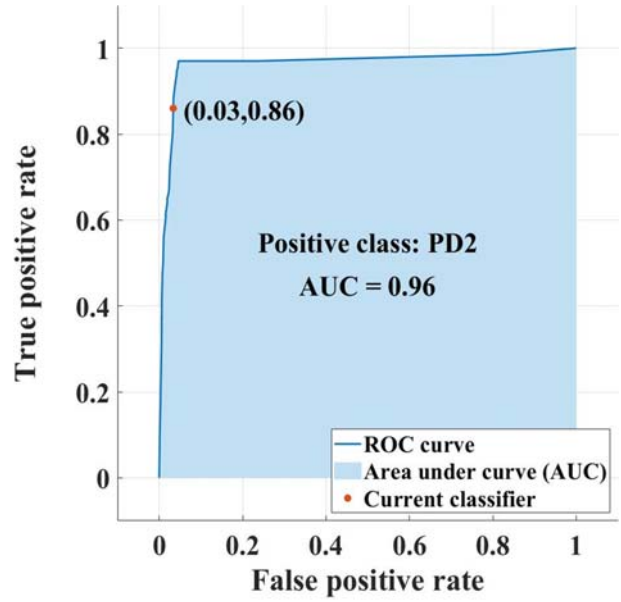

Fig. 13. ROC curve corresponding to the RUSBoosted Trees ensemble classifier training for the PD2 error.

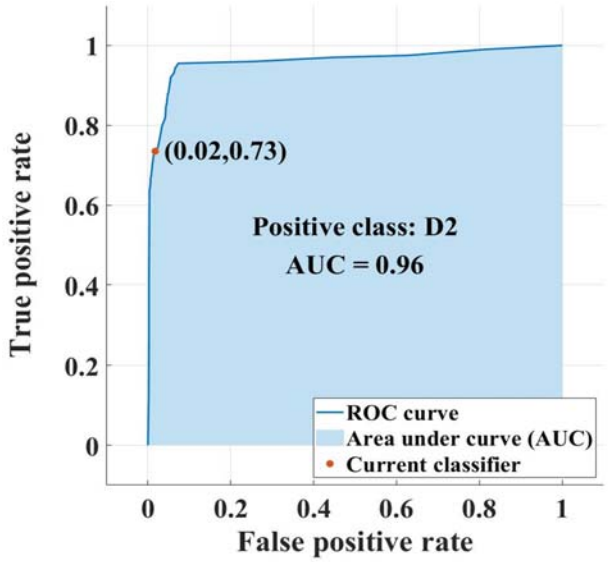

Fig. 14. ROC curve corresponding to the RUSBoosted Trees ensemble classifier training for the D2 error.

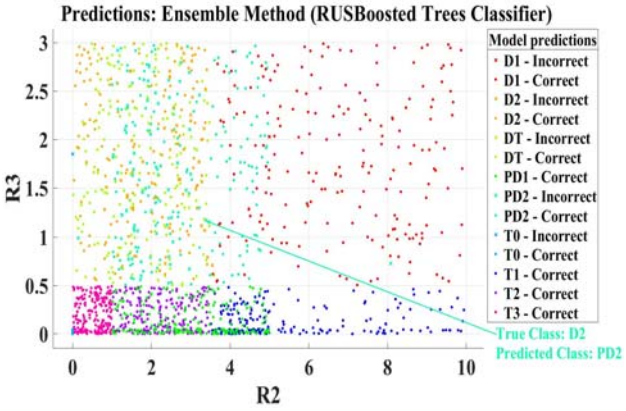

Fig. 15. Separation of defect classes using the RUSBoosted Trees ensemble classifier and attributes R2 and R3.

IV. Results of the Test for Fault Detection in Transformers Using Ensemble Bagged Tree Classifiers

The testing of the power transformer fault detection application presented in this paper was carried out on two 63 MVA 110/6.3 kV (Transformer-1) and 80 MVA 121/10.5 kV (Transformer-2) transformers undergoing prophylactic inspections. Their gas concentration values are given in Table V.

TABLE V.
Dissolved Gas Concentrations to Test the Proposed Transformer Fault Identification Method

Chromatographic analysis of gases dissolved in oil	Transformer-1 gas values [ppm]	Transformer-2 gas values [ppm]
Hydrogen H_2	19.46	455
Methane CH_4	69.92	755
Ethan C_2H_6	204.42	173
Ethylene C_2H_4	15.234	422
Acetylene C_2H_2	1.07	2
Carbon monoxide CO	154.94	1427
Carbon dioxide CO_2	1663.21	4234
Total dissolved combustible gases	465.044	3234

A. *Software Application Testing for Power Transformer Fault Detection - Type 1 Power Transformer*

In the first case, the following set of gas concentration values is used H_2 = 19.46 ppm, CH_4 = 69.92 ppm, C_2H_2 = 1.07 ppm, C_2H_4 = 15.234 ppm, and C_2H_6 = 204.42 ppm. These are used to obtain the following values of the 3 ratios defined in equations (1)-(3), which represent the inputs for the software application of the proposed random forest classifier: R1 = 10.699, R2 = 4.661, and R3 = 0.071.

After analysing the application using the Bagged Trees ensemble classifier, the fault T1 (see Fig.8) was identified, which is a thermal fault indicating temperatures between 150°C and 300°C. This fault indicates overheating due to flux concentration, most likely overheating of the LV or HV outputs due to faulty connections between the flexible joint connecting the LV or HV coil end to the copper terminal of the bushing on the LV or HV side, or poor soldering of the LV or HV coil end to the output flexible joint. The extent of the observed phenomenon is not dangerous for transformer availability.

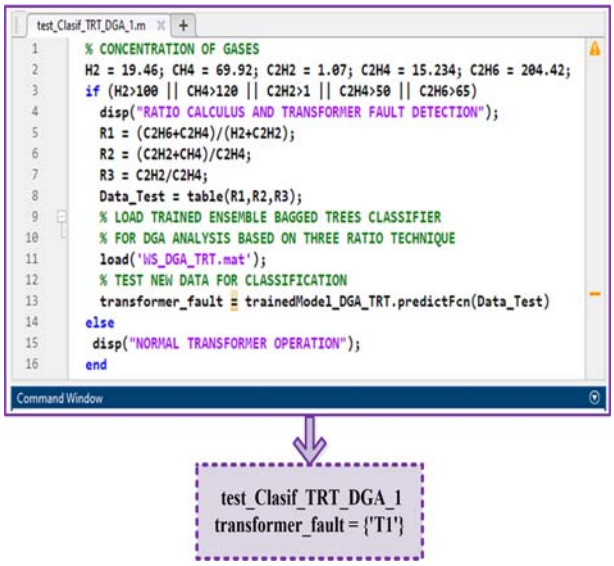

Fig. 16. Testing the Bagged Trees ensemble classifier - first test of the power transformer.

It is well known that cellulose insulation is affected by thermal degradation phenomena, so whenever a thermal defect is detected, it is imperative to determine the degree of polymerisation of the cellulose insulation by measuring the concentrations of furan compounds dissolved in oil.

As a result, the following recommendations have been made:

- Check the LV and HV winding outputs and retighten the flexible joint on the LV and HV terminals;
- Measure the concentrations of furan compounds dissolved in the oil and analyse the furan compounds to determine the state of degradation of the solid insulation and the cause of this state. The use of furan compound concentrations has the effect of increasing the accuracy of transformer faults identified by DGA [7];
- Repeat parameter measurements of the entire insulation system and complete oil analysis.

B. *Software Application Testing for Power Transformer Fault Detection - Type 2 Power Transformer*

In the second case, the following set of gas concentrations is used: H_2 = 455 ppm, CH_4 = 755 ppm, C_2H_2 = 2 ppm, C_2H_4 = 422 ppm, and C_2H_6 = 173 ppm. These are used to obtain the following values of the 3 ratios defined in equations (1)-(3), which represent the inputs for the software application of the proposed random forest classifier: R1 = 1.302, R2 = 1.793, and R3 = 0.004.

After analysing the application using the Bagged Trees ensemble classifier, the T2 defect was identified (see Fig.9), which is a thermal defect with temperatures between 300°C and 700°C.

According to the dissolved gas concentration values presented in Table V, the following aspects were identified:

- According to [13], the ethylene concentration decreases in case of a defect in the conductors (200 ppm < C_2H_4 < 2900 ppm). This means that the fault may be caused by overheating of the conductors due to eddy currents or poor connections between the output flexes in the winding and the terminals of the insulated bushings;
- CO = 1427 ppm > 1000 ppm and CO_2/CO = 2.96 < 3 in the presence of significant amounts of the other fault gases. Therefore, IEC 60599:2022 [11] indicates/specifies the involvement of paper in a defect with possible charring of the paper;
- Acetylene value in the oil above the required limit (2 > 1). This requires careful attention and weekly or even daily monitoring to determine if additional acetylene is being generated;
- The TDCG value of 3234 ppm classifies the transformer as Condition 3 - Extreme Caution according to IEEE Std.C.57-104:2019 [12], i.e. a high degree of cellulose and/or oil insulation degradation;
- Content of furan compounds was not determined.

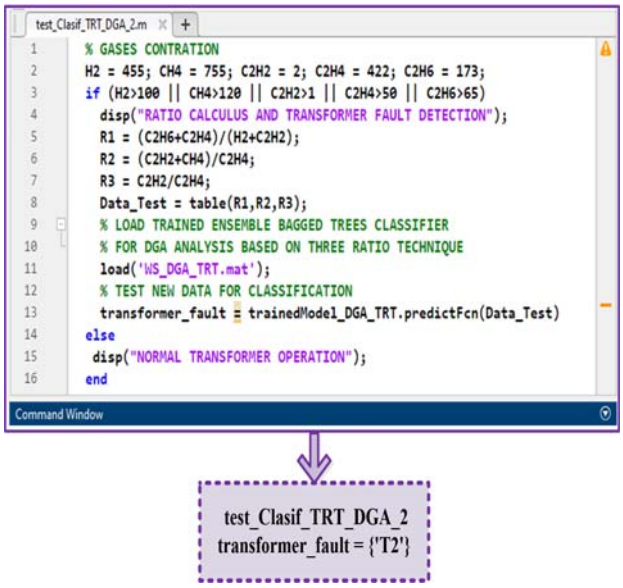

Fig. 17. Bagged Trees ensemble classifier test - power transformer second test.

As a result, the following recommendations have been made:

- Check the connections between the coil output flexible joints and the terminals of the insulated bushings and retighten the flexible joints on the LV and HV terminals;
- Measure the concentrations of furan compounds dissolved in the oil and analyse the furan compounds to determine the state of degradation of the solid insulation and the cause of this state;
- Repeat the DGA often enough to calculate the amount of gas produced per day for each gas;
- Complete oil analysis and repeat insulation system measurements.

V. CONCLUSIONS

This paper presents a method for identifying the fault condition of power transformers. It is based on the fact that the assessment of the condition of power transformers is mainly determined by the condition of the mixed insulation system, i.e. solid cellulose paper insulation and liquid insulating oil insulation. The TRT method is therefore used with good results for the early detection of power transformer faults.

The classification algorithm used was a machine learning algorithm based on ensemble and random forest algorithms from Matlab Statistics and Machine Learning toolbox. The validation of the power transformer fault detection application is carried out in the experimental section. For future work, the aim is to use combined classification algorithms with weight optimisation algorithms to increase accuracy.

ACKNOWLEDGMENT

This paper has been prepared within the framework of the NUCLEU programme under the National Research, Development and Innovation Plan for 2022-2027, with the support of the Romanian Ministry of Research, Innovation and Digitisation, Project No. PN 23 33 02 03 and the installation of national interest "System for generating, measuring and recording short-circuit currents" - SPMICS.

Contribution of authors:

First author –25%

First coauthor – 25%

Second coauthor – 25%

Third co-author– 25%

Received on September 16, 2024

Editorial Approval on November 25, 2024

REFERENCES

[1] M. Patil, A. Paramane, S. Das, U. M. Rao, and P. Rozga, "Health assessment of solid insulation of mineral oil-filled converter transformer," in *IEEE Transactions on Dielectrics and Electrical Insulation*, vol. 31, no. 3, pp. 1557-1564, June 2024.

[2] H. Cui, L. Yang, Y. Zhu, S. Li, A. Abu-Siada, and S. Islam, "A comprehensive analyses of aging characteristics of oil-paper insulation system in HVDC converter transformers," in *IEEE Transactions on Dielectrics and Electrical Insulation*, vol. 27, no. 5, pp. 1707-1714, October 2020.

[3] H. Syafruddin and H. P. Nugroho, "Dissolved gas analysis (DGA) for diagnosis of fault in oil-immersed power transformers : a case study," *The 4rd International Conference on Electrical, Telecommunication and Computer Engineering (ELTICOM),* Medan, Indonesia, 2020, pp. 57-62.

[4] O. Shutenko and O. Kulyk, "Comparative analysis of the defect type recognition reliability in high-voltage power transformers using different methods of DGA results interpretation," *IEEE Problems of Automated Electrodrive. Theory and Practice (PAEP)*, Kremenchuk, Ukraine, 2020, pp. 1-6.

[5] F. Mohamad, K. Hosny, and T. Barakat, "Incipient fault detection of electric power transformers using fuzzy logic based on Roger's and IEC method," *The 14th International Conference on Computer Engineering and Systems (ICCES)*, Cairo, Egypt, 2019, pp. 303-309.

[6] I. B. M. Taha, S. S. M. Ghoneim, and A. S. A. Duaywah, "Refining DGA methods of IEC code and Rogers four ratios for transformer fault diagnosis," *IEEE Power and Energy Society General Meeting (PESGM)*, Boston, MA, USA, 2016, pp. 1-5.

[7] A.-M. Aciu, M. C. Nițu, C.-I. Nicola, and M. Nicola, "Determining the remaining functional life of power transformers using multiple methods of diagnosing the operating condition based on svm classification algorithms," in *Machines*, vol. 12, no. 1, pp. 1-34, January 2024.

[8] O. E. Gouda, S. H. El-Hoshy, and H. H. E. L. Tamaly, "Condition assessment of power transformers based on dissolved gas analysis," in *IET Gener. Transmiss. Distrib*., vol. 13, no. 12, pp. 2299-2310, June 2019.

[9] O. E. Gouda , S. H. El-Hoshy, and H. H. E.L.-Tamaly, "Proposed three ratios technique for the interpretation of mineral oil transformers based dissolved gas analysis," in *IET Generation, Transmission & Distribution*, vol. 12, no. 11, pp. 2650-2661, June 2018.

[10] A.-M Aciu, S. Enache, and M.-C. Nițu, "A Reviewed turn at of methods for determining the type of fault in power transformers based on dissolved gas analysis," in *Energies*, vol. 17, no. 10, pp. 1-26, May 2024.

[11] IEC 60599:2022 ¾ *Mineral Oil-Impregnated Electrical Equipment in Service – Guide to the Interpretation of Dissolved and Free Gas Analysis; International Electrotechnical Commission*: Geneva, Switzerland, 2022.

[12] IEEE C57.104-2019 ¾ *Guide for the Interpretation of Gases Generated in Mineral Oil-Immersed Transformers; Institute of Electrical and Electronics Engineers:* Piscataway, NJ, USA, 2019.

[13] CIGRÉ Brochure 771 - *Advances in DGA Interpretation,* JWG D1/A2.47, July 2019, ISBN: 978-2-85873-473-3. CIGRE: Paris, France, 2019.

[14] A. Hechifa, A. Lakehal, L. Saidi, A. Nanfak, R. Kelaiaia, and M. El Amine Senoussaoui, "Improvement of transformer fault diagnosis using fuzzy rule and decision tree based on dissolved gas analysis," *The 1st International Conference on Renewable Solutions for Ecosystems: Towards a Sustainable Energy Transition (ICRSEtoSET)*, Djelfa, Algeria, 2023, pp. 1-6.

[15] S. F. Rakhmankulov, M. S. Garifullin, and I. F. Galiev, "Optimization of power transformer defect recognition algorithm with DGA based on probabilistic neural network," *International Russian Smart Industry Conference (SmartIndustryCon)*, Sochi, Russian Federation, 2024, pp. 121-126.

[16] L. Jin, D. Kim, K. Y. Chan, and A. Abu-Siada, "Deep machine learning-based asset management approach for oil-immersed power transformers using dissolved gas analysis," in *IEEE Access*, vol. 12, pp. 27794-27809, February 2024.

[17] A. Jamshed, K. Chatterjee, and N. Haque, "Random forest classifier based dissolved gas analysis for identification of power transformer faults using gas ratio data," *The 2nd International Conference for Emerging Technology (INCET)*, Belagavi, India, 2021, pp. 1-5.

[18] S. D. Patil, M. Dharme, A. J. Patil, G. C. A. K, R. K. Jarial, and A. Singh, "DGA based ensemble learning and random forest models for condition assessment of transformers," *The International Conference on Smart Generation Computing, Communication and Networking (SMART GENCON)*, Bangalore, India, 2022, pp. 1-6.

[19] H. Xu, X. Wang, Y. Qiu, and Y. Xu, "Towards DGA domain name detection via multi-feature coordinated representation and random forest," *The 11th International Conference on Information Systems and Computing Technology (ISCTech)*, Qingdao, China, 2023, pp. 510-518.

[20] M. -C. Niţu, A. -M. Aciu, M. Nicola and C. -I. Nicola, "Transformer Fault Detection Using DGA Based on Three Ratio Technique and Random Forest Algorithm," *2024 International Conference on Applied and Theoretical Electricity (ICATE)*, Craiova, Romania, 2024, pp. 1-6, doi: 10.1109/ICATE62934.2024.10748635.

DOI: 10.52846/AUCEE.2024.05

Analysis of the Performance of Distribution Transformers under Short Circuit Conditions. Experiments

Daniela Iovan*, Andrei-Alexandru Poenaru*, Cristian-Eugeniu Sălceanu*, Daniel-Constantin Ocoleanu*, Teodor Popa*, Dan Stefan* and Sorin Enache†

* National Institute for Research Development and Testing in Electrical Engineering-ICMET Craiova, Craiova, Romania, icmet@icmet.ro

† Faculty of Electrical Engineering, University of Craiova, Craiova, România, senache@em.ucv.ro

Abstract - **The design of power transformers is heavily influenced by their performance during short circuit. This paper explores the experimental analysis of a power transformer with circular concentric coils, utilizing metal foil conductor in the low-voltage winding, and a rated power of 2000 kVA. To validate its behavior, the study employs Frequency Response Analysis (FRA), a widely recommended diagnostic method for identifying internal faults in power transformers. Furthermore, the paper provides insights into the design specifics of power transformers used in renewable energy power plants. By highlighting the unique aspects and criticalities examined, this study establishes itself as a niche contribution to understanding safety in transformer operation. The research also delves into experiments conducted in a high-power laboratory to investigate how transformers respond to the dynamic effects of short circuit. Particular attention is given to the thermal and mechanical impacts of short circuit currents, with an emphasis on their negative consequences. Additionally, the paper discusses a system configuration where direct current (DC) produced by photovoltaic cells is converted into alternating current (AC) using one or more inverters connected to the low-voltage windings of a step-up transformer. Finally, the study underscores the importance of assessing the short circuit behavior of power transformer, focusing on the irreversible deformations caused by axial and radial forces during short circuit events.**

Cuvinte cheie: *transformator de distribuție, circuit de putere, scurtcircuit, plot, defect, înfășurare de joasă tensiune, centrala electrica, resurse regenerabile.*

Keywords: *distribution transformer, power circuit, short-circuit, tap, fault, low-voltage winding, power station, renewable resources.*

I. INTRODUCTION

A transformer is a static electrical device that transfers electricity from one circuit (the transformer's primary) to another (the transformer's secondary) by the law of electromagnetic induction. A transformer consists of a ferromagnetic core with two or more windings insulated from each other and from the core.

The winding that receives energy is called the primary winding (and behaves as a receiver), and the winding that supplies energy to an external circuit is called the secondary winding (and behaves as a generator) [1], [2], [3].

The magnetic flux, which varies in time with the frequency of the primary current, induces in the transformer windings an electromotive voltage of the same frequency, with values proportional to the number of turns of the windings.

Power transformers are subject to an increased failure rate due to the occurrence of external faults, which are characterized by short circuits caused by equipment within the distribution system to which the transformer is connected, as well as the occurrence of internal faults, which can occur within the transformer and are characterized by short circuits between turns of the same phase, short circuits between windings, and the tank or at the transformer terminals, environmental factors such as temperature, humidity and corrosive substances can also cause transformer failure.

If no action is taken during the service life, the superior quality of the modern insulators may deteriorate and the insulators will age, eventually leading to transformer failure, so it is imperative to check the condition of the insulators and insulating materials on a regular basis.

When a short circuit occurs, high currents flow through the transformer, not only heating the transformer, but also creating electromagnetic forces that can damage the transformer winding [1].

The flow of power and energy through the transformer causes active and reactive power losses due to losses in the magnetic circuit, losses in the windings due to the Joule effect, eddy currents or magnetostriction.

The presence of moisture in the transformer leads to a deterioration of the insulator condition and consequently to a high risk of heat induced solid insulation failure (e.g. in the paper barrier). Failures due to short-circuit currents are inevitable in split-winding transformers with stabilizing windings and the resulting transient electromagnetic force can cause damage to equipment [4].

A power transformer plays an essential role in power distribution systems. With the increase in grid capacity and transformer capacity, the number of short circuit accidents in power transformers has increased significantly [5], [6]. Studies discussing short-circuit fault can be found in the references listed below [9-13].

Transient short-circuit current can cause a short-circuit force that induces critical mechanical stress on a transformer when the short-circuit condition occurs. [7], [8].

II. Design Details of Transformers Used in Power Plants Producing Electricity from Renewable Energy Sources

One of the most important pieces of equipment in an electrical distribution network is the power transformer. The recent energy crisis, along with the push for new forms of green energy, has driven the need for distribution transformers to adapt to harmonics produced by electrical inverters and imbalances caused by unbalanced consumers or other factors. These transformers, which can handle up to 10 MVA, are designed to operate with low losses and voltage ratios that are tailored to specific needs [14].

Depending on the time of day, they function as either step-up or step-down transformers and must meet various individual, standard, or special requirements dictated by specific regulations.

One key issue is that the presence of harmonics results in additional losses within the transformer—both in the windings and the magnetic core—leading to increased heating and a lower thermal class for transformers in substations. The growing amount of energy generated by photovoltaic systems and subsequently converted and distributed through medium-voltage networks has posed new challenges for transformer designers, particularly in addressing the specific operational conditions in inverter circuits [15].

In these systems, the direct current (DC) generated by photovoltaic cells is converted into alternating current (AC) through one or more inverters connected to the low-voltage windings of a step-up transformer.

Fig. 1 illustrates the general configuration of such a system.

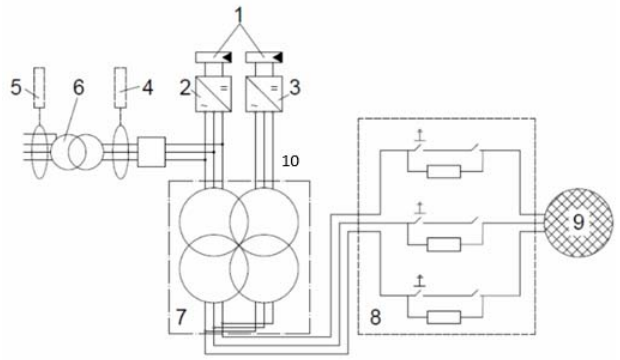

Fig. 1. Schematic system design of the MV-system (1 - photovoltaic generator; 2,3 - photovoltaic inverters; 4,5 - current transformer; 6 - auxiliary transformer; 7 - LV side of the MV transformer, 8 - regular MV switch-gear; 9 - MV grid; 10 - MV side of MV transformer).

The technical solutions used in the construction of these transformers vary from manufacturer to manufacturer, but generally the type of transformer with two secondary windings, each with half windings for both low voltage (LV) and high voltage (HV), arranged concentrically, is used.

When an inverter becomes inactive, current imbalance occurs, resulting in high loss currents and transformer heating. To avoid these effects, the solution is to use semi-winding on low voltage (LV) and high voltage (HV), arranged according to the diagram in Fig. 2.

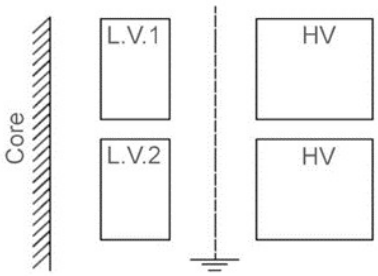

Fig. 2. Power transformer with 4 concentrated windings, two primary and two secondary.

The magnetic impedances of the LV1-HV and LV2-HV windings are almost equal, and the low voltage (LV) winding is axially split. However, this type of construction is large and LV connections are difficult to make. However, this design is preferred by most manufacturers of power transformers used in power plants producing electricity from renewable energy sources.

Since inverter-fed transformers are fed by low-voltage (LV) windings with significant harmonic content and are often subject to transient regimes, the most common type of transformer from a design point of view is the three-winding transformer: two LV windings and one HV winding [14].

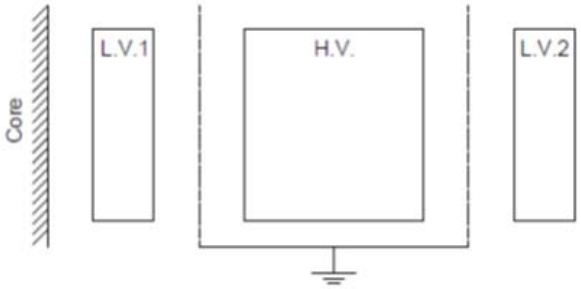

Fig. 3. Power transformer with 3 concentrated windings, two secondary and one primary.

One type of concentrated winding transformer used in renewable power plants is an 8.4 MVA power transformer with one 33 kV LV winding and two 0.66 kV HV windings with the following characteristics:

Transformer rated power, S_N = 8400 kVA; HV side voltage, U_{HV} = 33 kV ± 2 × 2.5%; LV side voltage, U_{LV} = 0.66 kV / 0.66 kV; rated current of energized winding, I_N = 147 A/3674 − 3674 A; vector group, ΔY11Y11; cooling type, Oil Natural Air Natural (ONAN); windings, aluminum conductor, non-circular (oval).

Short-circuit voltages:

- $U_{k\ 75°}$ = 7.35%-LV 2u-2v-2w;
- $U_{k\ 75°}$ = 7.49%-LV 3u-3v-3w.

Rated current short-circuit losses:

- $P_{k\ 75°}$ = 28,270 W-2u-2v-2w;
- P_k = 30,506 W-3u-3v-3w.

No-load losses according to rated conditions P_0 = 6200 W:

- 1U-1V-1W–HV winding;
- 2u-2v-2w–LV winding no. 1;
- 3u-3v-3w-LV winding no. 2.

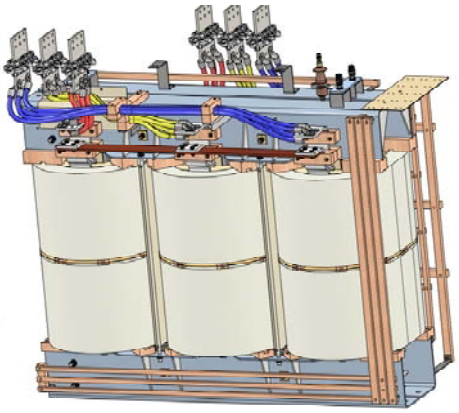

Fig. 4. Power transformer used in power plants to generate electricity from renewable energy sources.

III. Research Methodology

The method used for Frequency Response Analysis (FRA) is made with central conductor of the coaxial measurement should be connected directly to the transformer terminal using the shortest possible length of unshielded conductor. The shortest possible connection between the screen of the measuring lead and the flange at the base of the bushing was made using braid. A specific clamp arrangement or similar was used to make the earth connection as short as possible. This method was expected to give repeatable measurements up to 2 MHz.

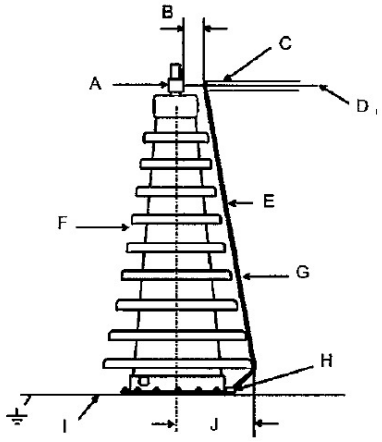

Fig. 5. Frequency Response Analysis connection method (A - connection clamp; B – unshielded length to be made as short as possible; C – measurement cable shield; D – central conductor; E – shortest braid; F – bushing; G – earth connection; H – earth clamp; I – tank; J – smallest loop).

Transformers up to 2500 kVA, 20/0.4 kV are essential components in distribution networks, playing a critical role in transforming voltage for distribution to consumers. Primarily used in substations and transformer stations, they are designed for efficient operation under normal and light overload conditions.

But sometimes, due to damage on the low-voltage side (0.4 kV), they have to withstand a short-circuit regime without damage. In general, well-designed and well-built older generation transformers can withstand the stresses (thermal and dynamic) produced by a short circuit.

In recent years, EU regulations on minimizing active losses, increasing material prices and reducing size have led to the emergence of a new generation of hermetically sealed transformers with new active part and tank manufacturing technology that makes them slightly vulnerable to electrodynamic stresses. From a thermal standpoint, they are also at the maximum temperature limit of oil and seals to make them more cost effective [15].

It is well known that the dynamic forces generated by a transformer short-circuit depend on its internal short-circuit impedance, but also on the external impedance of the circuit or network in which it operates, i.e.:

$$F = f(I^2) \ \text{[N]} \tag{1}$$

$$F = \frac{U}{\sqrt{3} \times (Z_t + Z_{r)}} \tag{2}$$

where: F = electrodynamic force; I = peak short-circuit current.

$$Z_t = \frac{u_k \times u_2}{100 \times S_N} \tag{3}$$

[Ω/phase] – phase impedance

$$Z_r = \frac{u^2}{Sr}[\Omega] \tag{4}$$

u_k = short-circuit voltage [%]

u = rated transformer voltage [kV]

S_N = transformer power [MVA]

S_r = apparent grid power [MVA]

Thus, the electrodynamic forces are proportional to the square of the peak current:

$$I = I \times k \times \sqrt{2} \ \ [\text{kA}_{\text{max}}] \tag{5}$$

$$k \times \sqrt{2} = f(X/R) \tag{6}$$

According to [3], Table 4:

$$1.51 \le k \times \sqrt{2} \le 2.55 \tag{7}$$

The ability of a transformer to successfully withstand a short-circuit regime shall be determined by special tests to withstand the dynamic effects of the short-circuit, preceded by routine tests.

In general, power transformers of the 2nd and 3rd categories (power over 100 MVA) cannot be tested under short-circuit conditions because of the limited power of the test stations, so the forces generated in this regime and the ability of the transformers to withstand them are checked by calculation.

Category I transformers hermetically sealed or with conservator, oil-immersed transformers, and dry-type transformers, fully equipped as in service, are first subjected to all individual tests:

- determination of the transformation ratio;
- determination of the switching system and the vector group;
- measurement of ohmic resistance of connections;

- dielectric tests (applied voltage, induced voltage, tg δ, partial discharges);
- dry-running tests including measurement of current and losses;
- measurement of short-circuit voltage, short-circuit impedance and active losses.

IV. Two-Winding Transformer Short-Circuit Test

The two-winding transformer short-circuit test consists of applying rated voltage to one winding of the transformer while the other winding is short-circuited to three phases.

In order to avoid magnetic saturation, it is preferable to supply the high-voltage winding, which is further away from the magnetic core, and there are two known methods of short-circuiting: pre-short-circuiting, where the low-voltage winding is short-circuited beforehand, and post-short-circuiting, where the low-voltage winding is short-circuited by means of a precision short-circuiting switch which closes after the high-voltage winding has been supplied.

The values of the short-circuit currents at the extreme and nominal taps [1, 3 and 5] corresponding to the minimum, nominal and maximum voltages of the tested transformer are calculated in [1-7].

The tests were carried out on a 2000 kVA, 33/0.4 kV, oil-immersed, hermetically sealed transformer and consisted of applying nine short circuits, three on each of the three taps (minimum, nominal and maximum) with the corresponding peak current value.

The transformer has the following characteristics:
$S_N = 2000$ kVA; $U_N = 33$ kV/0.4 kV;
$U_1 = 28.5$ kV; $u_{k75°} = 5.72\%$;
$U_4 = 33$ kV; $u_{k75°} = 6.1\%$;
$U_6 = 36$ kV; $u_{k75°} = 6.26\%$; $P_{k75°} = 16.361$ kW.

Applying (3) to the extreme and nominal taps, we obtain:

$$Z_1 = \frac{5.72 \times 28.5^2}{100 \times 2} = 23.23 \ (\Omega/\text{phase}) \quad (8)$$

$$Z_4 = \frac{6.1 \times 33^2}{100 \times 2} = 33.21 \ (\Omega/\text{phase}) \quad (9)$$

$$Z_6 = \frac{6.26 \times 36^2}{100 \times 2} = 40.56 \ (\Omega/\text{phase}) \quad (10)$$

$$Z_r = \frac{u^2}{s} = \frac{6.26 \times 36^2}{100 \times 2} = 1.29 \ (\Omega/\text{phase}) \quad (11)$$

The peak factor is chosen according to [3] and the expression: $$k \times \sqrt{2} = (1 + (e^{-\left(\theta + \frac{\pi}{2}\right)\frac{R}{X}} \sin\theta) \times \sqrt{2} \quad (12)$$

where e is the base of the common logarithm and θ is the phase angle, which is equal to arctan X/R in radians.

X is the sum of the reactances of the transformer and the system (X_t+X_s), in ohms and R is the sum of resistances of the transformer and the system (R_t+R_s), in ohms, were R_t is at reference temperature.

The result is: $k \times \sqrt{2} = 2.3$- tap 1; $k \times \sqrt{2} = 2.35$-tap 4;
$k \times \sqrt{2} = 2.37$ - tap 6.

Next, the currents are calculated and the peak current for each tap is determined:

$$I_1 = U_1 / \sqrt{3}Z = 0.6709kA; \ I_{peak1} = 1543 \ A_{max} \quad (13)$$

$$I_4 = U_4 / \sqrt{3}Z = 0.5736kA; \ I_{peak4} = 1348 \ A_{max} \quad (14)$$

$$I_6 = U_6 / \sqrt{3}Z = 0.51238kA; \ I_{peak6} = 1214 \ A_{max} \quad (15)$$

where: $Z=(Z_t+Z_r)$.

In order to assess the condition of the transformer after the short-circuit, in addition to the repetition of individual tests, the short-circuit inductance shall be measured with precision measuring equipment with an accuracy of at least 0.2 % and the permissible variation of the reactance after each short-circuit may be 2 %, 3 %, 4 % or 7.5 %, depending on the power of the transformer and the type of construction.

The nine short-circuits of 0.5 s duration were applied to the transformer in question, the oscillogram of the short-circuit currents and voltages was recorded, and the current variation during the short-circuit was followed.

The oscillograms shown in Fig. 6, Fig. 7 and Fig. 8 were obtained, and after each test, the short-circuit reactance was measured and compared to that measured before the tests.

After removing the tank and inspecting the active part, the faulty behavior of the transformer is confirmed. The following was observed: displacement of the high voltage coils, deformation of the low voltage terminal, confirmed by the displacement of the wedges on the front side of the windings [15].

Values obtained in the first experimental test on tap 6 and shown in Fig. 6. with terminals u2v2w2 short-circuited: voltage U_{U1V1}=32,8 kV; U_{V1W1}=33,3 kV; U_{W1U1}=33,2 kV; peak current I_{U1}=1238 A; equivalent effective current I_{U1}=478 A; I_{V1}=479 A; I_{W1}= 472 A; duration of the test t= 500 ms.

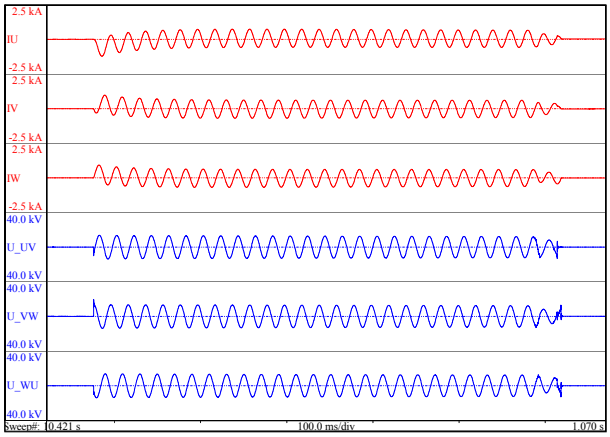

Fig. 6. Oscillogram recorded from the first experiment on tap 6 with short circuit terminals u2v2w2.

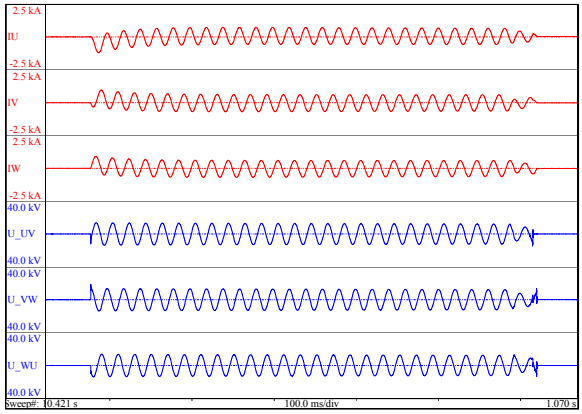

Fig. 7. Oscillogram recorded from the second experiment on tap 6 with short circuit terminals u2v2w2.

Values obtained in the second experimental test on tap 6 and shown in Fig. 7. with terminals u2v2w2 short-circuited: voltage U_{U1V1}=32.9 kV; U_{V1W1}=33.3 kV; U_{W1U1}=33.2 kV; peak current I_{U1}=1223 A; equivalent effective current I_{U1}=474 A; I_{V1}=474 A; I_{W1}= 471 A; duration of the test t= 500 ms.

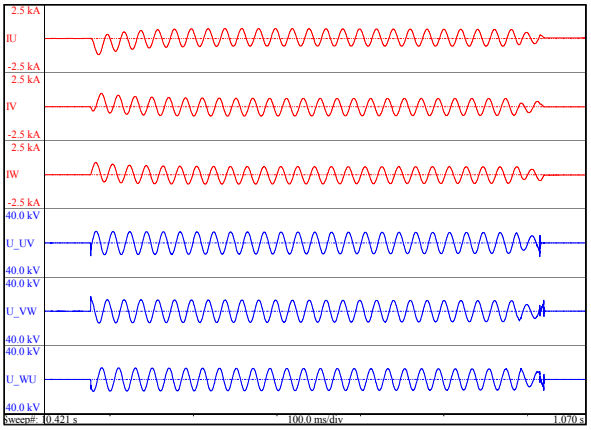

Fig. 8. Oscillogram recorded from the third experiment on tap 6 with short circuit terminals u2v2w2 .

Values obtained in the third experimental test on tap 6 and shown in Fig. 8. with terminals u2v2w2 short-circuited: voltage U_{U1V1}=32.9 kV; U_{V1W1}=33.3 kV; U_{W1U1}=33.2 kV; peak current I_{U1}=1213 A; equivalent effective current I_{U1}=472 A; I_{V1}=476 A; I_{W1}= 476 A; duration of the test t= 500 ms.

V. Verification Methods Using Frequency Response Analysis

Transformer behavior is also confirmed by Frequency Response Analysis (FRA), a recommended method for detecting internal transformer faults.

One of the most common fault modes in the power system is the short-circuit mode, in which power transformers (along with other equipment) are subjected to short-circuit currents and the mechanical stresses generated by these overcurrents during the fault.

Transformers can be damaged by mechanical stress caused by a short circuit. Problems are more common with high power transformers because their short circuit performance is rarely proven by experimental testing.

Frequency Response Analysis (FRA) is a method that provides information about various types of faults occurring in the transformer, such as winding insulation faults, tap changer faults, or winding displacement faults. However, this method does not provide quantitative data to assess the severity of defects.

Therefore, this method is recommended, but not required, to evaluate the condition of the transformer after a short circuit.

In this experiment, a low voltage signal was applied between one terminal of the test object and the tank.

The amplitude of the frequency response is the scalar ratio between the response signal (Vout) and the reference voltage (Vin) and is shown in Fig. 9 - Fig. 17 in dB as a function of frequency [14].

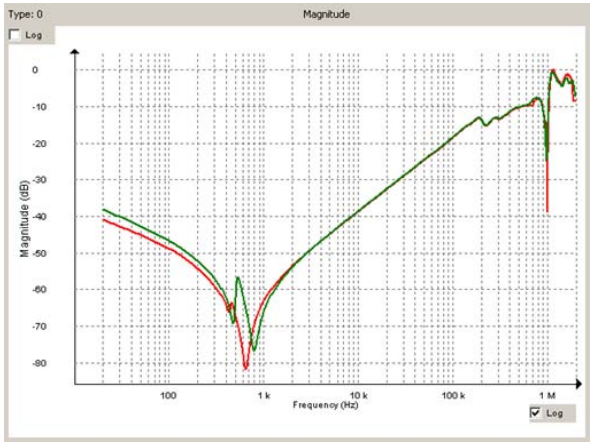

Fig. 9. FRA before and after short circuit on windings 1u-1v.

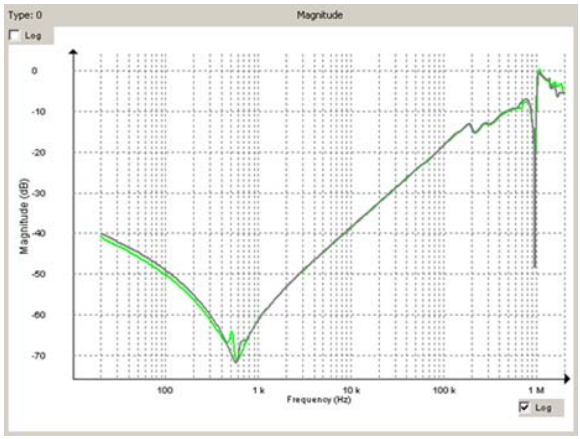

Fig. 10. FRA before and after short circuit on windings 1v-1w.

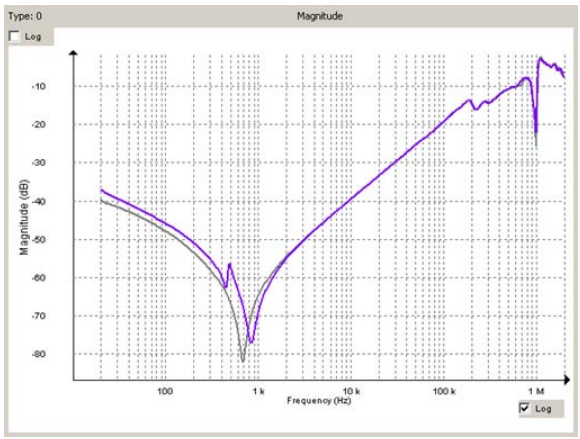

Fig. 11. FRA before and after short circuit on windings 1w-1u.

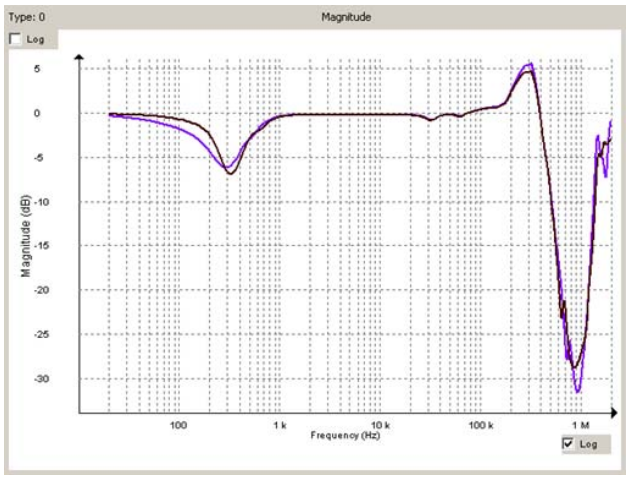

Fig. 12. FRA before and after short circuit on windings 2u-2w.

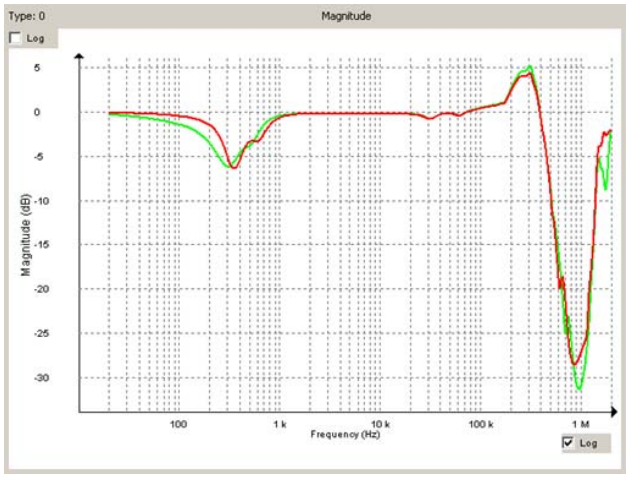

Fig. 13. FRA before and after short circuit on windings 2v-2w.

The phase of the frequency response is the phase difference between the input voltage (Vin) and the output voltage (Vout), expressed in degrees.

The 1 kHz to 1 MHz portion of the frequencies, corresponding to the windings, shows an identical variation before and after the test, indicating that no winding change occurred on the UVW phases, either high or low voltage. This is also confirmed by the variation of the short-circuit reactance.

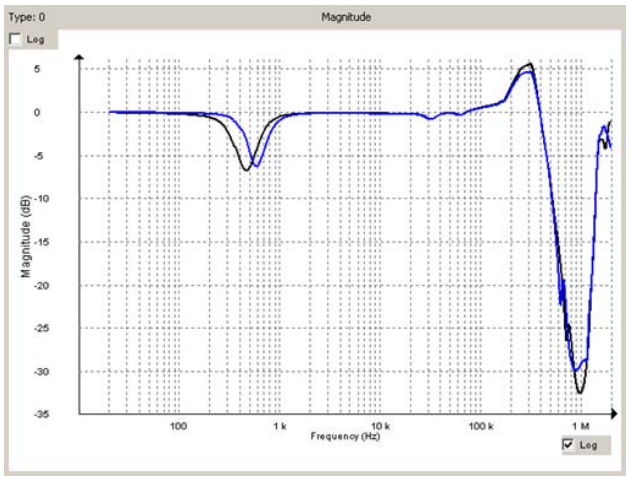

Fig. 14. FRA before and after short circuit on windings 2w–2u.

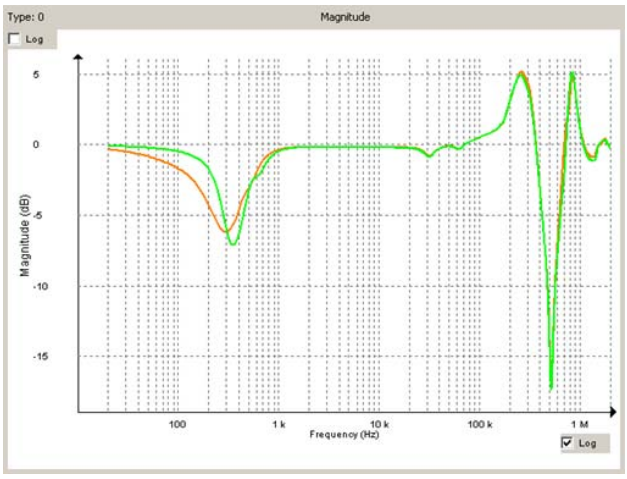

Fig. 15. FRA before and after short circuit on windings 3u-3v.

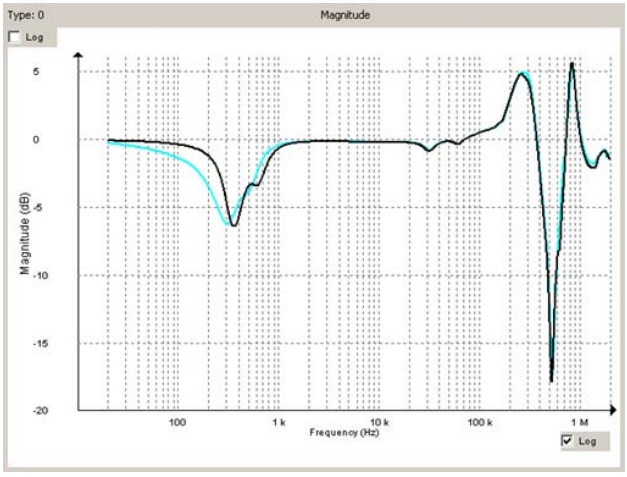

Fig. 16. FRA before and after short circuit on windings 3v-3w.

Since the frequency response of the transformer is closely related to the structure of the core and windings, various frequency response characteristics have been obtained. In Fig. 5 - Fig. 14, the frequency response can be divided into three regions: the low-frequency region, which is determined by the core; the medium-frequency region, which is determined by the interaction between the windings; and the high-frequency region, which is determined by the individual winding structure and internal connections [15].

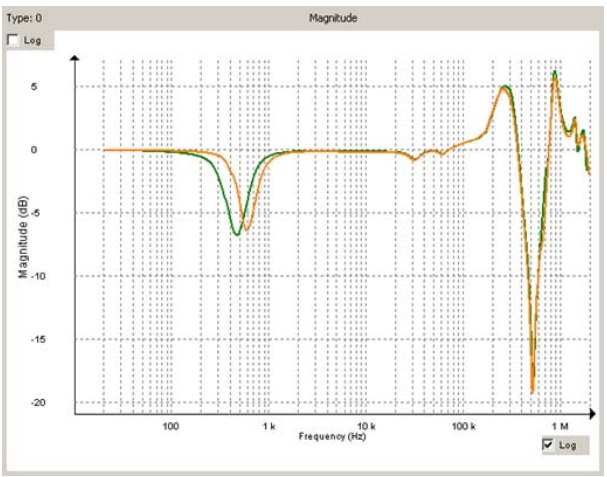

Fig. 17. FRA before and after short circuit on windings 3w-3u.

The frequency response was measured at 50 ohms impedance. Any coaxial cable connected between the terminal and the instrument had the appropriate impedance. The voltage measured at this input terminal was used as the reference signal, and the second voltage signal (the response signal) was measured at the second terminal to the tank.

VI. Results And Conclusions

The experiments were carried out on a 2000 kVA, 33/0.4 kV two-winding transformer as shown in Fig. 18.

In order to assess the condition of the transformer after the short-circuit, in addition to the repetition of individual tests, the short-circuit inductance shall be measured with precision measuring equipment with an accuracy of at least 0.2 % and the permissible variation of the reactance after each short-circuit may be 2 %, 3 %, 4 % or 7.5 %, depending on the power of the transformer and the type of construction.

If this variation exceeds the permissible limits, it is a sign that the windings have shifted during the short-circuit tests, and it is decided whether the transformer behaves correctly or not, according to [3], on the basis of the individual tests and the removal of the tank and inspection of the active part [15].

Fig. 18. Photo of the transformer used for experiments with short-circuited terminals.

The nine short-circuits of 0.5 s duration were applied to the transformer in question, the oscillations of the short-circuit currents and voltages were recorded, and the current variation during the short-circuit was monitored. The oscillograms shown in Fig. 6. – Fig. 8. were obtained and after each test the short-circuit reactance was measured and compared with that measured before the tests.

When measuring the reactance values after each of the 9 tests, a constant increase of the values up to max. 4.4%, slightly above the 4% limit was observed.

The transformer has circular concentric windings, the low voltage winding is made of aluminium foil, so the allowable reactance deviation is 4%. After removing the tank and inspecting the active part, the faulty behavior of the transformer is confirmed. The following was observed: displacement of the high voltage winding coils, deformation of the low voltage terminal, confirmed by displacement of the blades at the front of the winding as shown in Fig. 19, Fig. 20 and Fig. 21.

Tap 1 inductance values before and after experiments: UV: 141.97 and 147.81 mH with a variation of 4.11% VW: 137.83 and 143.97 mH with a variation of 4.45% and WU: 141.24 and 147.69 % with a variation of 4.56%.

Tap 4 inductance values before and after experiments: UV: 206,05 and 213,98 mH with a variation of 3.84% VW: 200.63 and 209.22 mH with a variation of 4.28% and WU: 204.9 and 213.65 % with a variation of 4.27%.

Tap 6 inductance values before and after experiments: UV: 254.72 and 264.02 mH with a variation of 3.65% VW: 248.06 and 258,01 mH with a variation of 4.01% and WU: 252.83 and 263.19 % with a variation of 4.09%.

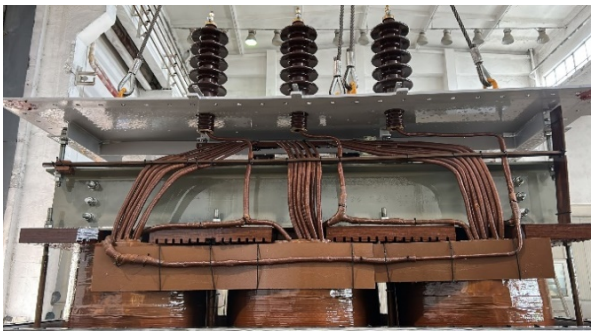

Fig. 19. Photo of the transformer after removal from the tank.

Fig. 20. Photo of the transformer after removal from the tank.

Fig. 21. Photo of the transformer after removal from the tank.

This article introduces the importance of analyzing the short-circuit behavior of power transformers and highlights the irreversible deformations due to axial and radial forces that occur in the windings of the transformer during a short-circuit.

Experiments show the importance of calculating short-circuit currents as a threat to transformer integrity.

In this article is presented experiments using SFRA method, which is an additional method of fault detection, visual inspection. This method makes it possible to detect

the effects of short-circuit currents and thus evaluate the effect of mechanical forces on the transformer windings.

The increase in the percentage value of the impedance will be investigated in future research, as this data is critical not only in short circuit experiments, but also in thermal and dynamic stability experiments. Increasing the impedance value will decrease voltage stability and affect other operating parameters [14].

The main conclusions drawn from the experiments are

• No-load transformer operation requires low iron losses (PFe);

• Unbalanced and unsymmetrical behaviors also require careful design attention;

• Surges during thyristor switching (max 500V/μs) require shielding of LV windings and additional insulation;

• Low-voltage windings with 2, 3 or more identical windings present terminal connection problems;

• Separation of the LV and HV windings by columns is necessary to eliminate the disadvantages caused by unbalanced and unsymmetrical conditions;

• Attempting to demonstrate compliance with international standards is a difficult challenge [13].

Future work will focus on analyzing the thermal design and load curve of this type of transformer in relation to specific environmental conditions at the installation site. Particular attention will be given to the increased loads when operating with an auxiliary power supply.

ACKNOWLEDGMENT

This research was funded by the Ministry of Research, Innovation and Digitization of Romania as part of the NUCLEU Program: PN 23 33 02 01.

Contribution of authors:
First author – 20%
First coauthor – 20%
Second coauthor – 20%
Third coauthor – 10%
Fourth coauthor – 10%
Fifth coauthor – 10%
Sixth coauthor – 10%.

Received on September 17, 2024
Editorial Approval on November 27, 2024

REFERENCES

[1] K. Marton, J. Kurimský, J. Balogh, "Partial discharges at transformer diagnostics," In: *Monitoring and diagnostic systems of transformers*, Teplicka nad Vahom, 2007.

[2] M. Gutten, R. Janura and M. Brandt, "Analysis of short-circuit effects on transformer state by frequency method," *2016 Conference on Diagnostics in Electrical Engineering (Diagnostika)*, Pilsen, Czech Republic, 2016, pp. 1-4.

[3] IEC 60076-5:2006 *Power Transformers - Part 5: Ability to Withstand Short Circuit.*

[4] L. Li, X. Liu, G. Zhu, H. Chen and S. Gao, "Research of short-circuit performance of a split-winding transformer with stabilizing windings", in *IEEE Transactions on Applied Superconductivity*, vol. 29, no. 2, pp. 1-6, March 2019.

[5] B. Zhang and Y. Li, "Research on radial stability of large transformers windings under multiple short-circuit conditions," *IEEE Trans. Appl. Supercond.*, vol. 26, no. 7, Oct. 2016.

[6] A. Bakshi and S. V. Kulkarni, "Analysis of buckling strength of inner windings in transformers under radial short-circuit forces," *IEEE Trans. Power Del.*, vol. 29, no. 1, pp. 241–245, Feb. 2014.

[7] S. H. Wang, H. J. Zhang, S. Wang, H. L. Li, and D. S. Yuan, "Cumulative deformation analysis for transformer winding under short-circuit fault using magnetic-structural coupling model", *IEEE Trans. Appl. Supercond.*, vol. 26, no. 7, Oct. 2016.

[8] H. J. Zhang et al., "Dynamic deformation analysis of power transformer windings in short-circuit ault by FEM," *IEEE Trans. Appl. Supercond.*, vol. 24, no. 3, Jun. 2014.

[9] J. Yuqi, Y. Yong, S. Xianjun, W. Shaoan, Z. Lin and X. Ning, "On Site Test Research and Application of Flexible Short-circuit Current Suppression Technology Based on 220kV Fast Circuit Breaker," *2021 International Conference on Electrical Materials and Power Equipment (ICEMPE)*, Chongqing, China, pp. 1-4, 2021.

[10] X. Yao et al., "Technology of AC Short-Circuit Current Controlled Fast Vacuum Breaking in a Short Arcing Time", *2020 IEEE International Conference on Applied Superconductivity and Electromagnetic Devices (ASEMD)*, pp. 1-2, 2020.

[11] G. Dimitrov, D. Dobrilov and R. Iliev, "Research of the possibility for limiting the currents of a single-phase short circuit in HV networks", *2020 12th Electrical Engineering Faculty Conference (BulEF)*, pp. 1-4, 2020.

[12] M. Rashevskaya, G. Lipinskiy and S. Tsyruk, "Applicability of Calculation Methods for Single-phase Short Circuit Currents in Grid with Voltage up to 1 kV", *2020 21st International Symposium on Electrical Apparatus & Technologies (SIELA)*, pp. 1-4, 2020.

[13] V. Sreeram, M. Rajkumar, S. S. Reddy, T. Gurudev and Maroti, "Short circuit performance of transformers in solar PV systems", *2021 31st Australasian Universities Power Engineering Conference (AUPEC)*, pp. 1-5, 2021.

[14] C. -E. Sălceanu, C. Dobrea, D. Ocoleanu, M. Nicola, D. Iovan, and M. -C. Nițu, "Experimental study of the dynamic short-circuit withstand capability of an 8400 kVA power transformer specially designed for photovoltaic applications", *Machines* 11, 2023.

[15] C. -E. Sălceanu, D. -C. Ocoleanu, D. Iovan, M. Ionescu, Ş. Şeitan and C. Boltaşu, "Experimental study of the behaviour of distribution transformers under short-circuit conditions", *2024 International Conference on Applied and Theoretical Electricity* (ICATE), Craiova, Romania, pp. 1-6, 2024.

DOI: 10.52846/AUCEE.2024.06

Assessment of Corona with Partial Discharge and Radio Interference Measurement Circuits

Elena-Denisa Burada [*] [†], Mihaela Popescu [*], Tania Nicoară [†], Viorica Voicu [†] and Ionel Dumbravă[†]

[*] University of Craiova, Faculty of Electrical Engineering, Craiova, Romania,
safta.elena.i4n@student.ucv.ro, mpopescu@em.ucv.ro

[†] National Institute for Research Development and Testing in Electrical Engineering, Craiova, Romania,
tnicoara@icmet.ro, cem@icmet.ro, iodum@icmet.ro

Abstract **- The paper presents how the physical phenomenon, corona discharge, can be assessed using circuits for measuring partial discharges (PD) and radio disturbances. In test circuits for PD measurement, corona discharges may also be present as a disturbing element at certain test voltages, even if all measures are taken to avoid them.**

The main features and differences between the PD measurement circuit and radio interference voltage measurement circuit are presented, which include the measurement systems and their calibration methods. So for the PD measurement are presented calibration of the PD circuit with the same impulse charge but using different type of filters at PD instrument (wideband and narrowband). For the radio interference voltage measurement is presented calibration of the test circuit with the same voltage but with using different frequencies at the electromagnetic interference receiver.

In a test circuit simulating the occurrence of corona discharges, corona discharges were evaluated at different test voltages using the same measurement frequencies for the two systems. Differences were observed between the results obtained with the same measurement frequencies for the two systems, differences that were maintained regardless of the measurement system used.

The UV spectrum and the electric field of these discharges are correlated with the applied voltage. To assess the corona discharges, the electric field generated by these discharges at the highest test voltages was also measured.

Cuvinte cheie: *descărcări corona, perturbații radio, sisteme de măsurare.*

Keywords: *corona discharge, radio disturbances, measurement systems.*

I. INTRODUCTION

Corona performance is one of the more important criterion when it comes to the design and construction of a transmission line. The high voltages at which modem transmission lines operate have increased the corona problem to the point to which they have become a concern to the power industry.

Consequently, these lines are now designed, constructed and maintained so that during dry conditions they will operate below the corona-inception voltage, meaning that the line will generate a minimum of corona-related phenomena. In foul weather conditions, however, water droplets, fog and snow can produce corona discharges [1].

One of the consequences of transmission line corona discharges is radio interference. Radio interference is a rather general term, which, by definition, refers to any unwanted disturbance within the radio frequency band, such as undesired electric waves in any transmission channel or device. This is also known as radio noise. Pulses of current and voltage are produced on transmission line conductors by corona discharges, which are pulsating in nature.

These pulses are characterized by rise and decay-time constants, in the order of a few nanoseconds to tens or hundreds of nanoseconds, and by repetition rates, which may be in the MHz range.

As a result of this, the frequency **s**pectrum of these pulses can cover a considerable portion of the radio frequency band.

The electromagnetic fields resulting from the corona discharges may, therefore, create unwanted disturbances in the operation of a transmission channel or device over a wide range of frequencies [2].

While the radio disturbance (radio noise) from a high voltage overhead power lines may be established only by site measurement, for the line equipment and other high voltage equipments, laboratory measurements of the radio interference voltage are foreseen.

Now, the evaluation of radio disturbances including corona discharges can be done by two methods corresponding to the IEC 60270 standard dedicated to partial discharge (PD) measurements [3] and CISPR TR 18-2 dedicated to methods for measuring radio disturbances [4].

From this perspective, the common element of the standards can be considered as quasi-peak (QP) detector used, however, in measuring systems with different characteristics. Even if the IEC 60270 standard has been significantly improved (ed.3.1 of 2015) it has kept the use of radio interference meters of quasi-peak (QP) type for the measurement of partial discharges, although this meter can have different readings for the impulses with the same charge but different pulse repetition rate.

The CISPR TR 18-2 and QP detector has become part of electromagnetic compatibility (EMC) tests for radio interference voltage (RIV) test on high voltage equipment.

Below, circuits and measuring systems specific to the measurement of partial discharges (including corona discharges characteristic of the external insulation of high voltage equipment) according to IEC 60270 and CISPR TR 18-2 standards will be presented.

II. MEASUREMENT OF PARTIAL DISCHARGES

Partial discharge measurement carried out in accordance with IEC 60270 has become an essential tool for quality assurance of high voltage equipment. The main objective of IEC 60270 is to standardize and unify the measurement of partial discharges in order to obtain comparable results for tests performed in different locations, with different equipment and by different operators.

To achieve this objective, IEC 60270 has defined a set of key processes and parameters that must be carefully followed [3].

The corona discharges being a particular case of partial discharges, which occur in gaseous media around conductors. The occurrence of PD generates small amplitude impulse current with very small rise and fall times (usually in the ns-µs range, depending on the insulating medium).

The frequency range of such a pulse basically contains the high frequency HF (up to 10 MHz), very high frequency VHF (up to 200 MHz) and ultra-high frequency UHF (above 200 MHz) range [5].

Principle parameter for PD evaluation is the apparent charge q, whose amplitude (pC) is obtained by integrating the detected current pulses.

It is achieved using the PD measurement system with its input impedance Z_{mi} [3]: coupling device (CD), transmission system (connecting cable CC) and measuring instrument (MI) by means of a coupling capacitor C_k connected in parallel with the tested object with C_a capacitance (Fig. 1).

An extra component of the circuit presented in figure 1 is the filter characterized by a high impedance (Z) at the measuring frequency to attenuate the radiofrequency currents in both direction, from the power supply used for generate the test voltage (U) to the test circuit and from the test circuit to the power supply.

Through the coupling device the input currents are converted into output voltage signals which are transmitted to the measuring instrument via the connecting cable.

The MI that processes the PD signals captured at the terminals of the tested object are either analogue, equipped with an electronic integrator, or digital with direct A/D conversion of the input PD pulses and then their digital integration or A/D conversion after the integration of the input PD pulses has been performed through a band-pass filter.

According to the standard IEC 60270, the PD measurement instrument uses two types of pass filters: wideband (bandwidth 100 kHz – 900 kHz, upper frequency max. 1 MHz) and narrow-band (midband frequency 50 kHz – 1 MHz, bandwidth 9 kHz – 30 kHz) [3].

No matter which measuring instrument you use, it is necessary to calibrate the measuring system in the complete test circuit by injecting from a calibrator connected to the terminals of the test object, current pulses proportional to the value of the injected charge (Fig. 2).

The calibrators consist of a generator that produces step voltage pulses of amplitude U_0 in series with a capacitor C_0, so that the calibration pulses are repetitive charges, each with amplitude $q_0 = U_0 C_0$.

In practice it is not possible to produce ideal step voltage pulses. Although other waveforms with longer rise times t_r (10% to 90% of the peak value) and finite decay times t_d (90% to 10% of the peak value) can inject virtually the same charge value, the response of different measuring systems or test circuits may be different due to the integration error caused by the increased duration of these current pulses.

Therefore the parameters (Fig. 3) which characterize the step voltage used by the calibrator must satisfy the following conditions: rise time ($t_r \leq 60$ ns), time to steady state ($t_s \leq 200$ ns), step voltage duration ($t_d \geq 5$ µs), amplitude deviation of step voltage U_0 between t_s and t_d ($\Delta U \leq 0{,}03\ U_0$).

The time parameters are measured from the origin t_0 of the step voltage, which refers to the point in time when the voltage value is equal to 10% of U_0.

Time to steady state t_s is the shortest time during which the deviation ΔU from the voltage U_0 remains first time less than 3%.

Step voltage duration t_d is the time after t_s at which the step voltage amplitude drops below 97% of U_0. After t_d, the voltage must fall continuously below 10% U_0 within a time interval greater than 500 µs (Fig. 3).

Figure 2 shows the calibration in a PD measuring circuit with PD measuring system in series with Ck: U is the high voltage from the power supply, G is the step voltage gen-erator of the calibrator, Co is the capacitor of the calibra-tor with his stray capacitance Cs , Zmi is the input imped-ance of the PD measuring system, CC is the cable, Ca is the object under test, Ck is the coupling capacitor and CD is the coupling device.

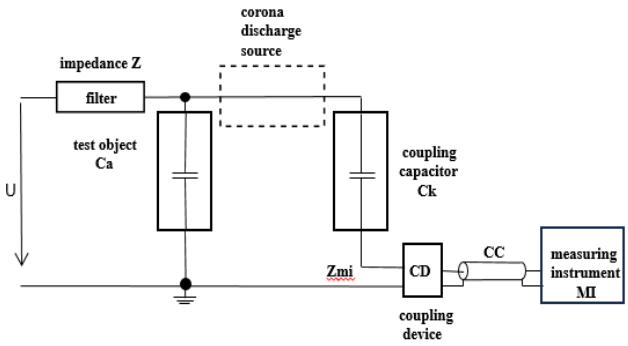

Fig. 1. PD measuring circuit.

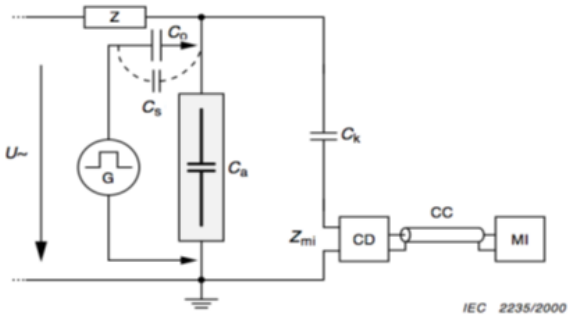

Fig. 2. Calibration in a PD measuring circuit with PD measuring system in series with Ck.

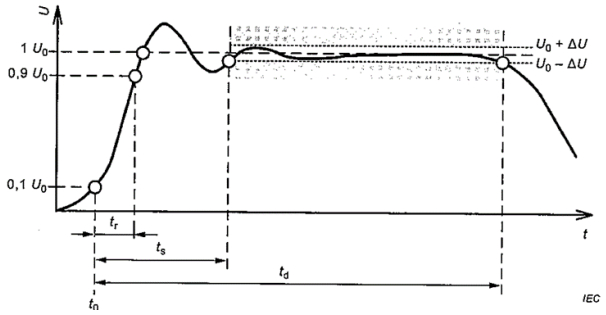

Fig. 3. The step voltage parameters of a calibrator.

The circuit presented in figure 1 was calibrated with 5 pC using a PD calibrator [9], which respects the parameters presented above.

The calibrator injects into the circuit (Fig.2) charge pulses of 5 pC with a pulse repetition frequency of 50 Hz. Different filters of the PD measuring system were used to acquire the charge pulses, wide-band filter (bandwidth 100 kHz – 900 kHz) and narrow-band filters (midband frequency 500 kHz and 1000 kHz with 9 kHz bandwidth). Figures 4 and figure 5 show the 5 pC pulse acquired by the PD measuring system with a wide-band filter (bandwidth 100 kHz – 900 kHz). At the top of each figure, the 5 pC pulse is presented on 20 ms (2 ms/div.) to visualize the partial discharges over a period of the power voltage applied in the circuit. This is useful for phase-resolved PD patterns obtained during any PD measurement (Fig. 4).The shape of this pulse is presented in figure 4 in the time domain, 500 µs/div. and in figure 5 is presented the frequency spectrum of this charge pulse used for calibration of the PD test circuit highlighting the bandwidth of the filter (Fig. 5).

In the same conditions, narrow-band filters of the PD measuring system were used, 500 kHz ± 4.5 kHz and 1000 kHz ± 4.5 kHz. Thus, figures 6 and figure 7 show the same 5 pC pulse acquired with a 500 kHz ± 4.5 kHz filter at PD measuring system (Fig. 6, Fig. 7).

Since it is the same PD pulse from the calibrator with a low pulse repetition frequency, no significant difference of the PD measuring system scale factors was observed for the selected frequency domains.

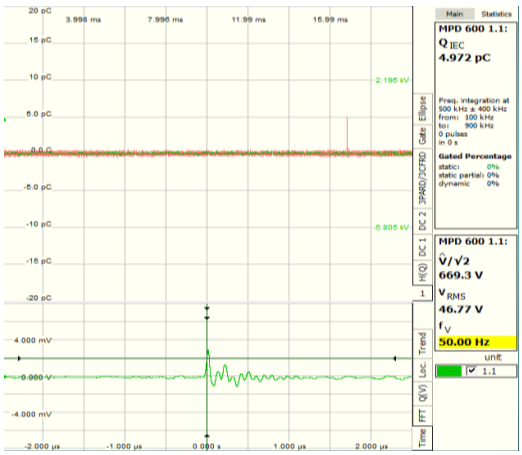

Fig. 4. PD measuring circuit calibration with 5 pC pulse and 500 kHz ± 400 kHz filter at PD measuring system.

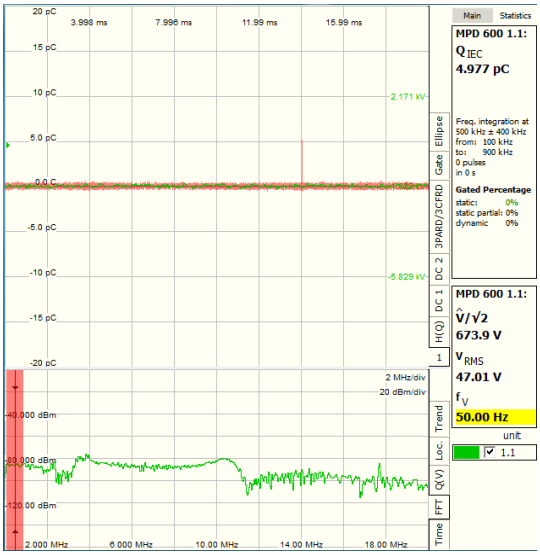

Fig. 5. Frequency spectrum of 5 pC pulse (500 kHz ± 400 kHz filter at PD measuring system).

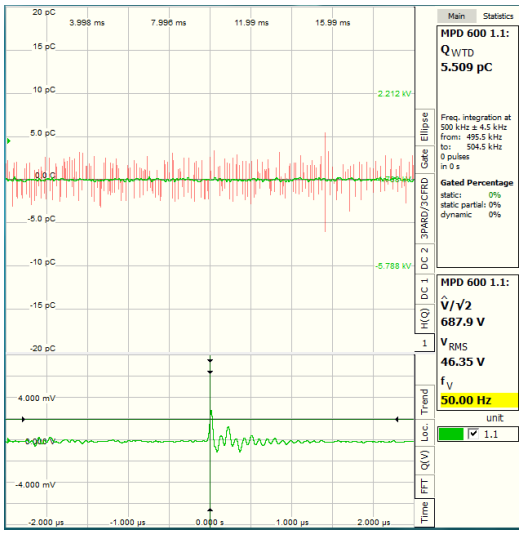

Fig. 6. PD measuring circuit calibration with 5 pC and 500 kHz ± 4.5 kHz filter at PD measuring system.

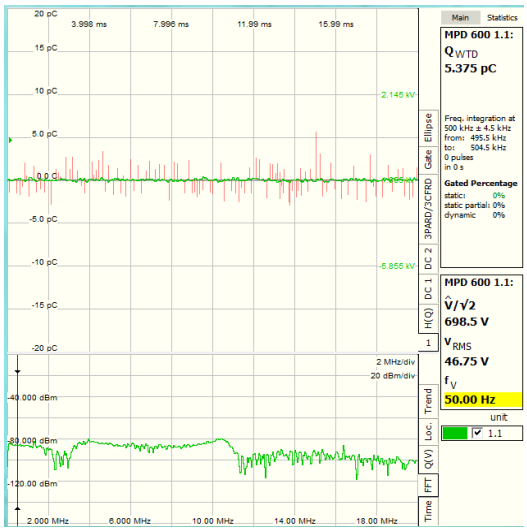

Fig. 7. Frequency spectrum of 5 pC pulse (500 kHz ± 4.5 kHz filter at PD measuring system).

III. Radio Interference Voltage Measurement

The measurement method according to the reference standard TR CISPR 18-2 TR CISPR 18-2 [4] can be used to measure the level of radio interference of high voltage equipment.

The main element of this measuring method is the measuring impedance, (300 ± 40) Ω, formed by the coupling capacitor C_k of 1nF and the resistance R_L (equivalent resistance of R_2 in series with the parallel combination of resistance R_1 and the input resistance R_i of the EMI receiver). To calculate the level of radio interference at different test voltages it is necessary to calibrate this test circuit.

For the calibration, a sine wave generator and a 20 kΩ resistor connected in series with the generator are used in order to inject a current of about 50 µA into the test circuit according to the CISPR standard. Calibration of the radio interference voltage measuring circuit shall be performed to account for the inherent attenuation of such a circuit.

As a consequence the attenuation (A) shall be calculated as the difference between the receiver EMI indications when injecting 1 V_{RMS} from a sine wave generator at a measurement frequency of 1 MHz or 500 kHz between the test object terminal and ground when the test object is disconnected from the test circuit and when it is connected to the test circuit.

Since this value is obtained from the calculation by injecting the same sinusoidal voltage values at the same measurement frequency, this contribution does not affect the measurement uncertainty.

The radio interference voltage level is obtained using the formulas [4]:

$$V = V_m + A + R \quad (\mathrm{dB\mu V}), \tag{1}$$

where:

V_m - value measured during the test (dBµV);

A - test circuit attenuation:

$$A = A_2 - A_1 \ (\mathrm{dB\mu V}) \tag{2}$$

A_1 - EMI receiver reading obtained when calibrating the test object connected in the test circuit;
A_2 - EMI receiver reading obtained when calibrating the test object disconnected from the test circuit;

R - correction factor with measurement resistance value, R_L,

If $R_2 = 275\ \Omega$ and $R_1 = R_i = 50\ \Omega$ (Fig. 8), then $R_L = 300\ \Omega$ and

$$R = 20\,log(300/(50/2)) = 20\,log(600/(50) = 21.6\ dB\mu V \tag{3}$$

The two values A, R are basically constants which are added to the value measured at the EMI receiver during the test at different values of the test voltage.

For the circuit shown in figure 8 the A values obtained at the two measuring frequencies 500 kHz and 1000 kHz are the same, even if the $A1$ and $A2$ values measured at the two measuring frequencies are different. Thus A = 5 $dB\mu V$ can be considered for both measurement frequencies.

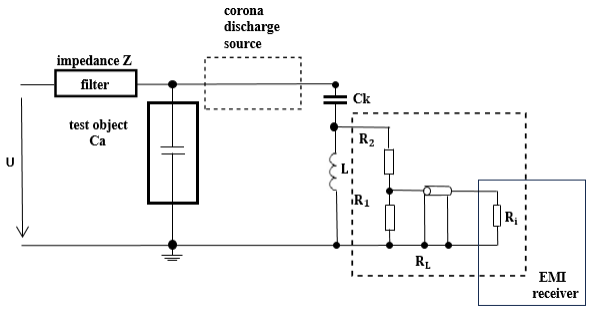

Fig. 8. RIV measuring circuit.

That is because the standards for high-voltage equipment, insulation strings and accessories used in the power transmission system specify permissible levels of radio interference voltage in µV, the value V, obtained in dBµV, is converted to µV.

IV. Practical Measurement and Comparison of PD and RIV Measurement

The corona discharges were simulated using the test circuit shown in figure 9, and a specialized video camera equipped with a visible spectrum channel and a UV channel, with a sensitivity to detect radio interferences of min. 22 dBµV at 1 MHz, was used to highlight the sources of corona discharges (Fig. 10).

Modern UV channel optical properties allow detection of ultraviolet radiation (wavelengths between 200-400 nm) emitted by the corona discharge, even in broad daylight, without being influenced by sunlight.

Corona discharges were assessed using a PD measurement system [6] which has the capability of histogram acquisition, oscilloscope-like visualization of an acquired signal and Fourier transform of this signal.

For the comparison, the narrow-band filters of the PD measuring system were used, 500 kHz ± 4.5 kHz and 1000 kHz ± 4.5 kHz. The results obtained at different test voltages, under the conditions of calibrating the test circuit with 5 pC, are shown in Table I [7].

Fig. 9. Test circuit for corona discharge simulation.

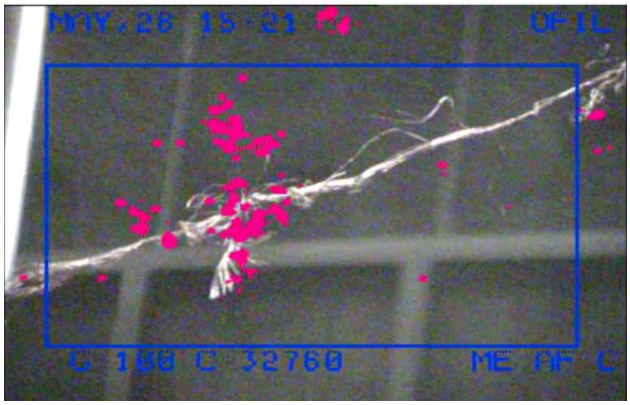

Fig. 10. Sources of corona discharges in the test circuit.

TABLE I.
PD MEASUREMENT AT TWO MEASURING FREQUENCIES

Voltage (kV)	PD level (pC)	
	500 kHz ± 4.5 kHz	1000 kHz ± 4.5 kHz
80	350	460
70	320	450
60	310	330
50	300	250
40	220	210
30	140	150
20	110	110

Where the measurement frequency is used of 500 kHz ± 4.5 kHz, figure 11 shows the entire test sequence with PD patterns at 80 kV test voltage.

PD measurement system use, figure 12 show a corona discharge pulse visualized in the time domain and its frequency spectrum.

If a measurement frequency is used of 1000 kHz ± 4.5 kHz, figure 13 shows the entire test sequence with PD patterns captured at the same test voltage (80 kV).

Figure 14 show a corona discharge pulse visualized in the time domain and its frequency spectrum.

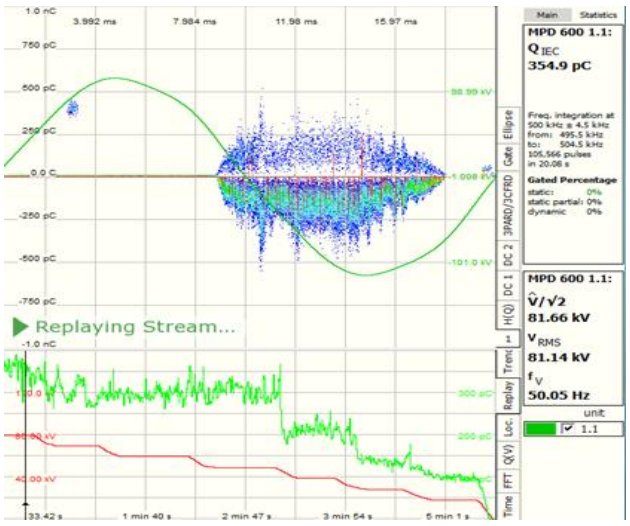

Fig. 11. PD patterns at test voltage 80 kV for the measurement frequency of 500 kHz ± 4.5 kHz.

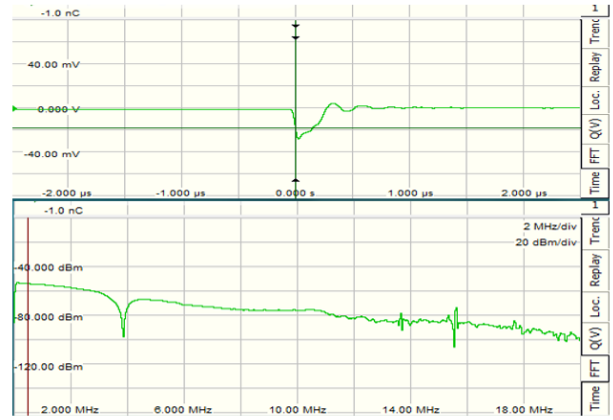

Fig. 12. PD pulse in time domain (up) and his frequency spectrum (down) measured at 80 kV test voltage for the measurement frequency 500 kHz ± 4.5 kHz.

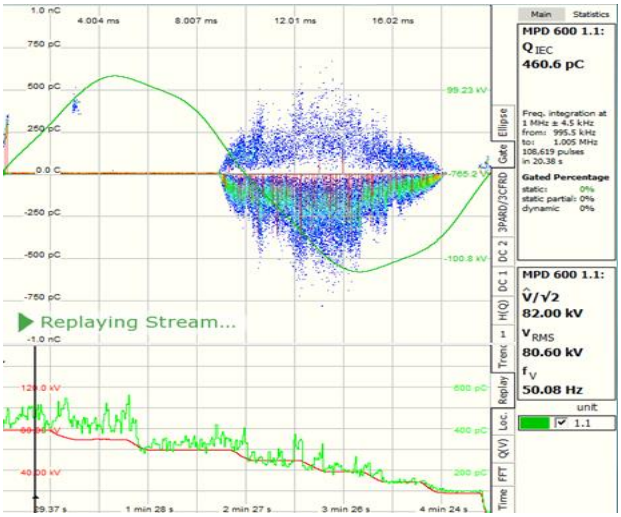

Fig. 13. PD patterns at test voltage 80 kV for the measurement frequency of 1000 kHz ± 4.5 kHz.

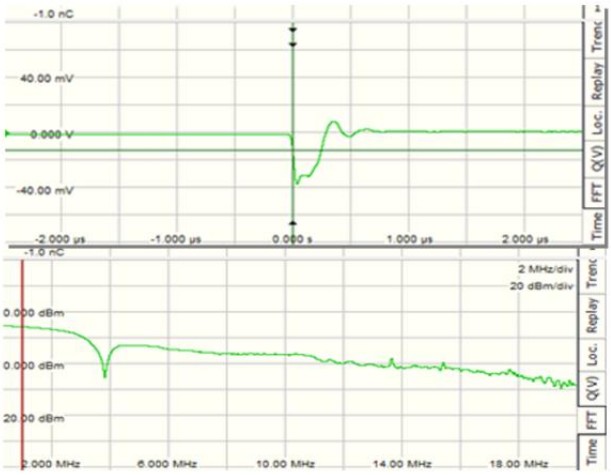

Fig. 14. PD pulse in time domain (up) and his frequency spectrum (down) measured at 80 kV test voltage for the measurement frequency 1000 kHz ± 4.5 kHz.

Therefore when calibrating the test circuit (5 pC) no differences were observed between the scale factor of the measuring system at the two measurement frequencies, the actual measurement showed a higher measured PD level at the measurement frequency of 1000 kHz ± 4.5 kHz for the higher test voltages (Table I, Fig. 11 and Fig. 13).

Experimental results using the RIV measuring system, at the same measurement frequencies, are presented in Table II. Calibration of the test circuit was carried out according to the method presented in Section III and no differences were observed between the circuit attenuation values determined at the two measurement frequencies. Higher RIV levels were also observed at the measurement frequency of 1000 kHz ± 4.5 kHz for higher test voltages.

TABLE II.
RIV MEASUREMENT AT TWO MEASURING FREQUENCIES

Voltage (kV)	RIV level (μV)	
	500 kHz ± 4.5 kHz	1000 kHz ± 4.5 kHz
80	602.55	1071.52
70	537.03	758.57
60	478.63	676.08
50	358.92	638.21
40	269.15	426.57
30	229.08	327.34
20	213.79	213.79

To evaluate the corona discharges, the electric field generated by these discharges at the highest test voltages was also measured, using the EHP-50F field probe mounted at a height of 1m, a distance of 2.6 m from the vertical plane of the discharge source and the NBM-550 analyser (Fig. 15), with the results shown in Table III [10].

Fig. 15. Circuit for electric field assessment.

TABLE III.
ELECTRICAL FIELD MEASUREMENT

Frequency [Hz]	Voltage [kV]	Measured electric field [kV/m]
50	80	5.789
	70	4.988
	50	3.543

The measured electric field was less than 10 kV/m limit (AL action trigger value according to Tab. B1 of Directive 2013/35/EU).

The limit is the AL value – "action levels (AL)" means operational levels set in order to simplify the process of proving compliance with the relevant ELV or, where appropriate, to take the relevant protective or preventive measures specified by Directive 2013/35/EU.

"Exposure limit values (ELVs)" means values established on the basis of biophysical and biological considerations, in particular on the basis of short-term and scientifically proven direct effects, i.e. thermal effects and electrical stimulation of tissues.

"ELV for health effects" means exposure values above which workers could be exposed to adverse health effects such as thermal heating or stimulation of nerve or muscle tissue.

"ELV for sensory effects" means exposure values above which workers could be exposed to temporarily disturbed sensory perceptions and temporary minor changes in brain functions [8].

Taking into account the above, the measured electric field does not have a harmful effect on the workers' health.

V. CONCLUSIONS

This paper presents how to evaluate corona discharges using different methods and measurement systems. Based on a laboratory test circuit simulating the occurrence of corona discharges, differences between the measured values at the standardized measurement frequencies 500 kHz ± 4.5 kHz and 1000 kHz ± 4.5 kHz could be observed for both measurement systems used.

This is because even if the two measurement circuits used have common elements, each of them has particularities that differentiate them, from the impedances of the measurement systems to the calibration methods of the circuits and that are reflected in the way the results are reported.

PD measurement system, which provides more information about the analysed phenomenon, indicated that there is a difference in PD pattern taking into account that the measurements were performed successively and not simultaneously.

The corona discharges were also evaluated from the point of view of the electric field generated which was below the electromagnetic field exposure limit value.

The phenomenon is important to study for configurations close to those used in the design of high voltage equipment and analysis in terms of electric field generated by discharges.

ACKNOWLEDGMENT

This work was developed with funds from the Ministry of Research, Innovation and Digitization of Romania as part of the NUCLEU Program PN 23 33 01 02.

Contribution of authors:

First author – 50%

First coauthor – 20%

Second coauthor – 10%

Third coauthor – 10%

Fourth coauthor – 10%

Received on September 12, 2024
Editorial Approval on December 2, 2024

REFERENCES

[1] Z. Wu, Q. Zhang, Z. Pei and H. Ni, "Correspondence between phase resolved partial discharge patterns and corona discharge modes," in *IEEE Transactions on Dielectrics and Electrical Insulation*, vol. 26, no. 3, pp. 898-903, June 2019.

[2] P. Lukes, M. Clupek and V. Babicky, "Discharge filamentary patterns produced by pulsed corona discharge at the interface between a water surface and air," in *IEEE Transactions on Plasma Science*, vol. 39, no. 11, pp. 2644-2645, Nov. 2011.

[3] IEC 60270:2015, ”High-voltage test techniques - Partial discharge measurements,”, ed.3.1, 2015.

[4] CISPR TR 18-2, ”Radio interference characteristics of overhead power lines and high-voltage equipment”, ed.3.0, 2017.

[5] CIGRE, TF 15.11/33.03.02 ”Knowledge rules for partial discharges diagnosis in service”, April 2003.

[6] Omicron ”MPD 600 partial discharges measurement and analysis system”.

[7] E. -D. Burada, M. Popescu, T. Nicoară, V. Voicu and I. Dumbravă, "Evaluation of corona in partial discharge and radio interference measurement circuits," *2024 International Conference on Applied and Theoretical Electricity (ICATE)*, Craiova, Romania, 2024, pp. 1-5.

[8] Directive 2013/35/EU of the European Parliament and of the Council of 26 June 2013 on the minimum health and safety requirements regarding the exposure of workers to the risks arising from physical agents (electromagnetic fields) (20th individual Directive within the meaning of Article 16(1) of Directive 89/391/EEC) and repealing Directive 2004/40/EC.

[9] ***https://www.megger.com/en-ca/products/cal1-cal2-and-cal3-calibration-impulse-generators

[10] ***https://www.narda-sts.com/en/products/emf-selective-measuring-devices/ehp-50

DOI: 10.52846/AUCEE.2024.07

Polynomial Models used in Optimization by Design of Numerical Experiments

Alin-Iulian Dolan
University of Craiova, Electrical Engineering Faculty, Craiova, Romania, adolan@elth.ucv.ro

***Abstract* - The paper presents two optimization methods based on the concept of design of experiments: the method by zooms and the method by slidings of designs. Two application variants are presented for each of them. One of the variants only requires access to the values of the objective function at different points in the feasible domain, grouped in designs of experiments, arranged successively, towards the most convenient values. The other variant uses the same technique, but the advance of the designs towards the optimal value is based on the information provided by second-order polynomial models that approximate the objective function on each design, which facilitates the convergence speed of the algorithm. The methods under discussion lend themselves very well to numerical simulations using the finite element method that can provide the values of the objective function at any point in the feasible domain that corresponds to a unique configuration of the simulated device. The paper presents a comparative study of the application of these methods in the two variants, on a 2-D numerical model of an electromagnetic device. Both in the case of the method by zooms and in the case of the method by slidings of designs, the results highlight the simplicity of the first application variant but also the high speed of convergence of the second one, especially for the method by zooms.**

Cuvinte cheie: *optimizare, proiectarea experimentelor, metoda elementului finit bidimensională.*

Keywords: *optimization, design of experiments, two-dimensional finite element method.*

I. INTRODUCTION

Optimization methods based on numerical simulations are very effective tools for improving the performance of electromagnetic devices. Therefore, the technique of design of experiments (DOE) [1]-[2] becomes indispensable in solving these problems, only changing the nature of the experiments from "real" to "numerical" The fact that it is still a topical technique is proven by many scientific works [3]-[12]. The DOE technique can be applied both for the screening of devices for optimization and for the actual optimization through different algorithms.

For example, in [3] the aim was to determine the influential parameters in order to optimize a double-cage induction motor, in [4] critical parameters were subjected to a detailed parametric analysis to select some of them for optimization of switched reluctance motor for ceiling fan design and in [5] through Ansys and Noesis Optimus software based on DOE and response surface methodology is investigated the effect of bump structures and loading conditions on the electromigration properties of solder bumps in Wafer-level chip-scale packaging.

Many works deal with actual optimization problems based on DOE such as [6] which presents the optimization of the operation of a boiler, aiming to reduce the gas-steam ratio to increase its efficiency, or [7] where the robust design by using DOE method and driving cycles is proposed to optimize the brushless direct current motors. Genetic algorithms and DOE were employed in [8] to optimize the stator slot V-shaped PM geometry and the dimension of the rotor bar. The response surface technology combined with DOE, FEM and sequential linear programming is applied in [9] to obtain an optimized linear actuator with permanent magnet for driving a needle in a knitting machine.

Other works focus on multi-objective optimization such of [10] in which DOE is used for adjustment of the limits of design variables to facilitate optimization with finite element method (FEM) of a permanent magnet machine. In [11 the DOE and the Kriging model are used to implement the multi-objective optimization design of the geometric parameters of linear switched reluctance motor with segmental mover and in [12] a combination between DOE and FEM was performed in order to minimize the permanent deflection and internal energy, taking into account three influential parameters.

Some works present the results of the application of different variants of optimization methods based on DOE [13]-[17]. In [13] an optimized solution was proposed for the geometric form of the toroidal modular coil of a superconducting magnetic energy storage device using the method by zooms in combination with FEM. Two geometric parameters were chosen to maximize the magnetic energy stored in a minimal volume of superconducting material. A similar solution was obtained in [14] by applying the method by slidings of designs, also based on DOE. The method by zooms was also applied in [15] to maximize the force developed by a direct current electromagnetic device. The optimization problem considered six parameters to synthesize the optimal geometric shape of the device. In search of a global maximum, in [16] an exhaustive method based on DOE was applied.

The work [17] describes in detail the method by zooms in two application variants: a simpler one that only requires access to the objective function values at different points in the feasible domain, grouped in successive experiment designs, oriented towards the most convenient values and a more complex second one, that, additionally, calculates second-order polynomial models that facilitate the increase of the convergence speed of the algorithm.

This paper adds to the study the method by slidings of designs, allowing comparisons between methods in terms of workload and convergence speed.

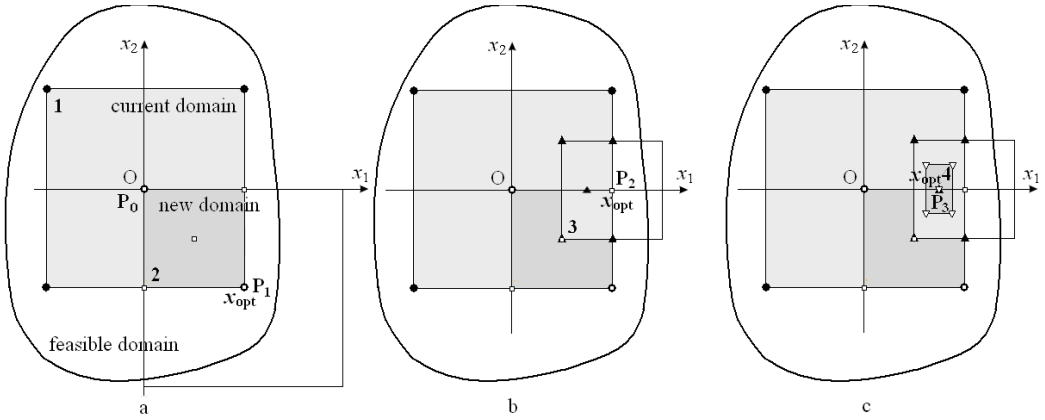

Fig. 1. Graphical illustration of the application of the optimization algorithm by zooms without model calculation [13].

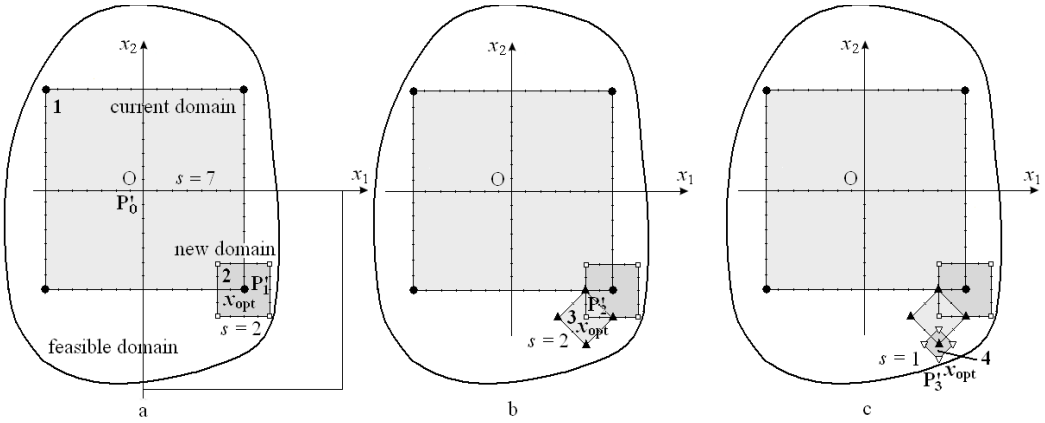

Fig. 2. Graphical illustration of the application of the optimization algorithm by slidings of designs without model calculation [14].

A. *Optimization method by zooms*

a) Variant without calculation of models

It directly uses the objective function values in the experimental points. Experimental designs centered on points determined by the algorithm (origin points) are used, formed by points arranged diagonally, on one side and on the other of the origin point, at equal distance from it, giving to the corresponding domain a hyper-rectangular shape. For k factors there are 2^k diagonal points relative to the origin. It starts with a design that covers most of the feasible domain. The algorithm of the variant without calculation of models is the following:

1) The first experiment is carried out in a point P_0 (Fig. 1) in the feasible domain (initial point) which is considered the first origin point;

2) The points diagonal to the origin point are established;

3) A number of $N = 2^k$ experiments are performed in the diagonal points (full factorial design);

4) If there is a diagonal point where the response is more convenient than the origin point, this point becomes the new origin point of the next iteration and step 2 is resumed (a "zoom" operation of the same size is made around the found diagonal point);

5) Otherwise, the dimensions of the initial design are reduced with the rates $\tau_k \geq 1$ and step 2 is resumed (usually $\tau_k = 2$, or 2^2, or 2^3 etc.).

The constraints on position can be taken into account when establishing diagonal points. If they are violated by one of the diagonal points, the dimensions of the design are reduced with rates $\tau_k > 1$ and the algorithm is restarted.

During the running of the algorithm it is possible that some points subject to analysis have already been analyzed in previous iterations (recovered points). Their number (N_{rec}) contributes to reducing the required number of experiments (N_{tot}).

b) Variant with calculation of second-order polynomial models

At each iteration, a second-order polynomial model F_{mod} for objective function F is calculated that allows determining the direction of the best values, the position and dimensions of the next design. The matrix equation of a second order model is written [2]:

$$F_{\text{mod}}(\boldsymbol{X}) = b_0 + \boldsymbol{X}^{\mathrm{T}} \cdot \boldsymbol{b} + \boldsymbol{X}^{\mathrm{T}} \cdot \boldsymbol{B} \cdot \boldsymbol{X} \tag{1}$$

$$\boldsymbol{X} = \begin{pmatrix} x_1 \\ \vdots \\ x_k \end{pmatrix}, \boldsymbol{b} = \begin{pmatrix} b_1 \\ \vdots \\ b_k \end{pmatrix}, \boldsymbol{B} = \begin{pmatrix} b_{11} & b_{12}/2 & \cdots & b_{1k}/2 \\ b_{12}/2 & b_{22} & \cdots & b_{2k}/2 \\ \vdots & \vdots & \ddots & \vdots \\ b_{1k}/2 & b_{2k}/2 & \cdots & b_{kk} \end{pmatrix} \tag{2}$$

An important simplification of the equation can be obtained if the model is viewed from a particular coordinate system ($S,x_1',x_2',\ldots,x_k'$), rotated and translated relative to the original system ($O,x_1,x_2,\ldots,x_k$) (Fig. 3a), so that only the terms containing x_j^2 , $j = 1, \ldots, k$ are kept.

Thus, the canonical analysis is used, which allows the determination of the origin and axes of the new system, as

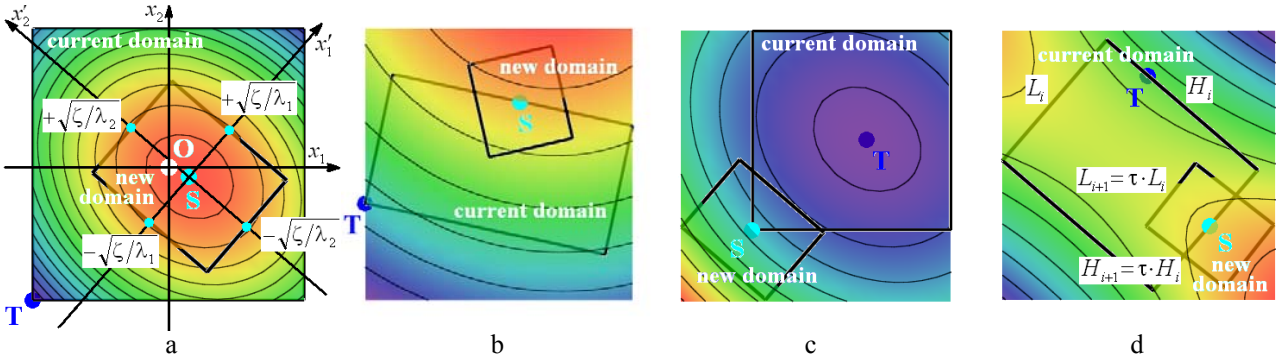

a b c d

Fig. 3. Graphical illustration of the application of the optimization algorithm by zooms with calculation of second order polynomial model in case the optimum sought is a maximum [17].

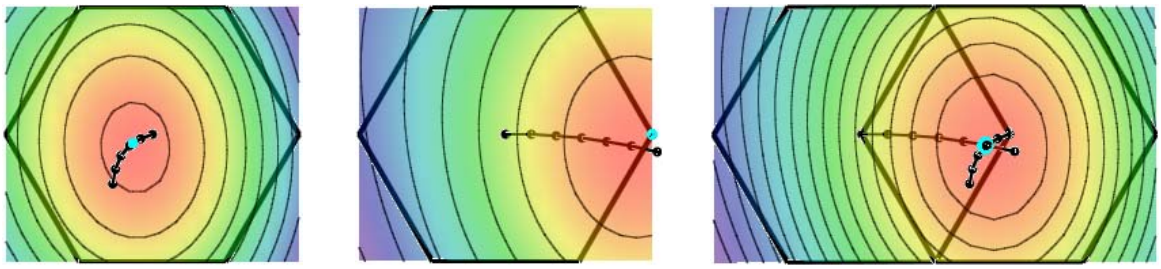

a b c

Fig. 4. The optimal paths and the optimal point.

well as the new form of the model, using the diagonal matrix $\boldsymbol{\Lambda}$ of the eigenvalues of $\boldsymbol{B}$ [2]:

$$\boldsymbol{B}\cdot\boldsymbol{M}=\boldsymbol{M}\cdot\boldsymbol{\Lambda} \tag{3}$$

where $\boldsymbol{M}$ = matrix of eigenvectors of $\boldsymbol{B}$.

The origin S(x_{1S}, …, x_{kS}) of the new system represents the optimal point (minimum or maximum) of the second order model restricted by the dimensions of the current domain.

This point can be found inside the current domain or on its border. Fig. 3 illustrates four possible cases for a two-dimensional domain in which the sought optimum is a maximum:

a) the model function has the same curvature as the objective function and the maximum of the model function is located inside the current domain (Fig. 3a).

b) the model function has the same curvature as the objective function but the maximum of the model function is located outside the current domain (Fig. 3b);

c) the model function has the opposite curvature of the objective function, admitting a minimum inside the current domain (Fig. 3c);

d) the model function has inflection point inside the current domain (Fig. 3d).

In case *a*, point S is identified with the maximum of the model function, being located inside the current domain. In cases *b*, *c*, *d*, point S coincides with the maximum of the model function restricted by its border, being located either on one of the sides (*b*, *d*) or in a corner of the current domain (c).

The axes of the new system are expressed as:

$$\boldsymbol{X}'=\boldsymbol{M}^{\mathrm{T}}\cdot\left(\boldsymbol{X}-\boldsymbol{X}_{\mathrm{S}}\right) \tag{4}$$

The equation of the model in the new system becomes:

$$F'_{\mathrm{mod}}(\boldsymbol{X}')=F_{\mathrm{mod}}(\mathrm{S})+\boldsymbol{X}'^{\mathrm{T}}\cdot\boldsymbol{\Lambda}\cdot\boldsymbol{X}' \tag{5}$$

$$\boldsymbol{X}'=\begin{pmatrix}x'_1\\ \vdots\\ x'_k\end{pmatrix},\quad \boldsymbol{\Lambda}=\begin{pmatrix}\lambda_1 & \cdots & 0\\ \vdots & \ddots & \vdots\\ 0 & \cdots & \lambda_k\end{pmatrix} \tag{6}$$

The next iteration of the algorithm will use a design of experiments with the sides oriented according to the axes of the new system.

The zoom effect is obtained by successively reducing the dimensions of the domains from one iteration to another with different percentages, depending on the signs of the eigenvalues λ_j. The reduction rate depends on the topology and on the variations of the objective function. Hyper-rectangular designs with three levels per factor ($p = 3^k$) are usually used.

It is denoted by T(x_T,y_T) = the minimum point of the model, S(x_S,y_S) = the optimal point of the model, pr = the percentage reduction of the surface of the current domain to obtain the new domain ($pr < 1$), τ = the reduction rate of each dimension of the current domain, ζ = the reduction percentage of the difference between the maximum and the minimum of the model and ρ = the coefficient of reduction of the difference between the maximum and the minimum of the model.

For the two-dimensional case, if all the eigenvalues λ_j have the same sign (Fig. 3a,b,c), starting from iteration i, the percentage pr is calculated first, then ζ, then the dimensions of the domain at iteration i+1, denoted by L_{i+1}, H_{i+1}. Only in the first iteration, a value $pr < 1$ is first chosen and then the coefficients ρ and ζ are calculated:

$$pr=\frac{\rho\cdot 4\cdot\left|F_{\mathrm{mod}}(x_{\mathrm{T}},y_{\mathrm{T}})-F_{\mathrm{mod}}(x_{\mathrm{S}},y_{\mathrm{S}})\right|}{\sqrt{\lambda_1\cdot\lambda_2}\cdot L_i\cdot H_i} \tag{7}$$

$$\rho = \frac{\sqrt{\lambda_1 \cdot \lambda_2} \cdot pr \cdot L_i \cdot H_i}{4 \cdot \left| F_{\text{mod}}(x_T, y_T) - F_{\text{mod}}(x_S, y_S) \right|} \quad (8)$$

$$\zeta = \rho \cdot \left(F_{\text{mod}}(x_T, y_T) - F_{\text{mod}}(x_S, y_S) \right) \quad (9)$$

$$L_{i+1} = 2 \cdot \sqrt{\frac{\zeta}{\lambda_1}}, \quad H_{i+1} = 2 \cdot \sqrt{\frac{\zeta}{\lambda_2}} \quad (10)$$

Thus, the new domain will be a hyper-rectangle that will circumscribe an ellipsoid with k axes and dimensions $\sqrt{\zeta/\lambda_j}$, $j = 1, \ldots, k$ and which will have $2 \cdot k$ vertices with coordinates $\left[\pm\sqrt{\zeta/\lambda_1}, \pm\sqrt{\zeta/\lambda_2}, \ldots, \pm\sqrt{\zeta/\lambda_k}\right]$.

These coordinates are valid in the system formed by the main axes Sx_1', Sx_2', …, Sx_k' associated with the second order model. They can be expressed in the original axis system $(O,x_1,x_2,\ldots,x_k)$ using the matrix relation:

$$\boldsymbol{X} = \boldsymbol{X}_S + \boldsymbol{M} \cdot \boldsymbol{X}' \quad (11)$$

If the eigenvalues λ_j have different signs, the coefficient τ will be calculated first using the percentage pr from the previous iteration, then L_{i+1}, H_{i+1}:

$$\tau = \sqrt{pr} \quad (12)$$

$$L_{i+1} = \tau \cdot L_i, \quad H_{i+1} = \tau \cdot H_i, \quad L_{i+1} \cdot H_{i+1} = pr \cdot L_i \cdot H_i \quad (13)$$

The algorithm of the variant with calculation of second order polynomial model is the following:

1) An origin point $P_0 = (x_1, \ldots, x_k)^T$ is defined in the feasible domain;

2) A design of N experiments centered in P_0 is made, with $N > p$ = the number of coefficients of the second-order polynomial (in 2-D it is rectangular domain, $N = 4^2 > p = 6$);

3) The associated second-order polynomial model is calculated;

4) Determine the optimal point S of the model on the current domain (the center of the new coordinate system);

5) Determine the opposite of the optimal point T of the model on the current domain (the minimum point, if the optimum is a maximum or the maximum point, if the optimum is a minimum);

6) The eigenvalues λ_j of matrix $\boldsymbol{B}$ and the axes of the new system are determined;

7) If all the eigenvalues λ_j have the same sign, first calculate the percentage pr, then calculate ζ (in the first iteration a value $pr < 1$ is chosen, then ρ and ζ are calculated). Otherwise, the coefficient τ is first calculated using the percentage pr from the previous iteration;

8) Calculate L_{i+1}, H_{i+1};

9) The coordinates of the vertices of the new domain are determined;

10) A design of N experiments centered in S and limited by the vertices calculated in step 9 is made, with $N > p$ = the number of coefficients of the second-order polynomial (in 2-D it is rectangular domain, $N = 3^2 > p = 6$) and the step 3 is repeated.

As advantages, the method provides a modeling of the objective function over the entire feasible domain and models the neighborhood of the optimal point more and more finely. Instead, the optimum found is a local one, the algorithm is computationally expensive and quickly generates designs with at least one point outside the feasible domain, due to the rotation of the domains. From an economic point of view, there are minimal chances of recovering points.

B. Optimization method by slidings of designs

a) Variant without calculation of models

It directly uses the objective function values in the experimental points. The algorithm uses only discrete factors; in the case of continuous factors, they are discretized into a finite set of values (N_{vk} = total number of values of factor k). A k-dimensional discretization network (grid) is defined, preferably regular, determined by some of the N_{vk} values of the k factors, which will be the support of the optimization algorithm, having great influence on the precision of the results. The structure and dimensions of the experimental designs used are established, in correlation with the dimensions of the feasible domain and of the discretization network.

Two types of experimental designs centered in network nodes determined by the algorithm (origin points) are used: diagonal designs formed by nodes of the network diagonally arranged, on one side and the other of the origin point, equidistant from it, and axial designs formed by nodes of the network axially arranged, on one side and on the other of the origin point, equidistant from it. For k factors there are 2^k diagonal points and 2^k axial points relative to the origin point.

The size of a design is defined by the parameter (step) s being the number of grid nodes traversed in a given direction (diagonal or axial), from the origin point to the points of the design ($s \geq 1$). Its value is initially established in correlation with the N_{vk} numbers. It starts with designs of relatively small dimensions compared to the dimensions of the feasible domain. The algorithm of the variant without model calculation is the following:

1) The first experiment is carried out in a node P_0 from the feasible domain (initial point) which is considered the first origin point (Fig. 2);

2) The points diagonal to the point of origin are established;

3) $N = 2^k$ experiments are performed in the diagonal points (full factorial design);

4) If there is a diagonal point where the answer is more convenient than the origin point, that point becomes the new origin point of the next iteration and step 2 is resumed (the current origin point slides towards the diagonal point);

5) Otherwise, the axial points of the origin point are established;

6) $N = 2^k$ experiments are performed in the axial points (full factorial design);

7) If there is an axial point where the answer is more convenient than the origin point, that point becomes the new origin point of the next iteration and step 2 is resumed (the current origin point slides towards the axial point);

8) Otherwise, the current value of step *s* is decremented by 1, if this is possible, and step 2 is resumed.

All new designs derive from the previous ones by slidings in diagonal or axial direction with different values of step *s*.

The constraints on position can be taken into account when establishing diagonal or axial points. In case they are violated by one of the diagonal or axial points, the current value of step *s* is decremented by 1, if this is possible and the algorithm restarts. The step *s* allows controlling the speed of the algorithm, which is the speed of slidings the designs in the feasible domain in search of the optimal point. A step that is too big can increase the speed but it can reduce the probability of reaching the optimal point, so a compromise is necessary depending on the situation.

b) Variant with calculation of second-order polynomial models

As in the case of the method by zooms, at each iteration a second-order polynomial model is calculated that allows determining the direction of the best values, the position and dimensions of the next designs (1), (2).

The slidings direction for the next iteration will be towards one of the design vertices / side centers, closest to the optimal (stationary) point of the model, on the current design. The designs used must comprise a number of experiments at least equal to the number of coefficients b_k, i.e. $N \geq k + 1$ experiments. The structure and dimensions of the used experimental designs are established in correlation with the dimensions of the feasible domain.

The sliding strategy (Fig. 5) establishes that if D-1 type Doehlert design is used, after determining the optimal (stationary) point S of the model on the current design, the position of the new design is chosen, of the same size, having as center the vertex closest to point S. In this way, 4 points are recovered from one iteration to another (economy design).

If at one of the iterations the optimal point of the model S is obtained inside the current design, then the optimal path is determined, representing the ridge line of the model (Fig. 4a). Another iteration is performed and a new optimal path is calculated (Fig. 4b). The intersection of the two optimal paths can provide an acceptable solution to the optimization problem (Fig. 4c).

The algorithm of the variant with model calculation is the following:

1) An origin point $P_0 = (x_1, \ldots, x_k)^T$ is defined in the feasible domain;

2) A design of N experiments centered in P_0 is made, with $N > p$ = the number of coefficients of the second-order polynomial (type D-1 Doehlert design, $N = 7 > p = 6$);

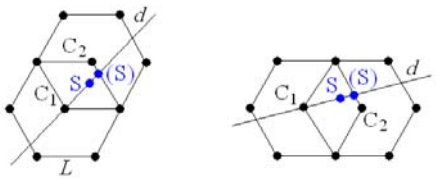

Fig. 5. Sliding strategy for two parameters [2].

3) The associated second-order polynomial model is calculated;

4) Determine the optimal (stationary) point S of the model on the current design;

5) Set the center of the new design at the vertex closest to point S;

6) If the optimum point is not inside the current design, repeat step 3 for the new design;

7) If the optimal point is inside the current design, the optimal path on the current design is determined;

8) If two optimal paths have not yet been determined, step 3 is repeated for the new design;

9) If two optimal paths have already been determined, the solution of the optimization problem is obtained by the intersection of the two optimal paths.

As convergence criteria [13] can be used the error specific to the method that compares the maximum difference between the values of the objective function F at the last iteration against the same value if all previous iterations are taken into account:

$$\varepsilon\,[\%] = \frac{f_{\max} - f_{\min}}{F_{\max} - F_{\min}} \cdot 100 \leq \varepsilon_{\max}\,[\%] \qquad (14)$$

or the relative error of the last objective function value $F^{(n)}$ compared to the previous iteration with a different value $F^{(m)}$:

$$\varepsilon_F\,[\%] = \frac{F^{(n)} - F^{(m)}}{F^{(m)}} \cdot 100 \leq \varepsilon_{F\max}\,[\%] \qquad (15)$$

II. Case Study

A. The object of study

Next, the application of the optimization method by zooms is presented to improve the performance of the direct current electromagnetic device analyzed in [18] (Fig. 6). For a comparative study, the simple variant of the method, which does not require calculation of models, was applied first, followed by the application of the variant that uses polynomial models of the second-order. Both variants combine the results of a large number of numerical simulations to find the maximum of the objective function represented by the force developed by the device at the air-gap $\delta = 1$ mm. The numerical model of the device was obtained by 2-D simulation using the FEMM program [19] coupled with the LUA language [20]. The force value was determined in the post-processing stage using the Maxwell Stress Tensor method. The geometrical parameters are given in Table I and the geometrical shape is shown in Fig. 6. The coil is supplied with voltage $U = 115$ V, has resistance $R_b = 2300\ \Omega$ and number of turns $w = 11500$.

TABLE I.
Geometrical Parameters of DC Device [18]

h (mm)	52.50	L_1 (mm)	6.35	δ (mm)	1.00
h_1 (mm)	7.90	L_2 (mm)	6.35	h_b (mm)	31.20
h_2 (mm)	7.90	L_{a1} (mm)	13.00	L_b (mm)	7.50
H (mm)	65.70	g (mm)	19.80		
L (mm)	50.90	$S_b=L_b \cdot h_b$ (mm^2)	234.00		

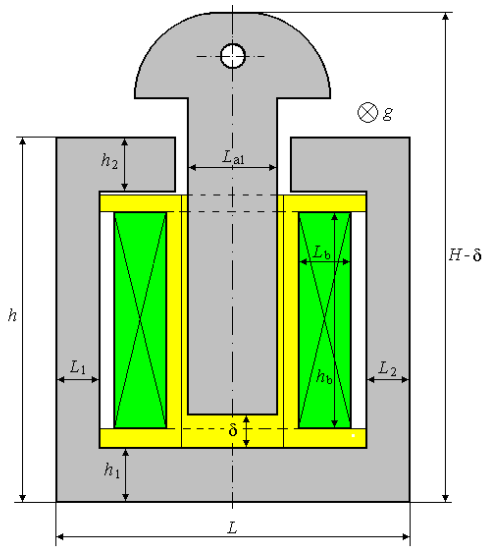

Fig. 6. Geometrical shape of the electromagnetic device [18].

B. *Formulating and solving the optimization problem*

The optimization problem [17] consists in maximizing the force developed by the device at the air-gap δ = 1 mm by varying two geometrical parameters: the ratio between the height and thickness of the coil (k_b) and the ratio between the thicknesses of the core yokes (k_{my}):

$$k_b = \frac{h_b}{L_b} \in [2 \div 6], \quad k_{my} = \frac{h_2}{h_1} \in [0.5 \div 2] \qquad (16)$$

The optimization is non-linear and subject to four equality constraints which maintain the overall dimensions of the device (core width L = ct., core height h = ct., total device height H = ct.) and coil section ($S_b = h_b \cdot L_b$ = ct.). The optimization problem is described mathematically as follows:

$$\mathrm{P}: \begin{cases} \max F(k_b, k_{my}) \\ k_{b\min} \le k_b \le k_{b\max} \\ k_{my\min} \le k_{my} \le k_{my\max} \\ g_h(k_b, k_{my}) - h = 0 \\ g_L(k_b) - L = 0 \\ g_H(k_b, k_{my}) - H = 0 \\ g_{Sb}(k_b) - S_b = 0 \end{cases} \qquad (17)$$

where the functions g_h, g_L, g_H, g_{Sb} depend on parameters k_b, k_{my} and on other geometric parameters not detailed here.

The algorithms of the two variants of the two methods were initialized with the point corresponding to the center of the feasible domain (P_0), close to the point describing the initial geometry (P_{in}) (Table I, Fig. 7).

The evolutions of the optimization algorithms are graphically illustrated in Figs. 7-8 and Figs. 11-12 for the variants without model calculation, respectively, Figs. 9-10 and Figs. 13-14 for the variants with second-order polynomial models. The calculated values are written in Tables II-V.

TABLE II.
EVOLUTION OF THE OPTIMIZATION ALGORITHM BY ZOOMS WITHOUT CALCULATION OF MODELS [17]

Iterations	N_{tot}	N_{rec}	k_b	k_{my}	F	ε (%)	ε_F (%)	L_b (mm)	h_b (mm)	h_1 (mm)	h_2 (mm)	L_1, L_2 (mm)	L_{a1} (mm)
0	1	-	4.000	1.250000000	22.939	-	-	7.65	30.59	7.29	9.11	6.35	12.70
1	5	1	3.000	1.625000000	24.380	100.00	6.28	8.83	26.50	7.81	12.69	5.76	11.52
2	5	2	2.000	2.000000000	24.496	46.50	0.48	10.82	21.63	8.46	16.91	4.77	9.53
3	5	2	3.000	2.000000000	24.818	20.15	1.32	8.83	26.50	6.84	13.67	5.76	11.52
4	5	1	2.500	2.000000000	24.924	17.20	0.43	9.67	24.19	7.60	15.21	5.34	10.68
5	5	3	2.500	1.953125000	24.878	12.73	-0.18	9.67	24.19	7.73	15.09	5.34	10.68
6	5	1	2.750	1.976562500	24.898	4.31	0.08	9.22	25.37	7.27	14.37	5.56	11.13
7	5	4	2.500	2.000000000	24.924	4.00	0.11	9.67	24.19	7.6	15.21	5.34	10.68
8	5	2	2.500	1.988281250	24.909	3.51	-0.06	9.67	24.19	7.63	15.18	5.34	10.68
9	5	1	2.625	1.994140625	24.915	2.63	0.02	9.44	24.78	7.42	14.80	5.45	10.91
10	5	4	**2.500**	**2.000000000**	**24.924**	**1.28**	**0.04**	**9.67**	**24.19**	**7.60**	**15.21**	**5.34**	**10.68**
TOTAL	**51**	**21**											

TABLE III.
EVOLUTION OF THE OPTIMIZATION ALGORITHM BY ZOOMS WITH SECOND-ORDER MODELS [17]

Iterations	N_{tot}	N_{rec}	k_b	k_{my}	F	ε (%)	ε_F (%)	L_b (mm)	h_b (mm)	h_1 (mm)	h_2 (mm)	L_1, L_2 (mm)	L_{a1} (mm)
0	1	-	4.000000	1.250000	22.939	-	-	7.65	30.59	7.29	9.11	6.35	12.70
1	16	0	3.000000	1.625000	24.380	100.00	6.28	8.83	26.50	7.81	12.69	5.76	11.52
2	9	1	2.475191	1.856124	24.753	29.97	1.53	9.72	24.07	8.03	14.90	5.31	10.63
3	9	1	2.510789	1.959299	24.867	8.55	0.46	9.65	24.24	7.69	15.07	5.35	10.70
4	9	1	**2.503167**	**1.993066**	**24.914**	**2.78**	**0.19**	**9.67**	**24.20**	**7.62**	**15.18**	**5.34**	**10.68**
TOTAL	**44**	**3**											

TABLE IV.
EVOLUTION OF THE OPTIMIZATION ALGORITHM BY SLIDINGS OF DESIGNS WITHOUT CALCULATION OF MODELS

Iterations	N_{tot}	N_{rec}	k_b	k_{my}	F	ε (%)	ε_F (%)	L_b (mm)	h_b (mm)	h_1 (mm)	h_2 (mm)	L_1, L_2 (mm)	L_{a1} (mm)
0	1	-	4.000	1.25000	22.939	-	-	7.65	30.59	7.292	9.114	6.351	12.701
1	5	1	3.750	1.34375	23.380	100.00	1.92	7.90	29.62	7.414	9.963	6.225	12.451
2	5	2	3.500	1.43750	23.768	66.40	1.66	8.18	28.62	7.541	10.841	6.087	12.173
3	5	2	3.250	1.53125	24.104	45.70	1.41	8.49	27.58	7.673	11.750	5.932	11.865
4	5	2	3.000	1.62500	24.380	32.86	1.15	8.83	26.50	7.811	12.693	5.759	11.518
5	5	2	2.750	1.71875	24.589	23.43	0.86	9.22	25.37	7.957	13.676	5.563	11.126
6	5	2	2.500	1.81250	24.707	14.97	0.48	9.67	24.19	8.111	14.702	5.338	10.675
7	5	2	2.750	1.90625	24.818	16.13	0.45	9.22	25.37	7.444	14.189	5.563	11.126
8	5	3	**2.500**	**2.00000**	**24.924**	**11.67**	**0.43**	**9.67**	**24.19**	**7.604**	**15.209**	**5.338**	**10.675**
TOTAL	**41**	**16**											

TABLE V.
EVOLUTION OF THE OPTIMIZATION ALGORITHM BY SLIDINGS OF DESIGNS WITH SECOND-ORDER MODELS

Iterations	N_{tot}	N_{rec}	k_b	k_{my}	F	ε (%)	ε_F (%)	L_b (mm)	h_b (mm)	h_1 (mm)	h_2 (mm)	L_1, L_2 (mm)	L_{a1} (mm)
0	1	-	4.000	1.250	22.939	-	-	7.65	30.59	7.292	9.114	6.351	12.701
1	7	4	3.800	1.380	23.668	100.00	3.18	7.85	29.82	7.219	9.962	6.251	12.503
2	7	4	3.600	1.510	23.740	49.26	0.31	8.06	29.02	7.162	10.814	6.144	12.288
3	7	4	3.400	1.640	23.371	50.23	-1.56	8.30	28.21	7.12	11.674	6.027	12.054
4	7	4	3.194	1.766	24.445	28.13	4.60	8.56	27.34	7.108	12.552	5.896	11.791
5	7	4	3.000	1.900	24.767	23.80	1.32	8.83	26.50	7.072	13.433	5.759	11.518
6	7	4	2.800	2.000	24.920	16.27	0.62	9.14	25.60	7.065	14.338	5.604	11.208
7	**7**	**4**	**2.664**	**2.000**	**24.954**	**10.63**	**0.14**	**9.37**	**24.97**	**7.272**	**14.759**	**5.489**	**10.978**
TOTAL	**50**	**22**											

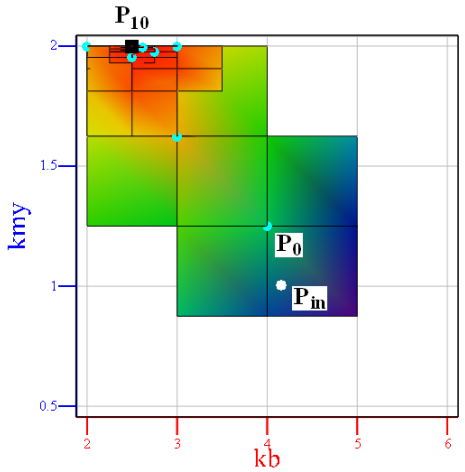

Fig. 7. Two-dimensional representation of the optimization algorithm of the method by zooms without calculation of models [17].

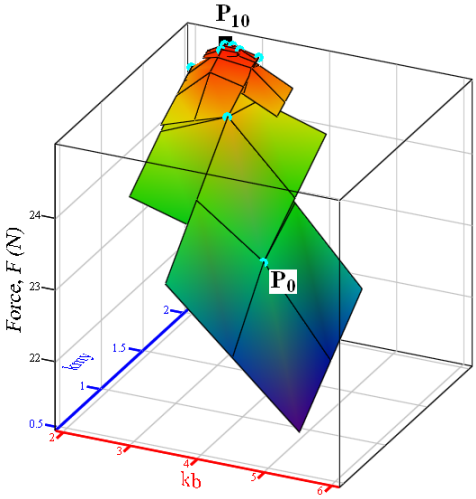

Fig. 8. Three-dimensional representation of the optimization algorithm of the method by zooms without calculation of models [17].

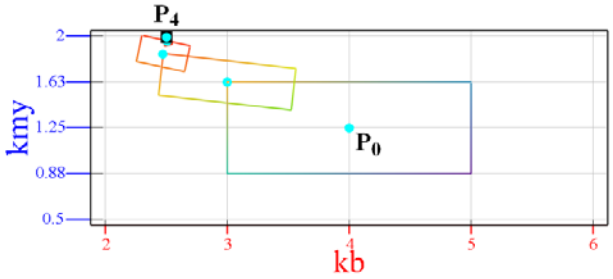

Fig. 9. Two-dimensional representation of the optimization algorithm of the method by zooms with second-order polynomial models [17].

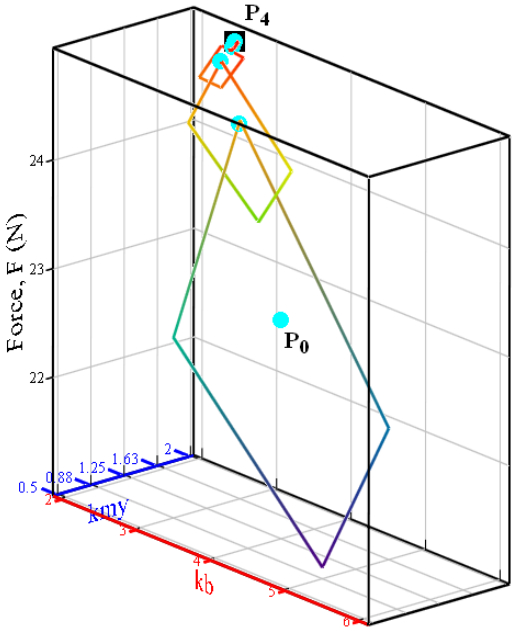

Fig. 10. Three-dimensional representation of the optimization algorithm of the method by zooms with second-order polyn. models [17].

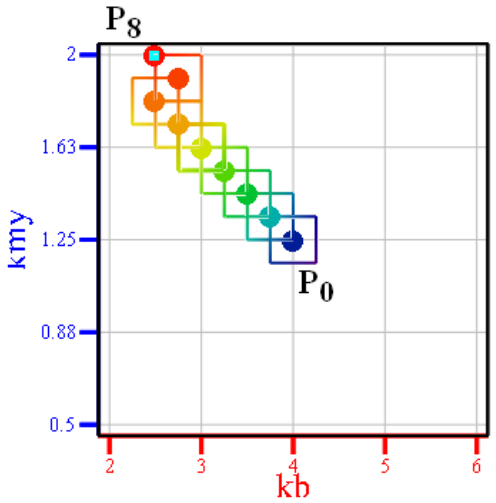

Fig. 11. Two-dimensional representation of the optimization algorithm of the method by slidings of designs without calculation of models.

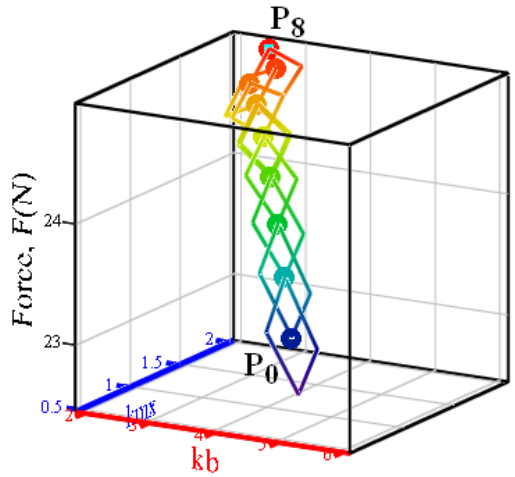

Fig. 12. Three-dimensional representation of the optimization algorithm of the method by slidings of designs without calculation of models.

Since in the last iteration the optimal point was obtained on the border of the domain, the determination of the optimal paths would not bring a great gain because their intersection would take place outside the feasible domain. Therefore, the algorithm stops at this point.

To facilitate the comparison between the methods and their application variants, Table VI compares the results derived from Tables II-V: the number of iterations (N_{it}), the number of experiments (simulations) actually performed ($N = N_{tot} - N_{rec}$)) and the force increase (ΔF).

It can be seen that similar results were obtained after a comparable number of actually performed numerical simulations. Although the second variant of the method requires additional complex calculations, it converges much faster.

TABLE VI.
COMPARISON BETWEEN APPLIED METHODS

Method	Variant	N_{it}	N	ΔF (%)
Zooms	Without models	10	30	8.66
	With 2-D polynomial models	4	41	8.61
Slidings of designs	Without models	8	25	8.66
	With 2-D polynomial models	7	28	8.78

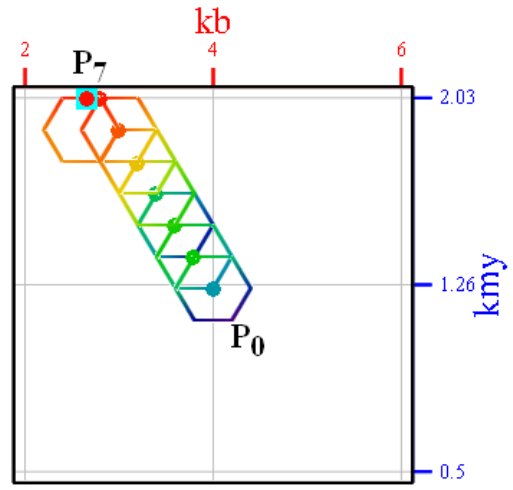

Fig. 13. Two-dimensional representation of the optimization alg. of the method by slidings of designs with second-order polyn. models.

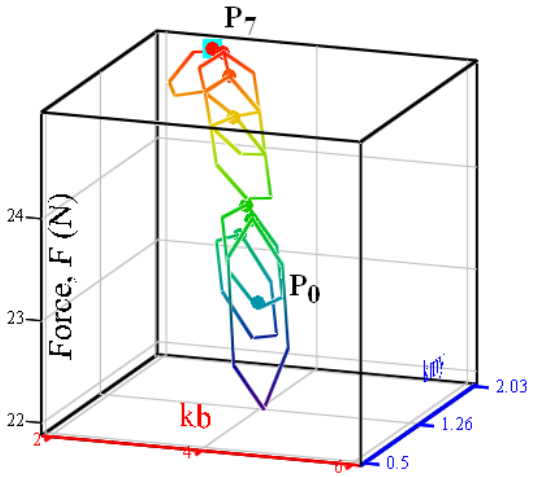

Fig. 14. Three-dimensional representation of the optimization algorithm of the method by slidings of designs with second-order polynomial models.

In Fig. 15 shows the optimal solution obtained by applying both, the method by zooms and the method by slidings of designs, in the variants without and with calculation of models (about the same solution) with the distribution of the magnetic flux density at the air-gap δ = 1 mm, obtained in FEMM, as a planar solution.

III. CONCLUSIONS

The paper presents two variants of two optimization method based on DOE and FEM, ones that only require access to the objective function values at certain points of the feasible domain and others that, in addition, calculates second order polynomial models that approximate the objective function on subdomains. The application on a 2-D numerical model of an electromagnetic device allowed a comparative study of them.

The results highlighted simplicity of the application of the first variant and the speed of convergence of the second for both methods, obtaining similar results with a number of iterations reduced to less than half, but at the price of increasing the number of simulations.

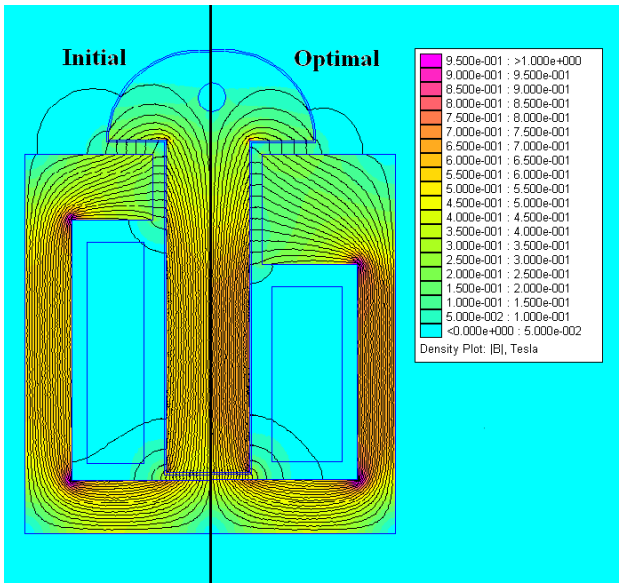

Fig. 15. The optimal solution obtained by the method by zooms (both variants) with the magnetic flux density distribution (δ = 1mm, planar FEMM solution) [17].

As disadvantages, the presented optimization methods determine a local optimum and require a numerical model of the device under optimization. The variants with model calculation are based on a mathematical apparatus of high complexity.

ACKNOWLEDGMENT

Source of research funding in this article: Research program of the Electrical Engineering Department financed by the University of Craiova.

Contribution of authors:

First author – 100%

Received on September 5, 2024

Editorial Approval on November 25, 2024

REFERENCES

[1] D. Montgomery, *Design and Analysis of Experiment*, 5-th Edition, Arizona State University, 2000.

[2] S. Vivier, *Optimization Strategies Using the Design of Experiments Method and Applications to Electrotechnical Devices Modeled by Finite Elements* (In French), Ph-D Thesis, Lille, 2002.

[3] A.-I. Constantin, and V. Fireteanu, "HyperStudy optimization of induction motors finite element assisted design," *2021 International Aegean Conference on Electrical Machines and Power Electronics (ACEMP) & 2021 International Conference on Optimization of Electrical and Electronic Equipment (OPTIM)*, pp. 191-197, 2021.

[4] V.K. Singh, and B. Singh, "Design and development of efficient energy outer rotor switched reluctance motor for ceiling fan," *IEEE International Electric Machines & Drive Conference (IEDMC)*, May 15-18, San Francisco, USA, pp. 1-7, 2023.

[5] L. Du, S. Deng, Z. Cui, R. Poelma, C. Beelen-Hendrikx, and K. Zhang, "Multi-parameters optimization for electromigration in WLCSP solder bumps," *XXV-th International Conference on Thermal, Mechanical and Multi-Physics Simulation and Experiments in Microelectronics and Microsystems (EuroSimE)*, April 07-10, Catania, Italy, pp. 1-4, 2024.

[6] L. Liu, K. Xu, X. He, and X. Cao, "Energy-saving optimization of the gas-fired boiler by DOE method," *Proceedings of the X-th International Forum on Electrical Engiuneering and Automation (IFEEA)*, pp.1-5, 2023.

[7] F. Mahmouditabar, A. Vahedi, and N. Takorabet, "Robust design of BLDC motor considering driving cycle," *IEEE Transaction on Transp. Electrification*, Vol. 10, No. 1, pp. 1414-1424, March, 2024.

[8] X. Li, J. Gong, X. Wang, N. Bracikowski, and F. Gillon, "Proposal of a novel line-start permanent magnet synchronous machine using fractional slot concentrated winding," *XXVI-th International Conference on Electrical Machines and Systems (ICEMS)*, November 05-08, Zhuhai, China, pp. 3027-3032, 2023.

[9] I. Yatchev, M. Rudnicki, K. Hinov, and V. Gueorgiev, "Optimization of a permanent magnet needle actuator," *COMPEL*, Vol. 31, Issue 3, pp. 1018-1028, 2012.

[10] N. Taran, V. Rallabandi, D.-M. Ionel, G. Heins, D. Patterson, and P. Zhou, "Design optimization of electric machines with 3-D FEA and a new hybrid DOE-DE numerical algorithm," *Proceedings of IEEE International Electric Machines & Drives Conference (IEMDC)*, May 12-15, San Diego, CA, USA, pp. 1-6, 2019.

[11] X. Yi, C. Zhu, C. Huang, D. Wang, and X. Wang, "Design optimization of linear switched reluctance motor with segmental mover," *XIII-th Int. Symposium on Linear Drives for Industry Applications (LDIA)*, July 01-03, Wuhan, China, pp.1-6, 2021.

[12] A. Bassiri Nia, M.Y. Yahya, and A. Faraokhi Nejad, "Optimization of graded metallic foam subjected to impulsive loading through DOE approach," *IX-th International Conference on Mechanical and Aerospace Engineering*, July 10-13, Budapest, Hungary, pp.1-5, 2018.

[13] A.-I. Dolan, and F. Stefanescu, "Optimization of modular toroid coil geometry of a superconducting magnetic energy storage device using design of experiments and FEM," *Proceedings of the XII-th IEEE International Conference on Applied and Theoretical Electricity - ICATE 2014*, October 23-25, Craiova, Romania, pp. 1-7, 2014.

[14] A.-I. Dolan, and F. Stefanescu, "Application of two direct optimization methods on a SMES device by DOE and FEM: method by zooms and method by slidings of plans," *Annals of the University of Craiova, Series: Electrical Engineering*, No. 38, Universitaria Publishing House, pp. 78-85, 2014.

[15] A.-I. Dolan, "Improvement of acting force of DC plunger-type electromagnet by six parameters optimization," *Proceedings of the XII-th International Conference on Electromechanical and Power Systems–SIELMEN 2019*, October 9-11, Iasi-Chisinau, pp. 1-5, 2019.

[16] A.-I. Dolan, "Exhaustive optimization method applied on electromagnetic device," *Annals of the University of Craiova, "Series: Electrical Engineering*, No. 46, Issue 1, Universitaria Publishing House pp.34-41, 2022.

[17] A.-I. Dolan, "Optimization by Zooms without and with Second-Order Polynomial Models Applied to a 2-D Simulation", *Proceedings of the XV-th IEEE International Conference on Applied and Theoretical Electricity - ICATE 2024*, pp. 1-6, Craiova, Romania, October 24-25, 2024.

[18] A.-I. Dolan, I. Yatchev, and K. Hinov, "Static force characteristics of a plunger type electromagnet," *International PhD Seminar - Numerical Field Computation and Optimization in Electrical Engineering*, Ohrid, Macedonia, September 20-25, pp. 67-71, 2005.

[19] https://www.femm.info/wiki/HomePage

[20] https://www.lua.org/

DOI: 10.52846/AUCEE.2024.08

Exploring NI AutoML Application for Simulated Waveforms

Eliza Maria Olariu* and Horia Hedesiu*

* Technical University of Cluj-Napoca / Electrical Engineering Department, Cluj-Napoca, Romania, Eliza.Olariu@campus.utcluj.ro

***Abstract* – This paper presents the importance of finding the suitable configurations for Artificial Intelligence and Machine Learning algorithms and correct data preprocessing for a waveform problem. In the Artificial Intelligence and Machine Learning area, this step is one of the most important and it influences the performance result of the model. The experiments of different configurations were done using National Instruments Automated Machine Learning (NI AutoML), a web application created for everyone that allows us to easily change the configurations of the model by just clicking some buttons. This work shows how the model performance is influenced by modifying what columns of data to use, by data splitting or by adding or deleting preprocessing steps in the pipeline. All the results obtained for the different experiments are analyzed in this paper. The proposed flow is generic enough to be applied for all the use cases. To exemplify the whole process, a synthetic data set obtained by generating current and voltage in an RL circuit was chosen and the experiments part was created. The data represent two waveforms: one for current and one for voltage and they represent data recorded during the test time. In the end process each test has a label associated: Pass or Fail. The classification problem was defined for help in improving the fail detection rate.**

Cuvinte cheie: *NI AutoML, forme de undă simulate, problemă de clasificare, preprocesarea datelor, inteligență artificială și învățare automată.*

Keywords: *NI AutoML, simulated waveforms, classification problem, data preprocessing, Artificial Intelligence and Machine Learning.*

I. Introduction

In the spotlight these days is Artificial Intelligence and Machine Learning area. This technique is on the increasing of development, and it is used in many domains to improve the quality of life. Better solutions can be created based on Artificial Intelligence and Machine Learning in different domains: in industry like the batteries industry from research [1] to production [2] and to monitoring [3] or in the healthcare for diagnostics, predictive analytics, personalized medicine and administration application [4].

In all cases, the data obtained can create a model that finds patterns and learns from previous information and helps in identifying the aspects of the new data [5]. There are many types of Artificial Intelligence and Machine Learning algorithms: supervised, unsupervised; for classification, regression; for tabular data, images, waveforms; exists something for each problem [6].

The first aspect in solving problems in the modern approach is to obtain data. It should be possible to use real data, recorded directly from the sensors or measurements from the environment, or it is possible to simulate them in laboratory [7]. Simulated data can be also applied together with real data or used in the beginning for training the models that will be deployed after that in the real systems.

An example of simulated waveforms data used in a predictive classification model is presented in [8]. Data generated is a way to simplify a battery data model and can help in presenting the full flow for a system that helps in monitoring battery performance [9]. This infrastructure can be used in Prognostics and Health Management [10] or in the testing phase of manufacturing [11].

After having the data, the next phase is understanding and transforming it into information. There are more preprocessing steps needed to clean, transform and prepare data for Artificial Intelligence and Machine Learning algorithms [12]. Last but not least, it is also important to find the correct parameters to the predictive model. Do more experiments and identify the suitable configuration for each problem to solve. National Instruments Automated Machine Learning (NI AutoML) is one of the web applications that allows the customers to create all the environment for defining all the experiments for finding the best configuration and the best model and also be able to monitor and change it with time passing and environment changing [13].

II. Classification Problem To Solved

A. Data set

The data set contains simulated waveforms generated using an RL series circuit that represents an object into the testing phase into a factory. Each measurement contains two waveforms that represent the current and the voltage and it is associated with a label that represents if the test was with success or failed (Fig. 1) [8].

The voltage (V) signal represents the input in the RL circuit. It is created as a sum of three sinus wave components with different frequencies and added on top a low-level noise signal. The output of the RL circuit generated the current signal (A). In the middle of the test time, parameters of the RL circuit can vary, and, in this case, it was considered that data provided from a failed test [8].

The data set contains 520 waveforms with 1000 test points and 5 columns:

- Current (A)
- Voltage (V)
- Index
- Unit
- Label.

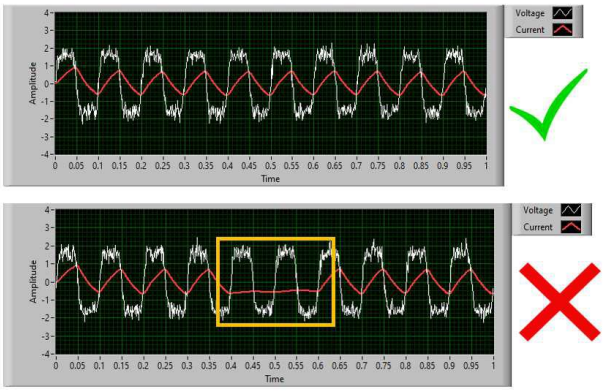

Fig. 1. Simulated waveform for success (top figure) and failed (bottom figure) having voltage (V) and the current (A) waveforms from the RL circuit [8].

B. *NI AutoML*

For defining the Artificial Intelligence and Machine Learning model, it was used NI AutoML application [13]. It has many configuration aspects that can be easily modified with simple clicks and trained in 9 different models and shows the best one [14]:

- AdaBoost Classifier – Adaptive Boosting - a statistical classification meta-estimator
- Baseline Classification – predicting on classes' distribution
- Decision Tree – create one decision tree with conditions rules
- Gradient Boosting – additive model base on decision trees
- LightGBM – based on Gradient Boosting
- Logistic Regression – algorithm for one-vs-rest
- Random Forest – create more decision trees with conditions rules
- Support Vector Classifier – divided the space in regions for each label
- XGBoost – Extreme Gradient Boosting – based on Gradient Boosting

For identifying the best model, one criterion can be selected. The application offers 6 different metrics [14]:

- Accuracy – correct classification divided to all classifications
- AUC – area under the ROC curve
- Recall – true positive divided to true positive and false negative
- Precision – true positive divided to true positive and false positive
- Balanced Accuracy - average recall obtained on each class
- F1 – harmonic mean of the precision and recall

Another criteria to select the best algorithm is Run Time, some of the algorithms take more time to be train comparing with the others. For some cases, time is also very important, like real time problem.

III. Experiments

NI AutoML configuration that was kept the same for all the experiments:

- Target selected value: label
- Prediction type: Binary Classification
- For the first part of the experiments, the metric used to select the best algorithm is area under the curve "AUC" (secund column in the table results). This metric will rank the positive label higher than the negative one [15].

A. *Experiments based on waveform used*

1) Used just Current (A): drop the Voltage column and create the prediction model using just features obtained from Current waveform.

Obtained results can be seen on Table I.

➔ Best model: Random Forest 0.865 AUC

2) Used just Voltage (V): drop the Current column and create the prediction model using just features obtained from Voltage waveform

Obtained results can be seen on Table II.

➔ Best model: Decision Tree 0.53 AUC

3) Used both Current (A) and Voltage (V): do not drop any columns and create the prediction model using features obtained from both Current and Voltage waveforms

Obtained results can be seen on **Error! Reference source not found.**II.

➔ Best model: Random Forest 0.859 AUC

TABLE I.
RESULTS OBTAINED FOR EXPERIMENT A 1) ORDER BY AUC COLUMN, BEST MODEL ON THE FIRST LINE

Model	Accuracy	AUC	Recall	Precision	Balanced Accuracy	F1	Run Time
Random Forest	0.9019	0.8649	0.913	0.9745	0.8649	0.9428	0:00:00
LightGBM	0.8692	0.8101	0.887	0.9623	0.8101	0.9231	0:00:06
XGBoost	0.8462	0.7971	0.8609	0.9612	0.7971	0.9083	0:00:02
Gradient Boosting	0.8712	0.7967	0.8935	0.958	0.7967	0.9246	0:00:48
AdaBoost Classifier	0.8731	0.7543	0.9087	0.9457	0.7543	0.9268	0:00:08
Decision Tree	0.7712	0.7475	0.7783	0.9547	0.7475	0.8575	0:00:00
Logistic Regression	0.8904	0.525	1	0.8897	0.525	0.9417	0:00:01
Support Vector Classifier	0.8846	0.5	1	0.8846	0.5	0.9388	0:00:02
Baseline Classification	0.4769	0.4942	0.4717	0.8821	0.4942	0.6147	0:03:40

TABLE II.
RESULTS OBTAINED FOR EXPERIMENT A 2) ORDER BY AUC COLUMN, BEST MODEL ON THE FIRST LINE

Model	Accuracy	AUC	Recall	Precision	Balanced Accuracy	F1	Run Time
Decision Tree	0.8269	0.5254	0.9174	0.8903	0.5254	0.9036	0:00:01
AdaBoost Classifier	0.8308	0.513	0.9261	0.8875	0.513	0.9064	0:00:08
Baseline Classification	0.5019	0.5011	0.5022	0.8851	0.5011	0.6408	0:05:51
Support Vector Classifier	0.8846	0.5	1	0.8846	0.5	0.9388	0:00:03
Random Forest	0.8846	0.5	1	0.8846	0.5	0.9388	0:00:01
LightGBM	0.8846	0.5	1	0.8846	0.5	0.9388	0:05:22
XGBoost	0.8827	0.4989	0.9978	0.8844	0.4989	0.9377	0:00:41
Gradient Boosting	0.8808	0.4978	0.9957	0.8842	0.4978	0.9366	0:00:43
Logistic Regression	0.2538	0.4406	0.1978	0.8273	0.4406	0.3193	0:00:01

TABLE III.
RESULTS OBTAINED FOR EXPERIMENT A 3) ORDER BY AUC COLUMN, BEST MODEL ON THE FIRST LINE

Model	Accuracy	AUC	Recall	Precision	Balanced Accuracy	F1	Run Time
Random Forest	0.8788	0.8591	0.8848	0.976	0.8591	0.9282	0:00:01
XGBoost	0.8712	0.8402	0.8804	0.9712	0.8402	0.9236	0:00:27
LightGBM	0.8404	0.8373	0.8413	0.9748	0.8373	0.9032	0:05:50
Gradient Boosting	0.8769	0.8362	0.8891	0.9692	0.8362	0.9274	0:01:06
Decision Tree	0.725	0.7721	0.7109	0.9703	0.7721	0.8206	0:00:01
AdaBoost Classifier	0.8808	0.7225	0.9283	0.9364	0.7225	0.9323	0:00:13
Logistic Regression	0.8981	0.6163	0.9826	0.9095	0.6163	0.9446	0:00:01
Support Vector Classifier	0.8846	0.5	1	0.8846	0.5	0.9388	0:00:05
Baseline Classification	0.5096	0.4764	0.5196	0.8755	0.4764	0.6521	0:07:23

Conclusion:

The best results were obtained for the case when it was used just Current waveform. This happened because the Current is the output of the simulated RL circuit and just the Current is influenced by R, L value modifications during the test.

➔ Best model: Random Forest 0.86 AUC

For the next experiment, it will be used just Current waveform.

B. *Experiments basd on selection positive class*

1) Used "Pass" value: in the previous examples it was used "Pass" value.

Obtained results can be seen on Table I.

➔ Best model: Random Forest 0.86 AUC

2) Used "Fail" value: change the value for positive class into "Fail"

Obtained results can be seen on Table IV.

➔ Best model: Random Forest 0.85 AUC

Conclusion:

The best results were obtained for the case when it was used "Pass" value for positive class. This is expected because the "Pass" value represents the success test simulated.

TABLE IV.
RESULTS OBTAINED FOR EXPERIMENT B 2) ORDER BY AUC COLUMN, BEST MODEL ON THE FIRST LINE

Model	Accuracy	AUC	Recall	Precision	Balanced Accuracy	F1	Run Time
Random Forest	0.8923	0.8522	0.8	0.5217	0.8522	0.6316	0:00:01
LightGBM	0.8635	0.8214	0.7667	0.4466	0.8214	0.5644	0:05:42
Gradient Boosting	0.8654	0.808	0.7333	0.449	0.808	0.557	0:00:42
XGBoost	0.8212	0.783	0.7333	0.3636	0.783	0.4862	0:00:26
AdaBoost Classifier	0.8135	0.7714	0.7167	0.3496	0.7714	0.4699	0:00:09
Decision Tree	0.6827	0.7192	0.7667	0.2335	0.7192	0.358	0:00:00
Logistic Regression	0.8962	0.55	0.1	1	0.55	0.1818	0:00:02
Baseline Classification	0.5269	0.5297	0.5333	0.128	0.5297	0.2065	0:04:58
Support Vector Classifier	0.8846	0.5	0	0	0.5	0	0:00:02

➔ Best model: Random Forest 0.86 AUC

For the next experiment, it will be used "Pass" value for positive class.

C. *Experiments based on preprocessing steps in pipeline*

1) Used default set up for waveforms: in the previous examples it was selected:

- add_missing_indicator
- infinity_to_nan
- mean_median_imputer
- nan_column_dropper
- datetime_features
- high_cardinality_dropper
- min_max_scaler
- match_variables
- waveforms_feature_extractor
- remove_special_json_characters
- id_label_encoder
- ordinal_encode_target
- smote

Obtained results can be seen on Table I.

➔ Best model: Random Forest 0.86 AUC

2) Delete SOTE step and data time feature extraction: deleted steps:

- datetime_features
- smote

Obtained results can be seen on Table V.

➔ Best model: Random Forest 0.82 AUC

3) Delete also MinMaxScaler step and high_cardinality_dropper step: deleted steps:

- min_max_scaler
- high_cardinality_dropper
- datetime_features
- smote

Obtained results can be seen on Table VI.

➔ Best model: Random Forest 0.82 AUC

TABLE V.
RESULTS OBTAINED FOR EXPERIMENT C 2) ORDER BY AUC COLUMN, BEST MODEL ON THE FIRST LINE

Model	Accuracy	AUC	Recall	Precision	Balanced Accuracy	F1	Run Time
Random Forest	0.7865	0.8214	0.7761	0.9781	0.8214	0.8655	0:00:01
LightGBM	0.8827	0.7888	0.9109	0.9544	0.7888	0.9321	0:04:01
XGBoost	0.8865	0.7764	0.9196	0.9506	0.7764	0.9348	0:00:23
AdaBoost Classifier	0.875	0.7337	0.9174	0.9399	0.7337	0.9285	0:00:05
Decision Tree	0.8423	0.7297	0.8761	0.9416	0.7297	0.9077	0:00:00
Gradient Boosting	0.7615	0.6986	0.7804	0.9398	0.6986	0.8527	0:00:25
Logistic Regression	0.8904	0.525	1	0.8897	0.525	0.9417	0:00:01
Baseline Classification	0.8096	0.5083	0.9	0.8865	0.5083	0.8932	0:04:57
Support Vector Classifier	0.1154	0.5	0	0	0.5	0	0:00:00

TABLE VI.
RESULTS OBTAINED FOR EXPERIMENT C 3) ORDER BY AUC COLUMN, BEST MODEL ON THE FIRST LINE

Model	Accuracy	AUC	Recall	Precision	Balanced Accuracy	F1	Run Time
Random Forest	0.7865	0.8214	0.7761	0.9781	0.8214	0.8655	0:00:00
LightGBM	0.8808	0.8094	0.9022	0.9606	0.8094	0.9305	0:04:24
XGBoost	0.8865	0.7764	0.9196	0.9506	0.7764	0.9348	0:00:23
AdaBoost Classifier	0.875	0.7337	0.9174	0.9399	0.7337	0.9285	0:00:04
Decision Tree	0.7615	0.6986	0.7804	0.9398	0.6986	0.8527	0:00:00
Gradient Boosting	0.7615	0.6986	0.7804	0.9398	0.6986	0.8527	0:00:24
Support Vector Classifier	0.8846	0.5	1	0.8846	0.5	0.9388	0:00:00
Logistic Regression	0.3096	0.4793	0.2587	0.8686	0.4793	0.3987	0:00:01
Baseline Classification	0.7788	0.4692	0.8717	0.8775	0.4692	0.8746	0:04:55

Conclusion:

The best results were obtained for the case when it was used all the default steps for waveform. If steps are deleted the performance goes down. Normalization, balance, adding more features or deleting high cardinality improves the results.

➔ Best model: Random Forest 0.86 AUC

For the next experiment, default preprocessing steps will be used for waveform.

D. *Experiments based on split configuration*

1) Used "Random" type with 60% training set, 20% validation set and 20% test set: in the previous examples it was used this configuration.

Obtained results can be seen on Table I.

➔ Best model: Random Forest 0.86 AUC

2) Used "Random" type with 80% training set, 10% validation set and 10% test set: change values to use more data from training

Obtained results can be seen on Table VII.

➔ Best model: LightGBM 0.75 AUC

TABLE VII.
RESULTS OBTAINED FOR EXPERIMENT D 2) ORDER BY AUC COLUMN, BEST MODEL ON THE FIRST LINE

Model	Accuracy	AUC	Recall	Precision	Balanced Accuracy	F1	Run Time
LightGBM	0.7212	0.7482	0.713	0.9619	0.7482	0.819	0:06:10
AdaBoost Classifier	0.7135	0.7438	0.7043	0.9614	0.7438	0.813	0:00:09
XGBoost	0.7135	0.7438	0.7043	0.9614	0.7438	0.813	0:00:35
Random Forest	0.6577	0.7341	0.6348	0.9669	0.7341	0.7664	0:00:00
Gradient Boosting	0.6635	0.7156	0.6478	0.9582	0.7156	0.773	0:00:53
Decision Tree	0.5231	0.6797	0.4761	0.969	0.6797	0.6385	0:00:00
Support Vector Classifier	0.8846	0.5	1	0.8846	0.5	0.9388	0:00:02
Logistic Regression	0.8308	0.4986	0.9304	0.8843	0.4986	0.9068	0:00:01
Baseline Classification	0.4769	0.4797	0.4761	0.876	0.4797	0.6169	0:08:10

3) Used "Cross-Validation" option: check this option in the UI of NI AutoML.

Obtained results can be seen in Table VIII.

➔ Best model: Random Forest 0.78 AUC

Conclusion:

The best results were obtained for the case when it was used "Random" type with 60% training set, 20% validation set and 20% test set.

➔ Best model: Random Forest 0.86 AUC

For the next experiment, it will be used "Random" split type with 60% training set, 20% validation set and 20% test set.

E. *Experiments based on metric to optimize*

1) Used "AUC" option: in the previous examples it was used this configuration.

Obtained results can be seen on Table I.

➔ Best model: Random Forest 0.86 AUC

2) Used "Accuracy" option:

Obtained results can be seen on Table IX.

➔ Best model: Random Forest 0.9 Accuracy

TABLE VIII.
RESULTS OBTAINED FOR EXPERIMENT D 3) ORDER BY AUC COLUMN, BEST MODEL ON THE FIRST LINE

Model	Accuracy	AUC	Recall	Precision	Balanced Accuracy	F1	Run Time
Random Forest	0.7385	0.7797	0.7261	0.9705	0.7797	0.8308	0:00:07
XGBoost	0.7673	0.7511	0.7696	0.9535	0.7511	0.854	0:00:26
LightGBM	0.7942	0.746	0.7978	0.9514	0.746	0.8728	0:01:04
Gradient Boosting	0.7038	0.7355	0.6826	0.9487	0.7355	0.8031	0:05:21
AdaBoost Classifier	0.7865	0.7145	0.7891	0.9396	0.7145	0.8683	0:00:56
Logistic Regression	0.6846	0.6239	0.6717	0.9107	0.6239	0.7903	0:00:06
Decision Tree	0.3635	0.5025	0.3217	0.8862	0.5025	0.4721	0:00:06
Support Vector Classifier	0.8846	0.5	1	0.8846	0.5	0.9388	0:00:18
Baseline Classification	0.4827	0.471	0.4674	0.8731	0.471	0.6152	0:31:34

TABLE IX.
RESULTS OBTAINED FOR EXPERIMENT E 2) ORDER BY ACCURACY COLUMN, BEST MODEL ON THE FIRST LINE

Model	Accuracy	AUC	Recall	Precision	Balanced Accuracy	F1	Run Time
Random Forest	0.9019	0.8721	0.9109	0.9767	0.8721	0.9426	0:00:01
Logistic Regression	0.8904	0.525	1	0.8897	0.525	0.9417	0:00:01
Support Vector Classifier	0.8846	0.5	1	0.8846	0.5	0.9388	0:00:03
Gradient Boosting	0.8692	0.8029	0.8891	0.9601	0.8029	0.9233	0:01:07
LightGBM	0.8692	0.7957	0.8913	0.9579	0.7957	0.9234	0:00:11
XGBoost	0.85	0.8138	0.8609	0.9659	0.8138	0.9103	0:00:06
AdaBoost Classifier	0.7731	0.7486	0.7804	0.9548	0.7486	0.8589	0:00:10
Decision Tree	0.6942	0.7112	0.6891	0.952	0.7112	0.7995	0:00:00
Baseline Classification	0.4923	0.4812	0.4957	0.8769	0.4812	0.6333	0:06:00

3) Used "Recall" option:

Obtained results can be seen on Table X.

➔ Best model: Logistic Regression and Support Vector Classifier 1 Recall

4) Used "Precision" option:

Obtained results can be seen on Table XI.

➔ Best model: Random Forest 0.97 Precision

5) Used "Balanced Accuracy" option:

Obtained results can be seen on Table XII.

➔ Best model: Random Forest 0.86 Balanced Accuracy

6) Used "F1" option:

Obtained results can be seen on Table XIII.

➔ Best model: Random Forest 0.95 F1

Conclusion:

The best results were obtained from the case when it was used Recall metrics for Logistic Regression and Support Vector Classifier. On this aspect, the metric can be chosen based on the problem that we want to solve, not based on the value obtain for it. In our case the best meaning is using AUC.

TABLE X.
RESULTS OBTAINED FOR EXPERIMENT E 3) ORDER BY RECALL COLUMN, BEST MODEL ON THE FIRST LINE

Model	Accuracy	AUC	Recall	Precision	Balanced Accuracy	F1	Run Time
Logistic Regression	0.8962	0.55	1	0.8949	0.55	0.9446	0:00:01
Support Vector Classifier	0.8846	0.5	1	0.8846	0.5	0.9388	0:00:02
Random Forest	0.9154	0.858	0.9326	0.9706	0.858	0.9512	0:00:00
LightGBM	0.8769	0.829	0.8913	0.967	0.829	0.9276	0:06:10
Gradient Boosting	0.8692	0.8246	0.8826	0.9667	0.8246	0.9227	0:00:44
AdaBoost Classifier	0.8481	0.7837	0.8674	0.9568	0.7837	0.9099	0:00:08
XGBoost	0.8365	0.8207	0.8413	0.9699	0.8207	0.901	0:00:27
Decision Tree	0.5769	0.7029	0.5391	0.9688	0.7029	0.6927	0:00:01
Baseline Classification	0.4808	0.4529	0.4891	0.8654	0.4529	0.625	0:04:54

TABLE XI.
RESULTS OBTAINED FOR EXPERIMENT E 4) ORDER BY PRECISION COLUMN, BEST MODEL ON THE FIRST LINE

Model	Accuracy	AUC	Recall	Precision	Balanced Accuracy	F1	Run Time
Random Forest	0.9154	0.858	0.9326	0.9706	0.858	0.9512	0:00:00
XGBoost	0.8365	0.8207	0.8413	0.9699	0.8207	0.901	0:00:27
Decision Tree	0.5769	0.7029	0.5391	0.9688	0.7029	0.6927	0:00:01
LightGBM	0.8769	0.829	0.8913	0.967	0.829	0.9276	0:06:10
Gradient Boosting	0.8692	0.8246	0.8826	0.9667	0.8246	0.9227	0:00:44
AdaBoost Classifier	0.8481	0.7837	0.8674	0.9568	0.7837	0.9099	0:00:08
Logistic Regression	0.8962	0.55	1	0.8949	0.55	0.9446	0:00:01
Support Vector Classifier	0.8846	0.5	1	0.8846	0.5	0.9388	0:00:02
Baseline Classification	0.4808	0.4529	0.4891	0.8654	0.4529	0.625	0:04:54

TABLE XII.
RESULTS OBTAINED FOR EXPERIMENT E 5) ORDER BY BALANCED ACCURACY COLUMN, BEST MODEL ON THE FIRST LINE

Model	Accuracy	AUC	Recall	Precision	Balanced Accuracy	F1	Run Time
Random Forest	0.9154	0.858	0.9326	0.9706	0.858	0.9512	0:00:00
LightGBM	0.8769	0.829	0.8913	0.967	0.829	0.9276	0:06:10
Gradient Boosting	0.8692	0.8246	0.8826	0.9667	0.8246	0.9227	0:00:44
XGBoost	0.8365	0.8207	0.8413	0.9699	0.8207	0.901	0:00:27
AdaBoost Classifier	0.8481	0.7837	0.8674	0.9568	0.7837	0.9099	0:00:08
Decision Tree	0.5769	0.7029	0.5391	0.9688	0.7029	0.6927	0:00:01
Logistic Regression	0.8962	0.55	1	0.8949	0.55	0.9446	0:00:01
Support Vector Classifier	0.8846	0.5	1	0.8846	0.5	0.9388	0:00:02
Baseline Classification	0.4808	0.4529	0.4891	0.8654	0.4529	0.625	0:04:54

TABLE XIII.
RESULTS OBTAINED FOR EXPERIMENT E 6) ORDER BY F1 COLUMN, BEST MODEL ON THE FIRST LINE

Model	Accuracy	AUC	Recall	Precision	Balanced Accuracy	F1	Run Time
Random Forest	0.9154	0.858	0.9326	0.9706	0.858	0.9512	0:00:00
Logistic Regression	0.8962	0.55	1	0.8949	0.55	0.9446	0:00:01
Support Vector Classifier	0.8846	0.5	1	0.8846	0.5	0.9388	0:00:02
LightGBM	0.8769	0.829	0.8913	0.967	0.829	0.9276	0:06:10
Gradient Boosting	0.8692	0.8246	0.8826	0.9667	0.8246	0.9227	0:00:44
AdaBoost Classifier	0.8481	0.7837	0.8674	0.9568	0.7837	0.9099	0:00:08
XGBoost	0.8365	0.8207	0.8413	0.9699	0.8207	0.901	0:00:27
Decision Tree	0.5769	0.7029	0.5391	0.9688	0.7029	0.6927	0:00:01
Baseline Classification	0.4808	0.4529	0.4891	0.8654	0.4529	0.625	0:04:54

IV. CONCLUSIONS

This paper presented the importance of finding the best parameters and the best preprocessing steps for Artificial Intelligence and Machine Learning model creation. The experiments presented used the simulated waveform data set.

NI AutoML was used as an Artificial Intelligence and Machine Learning application.

It was defined and presented results for 17 experiments that play with different configurations:

A. Experiments based on waveform used

1) Used just Current (A)

2) Used just Voltage (V)

3) Used both Current (A) and Voltage (V)

B. Experiments based on selection positive class

1) Used "Pass" value

2) Used "Fail" value

C. Experiments based on preprocessing steps in pipeline

1) Used default set up for waveforms

2) Delete SOTE step and data time feature extraction

3) Delete also MinMaxScaler step and high_cardinality _dropper step

D. Experiments based on split configuration

1) Used "Random" type with 60% training set, 20% validation set and 20% test set

2) Used "Random" type with 80% training set, 10% validation set and 10% test set

3) Used "Cross-Validation" option

E. Experiments based on metric to optimize

1) Used "AUC" option

2) Used "Accuracy" option

3) Used "Recall" option

4) Used "Precision" option

5) Used "Balanced Accuracy" option

6) Used "F1" option

The best results were obtained from experiment A 1) having:

- Used just Current (A) waveform
- Used "Pass" value for positive class
- Used default set up for preprocessing steps for waveforms
- Used "Random" type with 60% training set, 20% vali-dation set and 20% test set
- Using AUC metric

➔ Best model: Random Forest 0.86 AUC

In the future, using data taken directly from a real system can be used in this infrastructure to confirm all the aspects and analysis the differences and the similarity with simulated data.

ACKNOWLEDGMENT

This work used NI AutoML, one application from NI's AI infrastructure that the customers can obtain.

Source of research funding in this article: Research program financed by the Technical University of Cluj-Napoca.

Contribution of authors:

First author – 50%

First coauthor – 50%

Received on September 17,2024

Editorial Approval on December 2, 2024

REFERENCES

[1] T. Lombardo, et al. "Artificial intelligence applied to battery research: Hype or reality?," *Chem Rev*, June 2022, vol. 122, iss. 12, pp. 10899-10969, doi: 10.1021/acs.chemrev.1c00108.

[2] M. Faraji Niri, K. Aslansefat, S. Haghi, M. Hashemian, R. Daub, J. A. Marco, "A review of the applications of explainable machine learning for lithium–ion batteries: From production to state and performance estimation", *Energies*, 16, 6360, doi: 10.3390/en16176360, 2023.

[3] A. Prisacaru, P. J. Gromala, M. B. Jeronimo, Bongtae Han and Guo Qi Zhang, "Prognostics and health monitoring of electronic system: A review," *2017 18th International Conference on Thermal, Mechanical and Multi-Physics Simulation and Experiments in Microelectronics and Microsystems (EuroSimE*), Dresden, Germany, 2017, pp. 1-11, doi: 10.1109/EuroSimE.2017.7926248.

[4] G. S. Nadella, S. Satish, K. Meduri, and S. S. Meduri, "A systematic literature review of advancements, challenges and future directions of AI and ML in healthcare", *International Journal of Machine Learning for Sustainable Development*, vol.5, iss. 3, pp. 115-130, 2023.

[5] C. M. Bishop, *Pattern Recognition and Machine Learning*, New York: Springer, 2016.

[6] R. Agrawal, "Fundamentals of machine learning," *Machine learning for healthcare: Handling and managing data*, p. 1, 2020.

[7] T. Chamunorwa, D. Ursutiu, C. Samoila, H. Hedesiu, and H. A. Modran, "Electronic educational laboratory platform for students," in *Online Engineering and Society 4.0: Proceedings of the 18th International Conference on Remote Engineering and Virtual Instrumentation*. Springer, 2022, pp. 311–322.

[8] O. E. Maria, and H. Horia. "Improving manufacturing testing steps using artificial intelligence and machine learning algorithms trained on simulated waveforms" *2024 IEEE International Conference on Automation, Quality and Testing, Robotics (AQTR).* Cluj-Napoca, Romania, 2024, pp. 1-5.

[9] J. Peng, X. Zhao, J. Ma, et. al, "Enhancing lithium-ion battery monitoring: A critical review of diverse sensing approaches", *eTransportation*, vol. 22, 2024.

[10] M. Ahsan, S. Stoyanov and C. Bailey, "Prognostics of automotive electronics with data driven approach: A review," *2016 39th International Spring Seminar on Electronics Technology (ISSE)*, Pilsen, Czech Republic, 2016, pp. 279-284, doi: 10.1109/ISSE.2016.7563205.

[11] E. M. Olariu, C. Vlasin, O. Balaj, and H. Hedesiu, "Cloud based realtime data acquisition for industrial applications," in *2023 IEEE 29th International Symposium for Design and Technology in Electronic Packaging (SIITME)*, Craiova, Romania, 2023, pp. 324-328.

[12] L. Pierson, *Data Science For Dummies*, 3rd Edition, New Jersey: Wiley, 2021.

[13] E. M. Olariu, and H. Hedesiu, "Artificial intelligence and machine mearning using NI AutoML in industry-case study: Simulated waveforms", *2024 International Conference on Applied and Theoretical Electricity (ICATE)*, Craiova, Romania, 2024, pp. 1-4.

[14] scikit-learn, Machine Learning in Python, [cited 2024 December 8], Available from: https://scikit-learn.org/stable/

[15] Machine Learning, "Classification: ROC and AUC", [cited 2024 December 8], Available from: https://developers.google.com/machine-learning/crash-course/classification/roc-and-auc

DOI: 10.52846/AUCEE.2024.09

Pneumatic System for Compacting Food Waste Packaging

Ionel Laurenţiu Alboteanu[*], Mircea Adrian Drighiciu[*], Ecaterina Maria Drighiciu[†], Florin Ravigan[*]

[*] University of Craiova / Department of Electromechanical, Environmental and Applied Informatics, Craiova, Romania,
e-mail: lalboteanu@em.ucv.ro, adrighiciu@gmail.com, ravigan.florin@gmail.com

[†] Distributie Oltenia / Department of Construction, Craiova, Romania
e-mail: drighiciu.ecaterina@yahoo.com

***Abstract* – The paper presents an automatic system for compacting metal, plastic and glass waste from food consumption (boxes or empty cans). The compaction process is found in waste recycling systems. The purpose of this work is to analyze the main stages of designing an electro-pneumatic drive and automation system for a waste compactor used in food packaging, starting with the creation of the specifications document and ending with the development of a control structure in a classic version – control circuits with contacts and relays, or by using programmable logic controllers (PLCs). To design and validate the control circuits, the FLUIDSIM simulation environment was used, and the experimental validation involved building a functional small-scale model of the compaction device and analyzing its operation in laboratory conditions. Additionally, aside from the educational and research goals, which involve proposing a solution and verifying it through numerical simulation and on a small-scale experimental model, the work also aims to integrate the proposed solution into an automated packaging collection equipment within the Deposit-Return System (SGR). Packaging collection machines located in commercial centers do not have compaction modules integrated into their structure, and thus blockages often occur due to the rapid filling of the collection containers. The introduction of compaction modules would significantly reduce the waste volume and transportation costs for the collection centers.**

Cuvinte cheie: *sistem automat, compactare deseuri, automat programabil, diagrame grafcet, fluidSim, simulare. model experimental*

Keywords: *automatic system, metal waste compaction, programable logic controller, grafcet diagrams, fluidSim, simulation, experimental model*

I. INTRODUCTION

Metal is an exhaustible resource. However, it can be recycled endlessly without losing its qualities. Scrap metal is usually aluminum or steel. For example, recycled aluminum can be obtained with 74% to 95% less energy consumption than aluminum obtained through ore processing [1]. Steel can be obtained from empty cans. By recycling metal waste, the ore extraction process and the energy used for extraction and production can be reduced. Moreover, the greenhouse gas emissions, the pollution resulting from these processes, and the impact on the ozone layer are also considerably reduced. Recycling 1 kg of aluminum saves around 8 kg of bauxite, 4 kg of chemicals, and 14kWh of electricity [2].

Regarding the recycling of plastic materials, one of the most important PET waste recyclers in Europe presents the following advantages [3]:

- The production of new resources through PET recycling ensures a reduction in CO2 emissions by almost half compared to the same product obtained from raw materials derived from petroleum;
- Energy consumption is reduced by 30% compared to the energy required in the process of producing PET from virgin material;
- Fuel usage is reduced by up to 75% compared to the energy spent in the production of virgin material.

In the European Union market, with the introduction of the Deposit-Return System (SGR) [4], automated systems for collecting plastic, metal, or glass packaging from food and beverage consumption have been implemented. These machines have been installed in high-traffic areas (shopping centers, airports, etc.) for advertising purposes and to educate the public about the issue of waste recycling.

The main limitation of these machines is that they are not equipped with compaction functions to reduce volume and transportation costs.

This work presents an automatic system for compacting waste, primarily from beverage and food packaging (cans and tins).

The pressing (compacting) process of empty containers is a common function in waste recycling systems [5].

From the perspective of component elements and operation, the metal container compaction device presented as a direct application of pneumatic actuation and control systems can be considered a system where both sequential and parallel/concurrent activities can take place.

The authors have also addressed this research topic in the paper [6] but it was not developed sufficiently.

II. THE DESCRIPTION FOR THE COMPACTION SYSTEM

A. The Structure of the Compaction Device

The component elements of the compaction device are indicated in Fig. 1a.

The compactor consists of three pneumatic cylinders, C1, C2, and C3, along with the functional elements and equipment of such an actuation system (distributors, valves, stroke limiters, compressed air supply, air treatment elements, pressure switches, etc.) [6].

The pressing operation for the empty cans is carried out by pneumatic cylinder C2, which moves vertically (Fig. 1a, 1b). Cylinders C1 and C3 facilitate the complete opening and closing of the container designed to hold the emp-

ty cans during pressing. This container, specifically designed for the application, has a rigid metal parallelepiped structure capable of holding four empty cylindrical metal cans arranged in a single layer.

The empty cans are loaded into the storage container via a transport subsystem. This system includes a conveyor with either continuous or intermittent motion, combined with a gravity-based transfer mechanism (ramp) that allows the cans to roll into the container (Fig. 2).

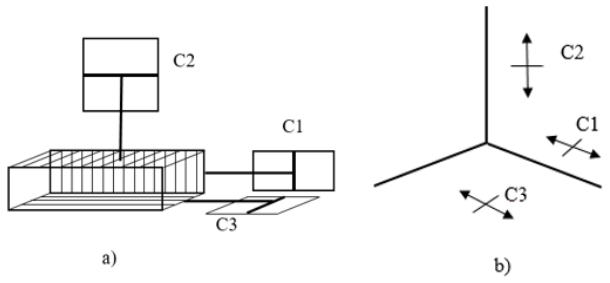

Fig. 1. The structure of the compaction device [6]: a) Representation of the arrangement of the pneumatic cylinders, b) Directions and planes of movement for the three cylinders.

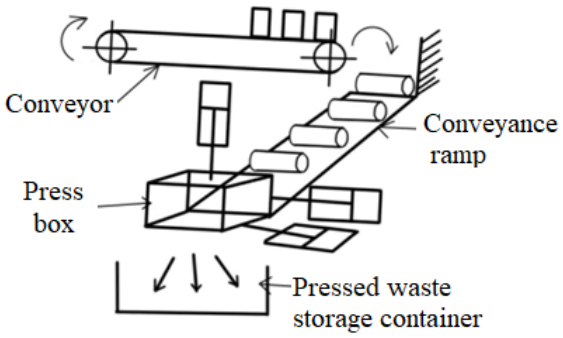

Fig. 2. Explanation of the arrangement of the components of the compaction system. [6]

The container can be dimensioned for a predetermined number of metal cans that are compacted in a complete operating cycle. The conveyor transporting the empty cans can be stopped after the agreed number of cans has been deposited in the pressing container, and restarted after the pressing cycle is completed. This prevents the accumulation of empty metal cans at the end of the transfer devices. The cans on the conveyor can be spaced by separation devices that are part of the conveyor's construction. An automatic counting device placed at the end of the conveyor determines the number of cans compacted during a complete sequence (complete cycle) of operation.

B. The Description of the Operation Protocol

A complete cycle operating scenario can be as follows [6]:

1) The conveyor transports the empty cans to the pressing container. At the end, each can falls freely onto the transfer ramp and rolls into the container – which can hold 4 empty cans. When the conveyor has transported 4 cans, it stops.

2) Cylinder C1 advances – thus, side 1 of the container is closed;

3) Main cylinder C2 advances – the operation of compacting the cans in the container is performed;

4) Cylinder C2 returns;

5) Cylinder C3 returns – its downward vertical movement from its initial position opens the space for ejecting the compacted cans;

6) Cylinder C3 advances – closing side 3 of the container;

7) Cylinder C1 returns – now side 1 of the container opens, and the device is returned to its initial state.

Another cycle can then begin, in the same sequence, after the container is refilled with another 4 empty containers.

The pneumatic actuation circuit diagram is shown in Fig. 3 Pneumatic cylinders C1, C2, and C3 are double-acting, powered from the same energy source. Each cylinder's strokes are provided by a 4/2 distributor with electrical control (solenoid valves). The extreme positions (initial and end-of-stroke) of C1 and C3 are indicated by signals from sensors S1 and S2, respectively S4 and S5. The initial position of the main cylinder C2 (with the rod retracted in the upper position) is signaled by sensor S3, with the return stroke commanded by pressure switch P (pneumo-electric transducer). Generally, the maximum working pressure in the compacting phase (advance stroke) can be adjusted according to the material being pressed.

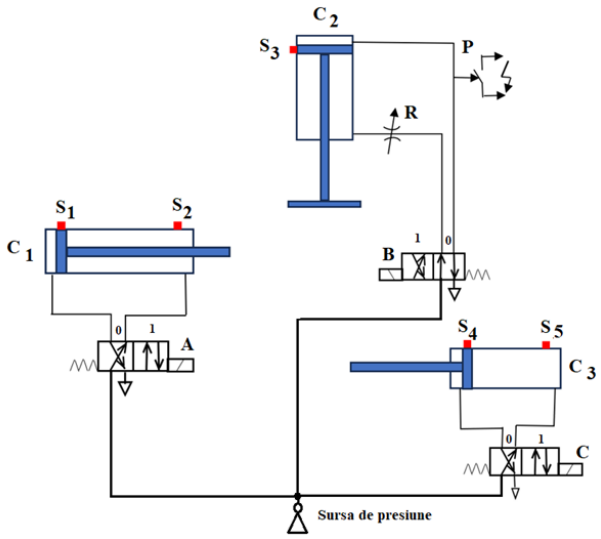

Fig. 3. Pneumatic drive diagram circuit.

In this version, the pneumatic circuit contains only one speed adjustment element for cylinder C2 (pneumatic resistor R). Thus, the piston speed of C2 can be adjusted in both strokes. Other pressure control and adjustment elements can be added later in the circuit, depending on the requirements for the most efficient operation of the entire device.

A contact and relay control circuit version is shown in Fig. 4. This ensures the specified operating sequences.

The notations in Figure 4 have the following meanings:

B1: Start button for the operating cycle;

K1…K5: Coils with associated contacts;

S1…S6: End-of-stroke sensors for the cylinders;

A, B, C: Coils of the pneumatic valves;

P: Pressure relay (pressure switch).

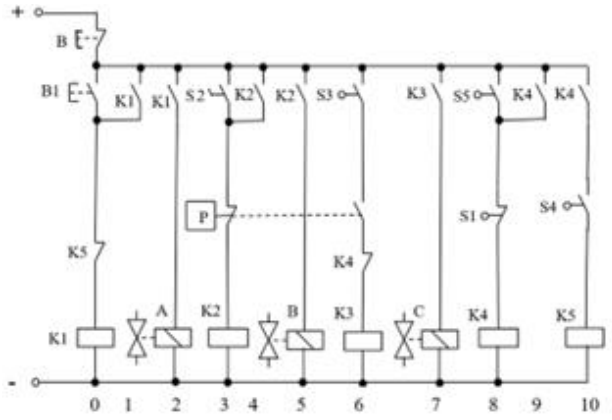

Fig. 4. Contact and relay control circuit diagram of the compaction device.

A detailed explanation of the operation of the diagram in Figure 4 is provided in [6]. A summary of the step-by-step sequential operation is presented in Figure 5.

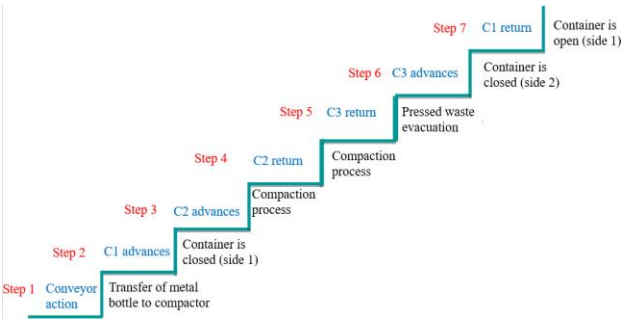

Fig. 5. Description of the sequential staged operation of the compaction system.

C. Dimensioning of pneumatic cylinders

The actuation circuits are supplied by a compressed air generation and conditioning system consisting of a compressor, air lubricator, dehumidifier, and pressure regulator [6].

In this setup, the operating circuit uses a pressure of $p_r = 6 \cdot 10^5$ N/m^2 = 6 daN/mm^2 = 6 bar.

For pneumatic cylinder C1 (Fig. 1), after a comparative analysis of several pneumatically actuated devices and considering that this cylinder performs a relatively short stroke and the weight of the movable vertical wall is not significant, it was determined that the static force it must overcome is Fs_1 = 10daN.

Thus, using the sizing formula:

$$D_{C1}=(15...18)\cdot\sqrt{\frac{Fs}{pr}}=(15...18)\cdot\sqrt{\frac{10}{6}}=19,35...23,22\ \ [mm] \quad (1)$$

A FESTO cylinder of type DSNU-S with a standardized diameter of D_{C1} = 25 mm can be selected [8].

Pneumatic cylinder C2 (Fig. 1) is the primary execution element of the device, responsible for the actual compaction of empty metal cans. The movement of its rod can be performed at a lower speed than that of the other cylinders, considering the specific requirements of the process. For this purpose, the pneumatic actuation circuit includes a pneumatic resistance that enables volumetric speed regulation of the cylinder rod by restricting the compressed air supply flow.

To generate the pressing force and maintain it at a maximum value throughout the technological operation, a force of Fs_2 = 60 daN is considered.

$$D_{C2}=(15...18)\cdot\sqrt{\frac{60}{6}}=43,2...51,84\ \ [mm] \quad (2)$$

A FESTO cylinder of type DSBC, to ISO 15552, with a standardized diameter D_{C2} = 63 mm can be selected [8].

Pneumatic cylinder C3 (Fig. 1) opens side 3 of the pressing chamber after the compaction operation has been completed, performing a linear movement over a stroke equal to the length of the pressing chamber. This action enables the compacted metal cans in the chamber to be discharged into the storage container for compacted waste, driven by the vertical wall.

Although it does not actively participate in the pressing operation, the weight of side 3 of the chamber must be designed to allow the pressing process to occur without deforming the chamber. Therefore, for this cylinder, it is considered that: Fs3 = 20 daN.

Ensure:

$$D_{C3}=(15...18)\cdot\sqrt{\frac{20}{6}}=27,38...32,86\ \ [mm] \quad (3)$$

In this case, a FESTO cylinder of type DSBC, compliant with ISO 15552, can also be selected, but with a standardized diameter of D_{C3} = 40 mm [8].

Table 1 provides a summary of the parameter values corresponding to the pneumatic cylinders used:

TABLE I.
THE MAIN DIMENSIONS OF THE PNEUMATIC CYLINDERS IN THE COMPOSITION OF THE DEVICE

Cylinders type	D_c [mm]	d_t [mm]	s_{max} [mm]	v_{med} [cm/s]
C1- double action	25	8	300	3
C1- double action	63	18	1 - 1500	10
C1- double action	40	10	1 - 1500	4

III. THE MODELING AND SIMULATION OF THE COMPACTION SYSTEM USING FLUIDSIM SOFTWARE

A. *Automatic Control Solutions for the Compaction Device based on Contacts and Relays*

The selected solution was validated by modeling the pneumatic actuation circuit in the FLUIDSIM software and simulating the operation of the control circuit in both step-by-step and continuous cycle modes. The pneumatic actuation circuit is illustrated in Fig. 5, while Fig. 6 depicts the variant of the contact and relay control circuit [6], [7], [8].

In the pneumatic circuit illustrated in Fig. 6, the three cylinders are equipped with magnetic sensors S1, S2, S3, as well as S5 and S6. The active stroke of cylinder C2, responsible for the pressing operation, extends across its entire length. A pressure switch, P, is integrated into the circuit of the active chamber downstream of the pneumatic resistance Rp. This switch deactivates the command for distributor B once the working pressure reaches the preset maximum value, enabling cylinder C2 to return to its initial position. The pneumatic resistance Rp creates a pressure drop in the supply circuit of cylinder C2 and also facilitates speed adjustment for its movement in both directions [6].

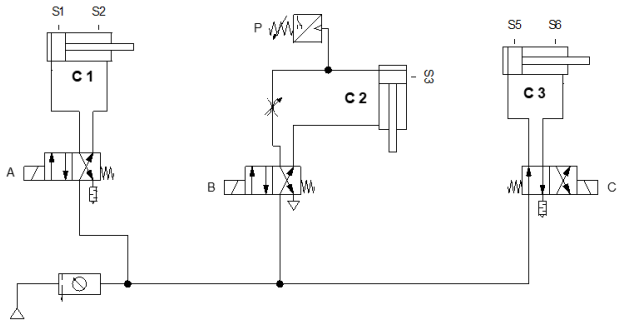

Fig. 6. The pneumatic actuation circuit built in FLUIDSIM.

The control scheme with contacts and relays ensures the sequential operation of the compacting device, according to the proposed scenario [9]. The timing relay RT in circuit 15 temporarily interrupts the power supply to coil K1 in circuit 1, thereby canceling the command of distributor A and returning C1 to its initial state. In the control scheme (Fig.7), the timing of RT is set to 3 time units, but the FLUIDSIM program allows this to be adjusted in accordance with the process specifications [10].

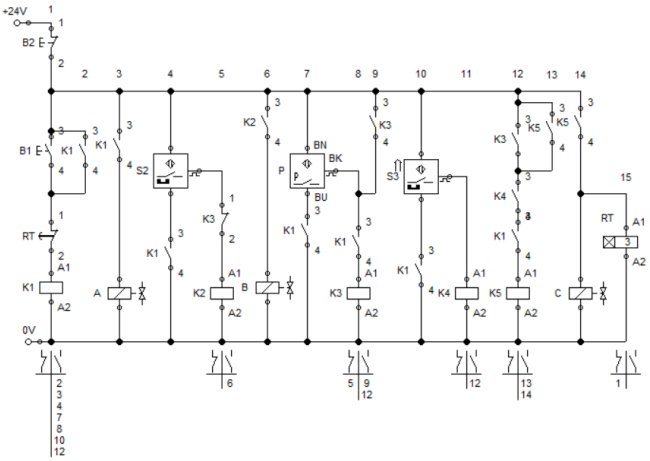

Fig.7. Contact and relay control circuit implemented in FLUIDSIM.

However, there are other solutions based on the proposed sequences, solutions that can lead to the optimization - to some extent - of the operating cycle by the simultaneous movements of some cylinders in the actuator circuit [11], [12]. One such variant is where, after the pressing is done and the main cylinder C2 returns to its initial position, the opening of wall 1 and the closing of the base 3 of the pressing tub are carried out simultaneously (Fig. 8). In this case, the forward stroke of cylinder C3 to the S4 sensor will be executed simultaneously with the return of cylinder C1 to its initial state, to the S1 sensor. This is the so-called "cycle with parallel sequences".

Both the pneumatic circuit diagram and the control schemes created with FLUIDSIM software were verified through both step-by-step simulation and continuous simulation of a complete cycle.

In the two analyzed versions, the duration of the pressing (compacting) operation of empty cans is implicitly established by adjusting the working pressure value of cylinder C2 at which the pressure switch is activated, and which must be correlated with the pressure value of the supply source of the entire circuit. This is the so-called state-based control, knowing that pressure is a state variable of the pneumatic actuator.

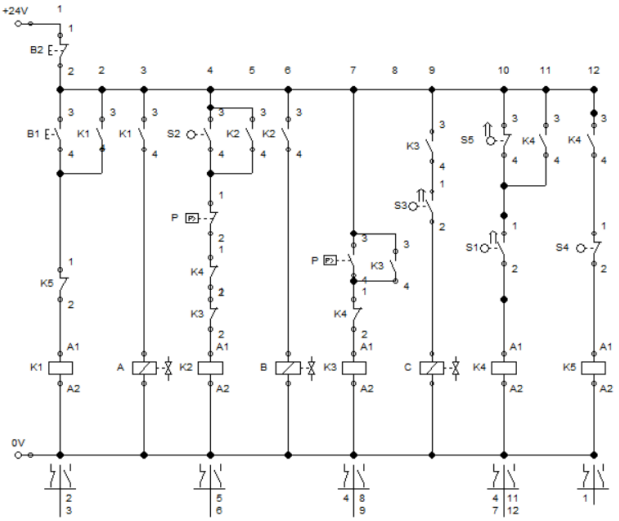

Fig. 8. Control scheme with contracts and relays – the "optimized" version

Another control possibility consists of using a time relay instead of the pressure switch P [6]. Thus, the rest of cylinder C2 at the end of the stroke for performing the pressing can be controlled by setting a time interval during which the coil of distributor B is commanded. After this duration elapses, distributor B is no longer commanded, allowing C2 to return to the initial state, to the end-of-stroke sensor.

This version is shown in Fig. 9. It can be observed that cylinder C2 is now equipped with two end-of-stroke sensors, S3 and S4 (Fig. 11a). The rest of C2 on sensor S4 after performing the pressing operation is timed by the time relay RT which has a normally closed contact with delay to open placed in circuit 4 of the control scheme (Fig. 9).

After the time set on relay RT expires, the RT contact in circuit 4 interrupts the power supply to coil K2 in circuit 4 and, implicitly, to coil B of the distributor.

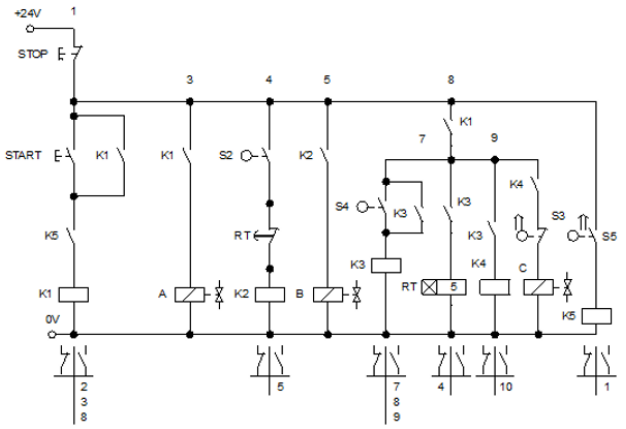

Fig. 9. Explanation for the timing of the main cylinder C2's advance.

In the state diagram corresponding to the operating cycle, the states (activated / deactivated) of the three distributors A, B, and C are also indicated. (Fig. 10).

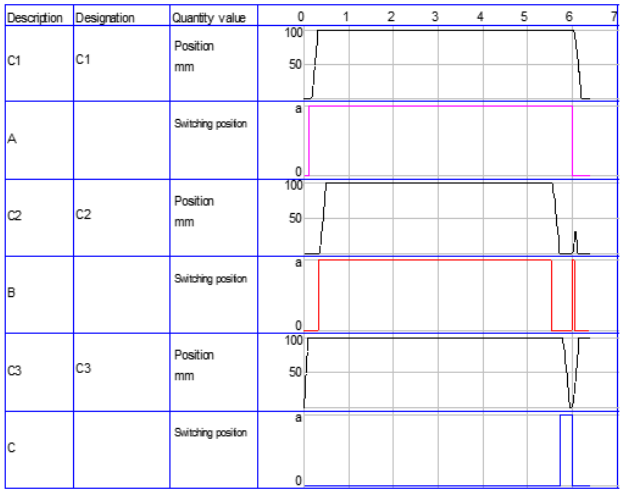

Fig. 10. The state diagram during an operating cycle for the variation presented in Fig. 9.

B. The Automatic Control of the Compacting Device with PLC

The FLUISIM program easily allows the modification of the control architecture configuration of the pneumatic actuator circuits, from the basic variant - control with contacts and relays - to a programmable controller (PLC - Programmable Logic Controller) structure [14], following the defining aspects of creating a GRAFCET structure [15].

Thus, in Fig. 11 is presented a structure of the pneumatic actuator circuit of the three cylinders C1, C2, and C3, controlled by the same distributors as in the previous variants where the operating scenario is ensured by a programmable controller.

The programmable controller (in the GRAFCET IN / OUT program) is equipped with two process communication ports (Fig. 11 b). The IN port connects the six sensors that equip cylinders C1, C2, and C3, as well as the START button - B1 for commanding an operating cycle.

The OUT port connects the coils of the distributors A, B, and C that control the cylinders.

The IN / OUT structure and the level I GRAFCET in images 11 b) and 11 c) are created without considering the timing of cylinder C2 at the end of the stroke when performing the pressing operation of empty boxes.

FLUIDSIM allows inserting timers in the GRAFCET IN / OUT component that allow evolution to another state after fulfilling the conditions (introduced in the model through transitions) ONLY after the time interval implemented by the timers elapses.

Proceeding exactly as in the contact and relay control version, it was introduced a timing of cylinder C2 at the end of the stroke (S4 = 1), associated with the duration of the pressing operation (Fig. 11 d).

The resulting GRAFCET (Fig. 11 d) contains another state (state 4), identical to state 3, in which the process remains "anchored" until the timing of the transition elapses. In other words, cylinder C2 retracts to its initial position not immediately upon reaching the end of the stroke, but only after the pressing has been executed.

In Fig. 12 is presented the resulting state diagram from the simulation in FLUIDSIM.

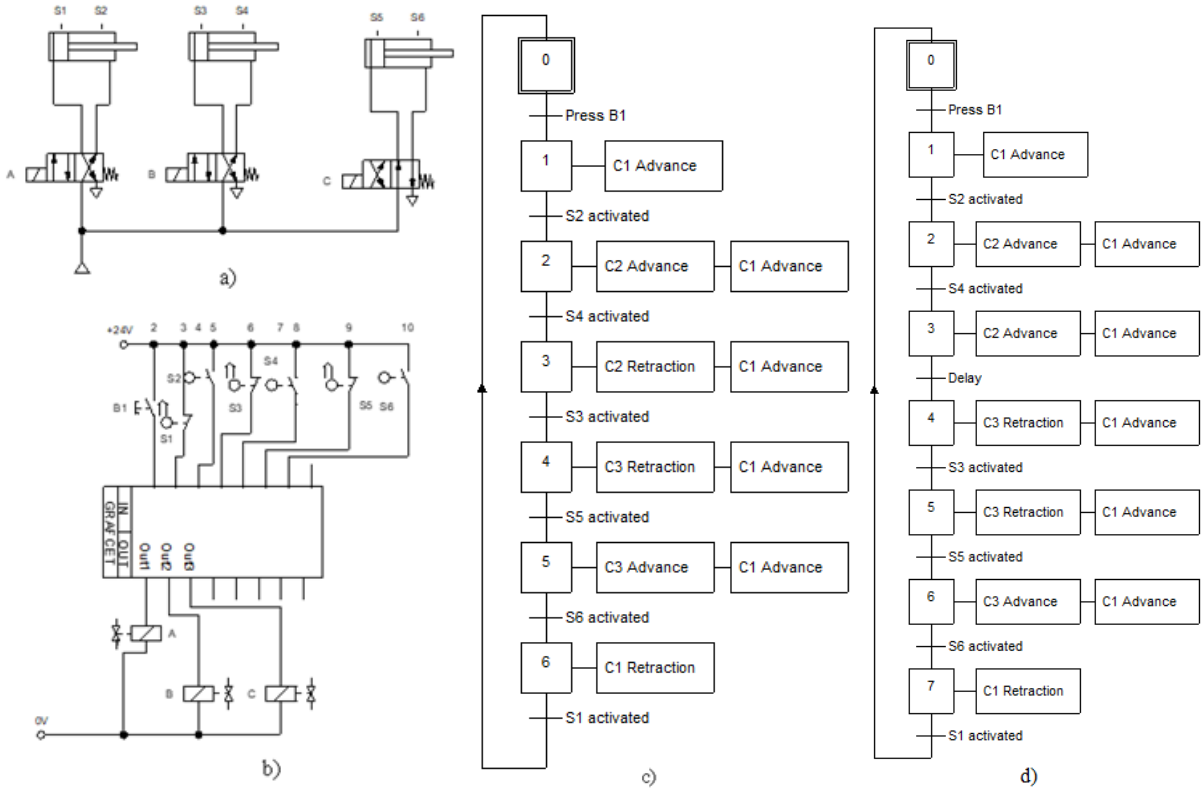

Fig. 11. The control structure with a PLC for the pneumatic actuation: a) Pneumatic actuator circuit; b) GRAFCET IN / OUT configuration; c) GRAFCET corresponding to the sequential cycle of the three cylinders; d) control structure of the compacting device with a timed GRAFCET model.

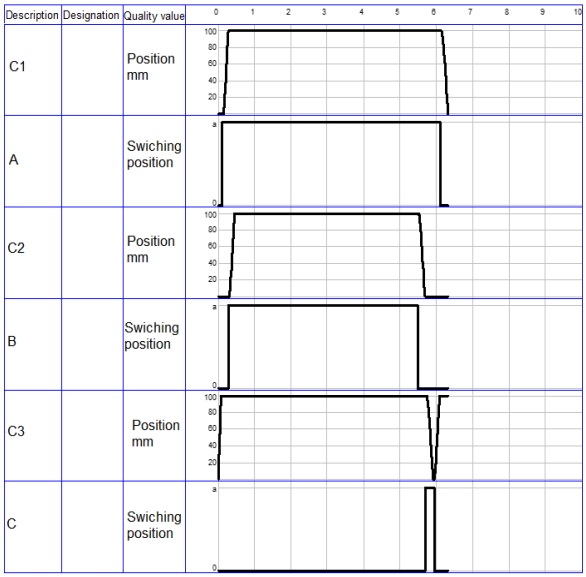

Fig.12. The state diagram corresponding to an operating cycle of the compactor.

The cylinder C2 remains at the end of the stroke on sensor S4 for an interval equal to 5 time units (value assigned to the timing of the transition between states 3 and 4 - Fig. 12) and only then, after distributor B is deactivated, it returns to the initial state.

IV. Software development for PLC

Both the simplification of the hardware and the use of as few components as possible, as well as the ease of programming the system, were key aspects considered during the design of the control system. [16], [17], [18], [19]

For the automatic control of the compaction process, it is proposed to use an Easy 719-AC-RC PLC, manufactured by EATON [20].

The Eaton Easy AC-RC-719 programmable logic controller was chosen due to the features it offers, namely: compact size; direct connection to the 230 V power supply; presence of a keyboard and screen; 6 outputs; and 14 inputs.

The Eaton Easy 719 is a programmable logic controller with built-in logic, a timer, counter, stopwatch, and arithmetic functions. It performs multiple tasks across various engineering fields.

The number of inputs and outputs can be expanded up to a maximum of 24 inputs and 16 outputs, with the possibility of connecting a single extension device.

The circuit diagrams are connected using LADDER diagrams, and each element is entered directly through an easy-to-use display.

Figure 12 shows the wiring diagram for connecting the PLC to the pneumatic drive.

For the development of the PLC program, it was used a dedicated software for Eaton Easy PLCs, called Easy Soft [21].

EASY-SOFT is a PC program that allows the creation, storage, simulation, and documentation of Easy connection diagrams, which can then be transferred to an Easy device prepared for operation

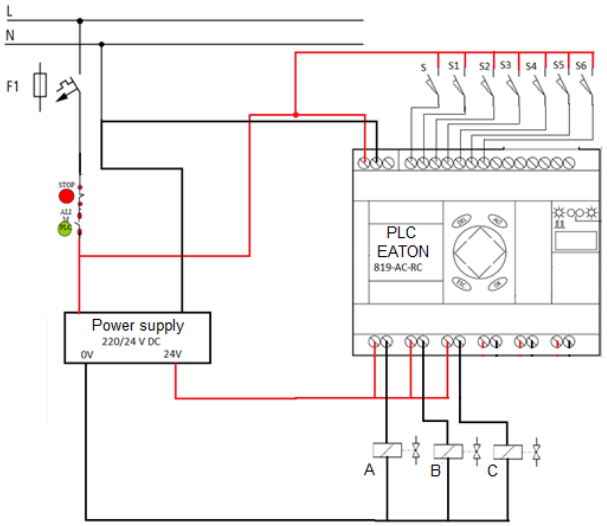

Fig. 13. Electrical wiring diagram of the PLC connections.

The program developed is shown in Figure 14 and represents the implementation of the timed version according to the GRAFCET diagram in Figure 11 d.

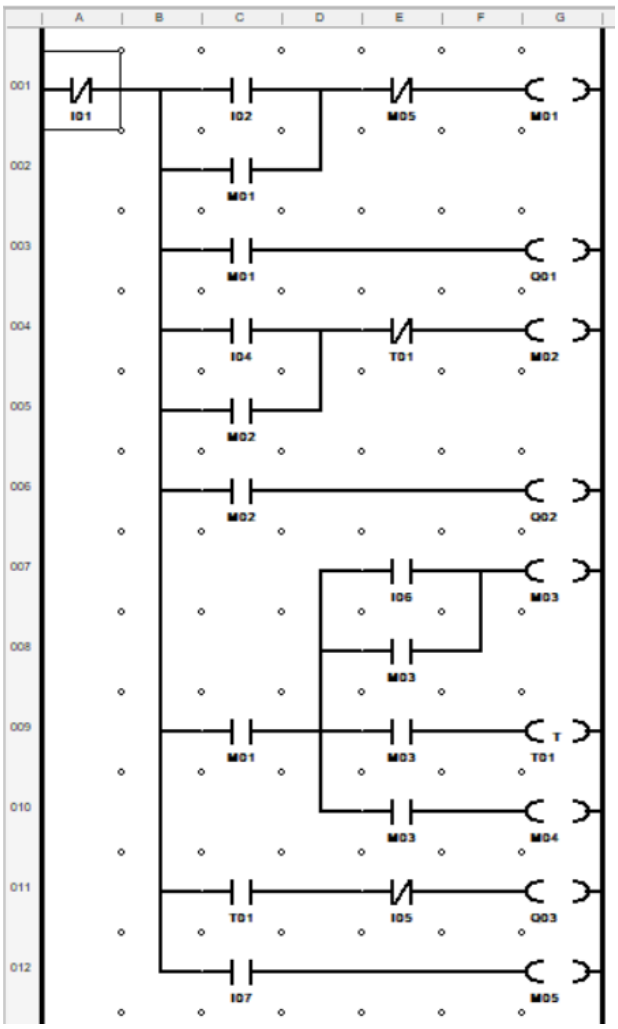

Fig. 14. Program developed for the PLC.

Notation meaning:

- I01 – input associated with sensor S;

- I02...I07 – inputs associated with sensors S1...S6;
- Q01...Q03 – outputs associated with coils A…C;
- M01...M05 – markers (elements for storing commands);
- T01 – timer element.

The correct operation of the program was verified through simulation. This feature is provided by the Easy Soft software in an intuitive and suggestive manner.

V. Development Of A Small-Scale Experimental Model

To experimentally validate the proposed solution for the metal waste compaction device, it was created a small-scale experimental model.

For the purpose of optimization and cost reduction, a solution was designed and implemented, featuring a minimal structure, while still respecting the basic function.

Simplifying considerations:

- The number of containers compacted in one working cycle is minimized;
- The feeding process for the compaction device is done manually;
- The pneumatic actuation for the compaction process includes two pneumatic cylinders;
- The control of the compaction process is done in a traditional manner using buttons for each step of the process.

The experimental model, shown in Figure 15, includes the following basic elements: 1. Collection container for compacted boxes; 2. Pneumatic cylinder for compacted box evacuation; 3. Pneumatic circuit distributor for compacted box evacuation; 4. Compaction device; 5. Control panel; 6. Pneumatic cylinder for compaction; 7. Pneumatic circuit distributor for box compaction; 8. DC power supply for powering the distributors; 9. Compressed air source (compressor, air preparation unit).

The pneumatic part of the experimental model consists of the pressure source, the compressed air storage tank, the air preparation unit (GPA), two distributors for directing the pneumatic fluid, two pneumatic cylinders, as well as the apparatus for regulating the pneumatic energy. These pneumatic components are produced by the company Festo [22].

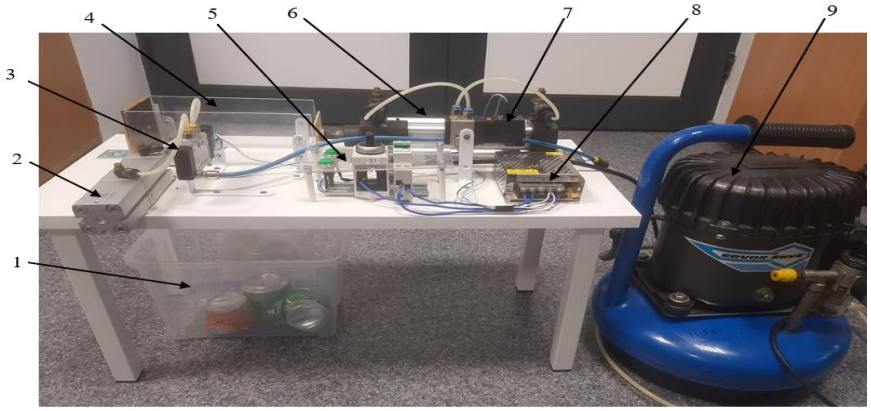

Fig. 15. Experimental model of the pneumatic compaction system.

After constructing the experimental model, its functionality was tested. Figure 16 shows an image taken during the process of compacting a metal waste resulting from the consumption of a beverage.

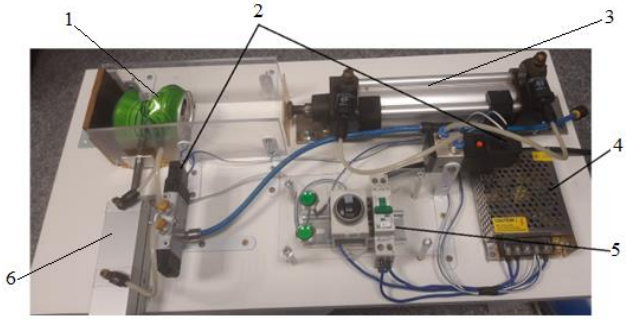

Fig. 16. An image from the compacting process: 1 - compacted container; 2 - distributors; 3 - cylinder for compaction; 4 - DC power supply; 5 - control panel; 6 - cylinder for ejecting the compacted waste.

The verification of the functioning of the experimental model was also done through the acquisition of the command signals. Thus, the graph in figure 17 shows the supply voltage signals for the valves that control the two pneumatic cylinders. The signal on the CH1 channel represents the supply voltage for the valve corresponding to the compaction cylinder, and the one on the CH2 channel for the valve of the compacted box discharge cylinder.

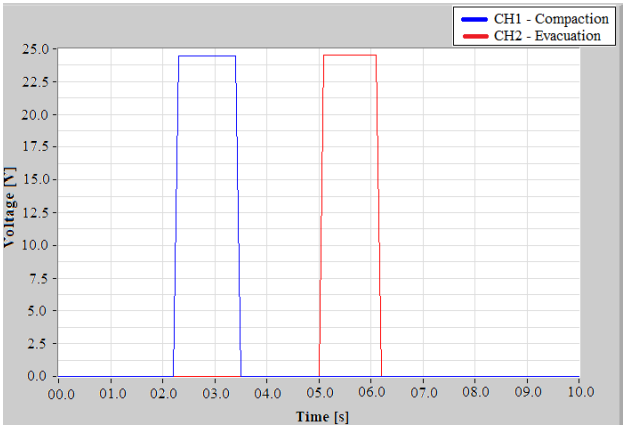

Fig. 17. Control signal diagram for pneumatic actuation.

As can be seen from the signal diagram, the time required to execute each operation within the compaction process is approximately 1.5 seconds. This can be modified by adjusting the execution speed of the pneumatic cylinders.

VI. CONCLUSIONS

The compacting device discussed in this paper can be utilized in residential settings, restaurants, specialized companies, or as part of larger waste recycling systems. Currently, the automated waste collection centers for glass bottles, metal cans, and plastic bottles, recently introduced in Romanian supermarkets, lack compacting capabilities. This device could be modified and integrated into such centers. Its inclusion would greatly decrease the volume of collected waste, thereby reducing transportation costs to regional recycling facilities.

As a result of the comparative analysis between the main types and structures of drives within electromechanical systems, it was concluded that pneumatic actuation meets the requirements imposed by the operation of various devices in high-cycle, repetitive automatic processes.

To properly configure the pneumatic actuation and automation circuit options, it is essential to use an initial stage involving modeling and simulation software. This approach enables users to identify the simplest and most efficient solutions for implementation. One such program, widely used in both educational settings and industrial applications, is FLUIDSIM.

In this paper, FLUIDSIM was utilized to design various pneumatic actuation and automation schemes for the compacting device. After configuring the circuits by connecting components available in the program's libraries, the proposed solutions were validated through step-by-step cycle simulations followed by continuous cycle simulations.

The authors used the FLUIDSIM software for the simulation of other automatic systems [6], [11], [12], [13], the validation of the simulations being also done experimentally on small-scale physical models.

The solutions found through the simulation of several drive circuit variants in FLUIDSIM led to the creation of a functional laboratory model, with a simplified structure compared to the initially designed one, but which meets the intended purpose very well.

Future research objectives:

- Completing the experimental model by adding additional drive modules;
- Automating the process by adding the PLC presented with the already developed program and equipping the execution elements with various types of position sensors;
- Integrating the device into a more complex electromechanical system, which would include an automatic system for feeding the compactor with empty cans and an automatic system for collecting the waste resulting from the compaction process.

ACKNOWLEDGMENT

Source of research funding in this article: Research program financed by the University of Craiova.

Contribution of authors:
First author – 40%
First coauthor – 30%
Second coauthor – 20%
Third coauthor -10%

Received on September 5, 2024
Editorial Approval on November 25, 2024

REFERENCES

[1] P. de Sa and J. Korinek, "Resource efficiency, the circular economy, sustainable materials management and trade in metals and minerals", *OECD Trade Policy Papers*, No. 245, OECD Publishing, Paris, 2021.

[2] M.A. Reuter, I.V. Kojo and O. Oyj, "Challenges of metals recycling", *Materia*, 2/2012, pp. 50-57.

[3] *** https://www.green-tech-global.com/ro/reducerea-co2

[4] *** https://returosgr.ro/en

[5] I. H. Siahaan and O. Soegihardjo, "Sustainability design of press machine for waste plastic bottle with electric motor" *IOP Conference Series: Materials Science and Engineering*, Volume 1034, 2021 [2nd International Conference on Mechanical Engineering Research and Application (iCOMERA 2020) 7th–9th October 2020, Malang, Indonesia].

[6] I.L. Alboteanu, M.A. Drighiciu, E.M. Drighiciu, "Automatic System for Compacting Metal Waste" *2024 International Conference on Applied and Theoretical Electricity (ICATE)*, 24-26 Oct. 2024, pp. 1-6

[7] I. O. Suryani, C. I. S. Nadia, D. S. Sinugroho and F. Triawan, "Component design concept of hydraulic gear pressing machine for plastic bottle waste recycle", *IOP Conference Series: Materials Science and Engineering*, Volume 1098, 2021, [the 5th Annual Applied Science and Engineering Conference (AASEC 2020)].

[8] *** Festo (n.d.). "Pneumatic Automation Solutions. Retrieved from Festo".

[9] *** Festo, "FluidSIM Pneumatics", User guide.

[10] R. Cojocaru, P. Bocănete, D. Deleanu, C. Frățilă, T. Axinte and M. Diaconu, "Analysis of pneumatic circuits with FluidSim", *"Hydraulica" Magazine of Hydraulics, Pneumatics, Tribology, Ecology, Sensorics, Mechatronics*, no.2/2021, pp. 70-75.

[11] L. Alboteanu, "Modeling an automatic processing station using FluidSim software", *"Hydraulica" Magazine of Hydraulics, Pneumatics, Tribology, Ecology, Sensorics, Mechatronics*, no.3/2017, pp. 27-30.

[12] L. Alboteanu, "Automatic system for handling fragile objects", *"Hydraulica" Magazine of Hydraulics, Pneumatics, Tribology, Ecology, Sensorics, Mechatronics*, no.4/2020, pp. 26-32.

[13] L. Alboteanu, G. Manolea and F. Ravigan, "Automatic sorting and handling station actuated by pneumatic drive", *Annals of the University of Craiova-Electrical Engineering Serie*s, No 2, 2018, pp. 63-70.

[14] R. Escobar, "From relays to microcontrollers: The adoption of technology in operant research", *Mexican Journal of Behavior Analysis*, vol. 40, no. 2/2014, pp. 127-153

[15] N. Soriya, "GRAFCET and Ladder Diagram", *Industrial Electronic and Control*, Topic 9, pp. 24.

[16] O. T. Adenuga and K. Mpofu, "Control system for electro-hydraulic synchronization on RBPT." *Procedia CIRP* no. 17, 2014, pp. 835 – 840.

[17] H. Wang, "Design of PLC-based hydraulic system for workpiece turnover." *Procedia Engineering* 15/2015, pp. 122-126.

[18] R. Singh, R. H. and Verma, "Development of PLC-based controller for pneumatic pressing machine in engine-bearing manufacturing plant", *Procedia Computer Science* no.125 /2018, pp. 449–458.

[19] K. Sudeep and D. R. Sridhar, "PLC based pneumatic punching machine," *Journal of Mechanical Engineering and Automation*, 2015,Vol 5(3B), pp. 76-80.

[20] ***https://www.eaton.com/us/en-us/catalog/machinery-controls/easy-programmable-relays.html

[21] *** https://www.eaton.com/ro/en-gb/catalog/industrial-control--drives--automation---sensors/easysoft-software.html

[22] *** https://www.festo.com/ro/ro/

DOI: 10.52846/AUCEE.2024.10

Simulations and Tests Regarding the Operation of Air Heaters for Industrial Buildings

Monica-Adela Enache*, Elena-Mihaela Enache† and Mara Pauliuc†

* University of Craiova/ Faculty of Electrical Engineering, Craiova, Romania, menache@em.ucv.ro

† "Ion Mincu" University/Faculty of Architecture, Bucarest, Romania, elena.enache2305@gmail.com

***Abstract* - This paper presents a series of simulations for the operation of a reluctance synchronous motor with continuous rotation (RSM), used for air heaters heating industrial buildings. The introduction aims at presenting the domain we analyze. On this occasion, several possibilities for mounting air heaters for industrial buildings are specified. Their operating methods are specified, with emphasis on the case of the reluctance synchronous motors. The mathematical model of these motors, written in the two axes theory, is detailed below; the significance of the quantities used is specified. With the help of this model, a Matlab program was carried out, for simulating the dynamic regimes, specific to the driving motor of air heaters. The paper presents a series of simulations, obtained by means of this program. The simulations regard a fault situation, materialized in an accidental decrease of the motor supply voltage. The graphs obtained refer to the main electrical, mechanical and magnetic quantities specific to the motor. They are accompanied by several relevant conclusions that emphasize the behavior of the motor in the analyzed dynamic regime. The following aspects are regarded: the evolution of the operation point, the influence on the phase current, the influence on the magnetization flux and the rotor speed. These characteristics were experimentally confirmed (indirectly) by emphasizing, in steady state, the evolution of the phase current for the initial and fault cases. The paper ends with references, organized in the order of citations.**

Cuvinte cheie: *cladiri industriale, aeroterme, motor sincron cu reluctanta variabila, model matematic, simulari, incercari.*

Keywords: *industrial buildings, air heaters, reluctance synchronous motor, mathematical model, simulations, tests.*

I. INTRODUCTION

The problem of disturbances that affect the operation of driving systems endowed with special motors is widely developed in the specialized literature.

Thus, electromagnetic compatibility issues are approached in conferences dedicated to these issues [1], [2], [3], energy quality issues are presented in specialized journals [4], [5], [6] or ways of measuring disturbances generated by different sources are emphasized [7], [8], [9].

This paper aims at analyzing a voltage disturbance situation for the operation of a RSM driving an air heater used in an industrial building.

Air heater is a high-performance heating device, which can heat an industrial space, in a relatively short time. It can be controlled by using a thermostat.

Air heaters can be mounted:

- on a side wall (Fig. 1);

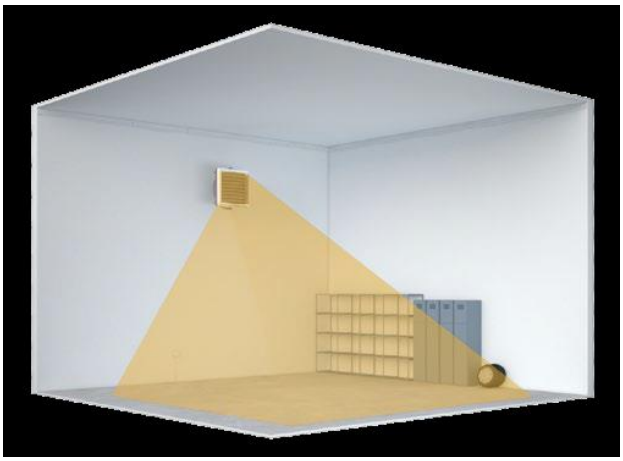

Fig. 1. Wall mounting [10].

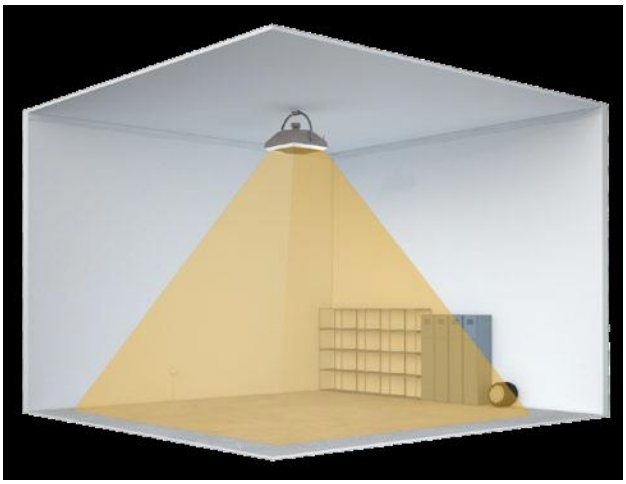

Fig. 2. Ceiling mounting [10].

- on the ceiling (Fig. 2).

The air heater produces hot air that must be distributed throughout the building space.

The air is drawn in by a fan. It has an optimized profile and the increase in the surface area of the blades ensures silent operation and low operating costs.

The fan is, in its turn, driven by an electric motor. This motor is generally a three-phase one, in case of industrial buildings.

Moreover, in order to avoid sparks and, therefore, possible explosions, alternating current motors are used.

The most recent version of such motors, used in industrial ventilation systems, is the reluctance synchronous one.

A particular operation regime of such motor is proposed for analysis below.

II. MATHEMATICAL MODEL

In order to carry out the simulations, the mathematical model of RSM, detailed in [11], was used.

The model, without considering the saturation, consists in five equations, the last one being the motion one. Their matrix form is presented in (1); this form is easy to implement in a Matlab computation program.

$$\begin{bmatrix} L_d & 0 & L_{md} & 0 & 0 \\ 0 & L_q & 0 & L_{mq} & 0 \\ L_{md} & 0 & L_D & 0 & 0 \\ 0 & L_{mq} & 0 & L_Q & 0 \\ 0 & 0 & 0 & 0 & \frac{J}{p} \end{bmatrix} \cdot \frac{d}{dt} \begin{bmatrix} i_d \\ i_q \\ i_D \\ i_Q \\ \omega \end{bmatrix} = \tag{1}$$

$$= \begin{bmatrix} u_d - R_s i_d + \omega L_q i_q + \omega L_{mq} i_Q \\ u_q - R_s i_q - \omega L_d i_d - \omega L_{md} i_D \\ - R_D i_D \\ - R_Q i_Q \\ \frac{3}{2} p\left(L_d i_d i_q + L_{md} i_D i_q - L_q i_q i_d - L_{mq} i_Q i_d\right) - m_r \end{bmatrix}$$

The notations used have the following meanings:

- u_d, u_q - the stator voltage components in the two axes theory;

- i_d, i_q - the components of the stator current in the two axes theory;

- i_D, i_Q - the components of the rotor current in the two axes theory;

- ω - rotor angular speed;

- R_s - stator resistance;

- R_D, R_Q - the rotor resistance components in the two axes theory;

- L_d, L_q - the stator inductance components in the two axes theory;

- L_{md}, L_{mq} - the components of the magnetization inductance in the two axes theory;

- p - the number of pole pairs;

- J - the inertia moment;

- m_r - the resistant torque.

III. SIMULATIONS

A Matlab program was carried out by means of the mathematical model presented above, for analyzing the operation of the RSM in a dynamic state. Thus, two operation situations, affected by external disturbances, have been simulated (Fig. 3); these disturbances were applied after an interval of 0.5 s from the moment of starting by direct coupling at the electrical network.

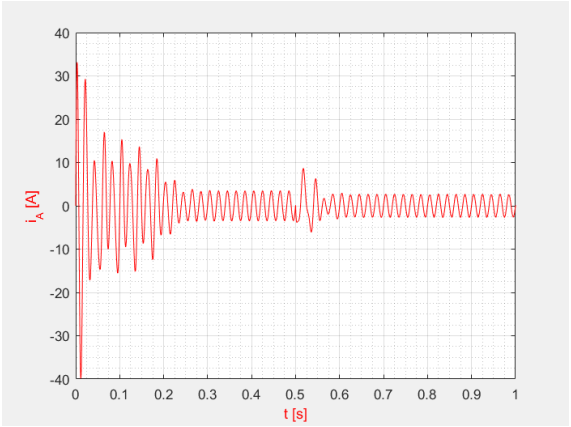

a)

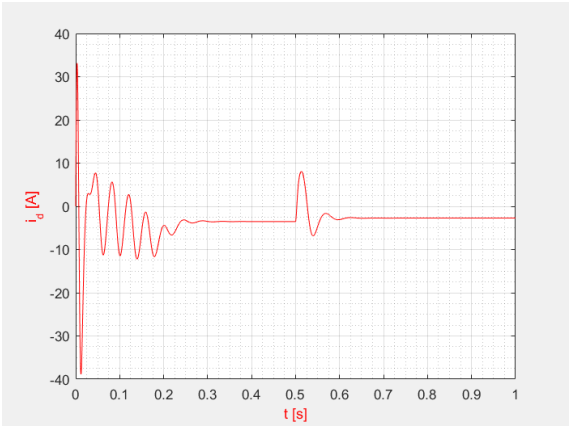

b)

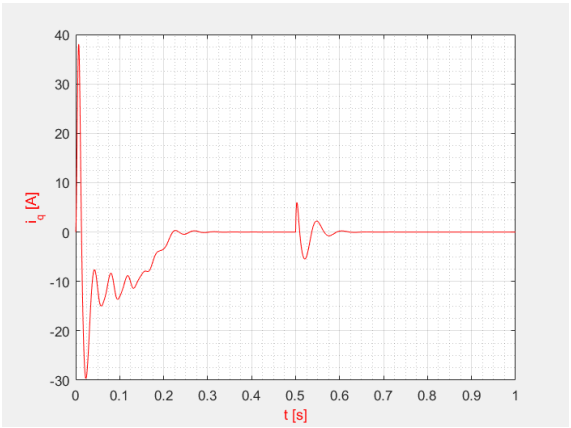

c)

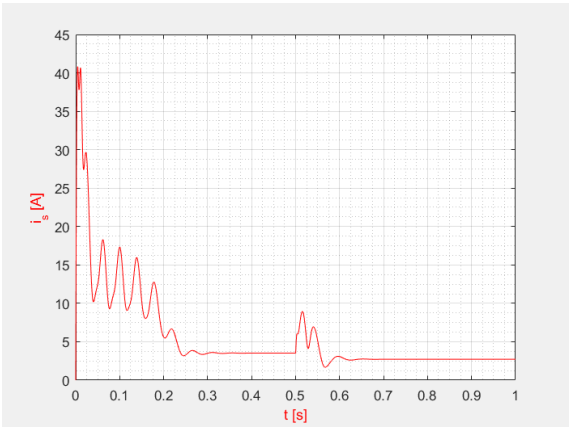

d)

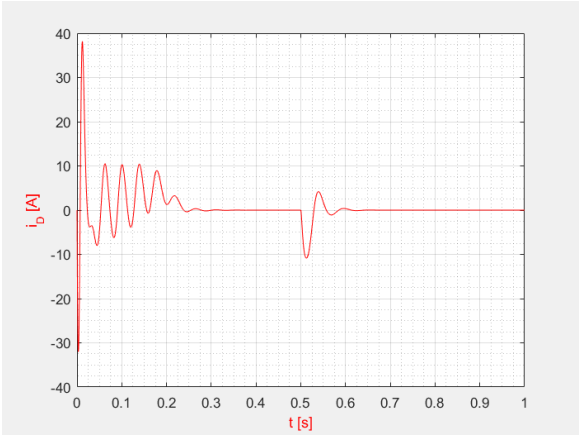
i_D [A]
t [s]

e)

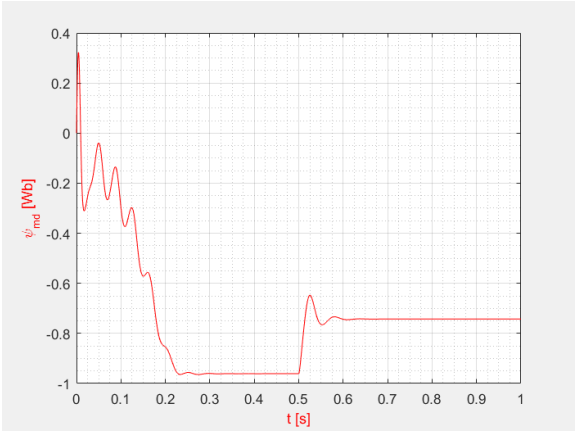
ψ_md [Wb]
t [s]

i)

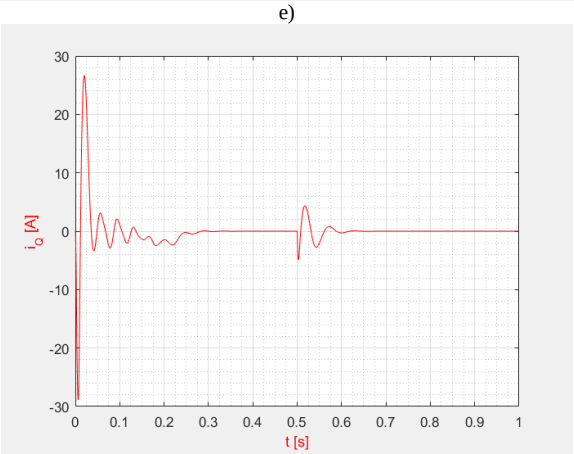
i_Q [A]
t [s]

f)

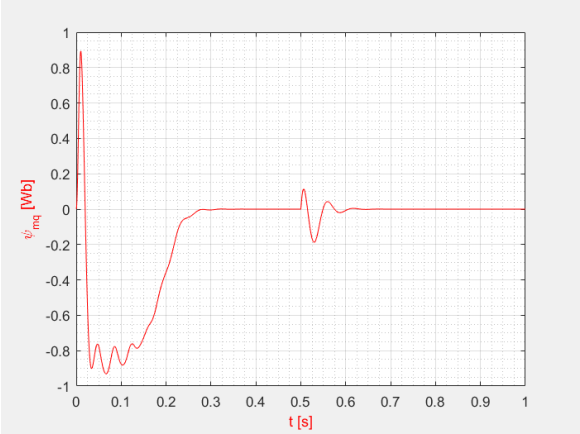
ψ_mq [Wb]
t [s]

j)

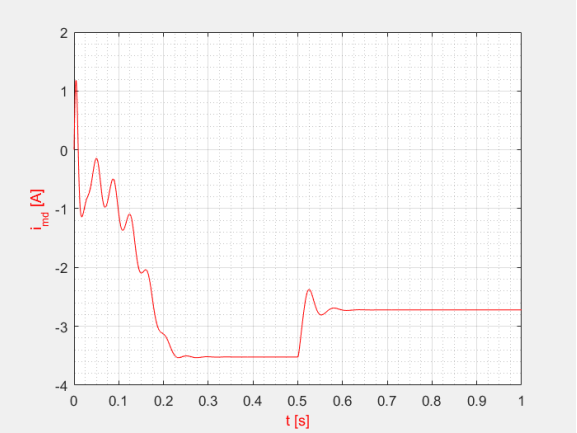
i_md [A]
t [s]

g)

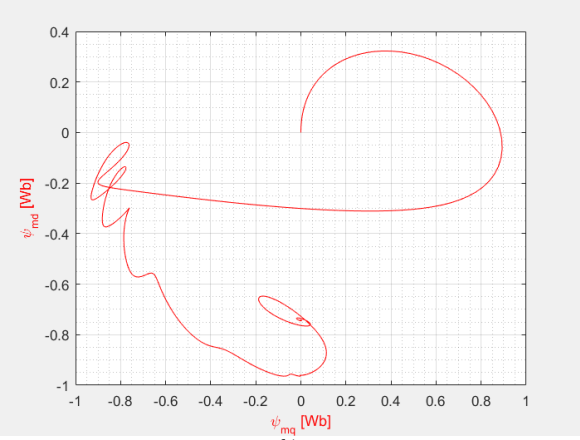
ψ_md [Wb]
ψ_mq [Wb]

k)

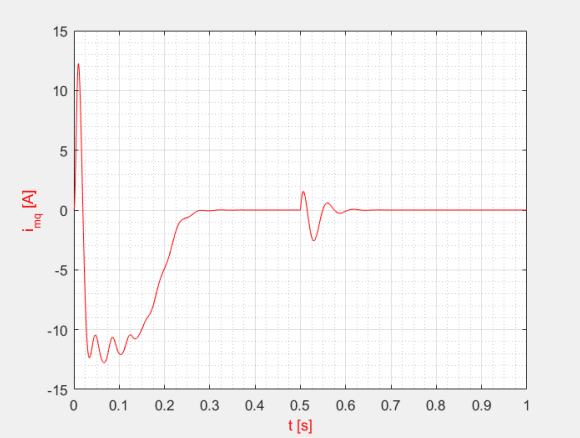
i_mq [A]
t [s]

h)

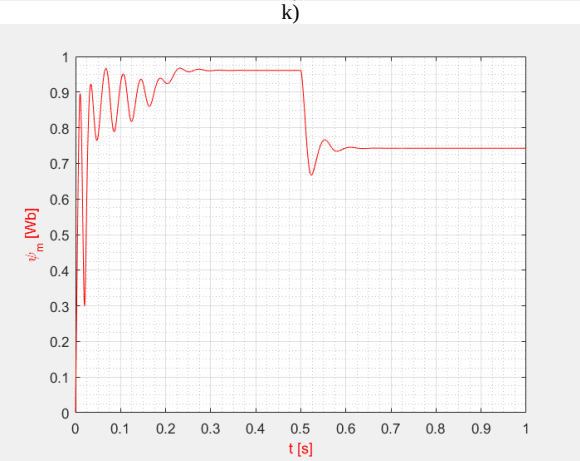
ψ_m [Wb]
t [s]

l)

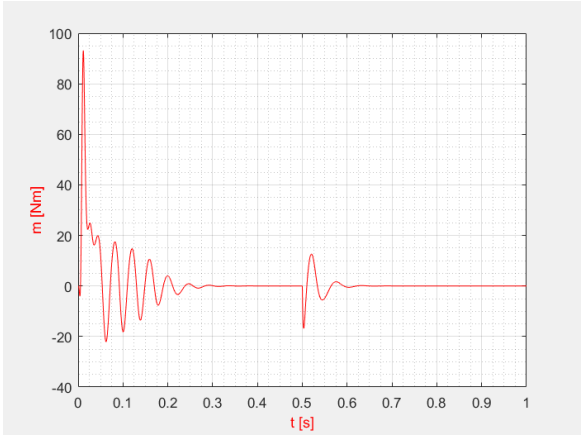

m)

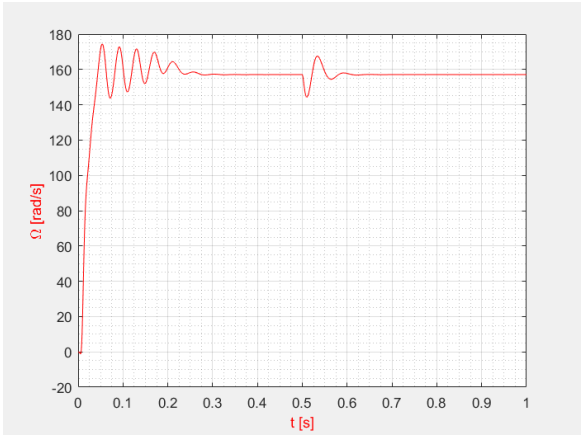

n)

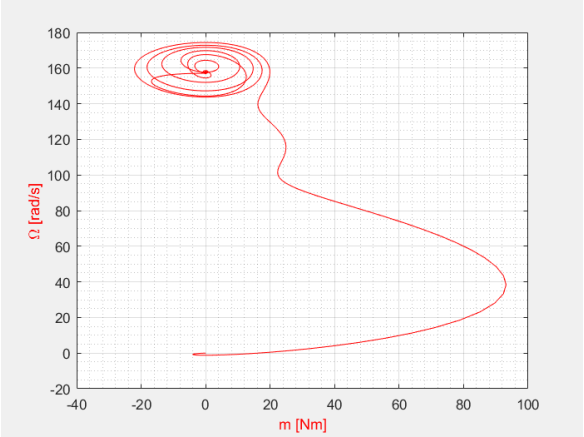

o)

Fig. 3. The characteristics obtained for the case of the decrease of the supply voltage value to 170 V, after 0.5 s from the no-load starting.

The situation refer to the decrease of the supply voltage value (Fig. 3 - the voltage decreases from the initial value of 220 V, down to 170 V);

The simulations were carried out for a motor rated as follows:

R_s = 3.77 Ω, R_D = 1.5 Ω, R_Q = 4.5 Ω, $L_{s\sigma}$ = 0.0081 H, $L_{D\sigma}$ = 0.0059 H, $L_{Q\sigma}$ = 0.0067 H, L_d=0.281 H, L_q=0.081 H; U = 220 V, p = 2, J=0.008 kg.m^2.

IV. Experimental Determinations

The electrical diagram of the measurement system is shown in figure 4.

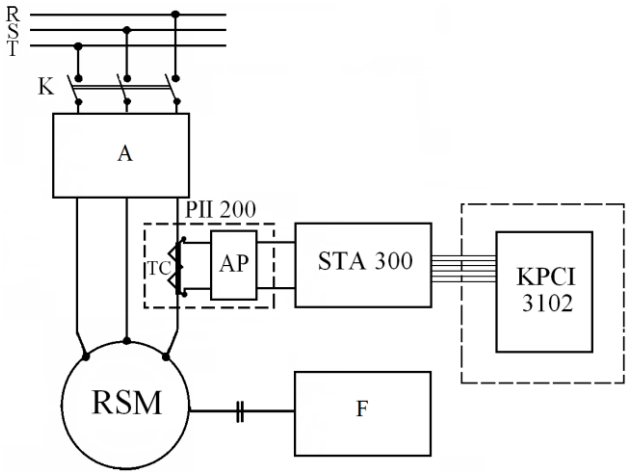

Fig. 4. Electrical diagram.

The meanings of the notations used are as follows:

- RSM – reluctance synchronous motor [11];
- A – autotransformer;
- F – fan;
- PII 200 - current transformer with adaptation block;
- STA 300 - connection block;
- KPCI 3102 - data acquisition board.

The motor used has a specially constructed rotor [12].

The rotor shaft is detailed in Fig. 5.

Its parameters are those used to obtain the simulations detailed previously.

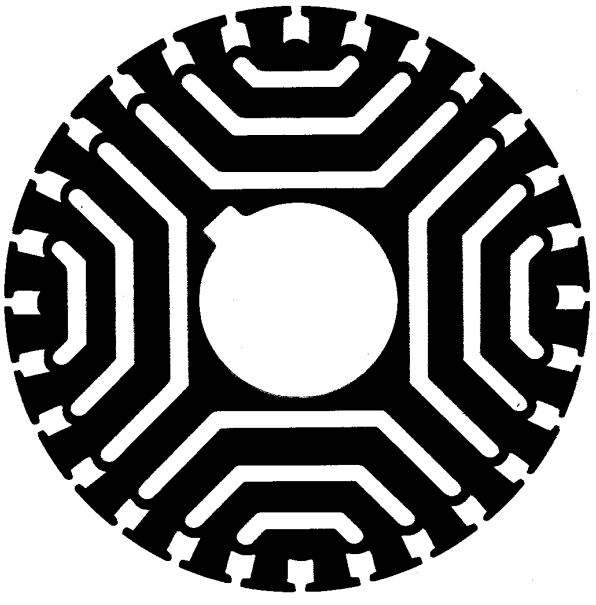

Fig. 5. The motor rotor shaft.

The experiments consisted in acquiring the current variations for a steady-state of the RSM, for two concrete situations:

- the steady-state operation at 220 V (Fig. 6);

- the steady-state operation at 170 V (Fig. 7).

Data were acquired by means of a data acquisition board, having a sampling frequency of 100 kHz [13].

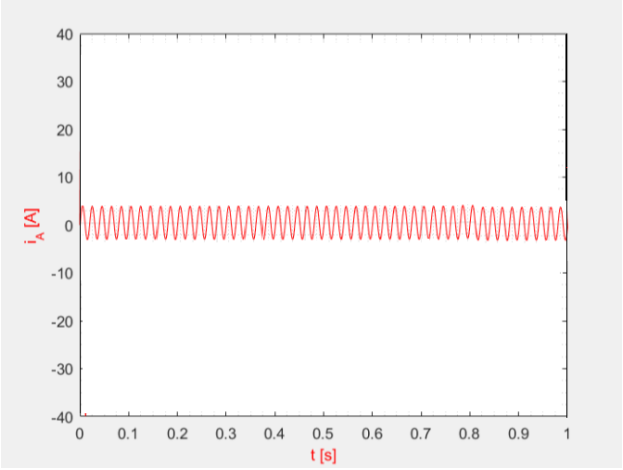

Fig. 6. The variation of the phase current, in case of steady-state operation, at 220 V.

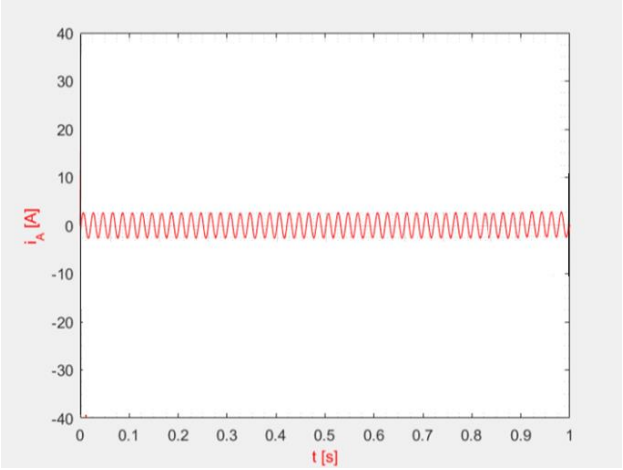

Fig. 7. The variation of the phase current, in case of steady-state operation, at 170 V.

Comparing these results with those depicted in Fig. 3.a (zone 0.3-0.5 s and zone 0.7-1 s), it is found that they are almost identical, which confirms the validity of the simulations (at least in steady state).

V. Conclusions

This paper presents a series of simulations that emphasize the dynamic regimes of RSM for industrial air heaters, in case of the supply voltage decrease.

General conclusion:

- the evolution of the operation point is suggestively visualized, especially in coordinates $\Omega = f(m)$.

Following the analysis of the simulations presented above, particular conclusions were obtained.

In the case of a decrease of the supply voltage value:

- a decrease in the voltage value leads to a decrease in the phase current;

- a decrease of the current also leads to a decrease in the magnetization flux;

- rotor speed is not affected.

Acknowledgment

Source of research funding in this article: Research program of the Electrical Engineering Faculty Craiova and the Faculty of Architecture Bucharest (financed by the University of Craiova).

Contribution of authors:
First author – 55 %;
First coauthor – 25 %;
Second coauthor – 20 %.

Received on September 17, 2024
Editorial Approval on December 2, 2024

References

[1] A. David, M. Tiemann, N. Haussmann, S. Stroka, M. Clemens, and B. Schmuelling, "Electromagnetic compatibility evaluation of wireless charging systems for public spaces: wireless power transfer for taxis", *IEEE Industry Applications Magazine*, Vol. 30, Issue: 1, pp. 59-67, Jan.-Feb. 2024.

[2] C. Liu, "Electromagnetic compatibility design of reinforced LCD", *2023 International Conference on Computer Science and Automation Technology (CSAT)*, Shanghai, China, 2023, pp. 320-323.

[3] S. Gadug, and B. Deshpande, "Assessing the impact of multipath propagation on electromagnetic compatibility of network nodes", *2nd International Conference on Futuristic Technologies (INCOFT)*, Belagavi, Karnataka, India, 2023, pp. 1-5.

[4] T. Qiao, Y. Cao, J. Tang, N. Deng, N. Zhao, and Y. Li, "Energy efficiency maximization for active IRS-assisted uplink NOMA systems", *IEEE Wireless Communications Letters*, vol. 13, no. 6, pp. 1561-1565, June 2024.

[5] M. Kumar, A. Kishor, P. K. Singh, K. Dubey, "Deadline-aware cost and energy efficient offloading in mobile edge computing", *IEEE Transactions on Sustainable Computing*, vol. 9, no. 5, pp. 778-789, Sept.-Oct. 2024.

[6] S. Mishra, R. K. Mallick, D. A. Gadanayak, P. Nayak, R. Sharma, G. Panda, M. S. Al-Numay, and P. Siano, "Real time intelligent detection of PQ disturbances with variational mode energy features and hybrid optimized light GBM classifier", *IEEE Access*, vol. 12, pp. 47155-47172, 2024.

[7] D.-Y. Kim, D.-H. Lee, U. Namkoong, "Conductive thin-film structure for EMP protection of operational infrastructure facilities: Measurement and verification up to 18 GHz", *IEEE Transactions on Electromagnetic Compatibility*, vol. 66, no. 3, pp. 869-878, June 2024.

[8] C. Zhou, D. P. Snyder, B. Epstein, Z. T. Robinson, G. Y. Jin, P. Y. Tang, R. G. Polcawich, and M. Roper, "Measurement of ambient magnetic field noise for through-the-earth (TTE) communications and historical comparisons", *IEEE Transactions on Electromagnetic Compatibility*, vol. 66, no. 3, pp. 720-727, June 2024.

[9] H. Miloudi, M. Miloudi, S. A. El Mehdi Ardjoun, M. Metwally Mahmoud, A. A. Telba, M. Denaï, U. Khaled, A. M. Ewais, "Electromagnetic compatibility characterization of start-capacitor

single-phase induction motor", *IEEE Access*, vol. 12, pp. 2313-2326, 2024.

[10] https://vent-sys.ro/aeroterma-pe-agent-termic/1344-aeroterma-volcano-vr3.html

[11] M. A. Enache, A. Campeanu, S. Enache, I. Vlad, "Contributions to simulating and monitoring vectorial control of reluctance synchronous motors", *Joint International Conference OPTIM-ACEMP, Optimization of Electrical and Electronic Equipment Aegean Conference on Electrical Machines & Power Electronics*, Brasov/Cheile Gradistei, 2017, pp. 287 – 292.

[12] M. A. Enache, *Transient Processes of Asynchronous and Synchronous Motors with Variable Reluctance* (in Romanian), Craiova: Sitech, 2015.

[13] http://www.distek.ro/ro/Produs/Modul-achizitie-USB-8-canale - 50kSa-s-Keitlhey-KUSB-3100-911.

DOI: 10.52846/AUCEE.2024.11

Aspects Regarding the Operation of Ventilation and Air Conditioning Systems for Industrial Halls

Monica-Adela Enache*, Elena-Mihaela Enache† and Mara Pauliuc†

* University of Craiova/ Faculty of Electrical Engineering, Craiova, Romania, menache@em.ucv.ro

† "Ion Mincu" University/Faculty of Architecture, Bucharest, Romania, elena.enache2305@gmail.com

***Abstract* – This paper emphasizes, once again, the importance of ventilation systems for ensuring thermal comfort in industrial spaces. For this purpose, a dynamic fault regime of variable reluctance synchronous motors (RSM) used to drive such systems (case of occurring an accidental resistive torque) is analyzed from a theoretical point of view (with experimental confirmation). At the beginning, an introduction in the issues of the paper is made. A brief bibliographic analysis and some relevant images regarding the air flow driven by industrial ventilation and air conditioning systems are presented. In order to analyze dynamic regimes of RSM, a Matlab program was carried out, by using a mathematical model written in the two axes theory. A series of graphs have been obtained by running it for a specific case; they emphasize the evolution over time of the main electrical, magnetic and mechanical quantities of the motor. There have been obtained different evolutions of the operation points in various coordinates (phase current, longitudinal and transverse currents of the stator and rotor, magnetization current, magnetization flux, magnetization flux components, torque and speed). The graphs obtained led to a series of relevant conclusions regarding the behavior of the driving motor of the installation (conclusions regard the way in which an increase in the resistant torque influences the values and durations of the analyzed dynamic quantities). The paper ends with Acknowledgment and the corresponding References.**

Cuvinte cheie: *sisteme de ventilatie, hale industriale, reluctance synchronous motor, dynamic regime, modelation, simulation, test.*

Keywords: *ventilation systems, industrial halls, reluctance synchronous motor, dynamic regime, modeling, simulation, test.*

I. INTRODUCTION

The problem of designing green industrial building is a nowadays problem that represents a challenge for any architectural office [1], [2], [3] and [4].

An important component of this design is the appropriate sizing of ventilation and air conditioning equipments, which ensure appropriate thermal comfort for people working in these buildings [5], [6], [7] and [8].

This paper aims at analyzing a relevant aspect regarding the behavior of an important component of such an installation - the driving motor (the problem also presented in [9], [10], [11] and [12]).

From the multitude of driving motors, a modern, simple, cheap and very reliable motor was chosen, the reluctance synchronous motor (RSM).

This way, this paper is also a natural continuation of the initial analysis presented in [13].

When it comes to the design of ventilation and air conditioning systems for industrial halls, the basic principles of fluid mechanics always are applied, irrespective of the specific requirements for the hall temperature.

These principles have an impact on the design and technology of ventilation installation, which means that they also influence operating costs.

For example, a vertical temperature gradient should be oriented to keep heat loss to a minimum, keeping the vertical temperature rise as low as possible, especially in the upper area of the hall.

A manner of doing this, is to maintain a maximum air circulation in the aisle.

The flow conditions will be optimized, for example, by using grid shelving systems that are permeable and have a generous gap between them and the floor.

The specific flow features of the torsion air distributors - including the patented Hoval Air-Injector - ensure that the air in the storage halls is distributed according to requirements.

In heating mode, a highly concentrated air flow is emitted at high speed from the distributor and a negative pressure difference occurs around the air column (Bernoulli distribution).

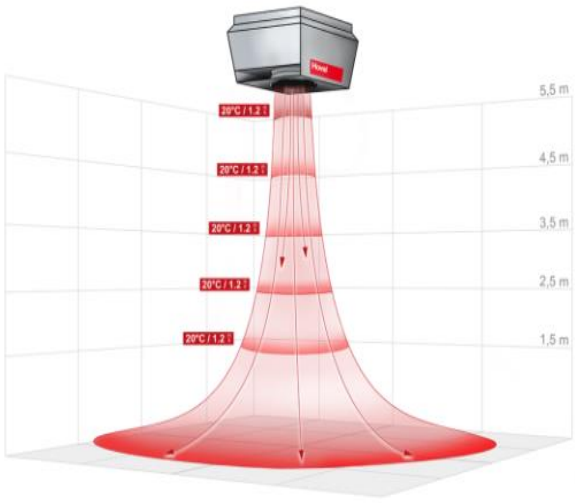

Fig. 1. Vertical airflow [14].

As a result, ambient air moves from the ceiling area and, to a less extent, from the upper shelves towards the air flow (Fig. 1).

As the penetration depth increases, the airflow is reduced, the surrounding negative pressure decreases, and the ambient air is induced (Fig. 2).

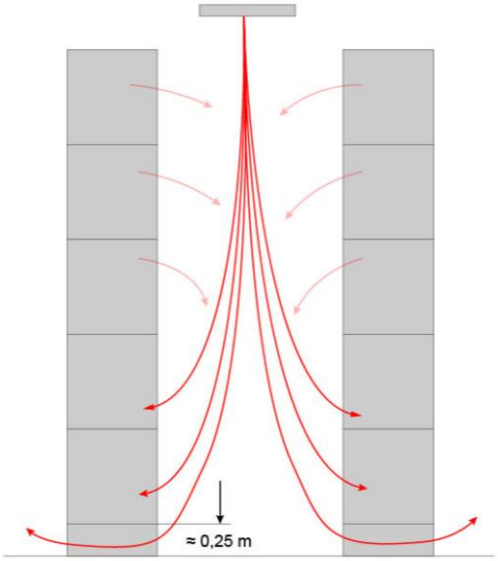

Fig. 2. Airflow through the aisle: air supplied vertically from above allows a low temperature gradient over the entire height. In a hall that is between eight and twenty meters high, the values will typically be somewhere between 0.15 Kelvin and 0.25 Kelvin [14].

The flow then reaches the shelves below.

In order to pass the flow efficiently to next shelves, a gap of 0.2 to 0.3 meters (m) must be left between the floor and the shelf.

The improved air distribution makes possible to optimize the flow for one, two or three aisles, with a series of air passages.

The rows of shelves restrict the symmetrical rotating flow of the torsion air distributors.

The fronts of the rows of shelves act as walls as regards the air flow, causing air jets on the surface of the walls (Coanda effect).

These have a wider coverage than open jets (Regenscheit formulation) and a higher installation height than in the case of free flow distribution.

The value can reach up to 1.5 m.

II. Mathematical Model

The present paper is a normal continuation of those presented in [13].

The starting point will be the mathematical model presented in [13], where it will be taken into account that the RSM has no excitation winding.

Thus, the mathematical model written in the fixed reference frame with respect to the rotor is obtained:

$$\begin{aligned} u_d - R_s i_d &= \frac{d\psi_d}{dt} - \omega\psi_q \\ u_q - R_s i_q &= \omega\psi_d + \frac{d}{dt}\psi_q \\ -R_D i_D &= \frac{d\psi_D}{dt} \\ -R_Q i_Q &= \frac{d\psi_Q}{dt} \end{aligned} \tag{1}$$

where:

$$\begin{aligned} \psi_d &= L_d i_d + L_{md} i_D \\ \psi_q &= L_q i_q + L_{mq} i_Q \\ \psi_D &= L_{md} i_d + L_D i_D \\ \psi_Q &= L_{mq} i_q + L_Q i_Q \end{aligned} \tag{2}$$

Substitute (2) into (1). We obtain:

$$\begin{aligned} u_d - R_s i_d + \omega L_q i_q + \omega L_{mq} i_Q &= L_d \frac{di_d}{dt} + L_{md} \frac{di_D}{dt} \\ u_q - R_s i_q - \omega L_d i_d - \omega L_{md} i_D &= L_q \frac{di_q}{dt} + L_{mq} \frac{di_Q}{dt} \\ -R_D i_D &= L_{md} \frac{di_d}{dt} + L_D \frac{di_D}{dt} \\ -R_Q i_Q &= L_{mq} \frac{di_q}{dt} + L_Q \frac{di_Q}{dt} \end{aligned} \tag{3}$$

To these relations is added the equation of motion:

$$\frac{3}{2} p\left(\psi_d i_q - \psi_q i_d\right) - m_r = \frac{J}{p}\frac{d\omega}{dt}, \tag{4}$$

respectively:

$$\frac{3}{2} p\left(L_d i_d i_q + L_{md} i_D i_q - L_q i_q i_d - L_{mq} i_Q i_d\right) - m_r = \frac{J}{p}\frac{d\omega}{dt}. \tag{5}$$

The meanings of the notations are as detailed in [13].

III. Simulations

With the help of this mathematical model, a Matlab program was created. This Matlab program developed for analyzing a particular fault regime has been used: an increase in the shaft resistant torque value. The simulation results are presented in Fig. 3.

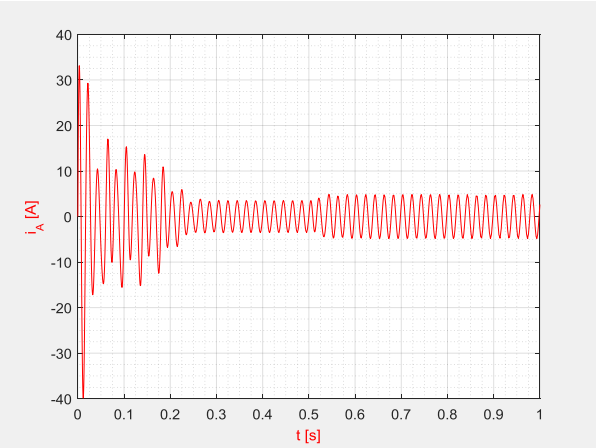

a)

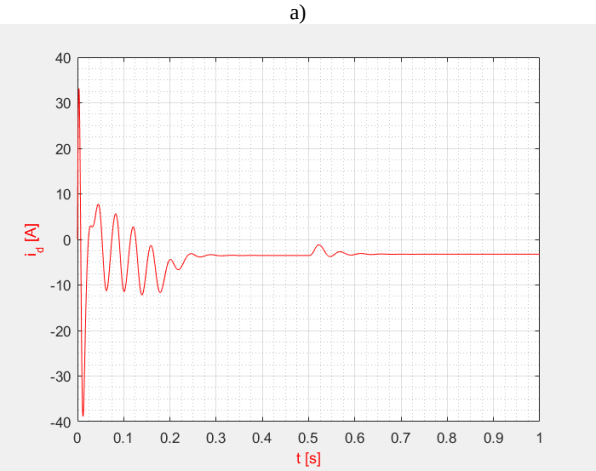

b)

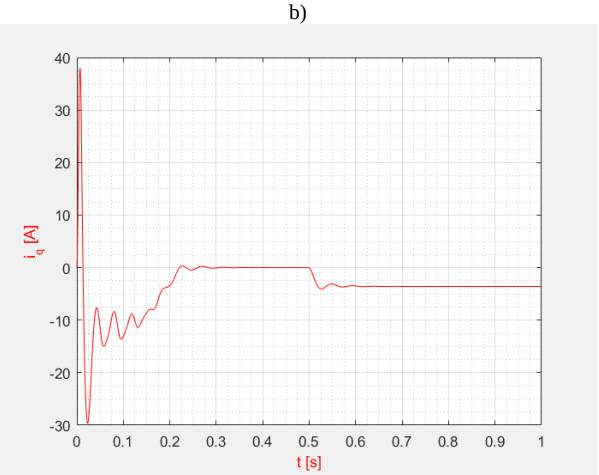

c)

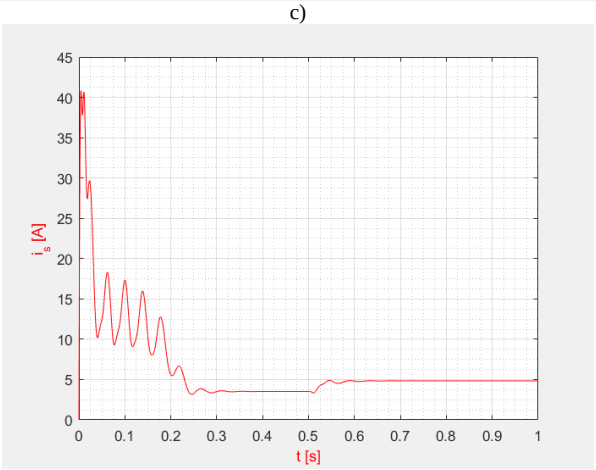

d)

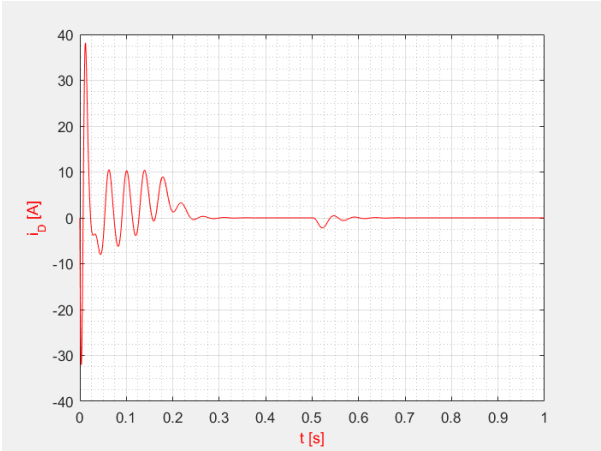

e)

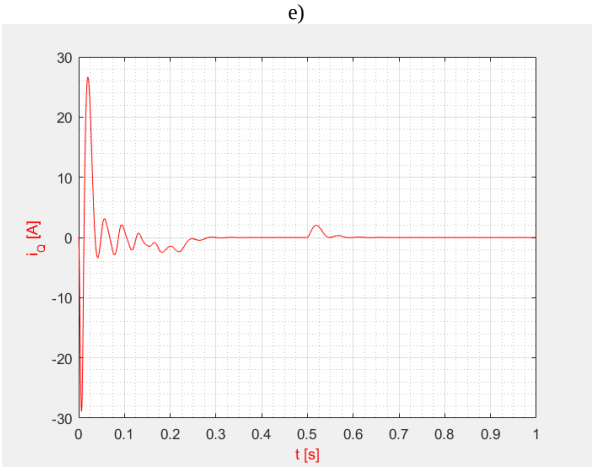

f)

g)

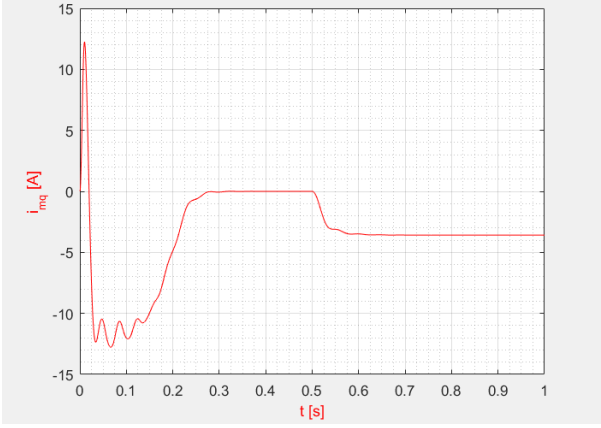

h)

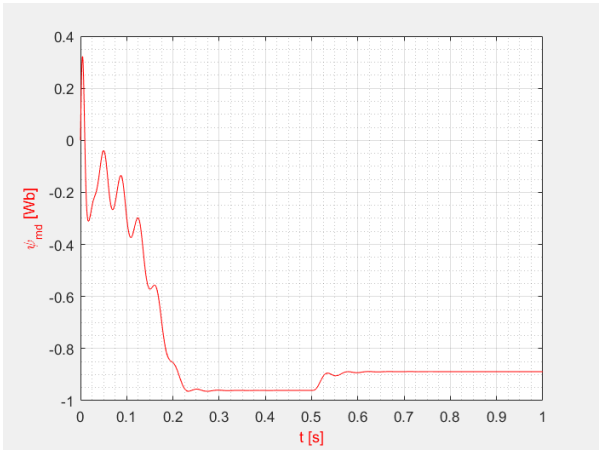

i)

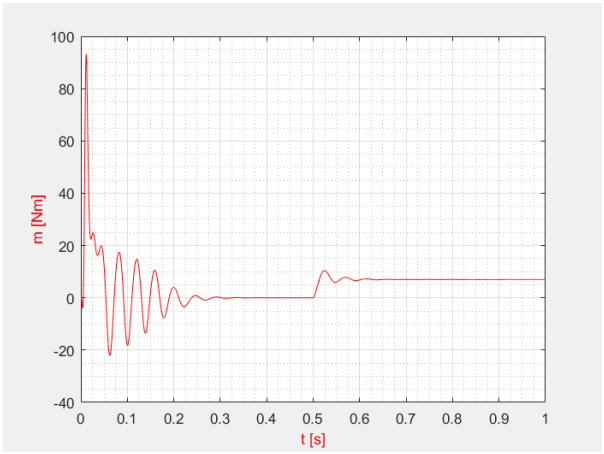

m)

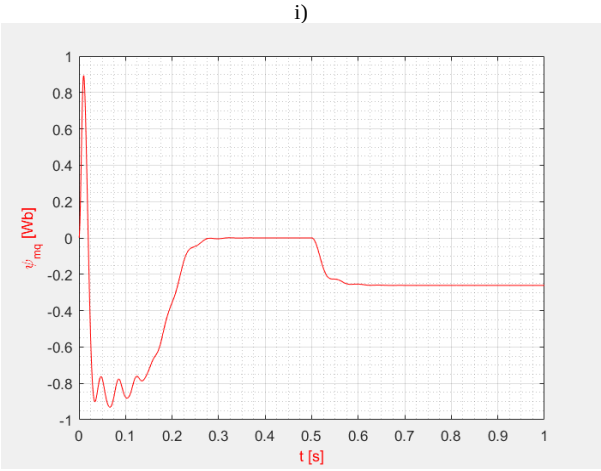

j)

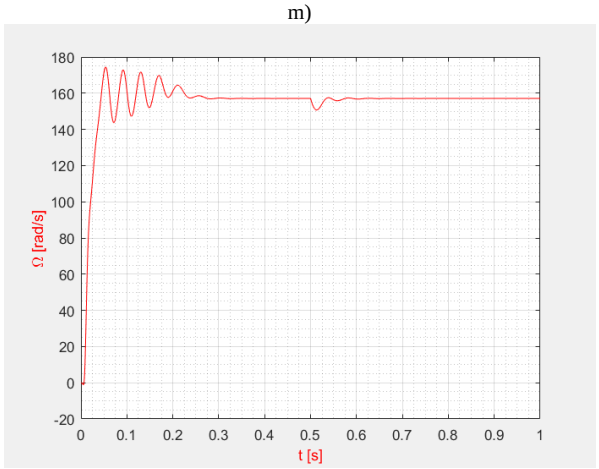

n)

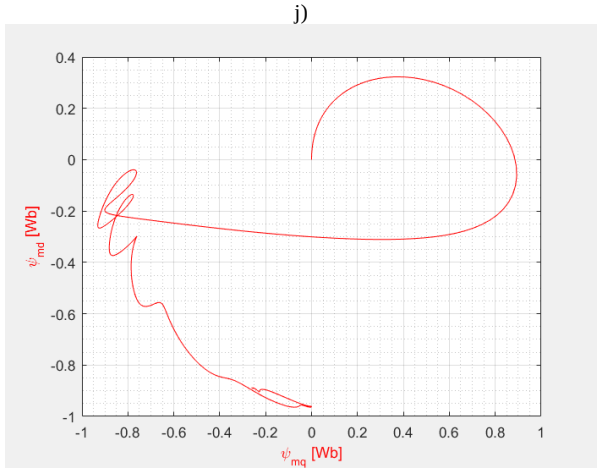

k)

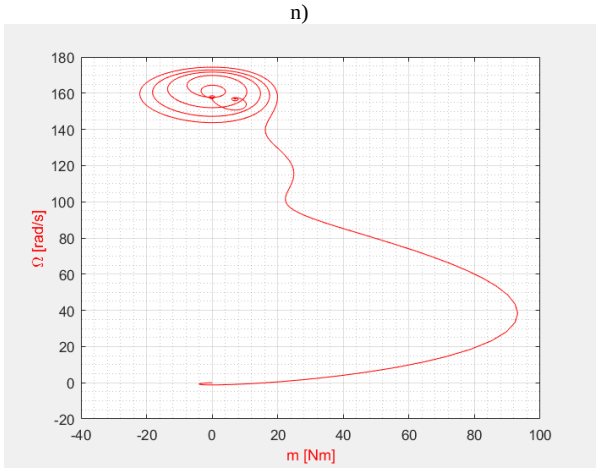

o)

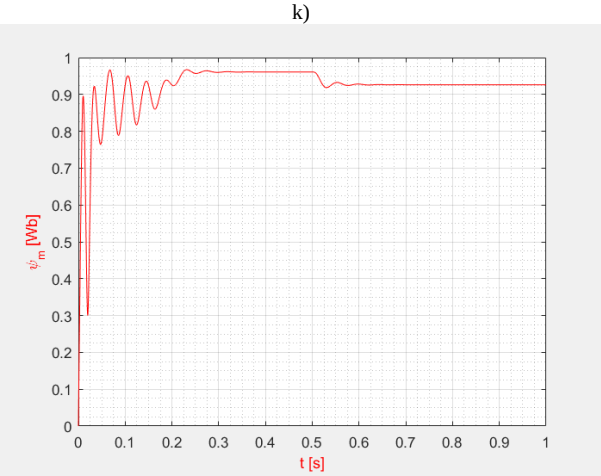

l)

Fig. 3. The characteristics obtained for the case of increasing the value of the resistant torque to 7.6 Nm after 0.5 s from starting.

The same motor as in [13] was used. The simulations were carried out for an motor rated as follows:

R_s = 3.77 Ω, R_D = 1.5 Ω, R_Q = 4.5 Ω, $L_{s\sigma}$ = 0.0081 H, $L_{D\sigma}$ = 0.0059 H, $L_{Q\sigma}$ = 0.0067 H, L_d=0.281 H, L_q=0.081 H; U = 220 V, p = 2, J=0.008 kg.m^2.

The graphs depicted in Fig. 3 have been obtained by running the program (the resistant torque increases from 0, initially, to 7.6 Nm).

IV. Experimental Determinations

The electrical diagram of the measurement system is shown in figure 4.

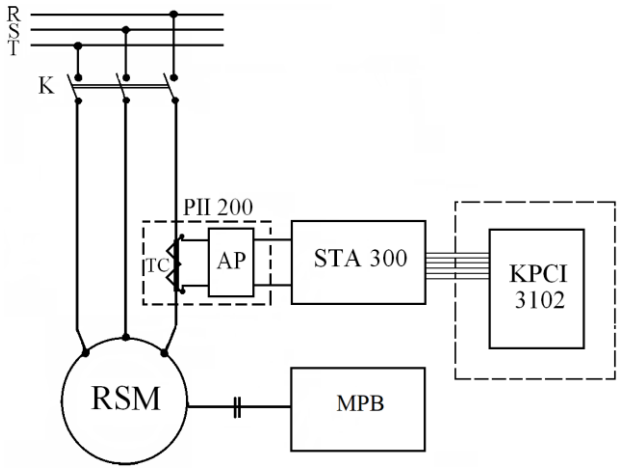

Fig. 4. Electrical diagram.

The meanings of the notations used are as follows:

- RSM - reluctance synchronous motor;
- MPB - magnetic powder brake;
- PII 200 - current transformer with adaptation block;
- STA 300 - connection block;
- KPCI 3102 - data acquisition board.

A magnetic powder brake [15] was used to load the motor.

It allows the resistive torque to be varied up to 10 Nm. A control block is used to change the torque.

Fig. 5. Magnetic powder brake [15].

The experiments consisted in acquiring the current variations for a steady-state of the RSM, for two concrete situations:

- the steady-state operation at 0 Nm (Fig. 6);
- the steady-state operation at 7.6 Nm (Fig. 7).

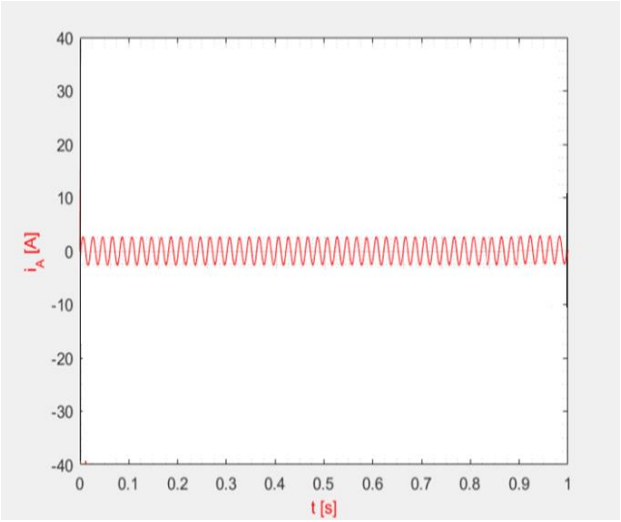

Fig. 6. The variation of the phase current, in case of steady-state operation, at 0 Nm.

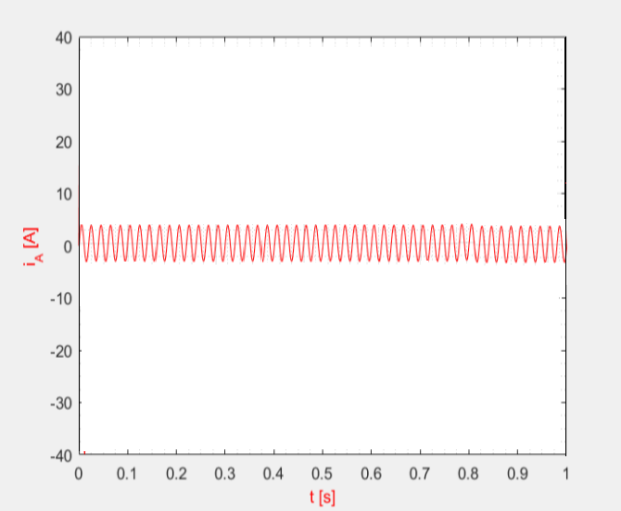

Fig. 7. The variation of the phase current, in case of steady-state operation, at 7.6 Nm.

Comparing these results with those depicted in Fig. 3.a (zone 0.3-0.5 s and zone 0.7-1 s), it is found that they are almost identical, which confirms the validity of the simulations (at least in steady state).

V. Conclusions

This paper presents a series of simulations that emphasize dynamic regimes of RSM, in case of certain external disturbances (an increase in the resistant torque).

Some of the conclusions obtained by analyzing the graphs presented above are presented below:

- occurring a resistant torque jump leads to an increase in the phase current;

- the current i_s also increases in the new steady state;

- after a short mechanical shock, occurred when the load was applied, the motor works stably at a slightly lower speed than the initial one;

- the motor has two stable operation points, corresponding to the two steady states (emphasized in the Ω=f(m) coordinates).

The conclusions were indirectly confirmed by previous experimental determinations.

ACKNOWLEDGMENT

Source of research funding in this article: Research program of the Electrical Engineering Faculty Craiova and the Faculty of Architecture Bucharest (financed by the University of Craiova).

Contribution of authors:

First author – 55 %;
First coauthor – 25 %;
Second coauthor – 20 %.

Received on September 7, 2024
Editorial Approval on November 25, 2024

REFERENCES

[1] H. Wang and W. Wang, "Optimization algorithm of green building landscape space environment based on geographic information system", *2024 International Conference on Telecommunications and Power Electronics (TELEPE)*, Frankfurt, Germany, 2024, pp. 897-901.

[2] P. Zhang, "Research on the use of BIM technology in green building design based on neural network learning", *IEEE Access*, Volume 12, 2024, pp. 94784-94792.

[3] Y. Zhang and X. Ren, "Research on green public building design based on computer 3D image vision technology", *2023 IEEE International Conference on Sensors, Electronics and Computer Engineering (ICSECE)*, Jinzhou, China, 2023, pp. 970-974.

[4] C. Rao, "Optimal design of green building based on Digital Media Technology", *2022 International Conference on Artificial Intelligence in Everything (AIE)*, Lefkosa, Cyprus, 2022, pp. 357-361.

[5] H. Zhou, Z. Li, Y. Liu, L. Mei, W. Lu, and J. H. Air, "Conditioning system design of power data center based on automatic control technology", *2024 IEEE 2nd International Conference on Image Processing and Computer Applications (ICIPCA)*, Shenyang, China, 2024, p.1-4.

[6] U. Chowdhury, J. Rodriguez, M. Tradat, Q. Soud, S. Wallace, and D. O"Brien, "Acoustics analysis of air and hybrid cooled data center", *2024 23rd IEEE Intersociety Conference on Thermal and Thermomechanical Phenomena in Electronic Systems (ITherm)*, Aurora, CO, USA, 2024, pp. 1-11.

[7] Z. Z. Bin Zainudin, S. H. Binti Yusoff, T. S. Gunawan, S. Y. Mohamad, I. J. Chowdhury, and S. N. Mohd Sapihie, "Load forecasting for air conditioning systems using linear regression and artificial neural networks", 2024 IEEE 10th International Conference on Smart Instrumentation, Measurement and Applications (ICSIMA), Bandung, Indonesia, 2024, pp. 234-239.

[8] J. Han, G. Zhang, Z. Ye, Z. Fu, N. Zhao, and S. Wang, "Pole pairs identification for sensorless permanent magnet single-rotary air-conditioning compressor", 2024 IEEE 19th Conference on Industrial Electronics and Applications (ICIEA), Kristiansand, Norway, 2024, pp. 1-6.

[9] J. Yi, C. Li, D. Zhang, X. Li, M. Jiang, and H. Zhao, "A fast and accurate loss model of converter-fed induction motor in central air-conditioning system", *IEEE Transactions on Power Electronics*, Volume: 38, Issue: 3, March 2023, pp. 3689-3699.

[10] G. Balasubramanian, P. Chandrasekar, and S. A. Alexandar, "Variable frequency drive operated air blower in air handling unit of heating, ventilation and air conditioning systems", *2022 IEEE Delhi Section Conference (DELCON)*, New Delhi, India, 2022, pp. 1-7.

[11] H. Hou, W. Yao, and W Zhang, "A novel control strategy of single phase brushless dc motor for automotive air conditioning", *2016 IEEE Vehicle Power and Propulsion Conference (VPPC)*, Hangzhou, China, 2016, pp. 1-5.

[12] S. Kikuchi, A. Takahashi, H. Mikami, S. Wakui, H. Kou, K. Tanaka, "Development of self-starting permanentmagnet synchronous motors for compressor drives", *2009 International Conference on Electrical Machines and Systems*, Tokyo, Japan, 2009, pp. 1-6.

[13] M. A. Enache, E.-M. Enache, and M. Pauliuc, "Simulations and tests regarding the operation of air heaters for industrial buildings", *Annals of the University of Craiova, Electrical Engineering Series*, 2024, in press.

[14] https://www.hoval.ro/blog/ro/sisteme-de-ventilatie-industriala-si-climatizare-hale.

[15] https://roitzheim-werkzeugmaschinen.de/LN-Lucas-Nuelle-Magnetpulverbremse-Steuergeraet-Set-SE-2662-5R-und-SE-2662-5S-gebraucht_1.

DOI: 10.52846/AUCEE.2024.12

Remote Communication in the Substation's SCADA System

Cosmin-Ionuț Toma*, Mihaela Popescu*, Mihăiță-Daniel Constantinescu* and Gabriel-Cosmin Buzatu*
*University of Craiova, Faculty of Electrical Engineering, Craiova, Romania, ctoma@em.ucv.ro, mpopescu@em.ucv.ro, mconstantinescu@em.ucv.ro, cosmin.buzatu@incesa.ro

***Abstract* - The aim of this paper is the implementation and validation of a mobile phone remote connection to a Supervisory Control and Data Acquisition system (SCADA) of a railway traction substation. The implementation was done not only to optimize the time in which the user intervenes within the electrical substations, in case of a fault or other event, but mostly to be able to react in unforeseen situations where the person in charge is not and cannot quickly reach the electrical substation or even the remote desktop. For this, the operator can connect to the system using the mobile phone and the corresponding mobile phone software using an interface similar to the remote desktop. Therefore, the operator can hand the fault and make the required actions or improvements. The proposed system gives the ability to optimize the intervention costs considering the required trips to the electrical substation, and even more the trip to the SCADA remote desktop station. Therefore, a wireless remote connection method is approached via the mobile phone network to the SCADA system.**

Cuvinte cheie: *sistem de monitorizare, control și achiziții de date, telefon mobil, control wireless, control la distanță, sistem wireless, stație electrică, dispozitiv electronic inteligent.*

Keywords: *supervisory control and data acquisition, mobile phone, wireless control, remote control, wireless system, electrical substation, intelligent electronic device.*

I. INTRODUCTION

Primary and secondary devices are used to decrease the number of potential single points of failure. Components are deployed for collecting data from different constituents within a switchgear assembly. This configuration has a provision for managing older components where it uses a data concentrator that talks to other devices, for example, an intelligent electronic device (IED) [1], [2].

Four main functions of the distribution automation system are introduced in this paper: monitoring function, control function, protection function and management function. The distribution automation system is the inevitable result of the development of the distribution network and will become even more important in the future to provide users with high quality energy [3], [4].

Innovations in next-generation communication technologies play a vital role in optimizing the operation of energy distribution grids, facilitating the creation of smart grid systems [5], [6].

The Supervisory Control and Data Acquisition (SCADA) system includes all the equipment and technical systems necessary to measure the values of the parameters of interest in the electrical substation and to control the execution elements.

All this equipment is dimensioned appropriately according to the number of parameters monitored at each feeder, respectively, and to have the possibility of connection with the control elements at the higher hierarchical level in order to transmit data and receive control signals. The energy parameters to be measured and monitored shall refer to the measurement of the parameters and energy consumption at the input of the feeder IED and to the measurement of the consumption parameters on the utilization side on the electrical substation, and shall be as follows:

- Currents (actual value: I_R, I_S, I_T, I_N);
- Voltages (line voltage actual value: U_{RS}, U_{ST}, U_{TR}; phase voltage actual value: U_R, U_S, U_T; average/maximum value for phase and line voltages); - Frequency (actual value of frequency in the supervised network: F);
- Active, reactive and apparent power (current value for each phase: P1, P2, P3, Q1, Q2, Q3, S1, S2, S3; total current value on the three phases: Σ P, Σ Q, Σ S; average/maximum value: ΣP, ΣQ, ΣS);
- Harmonics (current total harmonic distortion: $THDI_R$, $THDI_S$, $THDI_T$, $THDI_N$; line voltage total harmonic distortions: $THDU_{RS}$, $THDU_{ST}$, $THDU_{TR}$; phase voltage total harmonic distortions: $THDU_R$, $THDU_S$, $THDU_T$.

The SCADA system which was implemented in this paper had been applied to a railway electrical substation connected to the 110kV power grid. The catenary voltage for the Romanian railway system is 27.5 kV.

II. ARCHITECTURE OF WIRELESS MONITORING SYSTEM

The wireless monitoring system of the energy parameters for the electric substation is based on a SCADA architecture illustrated in Fig. 1, which assumes the existence of acquisition and control equipment at the local level for each consumer, one or more computers (servers) that centralize the monitored information and save it in a database and one or more computers on which a client application is running to present the monitored parameters.

The server applications acquire from the local acquisition and control equipment, in real time, the values

of the monitored parameters of the electrical equipment, process them and then save them in a local or central database. The client application acquires information from the database and presents it to the user through a Graphical User Interface (GUI).

Tracking the energy behavior of the electrical substation is based on a process of acquiring and analyzing a large amount of remote data.

Remote monitoring and control of the electrical substation which is based on gathering information on the status of the electrical substation via appropriate acquisition interfaces, transferring the information to the central monitoring level, remote control and recording of significant changes of local consumers [7].

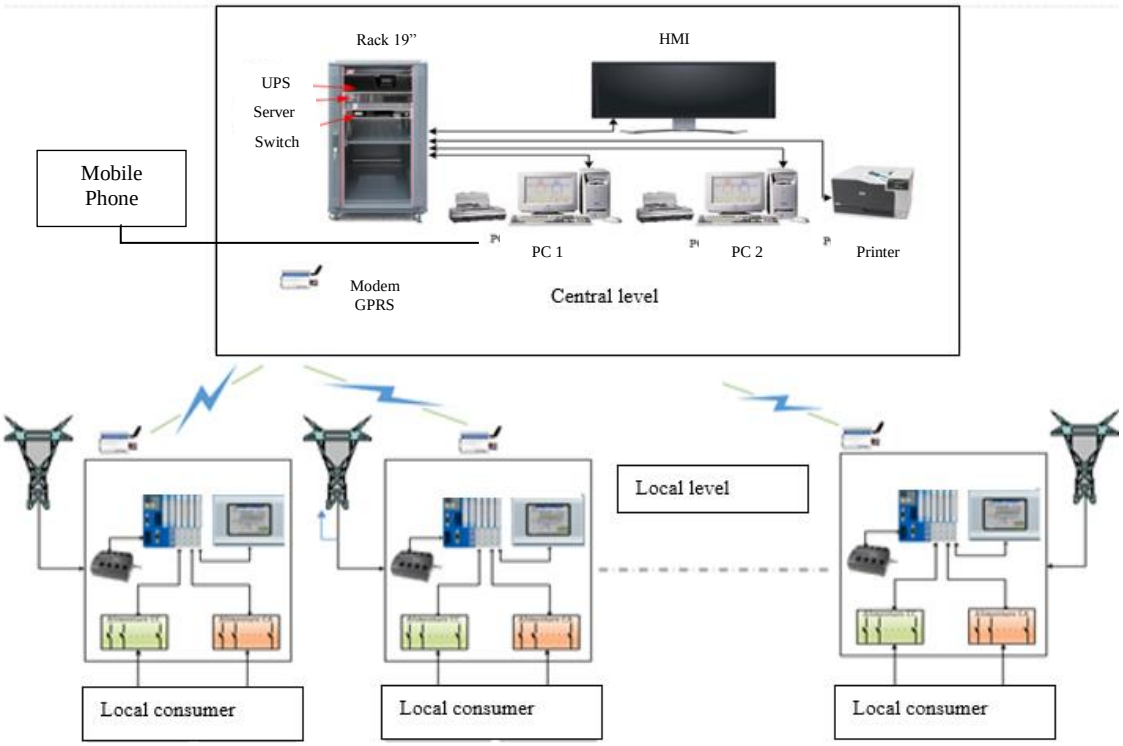

Fig. 1. Architecture of wireless monitoring system.

III. CENTRAL LEVEL

At the central monitoring level, a modular panel is placed inside, in which the computing and communication equipment necessary for the system operation is mounted.

SMART UPS type uninterruptible power supply ensures the operation of the SCADA equipment at the central level for a determined period of time in situations of accidental power supply voltage drops. It also provides protection for the equipment supplied by it in the event of variations in the supply voltage that may occur accidentally in the central supply network.

All the necessary hardware and software modules are installed in the Server computer for:

- data acquisition and processing from local consumers via the programmable logic controller (PLC) at the local level;
- real-time monitoring and storage of energy, configuration and status parameters for each local consumer
- ensuring quick and efficient access to stored information by authorized persons;
- real-time processing of commands to local PLCs;
- processing data from the system's non-volatile memory for displaying data on the Human machine interface (HMI) -Visualization Monitor;
- data processing for the preparation and printing of reports specific to system operation.

SWITCH equipment ensures the ETHERNET data communication between the system components: Server computer, GPRS (General Packet Radio Service) modem at the central level, workstation computers, HMI interface, and printer. Other computers with access rights in the SCADA network can also be coupled to the SCADA network at the request of the beneficiary.

4G Industrial Cellular 4G Router, with RS-232/485 port, with 10/100Mbps Ethernet ports and WiFi IEEE 802.11 provides GPRS communication with PLC equipment at local levels. The equipment also provides WiFi access to the SCADA system network for users with access rights.

In addition to the cabinet described above at the central level, other components of the SCADA system equipment are located.

HMI interface is represented by a 41" ultra HD display on which the information received from the local Programmable Logic Controllers, as well as the data processed by the central computer based on this information, are displayed. The display is coupled to the Server Computer as well as to the computing equipment connected to the internal SCADA network.

The printer is connected to the system via ETHERNET link and accessible to users with access rights coupled to the network, used to print specific operation reports (daily, weekly, monthly, etc.), malfunction reports and other reports according to user requests.

There are computers connected in network with the SCADA server and through which users with access rights realize:
- visualization of the status of the SCADA monitoring system component equipment;
- visualization of the electrical parameters received from each of the local equipment;
- remote control of the PLCs of each local consumer;
- visualization of the fault and alarm states of each local equipment;
- selection of the types of reports, of the visualization interval, to be printed for analysis and archiving;
- system configuration and maintenance.

The presented structure provides:
- CONTROL – the user can read and write/modify any parameter in the process (with password);
- VISUALIZATION - graphic screens, synoptic diagrams;
- ALARMS MANAGEMENT - they are cataloged by priority levels (can be acknowledged, deleted, archived, modified);
- DATABASE - high-performance database server, Microsoft SQL Server (allows multiple on-line access to the server database);
- RECIPES - allows the creation of upload to/from PLC of groups of point settings;
- REPORT MANAGER - allows the creation and generation of reports based on process measurements;
- GRAPHICS - facilities, based on ActiveX technology:
- multiple graphs in the same screen;
- unlimited number of lines in the same graph [8], [9].

IV. LOCAL LEVEL

At the local level of the monitoring system (illustrated in Fig. 2), the electrical substation has a workstation where the energy parameters can be monitored both from the single-wire scheme as well as the detail schemes of the feeder and auxiliary services in the substation. It must be mentioned that the diagram represents a single-phase system given the fact that the railway power system is single phase.

The substation includes the fixed installations for connection to the high-voltage power system and adaptation of the energy parameters (voltage, current, etc.) to the needs of the energy system:

- High Voltage Overhead Line (OHL) feeder (2-pole);
- High voltage power transformer feeder connected at the same phase-phase voltage;
- Single phase (1-phase) power transformer;
- Voltage Transformer for contact wire;
- Bus coupler bay;
- Feeder [10].

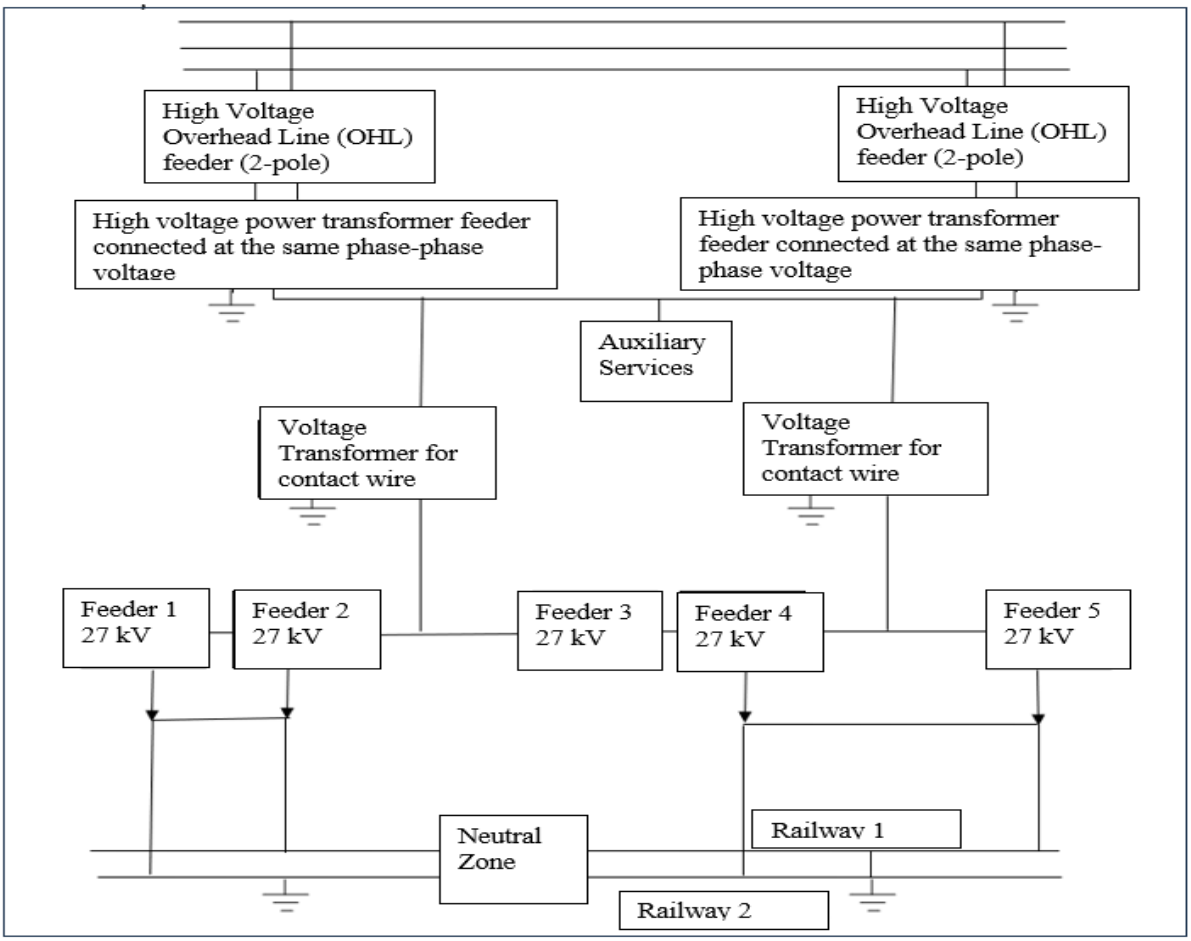

Fig. 2 Local level block diagram.

V. COMMUNICATION IN THE MONITORING SYSTEM

In the presented monitoring system, there are some specific data transmission situations.

The wireless communication is realized between the computer at the central level and a remote computer using dedicated software.

Communication at the central monitoring level, refers to:

- ETHERNET data communication between the system components at the central monitoring level and the need for a 4G industrial cellular router, with RS-232/485 RS-232/485 port, with 10/100Mbps Ethernet ports and WiFi IEEE 802.11 IEEE that provides GPRS communication with the PLC equipment at the local level.

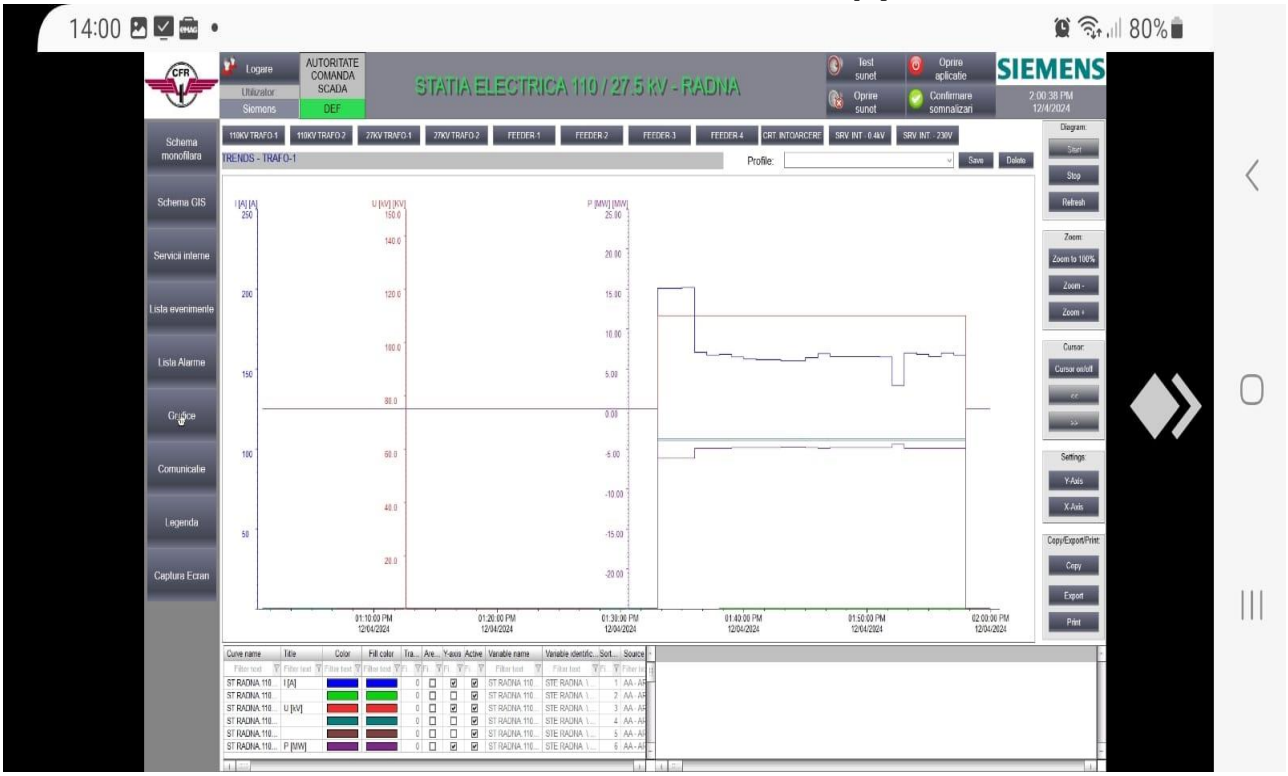

Fig. 3. Trafo 1 110kV trends.

The remote data transmission to the central monitoring level refers to the communication between the local level acquisition and control system with the next higher monitoring level, which is often quite far away; the most common and reliable solutions are GSM/GPRS communication networks, which implies the inclusion of a GSM/GPRS communication module at the local level.

Local communication refers to:

- the communication between the Programmable Logical Controller and the intelligent electronic device within the substation is an ETHERNET data communication;
- communication between intelligent electronic device and transducers which is realized by wire, in unified signal, usually (4...20) mA cc or (0...10) Vcc [11], [12], [13].

VI. EXPERIMENTAL RESULTS

An efficient solution for monitoring the energy parameters needed for interpreting the post-default analysis in power substations is the connection to the SCADA system using a mobile phone. The required operating systems are Windows for the computer and Android for the mobile phone. The remote connection between the two devices is established using a remote-control application called AnyDesk. To secure the data, a username and password are set up on the computer and entered into the AnyDesk mobile app installed on the mobile phone used to access the SCADA system. Access to the monitoring system is only allowed to the authorized personnel, which is registered to the AnyDesDesk mobile app installed on the mobile phone used to access the SCADA system.

Access to the monitoring system is therefore allowed only to persons who know the login data. The computer to which the mobile phone is connected is located at the central level of the SCADA system. The information transmitted in real time to the mobile phone, which makes the visualization of energy parameters value more efficient, thus allowing a quick post-failure analysis. The evolution of the energy parameters is illustrated in Fig. 3. It can be seen that the current varies between 150 A and 200 A, and the voltage is constant at 110 V. The power varies between -5 MW and -3MW. Each energy parameter is graphically represented with a different color in order to be able to efficiently interpret the information by the station operator. The feeder where the values are recorded is shown in blue font on the top left and is labeled "TRAFO-1".

These values are recorded after simulating the energy parameters with an injection kit used to check the stability

of the system. The injection kit is positioned in the clamps where the process signals arrive, thus simulating real situations. Along with the energy parameters, which are visualized on the phone, it is also possible to follow the list of events occurred in the electrical substation in chronological order, in order to understand the phenomena that occurred. This list gives necessary details about the name of the event, date and time, along with the place where the event had happened (illustrated in Fig. 4). A detail of the logged events is given in Fig 5.

An essential aspect in monitoring systems is the communication, which is represented on the graphical user interface with all its elements. This graphical user interface screen can be viewed on the phone, giving details of the communication status of each piece of equipment. Equipment marked with green color is in ok status and equipment marked with red color is affected by a communication problem.

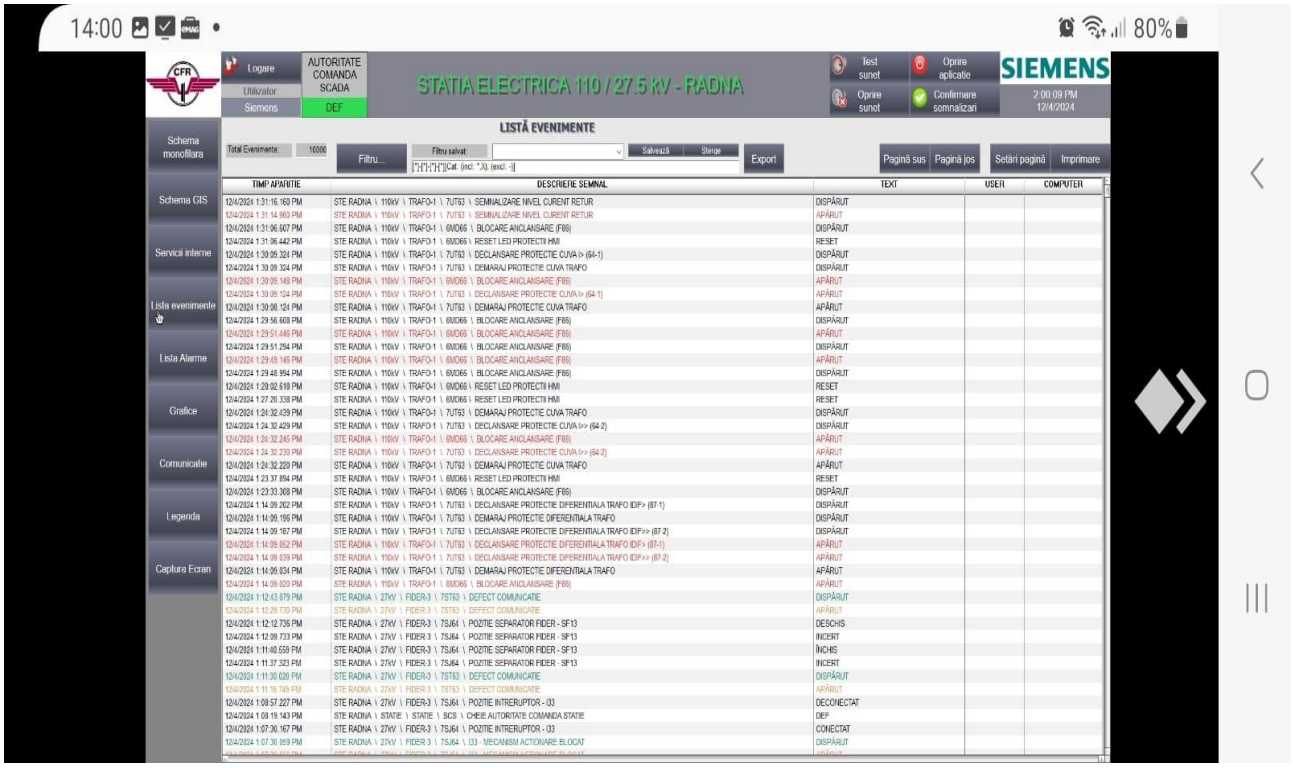

Fig. 4. Event list.

TIMP APARITIE	DESCRIERE SEMNAL	
12/4/2024 1:31:16.160 PM	STE RADNA \ 110kV \ TRAFO-1 \ 7UT63 \ SEMNALIZARE NIVEL CURENT RETUR	DISPĂRUT
12/4/2024 1:31:14.960 PM	STE RADNA \ 110kV \ TRAFO-1 \ 7UT63 \ SEMNALIZARE NIVEL CURENT RETUR	APĂRUT
12/4/2024 1:31:06.607 PM	STE RADNA \ 110kV \ TRAFO-1 \ 6MD66 \ BLOCARE ANCLANSARE (F86)	DISPĂRUT
12/4/2024 1:31:06.442 PM	STE RADNA \ 110kV \ TRAFO-1 \ 6MD66 \ RESET LED PROTECTII HMI	RESET
12/4/2024 1:30:09.324 PM	STE RADNA \ 110kV \ TRAFO-1 \ 7UT63 \ DECLANSARE PROTECTIE CUVA I> (64-1)	DISPĂRUT
12/4/2024 1:30:09.324 PM	STE RADNA \ 110kV \ TRAFO-1 \ 7UT63 \ DEMARAJ PROTECTIE CUVA TRAFO	DISPĂRUT
12/4/2024 1:30:09.148 PM	STE RADNA \ 110kV \ TRAFO-1 \ 6MD66 \ BLOCARE ANCLANSARE (F86)	APĂRUT
12/4/2024 1:30:09.124 PM	STE RADNA \ 110kV \ TRAFO-1 \ 7UT63 \ DECLANSARE PROTECTIE CUVA I> (64-1)	APĂRUT

Fig. 5. Details of event list.

To exemplify this scenario, we have interrupted the communication of the time server (NTP) - in the corresponding screen it can be visualized the time server (NTP) marked with red color having a communication problem (illustrated in Fig. 6).

VII. CONCLUSIONS

This paper shows a case study corresponding to a traction substation in Romania, for which the maintenance and monitoring time of the substation can be optimized by establishing mobile phone connectivity in the SCADA system.

In a substation, time is essential, so the SCADA system is completed with a mobile phone connection method, which gives a major advantage to the SCADA system. With this method of control, the system availability is higher, as well as the operator response time and the basic function of the SCADA system which is to remotely guarantee the control the electrical devices and networks, and to ensure their maintenance and reliability, is, therefore, realized.

The security of the system is a sensitive point, but adopting a user and password security solution can provide the necessary stability to the SCADA system.

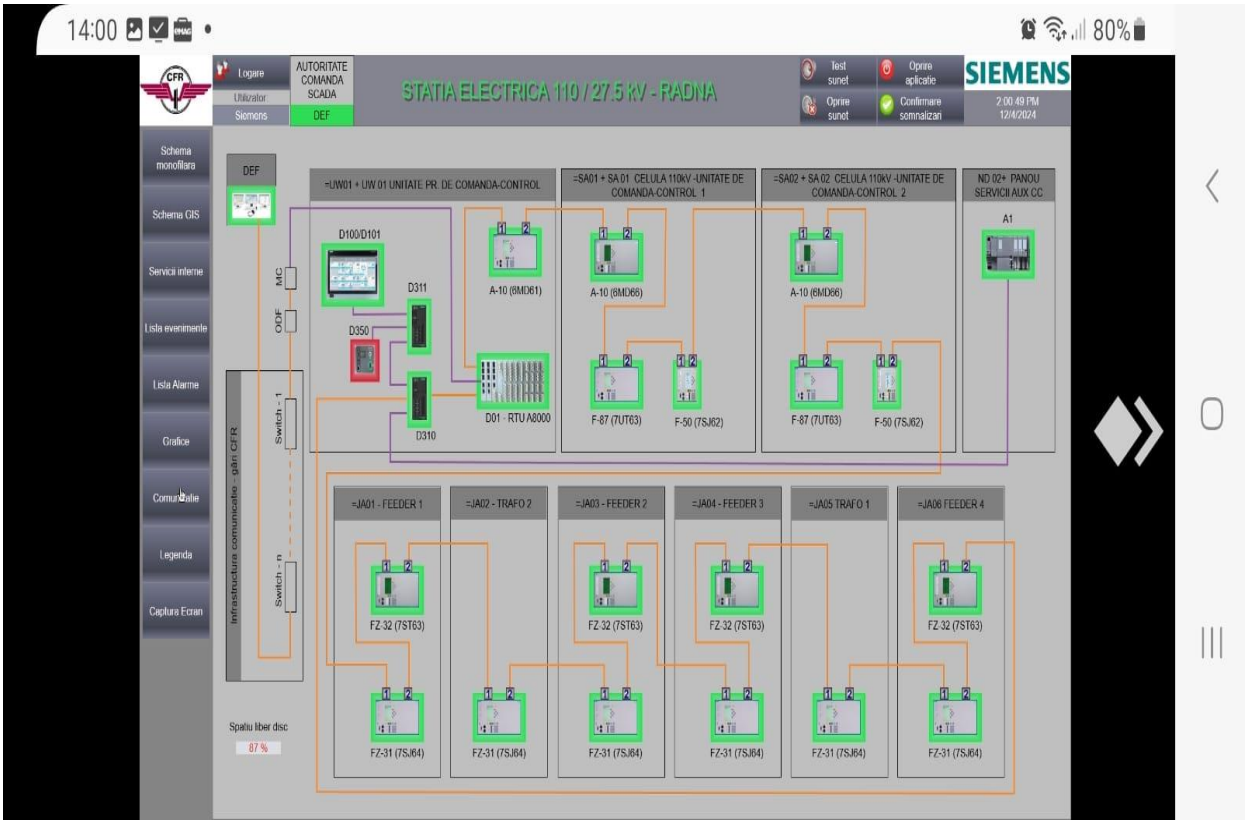

Fig. 6. Communication Screen.

ACKNOWLEDGMENT

Source of research funding in this article: Research program financed by the University of Craiova.

Contribution of authors:
First author – 40%
First coauthor – 20%
Second coauthor – 20%
Third coauthor – 20%

Received on September 10, 2024
Editorial Approval on December 3, 2024

REFERENCES

[1] D. E. Okojie, S. Mhlongo and U. B. Akuru, "Integrated Monitoring and Control System Architecture for 11 kV Substation," *2023 31st Southern African Universities Power Engineering Conference (SAUPEC)*, Johannesburg, South Africa, 2023, pp. 1-5, DOI: 10.1109/SAUPEC57889.2023.10057757.

[2] M. Sagi, B. Atlagic, D. Milinkov, B. Bogovac and S. Culaja, "High-performance distributed SCADA system architecture," *2012 16th IEEE Mediterranean Electrotechnical Conference*, Yasmine Hammamet, Tunisia, 2012, pp. 152-155, DOI: 10.1109/MELCON.2012.6196402.

[3] X. Zhou et al., "An overview on distribution automation system," *2016 Chinese Control and Decision Conference (CCDC)*, Yinchuan, China, 2016, pp. 3667-3671, DOI: 10.1109/CCDC.2016.7531620.

[4] I. Draganova-Zlateva and D. N. Geotgiev, "Digital Substations," *2021 13th Electrical Engineering Faculty Conference (BulEF)*, Varna, Bulgaria, 2021, pp. 1-6, DOI: 10.1109/BulEF53491.2021.9690844.

[5] H. Shabani, N. Julai, M. M. Ahmed, S. Khan, S. A. Hameed and M. H. Habaebi,"Wireless communication techniques, the right path to Smart Grid distribution Systems: A review," *2016 IEEE Student Conference on Research and Development (SCOReD)*, Kuala Lumpur, Malaysia, 2016, pp. 1-6, DOI: 10.1109/SCORED.2016.7810047.

[6] W. Wang, Y. Xu and M. Khanna, "A survey on the communication architectures in smart grid", *Elsevier Computer Networks*, vol. 55, 2011, pp. 3604–3629, DOI: 10.1016/j.comnet.2011.07.010.

[7] S. Gamboa and E. Orduña, "Hierarchically distributed architecture for large-scale integrated WAMPAC system," *2015 International Conference on Electronics, Communications and Computers (CONIELCOMP)*, Cholula, Mexico, 2015, pp. 16-20, DOI: 10.1109/CONIELECOMP.2015.7086946.

[8] S. Mnukwa and A. K. Saha, "Implementation of substation SCADA and automation systems in the Port of Durban," *2018 IEEE PES/IAS PowerAfrica*, Cape Town, South Africa, 2018, pp. 214-219, DOI: 10.1109/PowerAfrica.2018.8521141.

[9] S. Mnukwa and A. K. Saha, "SCADA and substation automation systems for the Port of Durban power supply upgrade," *2020 International SAUPEC/RobMech/PRASA Conference*, Cape Town, South Africa, 2020, pp. 1-5, DOI: 10.1109/SAUPEC/RobMech/PRASA48453.2020.9041078.

[10] R. Onea, *The Construction, Operation, and Maintenance of Fixed Traction Installations* (In Romanian), Bucharest: ASAB, 2004.

[11] S. Sharma, V. Kumar, P. Sharma, S. Gupta and A. Shukla, "SCADA communication protocols: Modbus & IEC 60870 – 5," *2022 1st International Conference on Sustainable Technology for Power and Energy Systems (STPES)*, SRINAGAR, India, 2022, pp. 1-6, DOI: 10.1109/STPES54845.2022.10006579.

[12] S. G. Low, X. N. Liang and S. -J. S. Tan, "IEC 61850 – An approach to facilitate interoperability in distribution automation," *2018 Asian Conference on Energy, Power and Transportation Electrification (ACEPT)*, Singapore, 2018, pp. 1-4, DOI: 10.1109/ACEPT.2018.8610748.

[13] C. -I. Toma, M. Popescu, M. -D. Constantinescu and G. -E. Subţirelu, "Wireless communication for SCADA system of a railway electrical substation," *2024 International Conference on Applied and Theoretical Electricity (ICATE)*, Craiova, Romania, 2024, pp. 1-6, DOI:10.1109/ICATE62934.2024.10749365.

DOI: 10.52846/AUCEE.2024.13

Comparative Analysis Concerning the Use of the Thermal Potential of Combustion Gases in Industrial Cogeneration Systems

Radu-Cristian Dinu*, Felicia-Elena Stan-Ivan* and Gabriel-Cosmin Buzatu*

* University of Craiova / Faculty of Electrical Engineering, Craiova, Romania, e-mail: rcdinu@elth.ucv.ro

Abstract – **Cogeneration is defined as the process of simultaneous production of heat and electricity, with the same installation (heat engine-electric generator group, turbine, etc.). Unlike classic Thermal Power Plants, cogeneration plants can be sized in correlation with the thermal energy requirement, which means that electricity is considered a "secondary" product. Throughout the article, taking into account the general theoretical aspects of the definition and operation of cogeneration systems, through the prism of specific energy indicators, the results obtained in the case of the implementation of a cogeneration system that uses the energy potential of gases are studied of combustion, for the production of the thermal agent for heating and preparation of hot water for consumption. of steam. From a functional point of view, at the level of a refinery, three superheated steam networks are needed, corresponding to three different pressure domains, which means that the results obtained in the study as the case may be, to refer to three distinct modes of operation of the cogeneration system. The main purpose of the operation of such a system for the combined production of electrical and thermal energy is to obtain as much energy as possible in the form of mechanical work by expanding steam in the turbines.**

Cuvinte cheie: *energie electrică, energie termică, cogenerare, producere, recuperare*

Keywords: *electricity, thermal energy, cogeneration, production, recovery.*

I. INTRODUCTION

In general terms, cogeneration means the production of electricity and thermal energy, using the same fuel, in the same installations [1].

Cogeneration installations have experienced a special development, due to the energy crises, and as a result of the Kyoto Protocol, regarding the reduction of greenhouse gas emissions [2].

Cogeneration systems have high efficiences and for this reason result in cost reductions for the production of electricity and thermal energy, as well as reducing the amount of polluting emissions.

Thermal energy can be produced as hot water, steam, hot air and can be used to heat buildings and to provide hot water for consumption or in technological processes.

Combined heat and power plants can be integrated near the final consumer. Under these conditions, it results in a minimization of transport and distribution losses and an improvement of the general performance of the electricity and/or heating agent distribution network.

The implementation of the cogeneration system presents several important advantages such as: the application of the most modern energy solutions, the rational use of fuel, lower production costs, the increase in the level of comfort in the apartments, the use of electricity and the pumping of the surplus into the national energy system, becoming electricity producers, which leads to investment efficiency [3].

II. GENERAL INDUSTRIAL COGENERATION TECHNOLOGIES

Industrial cogeneration systems are characterized by a much higher heating coefficient value. Industrial cogeneration systems can be economically efficient depending on the nature and degree of flattening of heat demand and its simultaneity with electricity demand [3], [4].

Industrial consumers mainly use steam, it being preferred to other thermal agents in heating and expansion processes in turbines and in other uses. Depending on the uses that the steam has, it is necessary for it to have certain qualities: temperature, pressure and position in relation to the phase balance curves [5].

The main industrial cogeneration systems are made with very low power backpressure groups (in piston groups), up to turbogenerator groups with superheated parameters, with condensing groups and adjustable outlets and, more recently, with condensing turbine groups with recovery the heat from the combustion gases from the technological furnaces [6].

Among the most widespread cogeneration technologies with steam turbines are: cogeneration system with counterpressure groups with high parameters (fig. 1), characterized by two pressure levels at the steam inlet to the turbines; cogeneration systems with groups with high parameters (fig. 2), which are equipped on the electric power production side with two groups of 19 MW each, simultaneously with the possibility of supplying heat to several groups of industrial consumers; cogeneration with condensing groups and adjustable outlets of 50 MW at live steam parameters of 130 at and 565°C (fig. 3) [1], [5], [6].

Lately, the development and modernization of industrial steam turbine cogeneration systems has led to the search and identification of efficient solutions for the production of both types of energy (electrical and thermal) both from the functional and economic point of view, as well as from the point of view of environmental protection.

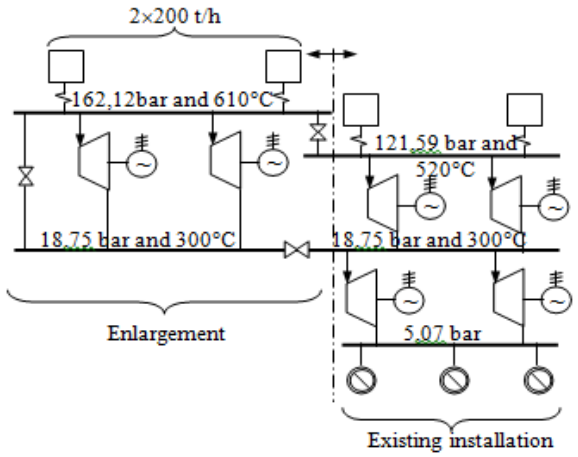

Fig. 1. Cogeneration system with backpressure groups with very high parameters [6]

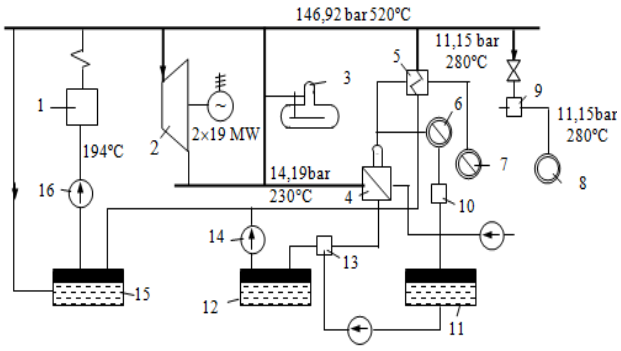

Fig. 2. Cogeneration system with high-parameter back-pressure groups:1 - forced-pass boiler; 2 - back-pressure turbine; 3 - heat accumulator; 4 - steam transformer battery; 5 - superheater; 6,7,8 - steam consumer group; 9 - reduction-cooling station; 10 - total demineralization plant; 11,12 - pressurized condensate tanks; 13 - degasser; 14 - feed pump; 15 - start-up tank; 16 - boiler water feed pump [4]

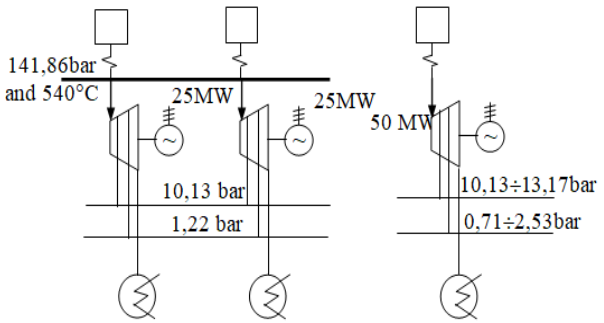

Fig. 3. Combined heat and power system with 25 MW condensing units with adjustable outlets and a 50 MW unit in expansion [3]

Such a solution can be considered as a cogeneration system with condensing turbine groups with heat recovery from the combustion gases of technological furnaces (fig. 4).

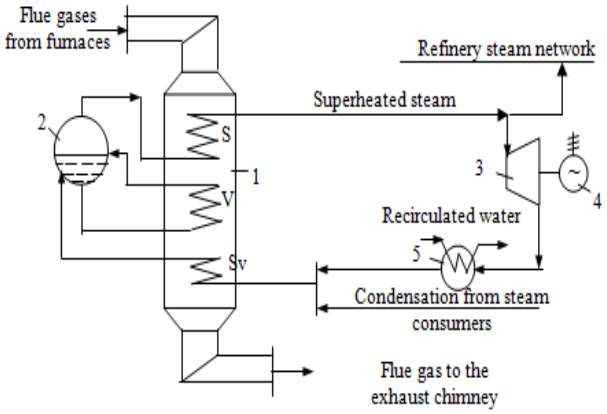

Fig. 4. Cogeneration system with heat recovery from combustion gases: 1 – recovery boiler; 2 – drum; 3 – turbine; 4 – generator; 5 – turbine condenser; E – saver; V – vaporizer; S - superheater [5]

Such an industrial cogeneration system, which is the subject of the energy efficiency analysis in this paper, is properly studied for three pressure ranges: low pressure steam network (p=3...6 bar); medium pressure steam network (p=12...25 bar); high pressure steam network (p=30...60 bar). [1]

The heat recovery plant basically complements a basic steam-operated plant working on the Clausius-Rankine cycle. The boiler of the basic plant produces saturated and superheated steam which in a certain proportion supplies different consumers, the unused superheated steam being diverted to a steam turbine coaxially mounted with an electric generator [7].

In the case of a variable demand for thermal energy, the system can work at maximum capacity, increasing the production of electricity. From the side outlets and through the final outlet, the T_2 turbine supplies all three steam networks of the refinery.

The cogeneration system with the recovery of heat from the combustion gases consists of a classic recovery boiler (1), for obtaining steam from the combustion gases, which is subsequently delivered to the networks corresponding to the respective state parameters at the refinery level [8]. Combustion gases circulate through the boiler under the action of an exhauster and are discharged into the atmosphere by means of a chimney with a high height. Part of the superheated steam is delivered to the refinery's steam network, with compatible parameters, when there is high demand from consumers, and the other part is expanded in the turbine (3). The turbine drives the electric generator (4) which supplies electricity to the refinery network. The steam released in the turbine is condensed and refuels the recovery boiler by means of a recirculation pump.

The realization of such cogeneration systems for the recovery of heat from the combustion gases, in comparison with the classical heat recovery systems, is possible only through steam generators. If during a period, the demand of steam consumers is low, the classic steam production system works with a very low economic efficiency, a possibility of efficiency being the expansion of steam not requested by consumers in turbines that drive electric generators.

In order to obtain as much energy as possible in the form of mechanical work by expanding the steam in the turbine, it is necessary that the pressure and degree of superheating of the steam be as high as possible [4].

III. Energy Indicators Of Cogeneration Systems With Combustion Gas Heat Recovery

The technical-economic parameters associated with this system of combined production of electricity and thermal energy are imposed by the heat potential of the combustion gases, by the flow rate and temperature level and by the quantity and quality of the steam produced.

These parameters are correlated through the physical properties of combustion gases and steam with the energy requirement at the level of the industrial consumer.

The determination of the technical-economic parameters is based on the values of the constructive-functional parameters of the cogeneration plant, which depending on the pressure level of the steam produced [4].

The analysis of the operation of the cogeneration system with heat recovery from the combustion gases is based on the following energy efficiency indicators [4], [6]:

1. The heat potential that can be recovered from the combustion gases:

$$Q_{ga} = m_{ga} \cdot \left(i_{ga}^{i} - i_{ga}^{e}\right)[kJ/s] \quad (1)$$

2. Steam flow produced in the boiler:

$$m_{steam} = \frac{Q_{ga}}{i_{ab}^{p} - i_{water}^{boiler}}[kg/s] \quad (2)$$

3. Steam turbine theoretical power:

$$P_T = m_{steam} \cdot \left(i_{ab}^{p} - i_{ab}^{e}\right)[kW] \quad (3)$$

4. Total area of heat exchange surfaces in the recovery boiler:

$$A_{sch,boiler} = \frac{Q_{ga}}{k \cdot \Delta t_{med}}[m^2] \quad (4)$$

5. Power required for boiler water supply pump:

$$P_{pump,al} = \frac{m_{steam} \cdot \Delta p}{\rho_a \cdot \eta \cdot 1000}[kW] \quad (5)$$

6. Water consumption at the turbine condenser:

$$m_{water} = \frac{m_{water} \cdot \left(i_{ab}^{e} - i_{cd}\right)}{c_{water} \cdot \Delta t_{water}}[t/h] \quad (6)$$

7. Energy efficiency of the recovery boiler:

$$\eta = \frac{Q_{steam}}{Q_{gas}} \cdot 100[\%] \quad (7)$$

8. Efficiency of electricity generation:

$$\eta_{el} = \frac{P_T \cdot \eta_{gen}}{Q_{ga}} \cdot 100[\%] \quad (8)$$

were m_{ga} is the mass flow of combustion gases, [kg/h], i_{ga}^{i} is the enthalpy of the combustion gases at the entrance to the recovery boiler, determined according to the temperature at which the combustion gases enter the boiler, [kJ/kg], i_{ga}^{e} is the enthalpy of the combustion gases at the exit from the recovery boiler, determined according to the temperature at which the combustion gases leave the boiler, [kJ/kg], i_{ab}^{p} is the enthalpy of steam entering the turbine, [kJ/kg], i_{water}^{boiler} is the enthalpy of the feed water of the recovered boilerr, [kJ/kg], i_{ab}^{e} is the enthalpy of the steam at the turbine exit, [kJ/kg], k is the global heat transfer coefficient, [W/(m^2·°C)], Δt_{med} is the average logarithmic temperature variation, [°C], Δp is the difference between the pump discharge pressure and suction pressure, [°C], ρ_a is the water density, [kg/m^3], η is the pump's average efficiency, [%], i_{cd} is the enthalpy of the condensate, [kJ/kg], c_{water} is the specific heat of water at constant pressure, [kJ/(kg·°C)], Δt_{water} is the cooling water temperature variation, [°C], Q_{steam} is the heat contained in the steam produced in the recovery boiler, [kJ/s], Q_{gas} is the heat contained in the combustion gases at the entrance to the recovery boiler, [kJ/s] and η_{gen} is the efficiency of the electric generator, [%].

IV. Data Required For Performing The Analysis

To carry out the case study, which aims to analyze the operation of industrial co-generation systems, using the thermal potential of the combustion gases, the following hypotheses will be taken into account:

- three different temperature regimes for the combustion gases at the boiler entrance will be considered heat recuperator: regime a, regime b and regime c (table 1);
- the temperature of the combustion gases at the exit from the recovery boiler is given in table.1;
- the flow of combustion gases entering the recovery boiler is determined by calculation, depending on the chemical composition of the combustion gases, related to the three thermal regimes studied;
- the pressure level of the steam produced by the recovery boiler is: 4 bar, 20 bar and 45 bar respectively;
- the chemical composition of the combustion gases is variable depending on the operating regime (table 1).

TABLE I.
INPUT PARAMETERS FOR PERFORMING THE ENERGY ANALYSIS RELATING TO THE OPERATION OF THE CONSIDERED COGENERATION SYSTEM [5], [9]

No. crt.	Parameter	Symbol	Unit Measure	Operating mode		
				a	b	c
1.	The temperature of the combustion gases at the entrance to the recovery boiler	t_{ga}^{i}	°C	676,30	483,80	351,70
2.	The temperature of the combustion gases at the exit from the recovery boiler	t_{ga}^{e}	°C	150	140	135
3.	The pressure of the steam produced in the recovery boiler	P_{steam}	bar	45	20	4

No. crt.	Parameter	Symbol	Unit Measure	Operating mode		
				a	b	c
4.	The temperature of the steam produced in the recovery boiler	T_{steam}	°C	400	400	300
5.	Water pressure at feed pump inlet [9]	$P_{water,\ al}$	bar	2	2	2
6.	Steam pressure at the turbine exit	p_{ab}^{e}	bar	0,06	0,06	0,06
7.	The temperature of the water supply to the recuperator boiler	t_{water}^{boiler}	°C	40	40	40
8.	The head of the steam at the exit of the turbine	x_{ab}	-	0,90	0,89	0,88
9.	Condensate pressure	p_{cd}	bar	0,10	0,10	0,10
10.	The average efficiency of the recovery boiler water supply pump [9]	η	%	70	70	70
11.	Global heat transfer coefficient in the recovery boiler [9]	k	$W/(m^2 \cdot K)$	45	45	45
12.	Fuel flow [9]	B_c	Nm^3/h	109,87	129,52	88,125
13.	The volume of wet combustion gases when burning one Nm^3 of fuel [9]	v_{ga}	Nm^3/Nm^3	29,59	20,20	26,54
14.	Chemical composition of combustion gases [9]	CO_2 O_2 CO N_2	% % % %	3,34 14,42 0,0004 82,23996	5,61 11,12 0,0000264 83,2636	4,19 13,61 0,00002 82,20998
15.	Excess air coefficient [9]	λ	-	4,42	2,07	3,10
16.	The temperature variation of the cooling water at the condenser	Δt_{water}	°C	5	5	5
17.	Average specific heat of cooling water at turbine condenser [9]	C_{water}	kJ/(kg·K)	4,184	4,184	4,184
18.	The efficiency of the electric generator	η_{gen}	-	0,995	0,995	0,995

V. RESULTS

Determining the energy efficiency indicators that characterize the operation of the cogeneration system with heat recovery from the combustion gases of a certain fuel, requires the use of the mathematical relationships presented in Part IV of this article.

For an eloquent presentation of the results obtained, considering that it is about three different operating regimes of the analyzed cogeneration system, it is resorted to the presentation of these results both in tabular form (table 2) and in graphic form, for the main indicators of energy efficiency (fig. 5...8).

TABLE II.
FUNCTIONAL ENERGY INDICATORS OF THE COENERATION SYSTEM WITH HEAT RECOVERY FROM COMBUSTION GASES RESULTS

No. crt.	The determined parameter	Symbol	Unit Measure	Operating mode		
				a	b	c
1.	Thermal potential, recoverable from combustion gases	Q_{ga}	kJ/h	2406654,78	1252213,51	691828,87
1.1	Combustion gas flow	m_{ga}	Nm^3/h	3251,05	2616,30	2338,84
1.2	Enthalpy of combustion gases at the entrance to the recovery boiler	i_{ga}^{i}	kJ/ Nm^3	937,76	663,05	472,98
1.3	Enthalpy of carbon dioxide from the combustion gases at the entrance to the recovery boiler	i_{CO2}	kJ/Nm^3	1405,64	958,31	668,97
1.4	Enthalpy of oxygen from the combustion gases at the entrance to the recovery boiler	i_{O2}	kJ/Nm^3	967,58	674,98	481,35
1.5	Enthalpy of nitrogen from the combustion gases at the entrance to the recovery boiler	i_{N2}	kJ/Nm^3	913,53	641,56	461,55
1.6	Enthalpy of carbon monoxide from the combustion gases at the entrance to the recovery boiler	i_{CO}	kJ/Nm^3	794,23	511,28	385,21
1.7	The enthalpy of the combustion gases at the exit from the recovery boiler	i_{ga}^{e}	kJ/kg	197,49	184,43	177,18
1.8	The enthalpy of the carbon dioxide from the combustion gases at the exit from the recovery boiler	i_{CO2}	kJ/Nm^3	261,56	232,01	223
1.9	Enthalpy of oxygen from the combustion gases at the exit from the recovery boiler	i_{O2}	kJ/Nm^3	198,95	183,76	177,11
1.10	Enthalpy of nitrogen from the combustion gases at the exit from the recovery boiler	i_{N2}	kJ/Nm^3	194,63	181,32	174,84
1.11	Enthalpy of carbon monoxide from the combustion gases at the exit from the recovery boiler	i_{CO}	kJ/Nm^3	157,73	147,34	141,99
2.	The flow of steam produced in the recovery boiler	m_{steam}	kg/h	794,14	406,99	222,79
2.1	The enthalpy of the steam produced in the recovery boiler	i_{ab}^{p}	kJ/kg	3202	3246	3065
2.2	Enthalpy of the water entering the recovery boiler	i_{water}^{bolier}	kJ/kg	171,5	169,2	167,7
3.	Theoretical steam turbine power	P_T	kW	193,46	106,85	48,78
3.1	Enthalpy of steam at the exit from the turbine	i_{ab}^{e}	kJ/kg	2325	2300,85	2276,7

No. crt.	The determined parameter	Symbol	Unit Measure	Operating mode		
				a	b	c
4.	The total area of the heat exchange surfaces, at the recovery boiler level, in the case of countercurrent flow	$A^{cc}_{sch,boiler}$	m^2	296,20	303,59	210
4.1	Average logarithmic difference in temperature during countercurrent flow	$\Delta t_{med,cc}$	°C	180,56	91,66	73,21
5.	Power required for boiler water supply pump	$P_{pump,al}$	kW	1,37	0,29	0,02
5.1	The difference between the water pressure entering the boiler and entering the pump	Δp	bar	43	18	2
5.2	The density of the water with which the boiler is fed	ρ_a	kg/m^3	992,22	992,22	992,22
6.	Water consumption at the turbine condenser	m_{water}	t/h	82,51	41,81	24,24
6.1	Condensate enthalpy	i_{cd}	kJ/kg	151,49	151,49	151,49
6.2	Condensate temperature	t_{cd}	°C	36,18	36,18	36,18
7.	The energy efficiency of the recovery boiler	η_{cz}	%	83,41	76,16	61,73
7.1	The heat contained in the steam produced in the recovery boiler	Q_{steam}	kJ/s	706,34	366,97	189,68
7.2	The heat contained in the combustion gases entering the recovery boiler	Q_{gas}	kJ/s	846,86	481,87	307,28
8.	The yield of electricity production	η_{el}	%	28,79	30,56	25,26

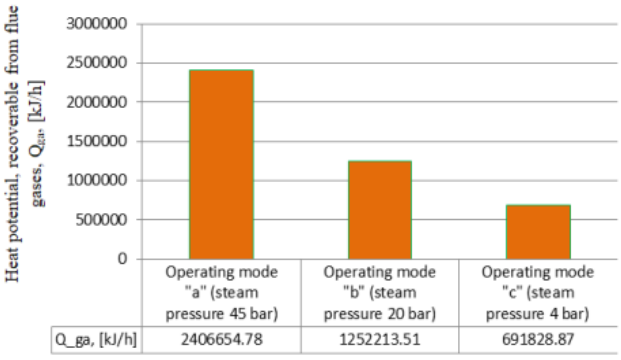

Fig. 5. The theoretical power of the steam turbine when operating in the three pressure regimes

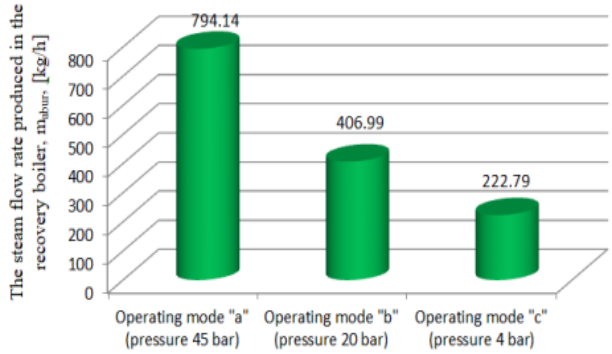

Fig. 6. The variation of the steam flow produced in the recovery boiler depending on the pressure regime of the steam produced

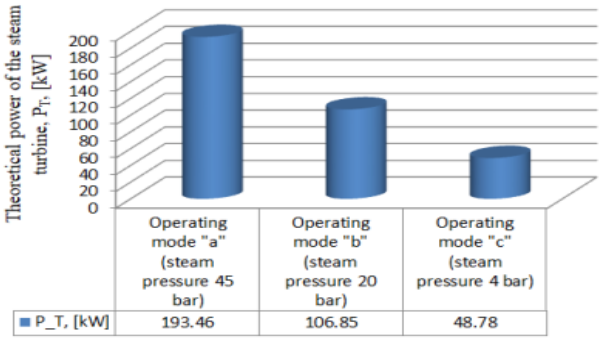

Fig. 7. The theoretical power of the steam turbine when operating in the three pressure regimes

From the analysis of the diagram in figure 6, it can be seen that with the increase in the pressure of the produced steam from 4 bar to 45, the steam mass flow rate increases approximately 3.56 times (from 222.79 kg/h to 794.14 kg/h).

The increase in the theoretical power at the turbine shaft is directly proportional to the increase in the pressure of the superheated steam released in the turbines, and from the diagram in figure 7, an increase in the electric power from 48.78 kW to 193.46 kW can be observed, i.e. approximately 4 times.

At the same time, the increase in the pressure of the steam produced in the boiler from 4 to 45 bar leads, in addition to the increase in the theoretical power of the steam turbine, to an increase in the yield of electricity production from 25.26% to 30.56% (fig. 8). It is observed that the highest electrical efficiency is obtained in the case of expansion of medium-pressure steam in the steam turbine, even if the electrical power produced is lower than in the variant of expansion of high-pressure steam.

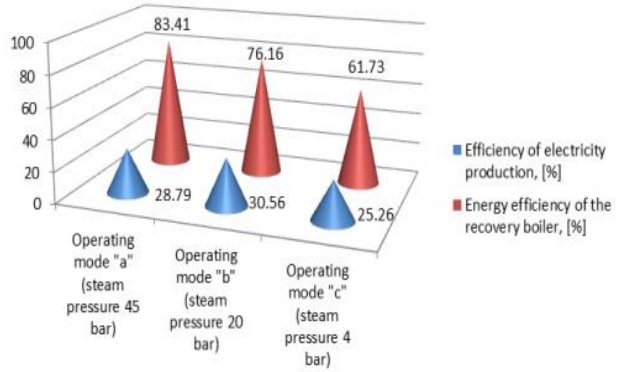

Fig. 8. The variation of the yield of electricity production, η_{el} and, of the energy yield of the recovery boiler depending on the pressure regime of the produced steam

Also, the same increase in the pressure of the steam produced in the recovery boiler, leads to the increase of the recovery boiler's load by approximately 35%, from 61.73% to 83.41% (fig.8).

VI. Conclusion

The cogeneration systems with the recovery of heat from combustion gases requires steam generators with special construction that allow operation at variable re-

gimes of flow rates, pressures, thermal energy and electricity.

When, in a certain period, the steam demand of thermal consumers is low, the operation of the steam production system would be performed with a reduced economic efficiency.

For the energy efficiency of the operation of such a system, functional measures are required that concern the expansion of steam not requested by thermal consumers on the industrial platform, in turbines that drive electric generators.

Obtaining the greatest possible amount of energy in the form of mechanical work by expanding the steam in the turbine is possible in the conditions where the pressure and degree of superheating of the steam are as high as possible.

In case of high pressure steam production (p_{steam}=45 bar), the efficiency of the recovery boiler is approximatively 83%, obtaining a flow of 0,22 kg/s, at a temperature of 400°C and a pressure of 45 bar, which implies a thermal potential of approx 706 kJ/s. The flow of combustion gases required in this case is 0.903 kg/s with a temperature of approximately 676°C, which represents a thermal potential of approximately 846 kJ/s.

The efficiency of electricity production under these conditions is approximately 29%.

In the case of medium pressure steam production (p_{steam}=20 bar), the efficiency of the recovery boiler is approximately 76%, obtaining a flow rate of 0.11 kg/s, at a temperature of 400°C and a pressure of 20 bar, which implies a thermal potential of approximately 367 kJ/s. The flow of combustion gases required in this case is 0.727 kg/s with a temperature of approximately 483°C, which represents a thermal potential of approximately 482 kJ/s.

The efficiency of electricity production under these conditions is approximately 30%.

In the case of low pressure steam production (p_{abur}=4 bar), the efficiency of the recovery boiler is approximately 62%, obtaining a flow rate of 0.06 kg/s, at a temperature of 300°C and a pressure of 4 bar, which implies a thermal potential of approximately 190 kJ/s. The flow of combustion gases required in this case is 0.650 kg/s with a temperature of approximately 351°C, which represents a thermal potential of approximately 307 kJ/s.

The efficency of electricity production under these conditions is approximately 25%.

Analyzing further the results obtained in the three operating regimes of the turbine cogeneration system with steam produced by recovering the thermal potential from the combustion gases, the following can be observed:

1. the cooling water flow required at the turbine condenser decreases with the decrease in the pressure of the generated steam, from 82.51 t/h in the case of steam produced at 45 bar, to 24.24 t/h in the case of steam produced at 4 bar , due to the variation of the steam flow rate;

2. the power required for the water supply pump of the boiler, although it increases approximately 68 times at the pressure of 45 bar compared to the pressure of 4 bar, the absolute level of consumption is quite small, representing approximately 0.71% of the electrical power produced by turbines - in the case of operating mode a, 0.27% of the electrical power produced by the turbines - in the case of operating mode b, respectively, 0.04% of the electrical power produced by the turbines - in the case of operating mode c operation;

3. The main disadvantage of increasing the pressure of the produced steam is represented by the increase in investment. This increase is due, on the one hand, to the need for a larger heat exchange surface (a 44.57% increase in the surface of the coils at a pressure of 20 bar compared to 4 bar) and, on the other hand, to the increase in thickness tube walls.

When the cogeneration system with the recovery of heat from the combustion gases does not operate in cogeneration mode, the production of low pressure steam is efficient, and if the installation operates in cogeneration mode, the production of steam of the highest pressure is very advantageous.

ACKNOWLEDGMENT

Source of research funding in this article: Research program of the Electrical Engineering Department financed by the University of Craiova.

Contribution of authors:

First author – 55%

First coauthor – 30%

Second coauthor – 15%

Received on September 3, 2024

Editorial Approval on November 28, 2024

REFERENCES

[1] V. Athanasovici et al. *Thermal Engineering Treatise. Heat Supply. Cogeneration* (*Tratat de inginerie termică. Alimentări cu căldură. Cogenerarea*), Bucharest: AGIR, 2010.

[2] R. C. Dinu, and I. Mircea, "Study of cogeneration systems in the chemical industry" ("Studiul sistemelor de cogenerare în industria chimică"), Scientific Bulletin of the Technical University of Civil Engineering, Bucharest, December 2006.

[3] R. C. Dinu, *Cogeneration Installations* (*Instalaţii de cogenerare*), course, University of Craiova, 2021, www.retele.elth.ucv.ro/Dinu Radu Cristian/ Cogeneration installations.

[4] R. C. Dinu, and N. Popescu, *Energetics of Cogeneration Power Plants* (*Energetica instalaţiilor de producere a energiei în cogenerare*), Craiova: Universitaria, 2013.

[5] L. C. Cosma, *Comparative Analysis Regarding the Operation of Industrial Co-generation Systems, using the Thermal Potential of Combustion Gases* (*Analiza comparativă privind funcţionarea sistemelor de co-generare industriale, folosind potenţialul termic al gazelor de ardere*), Dissertation, University of Craiova, Electrical Engineering Faculty, June 2024, sc. coord. R.-C. Dinu.

[6] R. C. Dinu, *Study of Cogeneration Energy Systems in Variable Regime* (*Studiul sistemelor energetice de cogenerare în regim variabil*), PhD Thesis, Technical University of Civil Engineering, Bucharest, 2006.

[7] M. Moldovanu et al., Modernization of Centrally Produced Heat Supply Systems using Low / Medium Power Cogeneration (Modernizarea sistemelor de alimentare cu energie termică produsă centralizat prin utilizarea cogenerării de mică/medie putere), project report "DHCAN. Promoting Cogeneration in Centrally Produced Thermal Energy Supply Systems in Romania", June 2004.

[8] *** *Cogeneration, a Technology Portrait*, Institute for Thermal Turbomachinery and Machine Dynamics, Graz University of Technology, Vienna, 2002.

[9] *** *ALRO Energy Balance for 2021*, (*Bilanţ energetic ALRO pentru anul 2021*), Research contract report no. 2C/2013, University of Craiova.

DOI: 10.52846/AUCEE.2024.14

Research Trends in Hybrid Power Supply Systems for Standalone Houses

Laurențiu-Alex Mustață* and Elena Helerea*

* Transilvania University, Faculty of Electrical Engineering and Computer Science, Department of Electrical Engineering and Applied Physics, Brașov, România, laurentiu.mustata@unitbv.ro, helerea@unitbv.ro

***Abstract* – This paper uses a bibliometric research approach to systematically analyse the tendences of research literature on Hybrid Power Supply Systems (HPSS) for standalone houses. The study explores the integration of hybrid energy solutions in residential applications, focusing on key areas such as design, supply strategies, and system control. A review of existing research reveals that while standalone energy systems are well-documented, studies addressing the combined aspects of hybrid system design, supply, and advanced control mechanisms remain limited. This gap highlights the need for more holistic approaches that consider the interaction between energy sources, management systems, and sustainability goals. Emphasis is placed on monitoring and control technologies, which are critical for optimizing system performance but are often explored in isolation from supply strategies. The analysis further shows that the complexity of research topics tends to narrow as more specific concepts are combined, resulting in significantly fewer studies that integrate all key aspects. Comprehensive studies addressing the full spectrum of hybrid design, supply, and control mechanisms are rare, with only one paper found in both Scopus and IEEE databases that covers these areas simultaneously. This indicates an important research gap and underscores the potential for future interdisciplinary work in developing sustainable HPSS for standalone houses in remote and off-grid settings.**

Cuvinte cheie: *sursă hibridă de alimentare, sistem off-grid, casă izolată, sustenabilitate economică, impact asupra mediului*

Keywords: *hybrid power supply, off-grid system, standalone house, economic sustainability, environmental impact*.

I. Introduction

The traditional energy sector is characterized by centralized generation and has served as the dominant model for energy distribution globally for many years. Due to its large-scale production, this model has the advantages of being a cost efficient and reliable power supply in urban areas. However, besides its limitations of high transmission losses and dependence on fossil fuels, this model also struggles to provide reliable energy access to geographically isolated remote areas, where extending the grid is costly and inefficient.

To address these challenges, off-grid systems, including diesel generators or standalone renewable solutions, have emerged as alternatives. Despite their potential, these systems face drawbacks like high operational costs, environmental concerns or energy intermittency due to reliance on favorable weather conditions. These limitations highlight the need for more robust and sustainable solutions.

To overcome the limitations of single-source systems, the integration of multiple energy sources has been applied as a promising solution. Hybrid Power Supply Systems (HPSS) combine two or more energy sources to meet the demands of off-grid applications. Energy intermittency is addressed by integrating renewable energy sources (solar, wind, etc.) with energy storage and backup systems (petrol, diesel, biogas, etc.). Standalone houses in remote regions are a common application of HPSS. By providing reliable and sustainable energy to these households, hybrid systems play an important role.

The growing focus on HPSS for standalone houses requires a comprehensive analysis of research trends, gaps, and emerging solutions to synthesize knowledge and guide future developments in the field.

This paper employs a bibliometric research approach to identify and analyse the existing body of literature on HPSS for standalone houses. It aims to uncover key characteristics of these systems, the factors influencing their development and implementation, and the challenges as well as opportunities shaping their future evolution.

II. Methodology

This chapter outlines the methodology applied in the analysis of HPSS for standalone houses. The methodology includes keyword searches, data sources, data processing techniques, and visualization strategies.

A. Bibliometric Methodology

A bibliometric approach was chosen to identify and analyse relevant academic literature. The search strategy applied specific English-language keyword combinations designed to target research publication/article titles, abstracts or keywords on standalone houses and hybrid supply systems. The keyword combinations used are presented in Table I.

These combinations were selected to capture studies focusing on system design, energy supply strategies, and operational control mechanisms of HPSS for standalone houses. The inclusion of the OR operator in terms like (“house” OR “home”) ensured coverage of both terminologies commonly used in different regions or disciplines. Terms such as “hybrid” AND “design” focused on the integration of multiple energy sources, while (“monitor” OR “control”) addressed technological aspects related to system management.

TABLE I.
KEYWORD FRAMEWORK FOR BIBLIOMETRIC RESEARCH ON STANDALONE HOUSE HYBRID POWER SUPPLY SYSTEMS

Factor of interest	Keyword combinations
Housing system design	"standalone" AND ("house" OR "home")
	"standalone" AND ("house" OR "home") AND "design"
Hybrid energy systems	"standalone" AND ("house" OR "home") AND "hybrid"
	"standalone" AND ("house" OR "home") AND "hybrid" AND "design"
Energy supply and distribution	"standalone" AND ("house" OR "home") AND "supply"
	"standalone" AND ("house" OR "home") AND "hybrid" AND "design" AND "supply"
Operational management and control	"standalone" AND ("house" OR "home") AND ("monitor" OR "control")
Integrated system development	"standalone" AND ("house" OR "home") AND "hybrid" AND "supply" AND ("monitor" OR "control")
	"standalone" AND ("house" OR "home") AND "hybrid" AND "design" AND "supply" AND ("monitor" OR "control")

To aid in the interpretation of the results, the colour code presented in Table I was used to establish a visual connection between the key factors of interest, the keyword combination search results in Table II and the graphs in the following section.

B. Data Sources

The Scopus and IEEE Xplore databases were selected as the sources for data collection. Both databases are widely recognized for their reliability and access to high-quality peer-reviewed publications. Scopus was chosen for its comprehensive coverage of multidisciplinary research, ensuring a broad view of studies. IEEE Xplore was included for its focus on engineering and technology-related research, which is important for understanding system design and technological advancements in HPSS.

C. Data Processing

The collected data were processed to display graphs of trends over time. Artificial Intelligence was also used to synthesize abstracts and identify recurring themes across the selected studies, including key factors influencing HPSS research and development, namely economic, environmental, and infrastructural aspects. This approach allowed for the efficient categorization of research topics and highlighted common areas of interest. Priority was given to papers with high citation metrics to ensure the inclusion of influential studies.

D. Visualization Techniques

To present the results, visualization techniques were used to create graphs showing year-by-year cumulative growth of publications in the field. These graphs highlight trends and the evolution of research interest, providing an accessible way to identify periods of increased activity in HPSS research for standalone houses. The graphs include all years with identified publications, including isolated spikes in research activity. From 2011 onward, they display consecutive years regardless of publication presence, ensuring that gaps or pauses in research remain visible. This method offers a comprehensive view of publication patterns over time and highlights periods of stalled research, which may indicate shifts in academic priorities or external influences on the field.

III. RESULTS AND OBSERVATIONS

A. General Bibliometric Results

Table II displays the number of publications identified in the Scopus and IEEE databases for the keyword combinations presented above for HPSS for standalone houses.

The combination "standalone" AND ("house" OR "home") yielded a large number of papers in both Scopus and IEEE. This reflects the broad coverage of foundational research on standalone housing systems in the literature.

The search focusing on standalone housing "design", "hybrid" systems and their combination showed a smaller number of publications, reflecting a narrower focus on architectural and system-level design aspects. This also suggests that there is still limited research on hybrid energy systems for standalone houses and that this technology is yet to be fully explored.

Including "supply" alongside the terms above gave 13 papers in Scopus and 10 in IEEE. This trend highlights a focused and specialized research area for energy supply strategies within standalone housing. The limited number of papers emphasizes the complexity and unique challenges associated with developing comprehensive solutions for standalone houses that incorporate hybrid energy systems.

The combination ("monitor" OR "control") with "standalone" AND ("house" OR "home") showed a significant research activity focused on the operational management, monitoring, or control of standalone housing systems.

Given that only one paper matched all the keywords selected, there seems to be a significant opportunity for future studies to address the gaps in this field. By doing so, studies could provide insights into effective integration strategies and innovations that would enhance the approach to sustainability, efficiency, control, and adaptability of energy systems in standalone housing.

TABLE II.
RESULTS FOR THE BIBLIOMETRIC RESEARCH KEYWORD FRAMEWORK IN THE SCOPUS AND IEEE DATABASES

Keyword combinations	No. of Scopus Papers	No. of IEEE Papers
"standalone" AND ("house" OR "home")	927	394
"standalone" AND ("house" OR "home") AND "design"	269	159
"standalone" AND ("house" OR "home") AND "hybrid"	114	52
"standalone" AND ("house" OR "home") AND "hybrid" AND "design"	38	24
"standalone" AND ("house" OR "home") AND "supply"	130	82
"standalone" AND ("house" OR "home") AND "hybrid" AND "design" AND "supply"	13	11
"standalone" AND ("house" OR "home") AND ("monitor" OR "control")	243	199
"standalone" AND ("house" OR "home") AND "hybrid" AND "supply" AND ("monitor" OR "control")	7	6
"standalone" AND ("house" OR "home") AND "hybrid" AND "design" AND "supply" AND ("monitor" OR "control")	1	1

B. *Key Trends Visualization*

This section introduces cumulative research graphs for three selected keyword combinations related to HPSS for standalone houses. These graphs provide insights into the evolution of research trends, allowing for a comprehensive understanding of the field's development.

1) Hybrid energy systems: These publications focus on designing hybrid energy systems for standalone houses. This reflects the growing need for combining different energy sources to achieve a stable and efficient energy supply.

- *"standalone" AND ("house" OR "home") AND "hybrid":* The cumulative graphs for Scopus (Fig. 1) and IEEE (Fig. 2) show 114 and 52 publications by 2024, respectively.

This indicates a systematically growing focus on hybrid energy systems for standalone houses.

- *"standalone" AND ("house" OR "home") AND "hybrid" AND "design":* The first paper using these keywords was published in 2011 in Scopus and 2006 in IEEE. By 2024, the number of publications reached 38 in Scopus (Fig. 3) and 24 in IEEE (Fig. 4).

This reflects a later emergence of this trend, which justifies the relatively lower number of papers.

2) Energy supply and distribution: This trend explores how energy is supplied to standalone houses. It demonstrates the importance of ensuring reliable energy delivery to individual homes, especially in areas not connected to centralized grids.

Challenges associated with optimizing energy distribution, managing intermittency, and integrating renewable sources effectively within these systems are considered. This area is important for advancing HPSS, as it directly impacts the feasibility and sustainability of standalone energy solutions.

- *"standalone" AND ("house" OR "home") AND "supply":* The first papers using these keywords were published in 1966. The cumulative publication trends for the Scopus database (Fig. 5) and for the IEEE database results (Fig. 6) illustrate steady growth over the years, with the number of publications reaching 130 in Scopus and 82 in IEEE by 2024.

- *"standalone" AND ("house" OR "home") AND "hybrid" AND "design" AND "supply":* The cumulative graphs for the Scopus (Fig. 7) and IEEE (Fig. 8) databases show a limited increase in research interest regarding the effective integration of HPSS systems, particularly in terms of system-level design.

The first studies using these keywords were published in 2011 in Scopus and in 2006 in IEEE. However, both databases show gaps of 2-3 years with no publications in this field. By 2024, the number of publications had reached 13 in Scopus and 11 in IEEE.

3) Operational management and control: This trend emphasizes the role of monitoring and controlling energy systems in standalone houses, highlighting the significance of optimizing energy use, efficiency, and reliability in these setups.

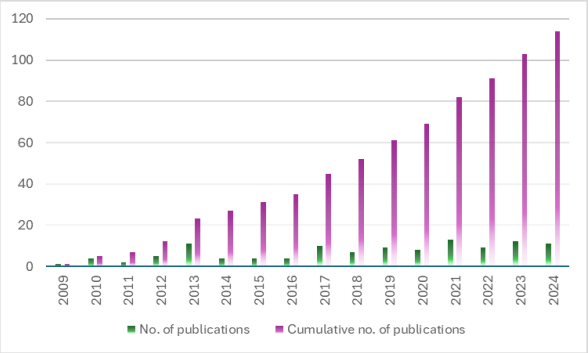

Fig. 1. Number of publications per year in the Scopus database for the keyword group: "standalone" AND ("house" OR "home") AND "hybrid".

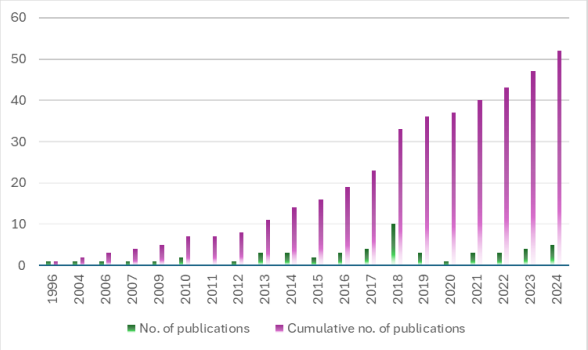

Fig. 2. Number of publications per year in the IEEE database for the keyword group: "standalone" AND ("house" OR "home") AND "hybrid".

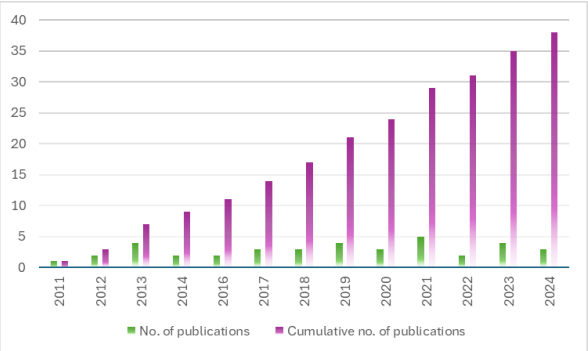

Fig. 3. Number of publications per year in the Scopus database for the keyword group: "standalone" AND ("house" OR "home") AND "hybrid" AND "design".

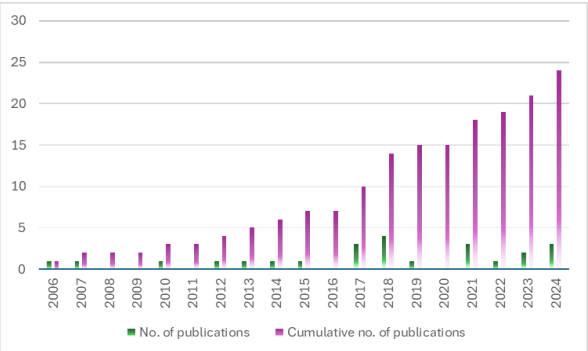

Fig. 4. Number of publications per year in the IEEE database for the keyword group: "standalone" AND ("house" OR "home") AND "hybrid" AND "design".

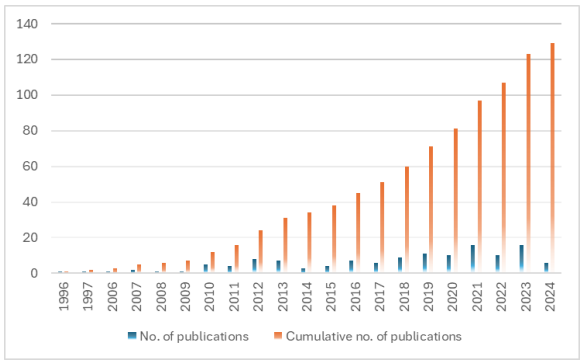

Fig. 5. Number of publications per year in the Scopus database for the keyword group: "standalone" AND ("house" OR "home") AND "supply".

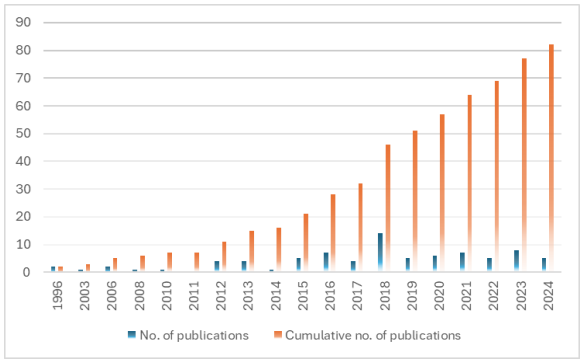

Fig. 6. Number of publications per year in the IEEE database for the keyword group: "standalone" AND ("house" OR "home") AND "supply".

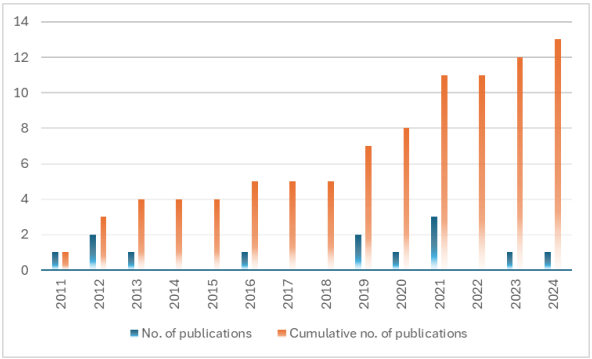

Fig. 7. Number of publications per year in the Scopus database for the keyword group: "standalone" AND ("house" OR "home") AND "hybrid" AND "design" AND "supply".

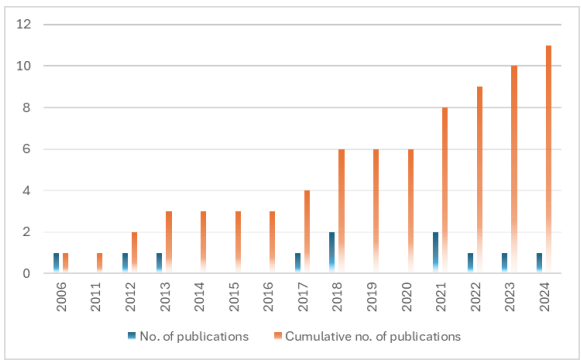

Fig. 8. Number of publications per year in the IEEE database for the keyword group: "standalone" AND ("house" OR "home") AND "hybrid" AND "design" AND "supply.

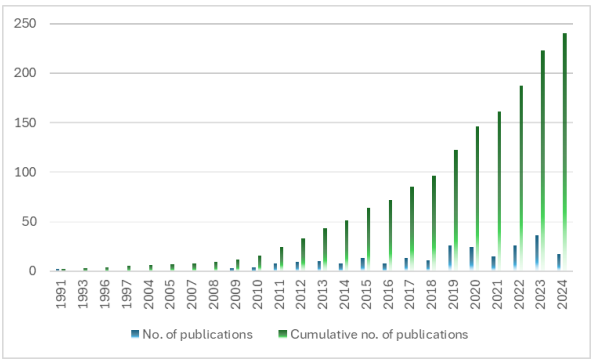

Fig. 9. Number of publications per year in the Scopus database for the keyword group: "standalone" AND ("house" OR "home") AND ("monitor" OR "control").

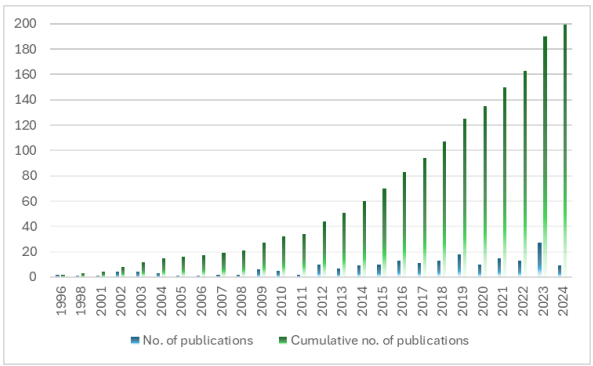

Fig. 10. Number of publications per year in the IEEE database for the keyword group: "standalone" AND ("house" OR "home") AND ("monitor" OR "control").

- *"standalone" AND ("house" OR "home") AND ("monitor" OR "control"):* The cumulative graphs for the Scopus (Fig. 9) and IEEE (Fig. 10) databases illustrate the growing research interest in this area. Although the first papers using these keywords were published in 1991 in Scopus and in 2006 in IEEE, the period between 1991 and 2011 saw only a few publications, indicating a delay in the focused research on this topic. The significant increase in publications after 2011 highlights a shift toward addressing the technological and operational challenges of efficiently managing standalone energy systems. By 2024, the number of publications had reached 243 in Scopus and 199 in IEEE, reflecting the growing importance of real-time control systems, monitoring tools, and adaptive management strategies in enhancing the performance and reliability of energy solutions for standalone houses.

C. *In-depth Analysis*

This section focuses on analysing three key factors influencing HPSS research and development: economic, environmental, and infrastructural aspects.

The research papers included in this section were selected based on their relevance to the authors' study objectives and their alignment with the three key factors, with some also being highly cited. The secondary set of keywords that refined the selection process include:

- Economic factors: Keywords such as price, cost, economic policy, financial incentives, and subsidy were used to identify literature addressing the economic viability and policy frameworks impacting HPSS adoption.

- Environmental factors: Keywords such as environmental impact, sustainability, emission reduction, and renewable energy policy were included to capture research addressing the environmental implications of HPSS.
- Infrastructural factors: Keywords such as off-grid systems, energy access, remote regions, distributed generation, and energy quality were used to identify studies on the application of HPSS in areas lacking extended grid infrastructure.

Table III summarizes the selected papers, which were identified based on their relevance to standalone house energy systems, their alignment with the focus areas of the authors, and their potential to advance HPSS research. The studies are categorized by the key factors.

Paper [1] presents the simulation of a PV hybrid system for an off-grid standalone house in remote Nigeria, focusing on energy supply and dynamic response to changes in input. The system includes a PV array, battery storage, and generator backup. It demonstrates the feasibility of standalone HPSS in remote areas and addresses the challenges of intermittency and storage management.

Paper [2] examines a standalone solar dish Stirling system for off-grid rural electrification in Tunisia. It highlights the integration of renewable energy sources with advanced thermal modelling and simulation. The study focuses on system autonomy, power stability, and reliability in remote areas.

TABLE III.
CLASSIFICATION OF MOST RELEVANT STANDALONE HOUSE HPSS RESEARCH RESULT PAPERS BY KEY FACTORS: ECONOMIC, ENVIRONMENTAL AND INFRASTRUCTURAL

Title	Year	Category
Dynamic Simulation of a Standalone Photovoltaic Hybrid System of a Remote house in Nigeria [1]	2021	Infrastructure
Performance evaluation of a stand-alone solar dish Stirling system for power generation suitable for off-grid rural electrification [2]	2016	Infrastructure/ Environment
Energy Management of PV/Wind/Battery Hybrid Energy System Based on Batteries Utilization Optimization [3]	2017	Infrastructure/ Environment
Hybrid diesel-wind system with battery storage operating in standalone mode: Control and energy management – Experimental investigation [4]	2017	Infrastructure
Optimal Economic Analysis of Hybrid off Grid (Standalone) Energy System for Provincial Capitals of Pakistan [5]	2019	Economic
Feasibility evaluation of a hybrid renewable power generation system for sustainable electricity supply in a Moroccan remote site [6]	2020	Environment/ Economic
Designing standalone hybrid energy systems minimizing initial investment, life cycle cost and pollutant emission [7]	2013	Environment/ Economic
Design, Optimization and Control of Standalone Solar PV/Fuel Cell Hybrid Power System [8]	2017	Environment/ Economic
A Stand-Alone Hybrid Renewable Energy System Assessment Using Cost Optimization Method [9]	2017	Environment/ Economic
Energy Management Strategy with a Hybrid Renewable Energy System for a Standalone House [10]	2024	Environment

Paper [3] presents energy management for PV-wind-battery hybrid systems operating in standalone or grid-connected modes, emphasizing grid stability and battery optimization.

Paper [4] investigates a hybrid diesel-wind system with battery storage for standalone operation. It presents experimental results under various wind and load conditions, emphasizing control and energy management strategies. The study provides insights into the operational challenges and effectiveness of hybrid systems in isolated settings.

Paper [5] designs a technical and economically feasible standalone/hybrid (PV/Wind/Diesel/Battery) off-grid system to increase renewable energy contributions in Pakistan's total energy mix. The focus is on financial viability, using HOMER Pro for optimization.

Paper [6] assesses various hybrid renewable energy systems (PV, Wind, Biomass) for a remote Moroccan village, focusing on cost-effectiveness and sustainability.

Paper [7] presents a model to minimize initial investment, life cycle cost, and pollutant emissions in standalone hybrid energy systems. The study emphasizes the integration of renewable energy sources in early design stages.

Paper [8] optimizes a standalone solar PV/fuel cell hybrid system for a community (~150 houses). Balances renewables, costs, and emissions. Integrates solar-based hydrogen production with negligible CO2 emissions and high system efficiency.

Paper [9] utilizes the HOMER software to optimize hybrid systems (solar, wind, hydrogen, and battery). Identifies combined battery-hydrogen storage as cost-effective and efficient for rural homes and farms in remote areas.

Paper [10] explores the energy management of a PV-battery-diesel hybrid system, ensuring optimized battery life and minimal diesel use. Focused on dynamic energy demands under seasonal variations.

IV. DISCUSSIONS

While providing valuable insights into technical solutions, there is a noticeable gap in direct discussions on economic implications and financial incentives. Future research should delve deeper into financial mechanisms, such as subsidies, grants, and innovative financing models, to make HPSS economically viable, especially in economically disadvantaged regions.

Regarding the environmental aspect, the literature significantly emphasizes sustainability, emission reduction, and integrating renewable energy sources in standalone systems. However, more detailed lifecycle analyses are required to guide policy development effectively, particularly concerning the full environmental footprint of HPSS components.

In terms of infrastructural aspects, research focuses on HPSS in off-grid, remote regions with limited access to conventional energy infrastructure. Papers often address the challenges of system autonomy and reliability in isolated settings. More research is needed to develop practical solutions that are technically viable, economically sustainable, and environmentally sound, including innovations in microgrid systems, smart grids, and energy efficiency measures.

These discussions show that while significant strides have been made in understanding HPSS for standalone houses, there is still a need for more focused research on

economic aspects and a deeper understanding of the financial mechanisms supporting these systems. The environmental implications are well-documented but require more in-depth study to guide policy development effectively. The infrastructural challenges, particularly in remote regions, remain a critical area of focus for advancing HPSS solutions.

A. New research directions

Future research on standalone house energy systems should prioritize integrating advanced optimization techniques and exploring innovative configurations, such as DC nanogrids and hybrid nanogrids, to enhance economic viability and environmental sustainability. DC nanogrids, which operate using direct current for efficient energy distribution and reduced conversion losses, and hybrid nanogrids, combining multiple renewable energy sources, offer promising pathways for improving energy reliability and cost-effectiveness. Sophisticated algorithms, like improved genetic algorithms and multi-objective optimization models, can further refine system sizing and optimize the integration of diverse energy sources, ensuring scalability across varied geographic and climatic conditions.

Emerging concepts such as Local Energy Communities (LECs) and Energy as a Service (EaaS) present transformative opportunities for the adoption of standalone and hybrid energy systems. LECs, where households share surplus energy within a microgrid, enhance energy access and foster cooperative resource utilization, while EaaS models provide flexible, subscription-based energy solutions that reduce the burden of upfront costs. EaaS is a business model where LEC members pay for energy services rather than owning and maintaining the energy infrastructure themselves. Instead of investing in costly energy systems like solar panels, batteries, or heating/cooling equipment, customers subscribe to an EaaS provider who manages, operates, and optimizes these assets on their behalf. This model offers greater flexibility and accessibility, as customers only pay for the energy they consume or for specific energy-related services.

Research should explore how these models can be integrated with nanogrids to create resilient, decentralized energy ecosystems, especially for rural or underserved areas, and policy frameworks and investments should support the transition to these advanced models.

By addressing the interconnections between economic, environmental, and infrastructural factors, future work can help accelerate the deployment of hybrid nanogrids and foster a sustainable energy transition on both local and global scales.

V. CONCLUSIONS

In this paper, a bibliometric research approach to examine and analyse the existing body of literature on Hybrid Power Supply Systems for standalone houses is developed. The study identified the defining features of these systems, the factors that drive their development and implementation and understand the challenges and opportunities that will shape their future evolution.

Limitations of this study include reliance on English-language publications and potential biases in the database's indexing of certain fields or journals, which may affect the comprehensiveness of the collected data. Despite this, the study provides a valuable overview of the current landscape of HPSS for standalone houses. The insights gained from this analysis will guide future research and the development of more sustainable and scalable energy solutions, improving energy access in remote and isolated regions.

ACKNOWLEDGMENT

Source of research funding in this article: Research program of the Transilvania University.

Contribution of authors:

First author – 50%

First coauthor – 50%

Received on September 10, 2024

Editorial Approval on November 27, 2024

REFERENCES

[1] J. C. Ozogbuda, and M. T. Iqbal, "Dynamic simulation of a standalone photovoltaic hybrid system of a remote house in Nigeria," in *2021 IEEE 12th Annual Information Technology, Electronics and Mobile Communication Conference (IEMCON)*, Vancouver, BC, Canada: IEEE, Oct. 2021, pp. 0343–0349. doi: 10.1109/IEMCON53756.2021.9623160.

[2] Y. Kadri, and H. Hadj Abdallah, "Performance evaluation of a stand-alone solar dish Stirling system for power generation suitable for off-grid rural electrification," *Energy Convers. Manag.*, vol. 129, pp. 140–156, Dec. 2016, doi: 10.1016/j.enconman.2016.10.024.

[3] A. Sassi, N. Zaidi, O. Nasri, and J. Ben Hadj Slama, "Energy management of PV/wind/battery hybrid energy system based on batteries utilization optimization," in *2017 International Conference on Green Energy Conversion Systems (GECS)*, Hammamet, Tunisia: IEEE, Mar. 2017, pp. 1–7. doi: 10.1109/GECS.2017.8066133.

[4] D. Saheb Koussa *et al.*, "Hybrid diesel-wind system with battery storage operating in standalone mode: Control and energy management – Experimental investigation," *Energy*, vol. 130, pp. 38–47, Jul. 2017, doi: 10.1016/j.energy.2017.04.127.

[5] M. H. Nawaz, M. U. Khan, A. Zahra, M. Ali, R. Wazir, and K. Ullah, "Optimal economic analysis of hybrid Off Grid (standalone) energy system for Provincial Capitals of Pakistan : A comparative study based on simulated results using real-time data," in *2018 International Conference on Power Generation Systems and Renewable Energy Technologies (PGSRET)*, Islamabad, Pakistan: IEEE, Sep. 2018, pp. 1–6. doi: 10.1109/PGSRET.2018.8685991.

[6] H. El-houari *et al.*, "Feasibility evaluation of a hybrid renewable power generation system for sustainable electricity supply in a Moroccan remote site," *J. Clean. Prod.*, vol. 277, p. 123534, Dec. 2020, doi: 10.1016/j.jclepro.2020.123534.

[7] A. T. D. Perera, R. A. Attalage, K. K. C. K. Perera, and V. P. C. Dassanayake, "Designing standalone hybrid energy systems minimizing initial investment, life cycle cost and pollutant emission," *Energy*, vol. 54, pp. 220–230, Jun. 2013, doi: 10.1016/j.energy.2013.03.028.

[8] C. Ghenai, T. Salameh, and A. Merabet, "Design, optimization and control of standalone Solar PV/Fuel cell hybrid power system," in *2017 International Renewable and Sustainable Energy Conference (IRSEC)*, Tangier: IEEE, Dec. 2017, pp. 1–5. doi: 10.1109/IRSEC.2017.8477338.

[9] A. Ahadi, and X. Liang, "A stand-alone hybrid renewable energy system assessment using cost optimization method," in *2017 IEEE International Conference on Industrial Technology (ICIT)*, Toronto, ON: IEEE, Mar. 2017, pp. 376–381. doi: 10.1109/ICIT.2017.7913260.

[10] L.-A. Mustață, G.-D. Sorea, and E. Helerea, "Energy management strategy with a hybrid renewable energy system for a standalone house," in *2024 International Conference on Applied and Theoretical Electricity (ICATE)*, Craiova, Romania: IEEE, Oct. 2024, pp. 1–6. doi: 10.1109/ICATE62934.2024.10748699.